ABSTRACT

Title of dissertation:	FUNDAMENTAL UNDERSTANDING OF THE CYCLOIDAL-ROTOR CONCEPT FOR MICRO AIR VEHICLE APPLICATIONS
	Moble Benedict, Doctor of Philosophy, 2010
Dissertation directed by:	Professor Inderjit Chopra Department of Aerospace Engineering

The cycloidal-rotor (cyclorotor) is a revolutionary flying concept which has not been systematically studied in the past. Therefore, in the current research, the viability of the cyclorotor concept for powering a hover-capable micro-air-vehicle (MAV) was examined through both experiments and analysis. Experimental study included both performance and flow field measurements on a cyclorotor of span and diameter equal to 6 inches. The analysis developed was an unsteady large deformation aeroelastic analysis to predict the blade loads and average aerodynamic performance of the cyclorotor. The flightworthiness of the cyclorotor concept was also demonstrated through two cyclocopters capable of tethered hover.

Systematic performance measurements have been conducted to understand the effect of the rotational speed, blade airfoil profile, blade flexibility, blade pitching amplitude (symmetric and asymmetric blade pitching), pitching axis location, number of blades with constant chord (varying solidity), and number of blades at same rotor solidity (varying blade chord) on the aerodynamic performance of the

cyclorotor. Force measurements showed the presence of a significant sideward force on the cyclorotor (along with the vertical force), analogous to that found on a spinning circular cylinder. Particle image velocimetry (PIV) measurements made in the wake of the cyclorotor provided evidence of a significant wake skewness, which was produced by the sideward force. PIV measurements also captured the blade tip vortices and a large region of rotational flow inside the rotor.

The thrust produced by the cyclorotor was found to increase until a blade pitch amplitude of 45° was reached without showing any signs of blade stall. This behavior was also explained using the PIV measurements, which indicated evidence of a stall delay as well as possible increase in lift on the blades from the presence of a leading edge vortex. Higher blade pitch amplitudes also improved the power loading (thrust/power) of the cyclorotor. When compared to the flat-plate blades, the NACA 0010 blades produced the highest values of thrust at all blade pitching amplitudes. The NACA blades also produced higher power loading than the flat plate blades. However, the reverse NACA 0010 blades produced better power loadings at lower pitching amplitudes, even though at high pitch amplitudes, regular NACA blades performed better. Among the three NACA sections (NACA 0006, NACA 0010 and NACA 0015) tested on the cyclorotor, NACA 0015 had the highest power loading followed by NACA 0010 and then NACA 0006.

The power loading also increased when using more blades with constant chord (increasing solidity); this observation was found over a wide range of blade pitching amplitudes. Asymmetric pitching with higher pitch angle at the top of the blade trajectory than at the bottom produced better power loading. The chordwise op-

timum pitching axis location was approximately 25–35% of the blade chord. For a constant solidity, the rotor with fewer number of blades produced higher thrust and the 2-bladed rotor had the best power loading. Any significant bending and torsional flexibility of the blades had a deleterious effect on performance. The optimized cyclorotor had slightly higher power loading when compared to a conventional micro-rotor when operated at the same disk loading. The optimum configuration based on all the tests was a 4-bladed rotor using 1.3 inch chord NACA 0015 blade section with an asymmetric pitching of 45° at top and 25° at bottom with the pitching axis at 25% chord.

The aeroelastic analysis was performed using two approaches, one using a second-order non-linear beam FEM analysis for moderately flexible blades and second using a multibody based large-deformation analysis (especially applicable for extremely flexible blades) incorporating a geometrically exact beam model. An unsteady aerodynamic model is included in the analysis with two different inflow models, single streamtube and a double-multiple streamtube inflow model. For the cycloidal rotors using moderately flexible blades, the aeroelastic analysis was able to predict the average thrust with sufficient accuracy over a wide range of rotational speeds, pitching amplitudes and number of blades. However, for the extremely flexible blades, the thrust was underpredicted at higher rotational speeds and this may be because of the overprediction of blade deformations. The inclusion of the actual blade pitch kinematics and unsteady aerodynamics was found crucial in the accurate sideward force prediction.

FUNDAMENTAL UNDERSTANDING OF THE CYCLOIDAL-ROTOR CONCEPT FOR MICRO AIR VEHICLE APPLICATIONS

by

Moble Benedict

Dissertation submitted to the Faculty of the Graduate School of the
University of Maryland, College Park in partial fulfillment
of the requirements for the degree of
Doctor of Philosophy
2010

Advisory Committee:
Professor Inderjit Chopra, Chair/Advisor
Professor J. Gordon Leishman
Professor James Baeder
Professor J. Sean Humbert
Professor Balakumar Balachandran

Dedication

To my parents and my wife.

Acknowledgments

I would like to thank my advisor, Dr. Inderjit Chopra for giving me the opportunity and freedom to work on many challenging and extremely interesting projects over the past six years. He has always been an inspiration for me. I am extremely thankful for all the support and guidance he has provided throughout my graduate studies. There has never been an occasion when I have knocked at his door and he has not spared me time. It has been a pleasure to work with and learn from such an extraordinary individual.

I am extremely grateful to Dr. Gordon Leishman for all the guidance he has provided in my research and in the art of writing excellent technical papers. My sincere thanks go out to Dr. James Baeder, Dr. Sean Humbert and Dr. Balakumar Balachandran for agreeing to serve on my thesis committee, for all their priceless suggestions and sparing their precious time reviewing the manuscript.

I am very thankful to Teju Jarugumilli, an undergraduate student who has worked very closely with me for the past two and a half years. He has been very instrumental in this research. I would like to thank all the other undergraduate students, Raghav Gupta, Jonathan Elliot and Elena Shrestha, who have worked with me over the past two years. I am extremely thankful to Manikandan Ramasamy for helping me with the PIV studies. Mani's persistence and dedication to research has been very inspirational for me and I could never forget those instances where his motivational pep talks have really lifted up my spirits. I would also like to thank Mattia Mattaboni and Dr. Masarati for the MBDyn analysis.

I owe my deepest thanks to my family - my mother, Mary Benedict, my father, Mathew Benedict and my sister Twinkle Benedict, who have always stood by me and guided me through my career, and have pulled me through against impossible odds at times. I would not have been where I am today without them. My wife, Rincy Mathew has been my constant source of inspiration for the past six years. I cannot thank her enough for understanding me, motivating me and bearing with my busy life for these many years. She has played a very prominent role in me successfully completing my PhD.

It is impossible to remember all, and I apologize to those I have inadvertently left out.

Table of Contents

List of Figures

xiii

Nomenclature

a	nondimensionalized location of 3/4-chord ahead of the pitching axis, η_r/c
$\bar{a}_b$	acceleration vector of an arbitrary point on the blade
A	cyclorotor rectangular projected area, $(b \times D)$
AR	aspect ratio of the blades, b/c
b	blade span
c	blade chord
C_d	drag coefficient
C_{d_i}	induced drag coefficient
C_{d_0}	profile drag coefficient
C_l	lift coefficient
C_{l_c}	circulatory lift coefficient
$C_{l_{nc}}$	noncirculatory lift coefficient
C_{l_α}	lift curve slope
C_P	power coefficient, $P/\rho A(\Omega R)^3$
C_T	thrust coefficient, $T_{Res}/\rho A(\Omega R)^2$
D	diameter
DL	disk loading, T_{Res}/A
e	oswald's efficiency factor
e_g	chordwise location of the blade c.g. ahead of the elastic axis
EI_y	flapwise blade bending stiffness
EI_z	lagwise blade bending stiffness
F_n, F_c	blade normal and chordwise forces
F_w, F_v	blade forces along the radial and tangential directions in the undeformed rotating frame
F_Z, F_Y	blade forces in the inertial frame along Z and Y axis respectively
FM	figure of merit
GJ	blade torsional stiffness
I_0	blade rotational moment of inertia about c.g. axis
k	reduced frequency
L_1, L_2, L_3, L_4	linkage lengths of the four-bar mechanism for blade pitching
m	mass per unit length of the blade
$\dot{m}$	mass flow rate per unit span
M	mass matrix
M_ϕ	blade pitching moment in the undeformed frame
N_b	number of blades
P	aerodynamic power
PL	power loading (thrust/unit power)
P_Y	momentum of the fluid per unit span in Y-direction
P_Z	momentum of the fluid per unit span in Z-direction

$\bar{r}$	position vector of an arbitrary point on the deformed blade
q	blade pitch rate
q_e	unsteady effective blade pitch rate
R	radius of the cyclorotor
s	non-dimensional distance traveled by the airfoil in semi-chords
t	blade thickness for the flat plate blades
T_{DU}	transformation matrix from an undeformed to deformed coordinate system
T_u, T_d	upstream and downstream thrust in the double multiple streamtube inflow model
T_z, T_y	rotor thrust in the inertial frame along Z and Y axis respectively
T_{Res}	resultant thrust
U_P	velocity component normal to the blade chord
U_T	velocity component tangential to the blade chord
v_i	induced velocity in the uniform inflow model
v_u, v_d	upstream and downstream induced velocities in the multiple streamtube inflow model
$\bar{V}_b$	velocity vector of an arbitrary point on the blade
$\bar{V}_w$	wind velocity vector at an arbitrary location on the blade
V	resultant fluid velocity
v, w	fluid velocity along $Y(\hat{J})$, and $Z(\hat{K})$ directions, respectively
v, w	tangential and radial blade deformations, deformations along $Y_R(\hat{j})$, and $Z_R(\hat{k})$ directions, respectively
w	wake velocity in multiple streamtube model
X_ξ, Y_η, Z_ζ	blade deformed coordinate system
$X(\hat{I}), Y(\hat{J}), Z(\hat{K})$	cyclorotor non-rotating inertial coordinate system
$X_R(\hat{i}), Y_R(\hat{j}), Z_R(\hat{k})$	cyclorotor undeformed rotating coordinate system
$X_\alpha(s), Y_\alpha(s)$	circulatory deficiency functions for angle of attack (α)
$X_q(s), Y_q(s)$	circulatory deficiency functions for pitch rate (q)

Greek Symbols

α	quasi-steady blade section angle of attack
α_e	unsteady effective angle of attack
β	phase angle subtended by the resultant thrust vector with vertical

η, ζ	coordinates parallel and normal to the blade chord in the deformed blade coordinate
η_r	chordwise location of 3/4-chord ahead of the pitching axis
ζ	wake age
ϕ	phase angle of the resultant vector
$\phi(s)$	wagner function
$\hat{\phi}$	blade sectional elastic twist
κ	inflow correction factor in the single streamtube model
ρ	air density
σ	rotor solidity, $Nbc/2\pi R$
Ψ	azimuthal position of the blade
Ω	rotational speed
θ	rigid blade pitch angle
θ_1	effective sectional geometric angle, $\theta + \hat{\phi}$

Abbreviations

BEMT	Blade Element Momentum Theory
CFD	Computational Fluid Dynamics
CSD	Computational Structural Dynamics
c.g.	center of gravity
DARPA	Defense Advanced Research Projects Agency
D-MS	Double-Multiple Streamtube
DoD	Department of Defense
DTMB	David Taylor Model Basin
FEM	Finite Element Model
LE	Leading Edge
LSB	Laminar Separation Bubble
MAV	Micro Air Vehicle
NUS	National University of Singapore
PIV	Particle Image Velocimetry
RANS	Reynolds Averaged Navier Stokes
SBIR	Small Business Innovation Research
SNU	Seoul National University
TE	Trailing Edge
UAV	Unmanned Aerial Vehicle
UVLM	Unsteady Vortex Lattice Method
VTOL	Vertical Take-off and Landing

Chapter 1

Introduction

In recent years, interest has been growing in a new class of very small fight vehicles called micro-air-vehicles (MAVs), which can prove to be an extremely important asset to the military as the battle grounds of the future move to restricted, highly populated urban environments. In the United States, the development of MAVs has been spearheaded by the Department of Defense (DoD) for a wide variety of civilian and military applications. The need for such miniature flying vehicles was first identified in 1992 through a DARPA2/RAND Corporation workshop on "Future Technology-Driven Revolutions in Military Operations", which investigated the concept of mobile microrobots at the 1-cm/1-g scale [1]. This was followed by a series of feasibility studies at the MIT Lincoln Laboratory and the U.S. Naval Research Laboratory, and this led to the creation of a DARPA Small Business Innovation Research (SBIR) program in the fall of 1996 to develop this new dimension in flight [2]. According to this program, the formal definition of a Micro Air Vehicle, or MAV, was an aircraft that would have no dimension larger than 6 inches, weigh approximately 100 g (which included a payload weight of 20 g) and have an endurance of one hour. The payload would typically be some type of sensor, optical, chemical or radiological, for example, and/or a radio transmitter. The envisioned military use of such an aircraft was as man-portable, eye-in-the-sky flying robot that could be
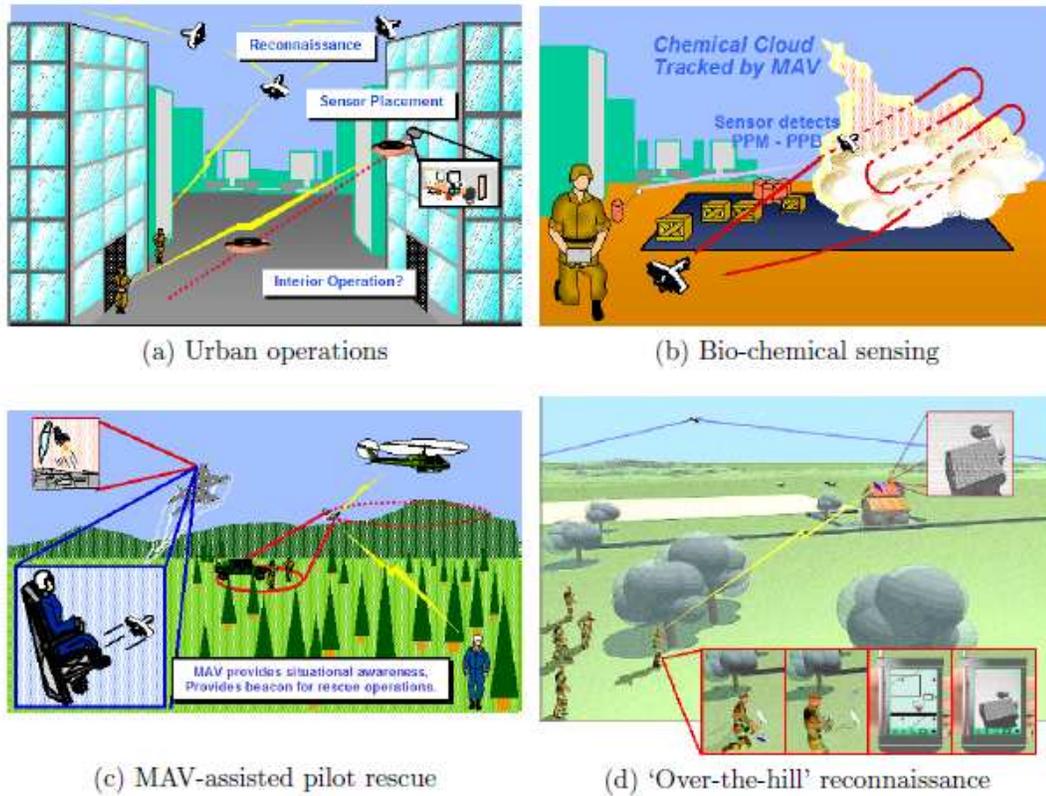
Figure 1.1: **Various MAV applications [2].**

carried and operated by an individual soldier, for increased situational awareness while minimizing exposure of him or herself to risk. Because of their small size and weight, these aircraft would have a much smaller footprint compared to the larger UAVs.

MAVs gained increasing interest recently because electronic surveillance and detection sensor equipment have become miniaturized so that the entire payload can be made less than 20 grams [3]. MAVs, being small and compact systems, offer several advantages such as easily transportable by a single operator, mobile platform, rapid deployment, low radar cross section, low noise and low production cost. The primary missions of interest for MAVs include surveillance, detection, communica-

Table 1.1: MAV design requirements [4].

Specification	Requirements	Details
Size	< 15.24 cm	Maximum dimension
Weight	≈ 100g	Objective GTOW
Range	1 to 10 km	Operational range
Endurance	60 min	Loiter time on station
Altitude	< 150 m	Operational ceiling
Speed	15 m/s	Maximum flight speed
Payload	20 g	Mission dependent
Cost	$1500	Maximum cost

tions, and placement of unattended sensors. Surveillance missions include video, infrared images of the battle field (referred to as the "over the hill" problem) and urban areas (referred to as "around the corner") (Fig. 1.1). These real-time images can provide the number and location of opposing forces. This type of information can be extremely useful in hostage rescue and counter-drug operations. Because of the availability of very small sensors, detection missions include the sensing of biological agents, chemical compounds and nuclear materials. MAVs may be also used to improve communications in urban or other environments where full-time line of sight operations are important. To establish guidelines for vehicle designs, an urban mission was assumed, and a set of baseline requirements was developed. These vehicle and mission performance requirements are summarized in Table 1.1 [4].
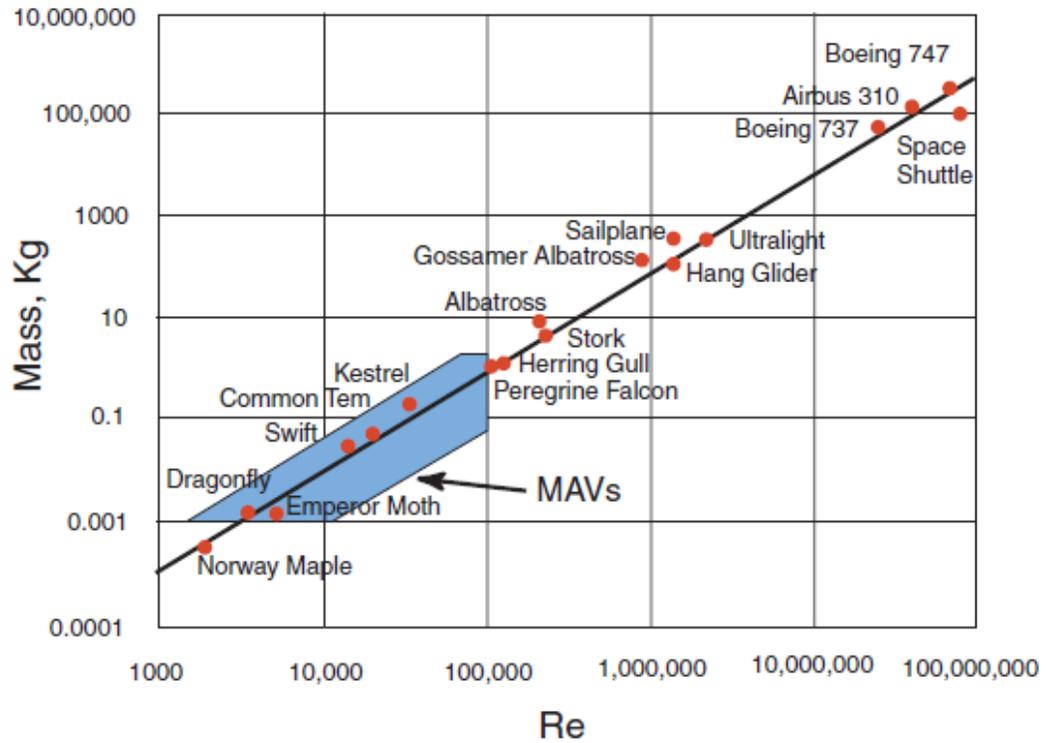
Figure 1.2: **MAV flight regime: Mass vs. Reynolds number [5].**
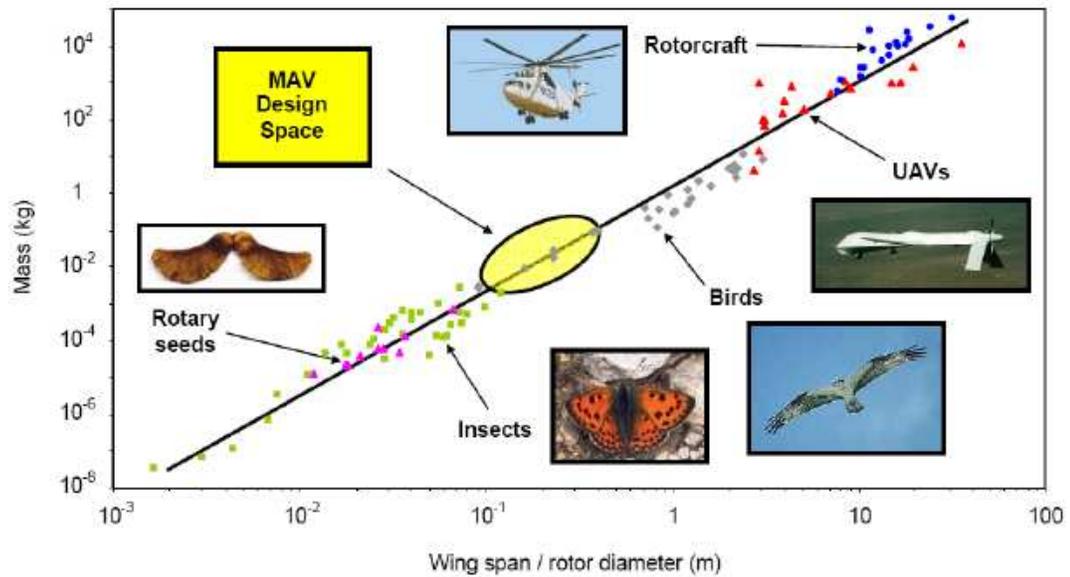
Figure 1.3: **MAV flight regime: Mass vs. Size [5].**

4

Significant technical barriers must be overcome before MAVs can be realized. These includes issues in small-scale power generation and storage, navigation, and communications as well as propulsion, aerodynamics, and control. One of the most interesting and least understood aspect of small-scale flight is the aerodynamics. The combination of small scale and low velocities results in a flight regime with very low Reynolds numbers. Figure 1.2 shows mass vs. Reynolds number for a wide range of animals and aircraft. MAVs lie within the shaded region at the lower left corner of the graph, bounded by Re between 2,000 and 100,000. This places MAVs in a regime totally alien to conventional aircraft. The mass vs. wingspan for MAVs and other larger UAVs is presented in Fig. 1.3.

In order to better understand these barriers, it is important to compare the performance of various existing flying MAV designs. Table 1.2 summarizes the size, weight, and some of the performance parameters of a few recent MAV designs [4]. This table clearly shows that the majority of current fixed-wing and rotary-wing designs rely on battery power for energy, conventional airfoil shapes for achieving lift, and propellers or rotors for achieving thrust. All, with the exception of Microbat, rely on conventional steady-state aerodynamic principles for generating thrust and lift. Similar to small insects and birds, CalTech/Aerovironment's Microbat uses flapping of its wings via an electric motor to generate thrust and lift, suggesting possibly a new paradigm shift in the design and development of future micro air vehicles.

Figure 1.4 displays the weight of various MAV designs vs endurance or maximum hover time. Although these represent substantial progress in the field, the

Table 1.2: Design and performance parameters of some representative MAVs [4].

Vehicle properties	Black Widow	Hoverfly	LUMAV	MicroSat	Microbat	MICOR
GTOW, g	80	180	440	110	10.5	103
Cruise speed, m/s	13.4	15-20	5	13.4-15.6	5	2
Wing loading, N/m^2	40.3	–	–	70.9	40	–
Disk loading, N/m^2	–	70	185	–	–	25
Wing span, cm	15.24	18	15.24	22.86	15.24	15.24
Max L/D	6	N/A	N/A	6	N/A	5
Endurance, min	30	13.2	20	25	2 min 16 s	3
Hover endurance, min	N/A	7.3	N/A	N/A	N/A	3
Power Source	Battery	Battery	IC engine	Battery	Battery	Battery
Energy density, $W-h/kg$	140	140	5500 methanol	150	100	150
Hover power	N/A	24.5	70	N/A	N/A	11
Hover FM	N/A	0.39	0.41	N/A	N/A	0.55
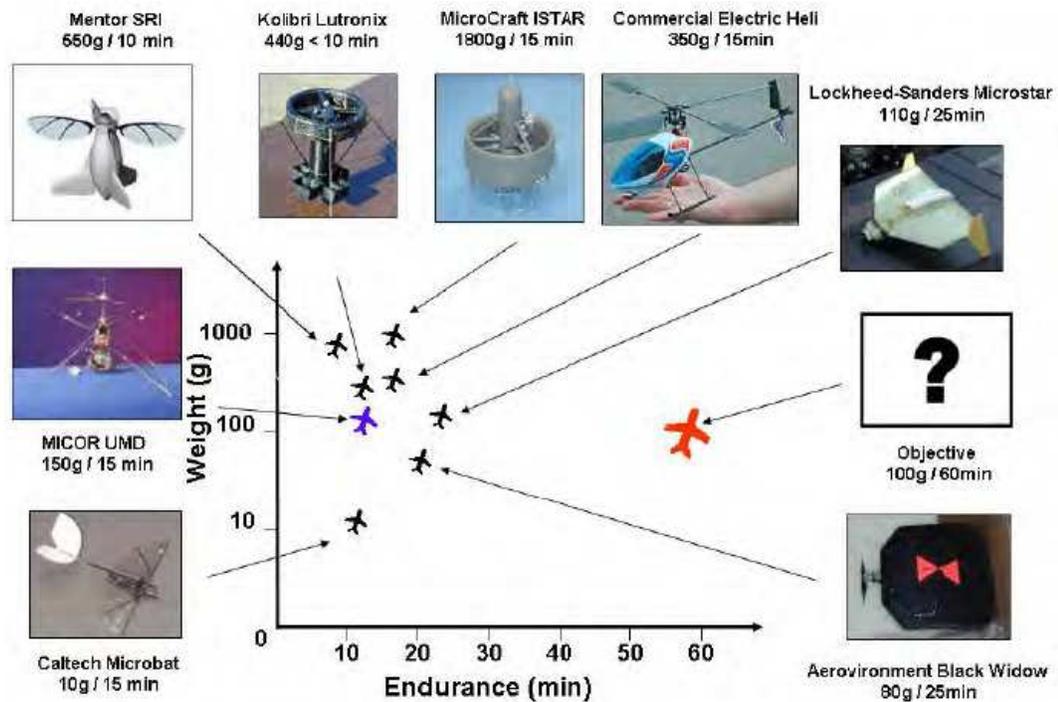
Figure 1.4: **Weight vs. Endurance for some of the existing MAVs [5].**

Comparison of Vehicle Mass Fractions

	Structure	Payload	Fuel/Pro pulsion	Electroni cs/Avioni
■ Black Widow	18	9	64	9
□ MICOR	12	9	70	9
■ Microbat	24	0	58	18
■ Boeing 767	35	17	39	9
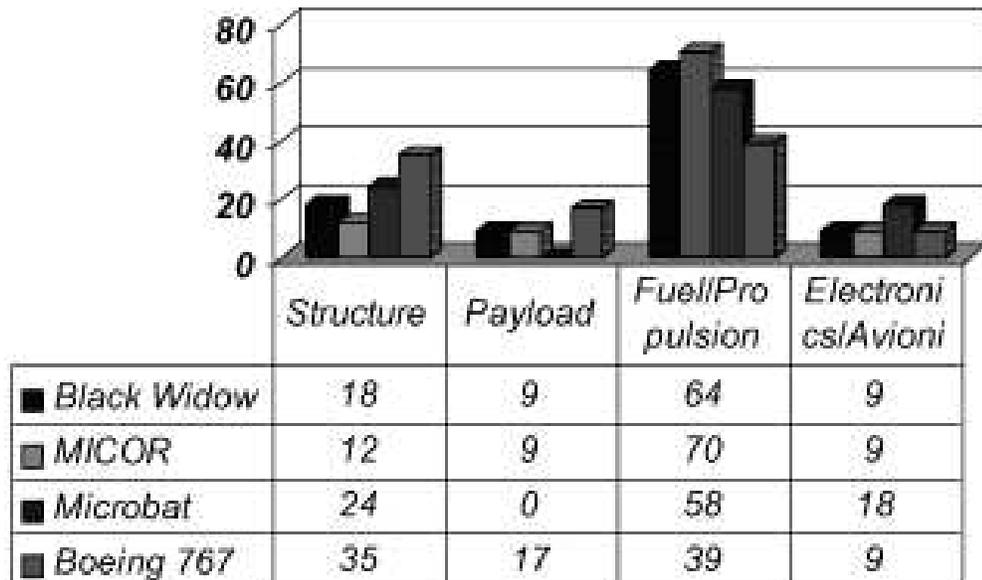
Figure 1.5: **Mass fraction of MAVs compared aganist a Boeing 767 [4].**

7

fact that none has been able to achieve true long-loiter times (>60 min) or efficient hovering flight is a testament to the difficulty of flying extended missions with small vehicles. Careful inspection of these vehicle designs reveals a variety of technical challenges for aerospace design engineers. For example, a detailed breakdown of the mass fractions of three of these vehicles reveals a number of shortcomings when compared to full-scale systems. Figure 1.5 displays the mass fractions of three microflyers compared to a full-scale Boeing 767 commercial jetliner [4]. Notice that for the small-scale flyers, the mass fraction of the propulsion system (batteries/power and motor/transmission) is in excess of 60% of the total vehicle mass.

Closer examination of biological fliers reveals that existing MAV designs cannot match the aerodynamic performance of insects and small birds in terms of stability, maneuverability, or efficiency. This should come as no surprise because design tools at this scale of flight are not available. In addition, the underlying physics that are responsible for the better performance of nature's great flyers is still not well understood. At the low Reynolds numbers where these MAVs operate, viscous effects in the flow are dominant over the inertial ones, boundary layers are thick and vulnerable to easy separation and undergo several complex phenomena. Separation, transition, and reattachment can all occur within a short chordwise distance, forming laminar separation bubbles that have a strong adverse effect on the lifting surface characteristics. Therefore, in order to design more efficient and maneuverable MAVs, it is important to clearly understand the aerodynamics at these low Reynolds numbers.

1.1 Low Reynolds Number Aerodynamics

The optimal airfoil shape for a wing to obtain maximum lift-to-drag ratio depends on the size and operating speed of the wing. This dependence is called scale effect. The significance of scale effect was first recognized in the 1930s. This relates to the phenomenon that an airfoil that has excellent qualities on an insect or bird may not exhibit these qualities when scaled up to a full-scale airplane wing, and vice versa. In fluid dynamics, the sense of scale is best quantified by a non-dimensional parameter called the Reynolds number (Re), which is proportional to the product of the size and the velocity of the object that is moving relative to the fluid. As shown in Fig. 1.2, large aircraft, such as commercial airliners, operate at Reynolds numbers in the tens of millions, whereas MAVs operate in a Reynolds number regime of approximately 10,000 to 50,000 three orders of magnitude lower. The Reynolds number is given by the formula

$$Re = \frac{\rho v l}{\mu} \tag{1.1}$$

where ρ is the density of the fluid, μ is the dynamic viscosity of the fluid, v is the relative velocity between the object and the fluid, and l is a characteristic length of the object. Reynolds number can be considered as a ratio between the inertial forces and the viscous forces that act on fluid elements in the flow. At high Reynolds numbers, the inertial forces dominate, while at low Reynolds numbers, the nature of the flow is more strongly affected by the effects of viscosity. When inertial forces dominate the flow (ie. high Re), then the flow becomes turbulent and disorganized because local increases in momentum cause instability. When $Re > 10^6$, most of

the boundary layer on the wing is turbulent. At lower Reynolds numbers, when viscosity is dominant, the flow is laminar and smooth because viscosity distributes and transports momentum throughout the flow. As far as airfoils are concerned, this results in two immediate effects: first, a decreased ability of the fluid to withstand adverse pressure gradients, and therefore to separate easily from the surface of the airfoil, thereby reducing the maximum lift capability and increasing the pressure drag; and second, an increase in the skin friction drag when the flow does remain attached to the airfoil. Together, these effects result in extremely low lift-to-drag (L/D) ratios for airfoils in low-Reynolds-number flows. Certain airfoil shapes, similar to those found in bird and insect wings, are optimized for low-Re flight, and these do far better in this flight regime than 'conventional' airfoils that have been designed for larger, manned aircraft; however, the highest L/D ratios achieved by even these optimized, low-Re airfoils are still substantially lower than those achieved by the conventional airfoils at higher Reynolds numbers.

The earliest systematic study of low Reynolds number aerodynamics was conducted by Schmitz during the 1930s [6]. This study focussed on three different airfoil shapes: a thin flat plate, a thin cambered plate, and a thick cambered airfoil (N60 airfoil) and the forces generated by airfoils was measured in the Reynolds number range $2 \times 10^4 < Re < 2 \times 10^5$. One of the important conclusion from the study was that the thick cambered airfoil has a critical Reynolds number where the performance changes drastically. Figure 1.6 is a plot of his results for the N60 airfoil across a range of Reynolds numbers. In this plot, the lift coefficient (C_l) and drag coefficient (C_d) are called c_a and c_w (the German convention). Also, the plot only shows
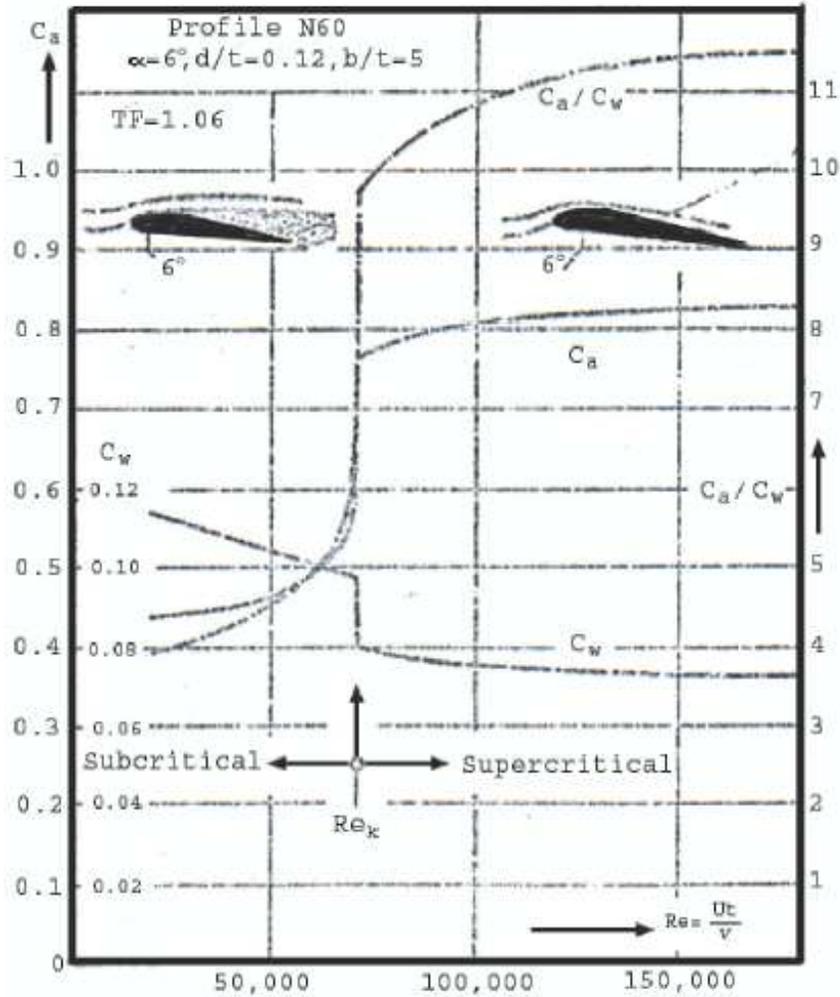
Figure 1.6: **Variation of the maximum lift, minimum drag, and maximum lift-to-drag ratio of the N60 airfoil plotted with Reynolds number (Schmitz [6]).**
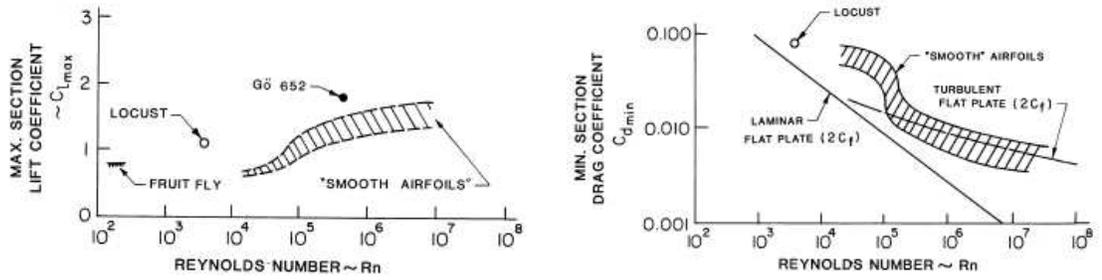
(a) Maximum lift coefficient ($C_{l_{max}}$).

(b) Minimum drag coefficient ($C_{d_{min}}$).

Figure 1.7: **Variation of maximum lift coefficient and minimum drag coefficient with Reynolds number (Mcmaster and Henderson [10]).**

the maximum C_l, minimum C_d, and the maximum lift-to-drag ratio (C_l/C_d). Above the critical Re range, the maximum C_l and maximum C_l/C_d is much higher than below, and the minimum C_d has the opposite trend. When an airfoil is below its critical Re range, the flow is dominated by viscous forces and remains laminar over the entire airfoil. Above this range, the flow will transition to turbulent somewhere along the airfoil.

Over the next few decades, Schmitzs results were verified and expanded upon by many researchers such as, Abbott [7], Riegels [8], and Althaus et al [9]. For most airfoil sections, the critical Reynolds number is in the range $10^4 - 10^6$. McMasters and Henderson [10] generalized these results in 1979 by plotting the maximum lift, minimum drag, and lift-to-drag ratios of airfoils across this range of Reynolds number, with a wide band as shown in Figs. 1.7(a), 1.7(b) and 1.8, respectively. For the smooth airfoils, the maximum lift coeffcient drops around the critical Reynolds number (Fig. 1.7(a)) and the minimum drag coefficient increases steeply (Fig. 1.7(b)) around the same Reynolds number range. As shown in Fig. 1.8, in general, smooth
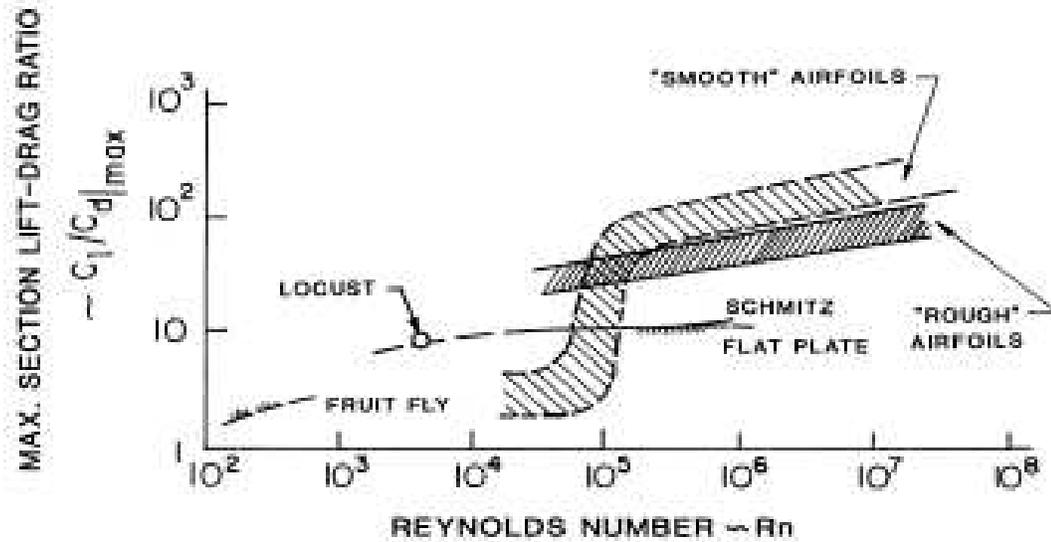
Figure 1.8: **Variation of maximum C_l/C_d with Reynolds number (Mcmaster and Henderson [10]).**

airfoils have a higher lift-to-drag ratio than rough airfoils at high Reynolds numbers ($> 10^5$). However, roughness improves the performance of airfoils at low Reynolds numbers. At low Reynolds numbers smooth airfoils experience a large drop in lift-to-drag ratio, whereas, the rough airfoils perform almost as well as they did at higher Reynolds number. Some representative airfoil sections for operating in this transitional range are shown in Fig. 1.9 [11]. At the low end, there are insects, with the interesting feature that it is not necessary to have a smooth surface; in fact, it is likely that the discontinuities are desirable to delay flow separation. For birds, however, smoothness begins to be important, as shown by the pigeon section. In the middle range is the Eppler 193, an airfoil with excellent performance at a Reynolds number of about 100,000.

Mueller performed extensive flow visualization and force measurement ex-
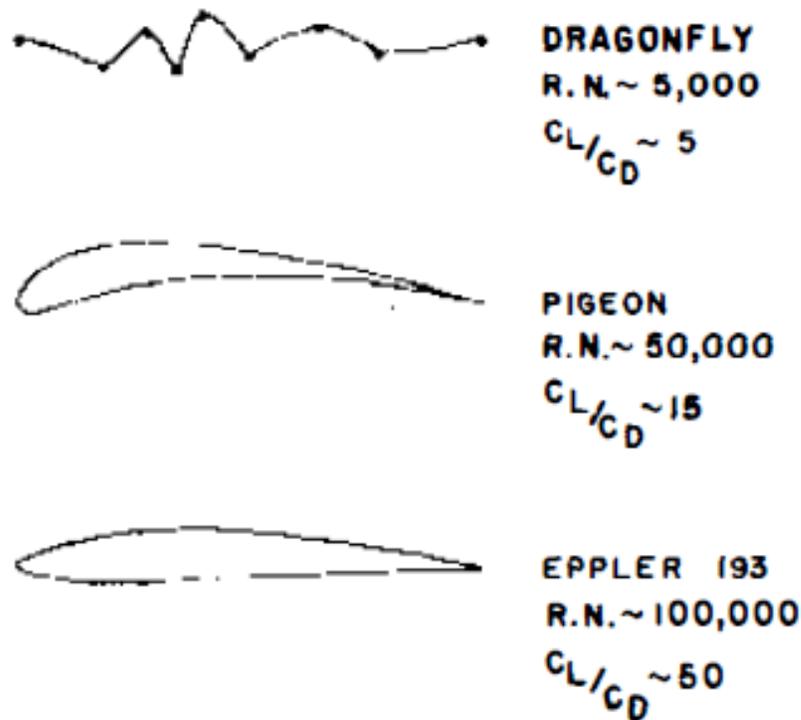
Figure 1.9: **Low Reynolds number airfoils [11].**

periments to understand the reason for the degradation of airfoil performance at low Reynolds numbers [12]. His studies focused on measuring the lift and drag forces on the symmetric NACA 663-018 airfoil at a Reynolds number range of $4 \times 10^4 < Re < 4 \times 10^5$. As shown in Fig. 1.10(a), the lift measurements made at $Re = 4 \times 10^4$ show a dramatic change at an AOA of 8°, whereas this phenomenon was not seen at a higher Reynolds number (4×10^5) (Fig. 1.10(b)). Using smoke visualization, Mueller showed that the drastic increase in lift coefficient found at $Re = 4 \times 10^4$ and 8° is due to the formation of a Laminar Separation Bubble (LSB) at that angle of attack. OMeara and Mueller [13] showed that the length of the sep-aration bubble tends to increase with a reduction in Reynolds number. A reduction in the turbulence intensity also tends to increase the length of the bubble. The lift-

14
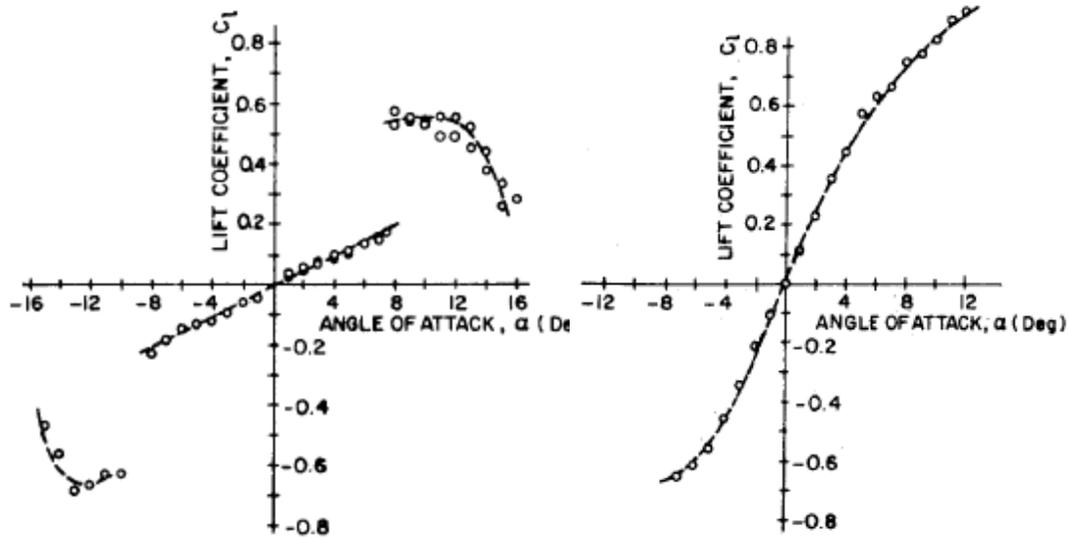
(a) Re $= 4 \times 10^4$.   (b) Re $= 4 \times 10^5$.

Figure 1.10: **2-D lift coefficient measured by Mueller at two different Reynolds numbers [12].**

curve slope is affected by separation bubbles. A longer bubble is usually associated with a decrease in the lift-curve slope [14]. The laminar separation bubble will be discussed in more detail later in this section.

Mueller also performed numerous experiments on low aspect ratio $(AR < 3)$ finite wings [15, 16]. Compared to the 2-D case, for the finite low AR wings, the linear region of the C_l vs. α curve was longer and α_{stall} tended to increase. Moreover, there was no abrupt stall for low aspect-ratio wings. The C_l often reached a plateau and then remained relatively constant, or even started to increase, for increasing angles of attack. Changing the aspect ratio of the models did not appear to have a measurable effect on the drag coefficient at Re=80,000. With cambered plates, minimum C_D was slightly larger than for flat plates. The maximum lift coefficient was also larger, as expected. Overall, lift-to-drag ratios for cambered plates were

15

higher. Moreover, the variation of C_l with angle of attack at small angles was less linear for cambered plates than for flat plates. Tests performed with two different trailing edges, sharpened, and elliptical, showed absolutely no difference in both lift and drag for both infinite and finite wings. This observation was consistent with Laitone [17], who showed that at low Reynolds numbers, a sharp trailing edge is not as critical as for larger Reynolds numbers. Even an elliptical or sharp leading edges did not make any difference. However, Laitone [17] did notice a significant increase in lift at Re = 20,700 for a thicker reversed NACA 0012 airfoil (the sharp trailing edge was facing the flow) (Fig. 1.13(b)). Increase in turbulence in the flow reduced the drag at low angles of attack, may be due to the earlier laminar shear layer transition; however, at high angles of attack, when the flow was already separated, increase in tubulence increased the drag.

One of the most extensive low Reynolds airfoil studies was conducted by Michael Selig starting in 1986 at Princeton University [18]. In this study, lift and drag were measured for 60 airfoils primarily at a Reynolds number range of $6 \times 10^4 < Re < 3 \times 10^5$. The lift was measured directly using a strain-gage force balance, while the drag was estimated by the wake deficit measured by a pitot tube traversed vertically through the wake. This study showed that at Re > 10^5, the drag polar of all the airfoils were qualitatively similar to drag polars at all higher Reynolds numbers. However, as Reynolds number was decreased below this number, many of the airfoils had a significant increase in drag coefficient at moderate lift co-efficients, while the drag coefficient at low and high lift coefficients is relatively low. This can be seen in Fig. 1.11, where the drag polar for the Eppler 387 (E387) airfoil,
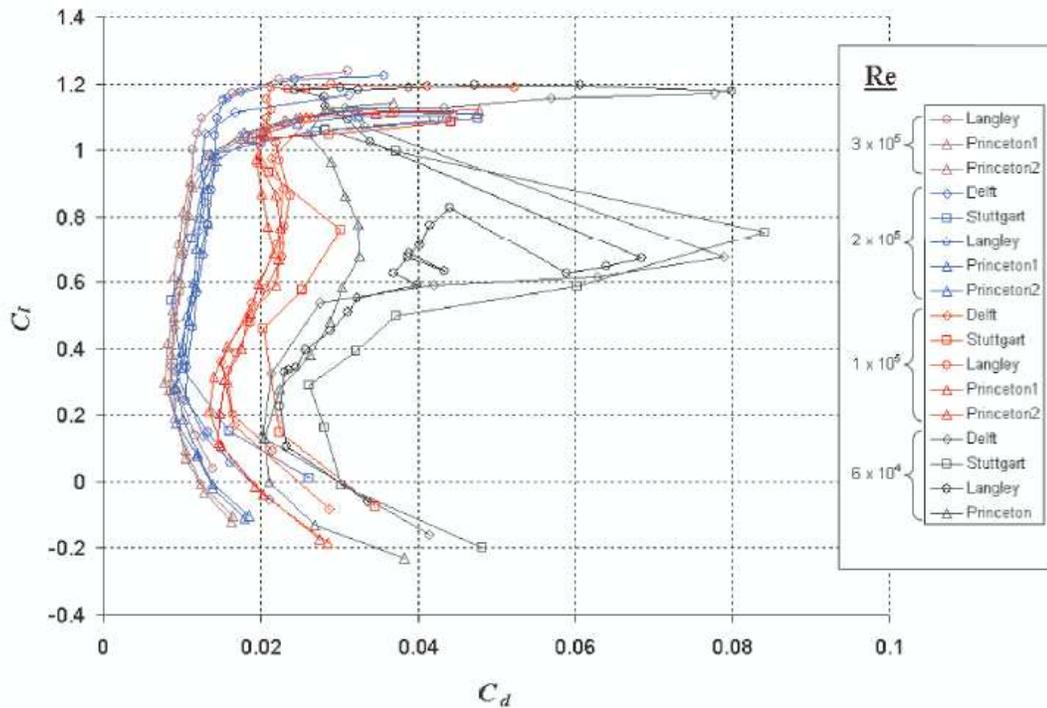
Figure 1.11: **McArthur's compilation of low Reynolds number C_l and C_d from various facilities [19].**

as measured by various facilities, is plotted across a range of Reynolds numbers [19]. The two most interesting features of Fig. 1.11 are that there is more disagreement at the lowest Re and that, despite this disagreement, there is a consistent, qualitative change in the shape of the curve at the lowest Re. The data obtained at the lowest Re are less repeatable than data obtained at higher Re mainly because of three reasons [19]. (1) The forces measured here are much smaller than the higher Re, thus the relative uncertainty in the measurement is much higher. (2) The forces generated are much more sensitive to free-stream turbulence, surface roughness, and model geometry. (3) Different measurement techniques can return different results.

The most common explanation for the unusual behavior of airfoils and wings

17
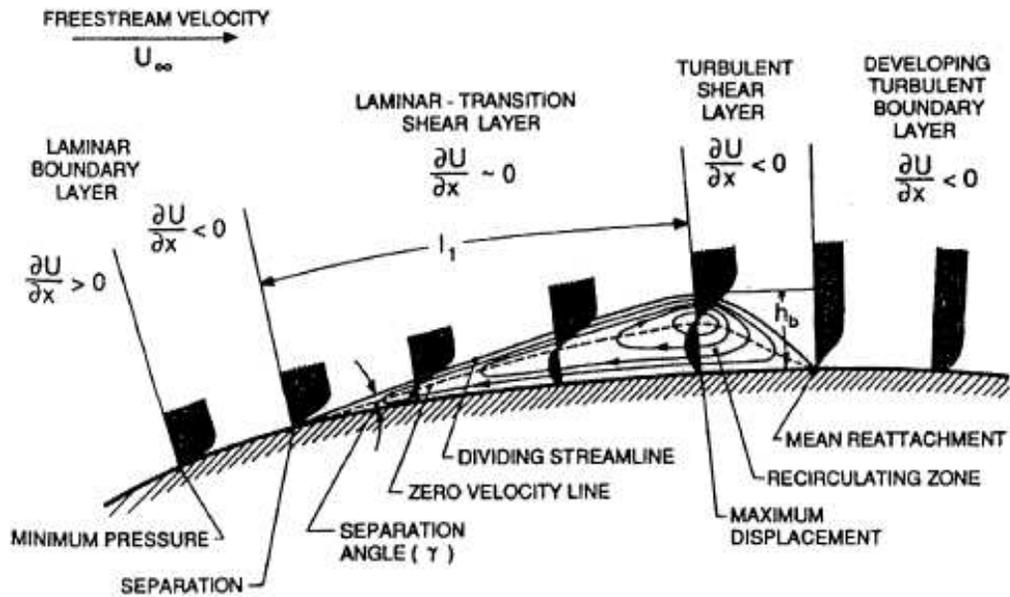
Figure 1.12: **Laminar separation bubble [19].**

at these low Re ($10^4 < Re < 10^5$) is the existence of a laminar separation bubble

(LSB) at certain angle of attacks. Selig claims that the LSB causes the peculiar

drag increase at moderate lift coefficients. As demonstrated in Fig. 1.12 [19], an

LSB typically begins with a laminar boundary layer that encounters an adverse

pressure gradient, which causes the boundary layer to separate. The laminar sepa-

rated shear flow is unstable and transitions to a turbulent separated shear flow. The

turbulence then transports momentum from the free-stream, across the shear layer,

and down towards the surface. When the momentum transport is sufficient, the

turbulent boundary layer is considered to be reattached to the surface, thus closing

the separation bubble. Laminar separation bubbles occur on the upper surface of

most airfoils at Reynolds numbers above about 50,000. These bubbles become larger

as the Reynolds number decreases, usually resulting in a rapid deterioration in per-
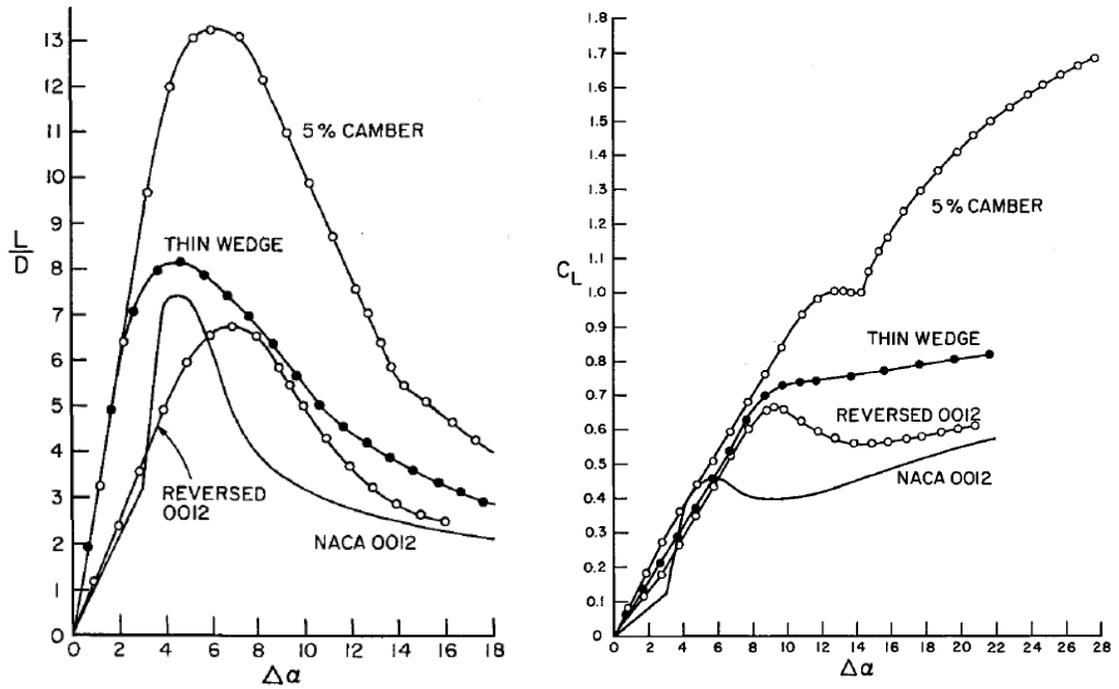
(a) Variation of L/D ratio with angle of attack.

(b) Variation of lift coefficient with angle of attack.

Figure 1.13: **Variation of C_l and C_l/C_d with angle of attack at Re=20,700 for wings of aspect ratio = 6 (Laitone [17]).**

formance, i.e., substantial decrease in L/D. However, for airfoils operating in excess of 10^6 Reynolds number, this adverse gradient normally occurs after transition so that it is impressed on a turbulent boundary layer that can negotiate quite severe adverse pressure gradients without separation.

Laitone performed systematic tests on finite wings (aspect ratio = 6) in a Reynolds number range of $2 \times 10^4 < Re < 7 \times 10^4$ [17]. Laitone claimed that his data is the first and only reliable force measurements at $Re < 10^5$ because his force balance has an uncertainty of 0.1 mN while Schmitz was 1 mN and Mueller had a 10 mN resolution. In addition, the wind tunnel used in this study had much

19

lower turbulence levels (0.02%). Laitone measured the lift and drag of a thin wedge (which approximated a flat plate), a 5% cambered plate, and the NACA 0012 at angles of attack from zero lift to well beyond stall. As shown in Fig. 1.13(a), at Re = 20,700, the 5% cambered plate achieves the highest lift-to-drag ratio, while the NACA 0012 had the lowest, even lower than a simple thin wedge. The results (Fig. 1.13(b)) also shows that the NACA 0012 has a higher lift coefficient when it is placed backwards in the flow, that is, when the trailing edge is used as the leading edge. These results indicate that a small leading edge radius is preferred at this range of Reynolds numbers.

Mueller [16] and Carmichael [20] summarized the performance of airfoils in different low Reynolds number regimes. In the Reynolds number range between 1,000 and 10,000, the boundary layer flow is laminar and it is very difficult to cause transition to turbulent flow. Mostly large insects such as dragon fly, hawkmoth, etc., fly in this regime. The dragon fly wing has a sawtooth single surface airfoil. It has been speculated that eddies in the troughs help keep the flow from separating. It has also been been found that both blunt leading and trailing edges enhance the aerodynamic performance. For chord Reynolds numbers between 10,000 and 30,000, the boundary layer is again completely laminar and artificial tripping has not been successful. If the boundary layer separates, it does not reattach.

The range between 30,000 and 70,000 is of great interest to MAV designers as well as model aircraft builders. The choice of an airfoil section is very important in this regime since relatively thick airfoils (i.e., 6% and above) can have significant hysteresis effects caused by laminar separation with transition to turbulent flow.

Also below chord Reynolds numbers of about 50,000, the free shear layer after laminar separation normally does not transition to turbulent flow in time to reattach. Near the upper end of this range, the critical Reynolds number can be decreased by using boundary layer trips. Thin airfoil sections (i.e., less than 6% thick) at the upper end of this regime can exhibit reasonable performance. At Reynolds numbers above 70,000 and below 200,000, extensive laminar flow can be obtained and therefore airfoil performance improves although the laminar separation bubble may still present a problem for a particular airfoil.

1.2   Conventional MAV Designs

From an aerodynamics perspective, the key challenge for an MAV designer is the low lift-to-drag ratios of even the most optimized airfoil geometries (L/D tend to range from 2 to 8). Several fixed-wing MAVs have already been successfully tested [21–25]. One particular example [24, 25] has a weight of 80 grams and a flight endurance of about 30 minutes. Even though fixed-wing MAVs may be the best performers today in terms of the imposed size and weight constraints, they lack the ability to hover or to operate in highly constrained environments. These latter attributes are important for many missions, including surveillance in constrained environment. Therefore, the development of efficient hovering concepts will lead to more versatile and useful MAVs with expanded flight envelopes.

At present, rotary-wings/helicopters is the most practical choice for hovering and low-speed flight. To this end, several hovering-capable MAVs based on single

main rotor or coaxial rotor configurations have been successfully built and flight-tested [4, 26, 27]. However, hovering and low-speed flight are already states of high power consumption, the situation is further exacerbated by the degraded performance of conventional airfoils at the low Reynolds number range (10,000 – 50,000) at which these MAVs operate. In fact, most MAVs based on conventional rotors have shown relatively low performance, e.g., the maximum figure of merit achieved to date is only about 0.65 [4]. Whereas, full-scale rotors achieve FM values in the range from 0.7 to 0.85. In a full-scale rotor, typically 30% of the power is consumed by the profile losses and 70% by the induced losses. However, at low Reynolds numbers, the profile power has a much larger influence over the total power required by the rotor. At high thrust coefficients, the contribution of profile power goes up to 45%. The performance of some of the existing fixed-wing and rotary wing MAVs are given in Table 1.2. None of the present rotary-wing MAVs have hover-endurance more than 15 minutes. This implies that scaling down full-scale concepts such as fixed-wings and helicopters may not be the right approach for operating in a completely different aerodynamic regime. Therefore, investigating alternate solutions such as flapping wings, cyclorotors, etc., is important because they might have potential for better performance at the low Reynolds numbers.

As far as the flapping wings are concerned, the birds and insects are elegant designs of nature for operating in these Reynolds numbers, but the man-made flappers could barely take-off and are not even comparable to these natural flyers in terms of performance. The efficiency of the flappings wings is still debatable, even though it has been shown that the unsteady effects could enhance the lift of these wings
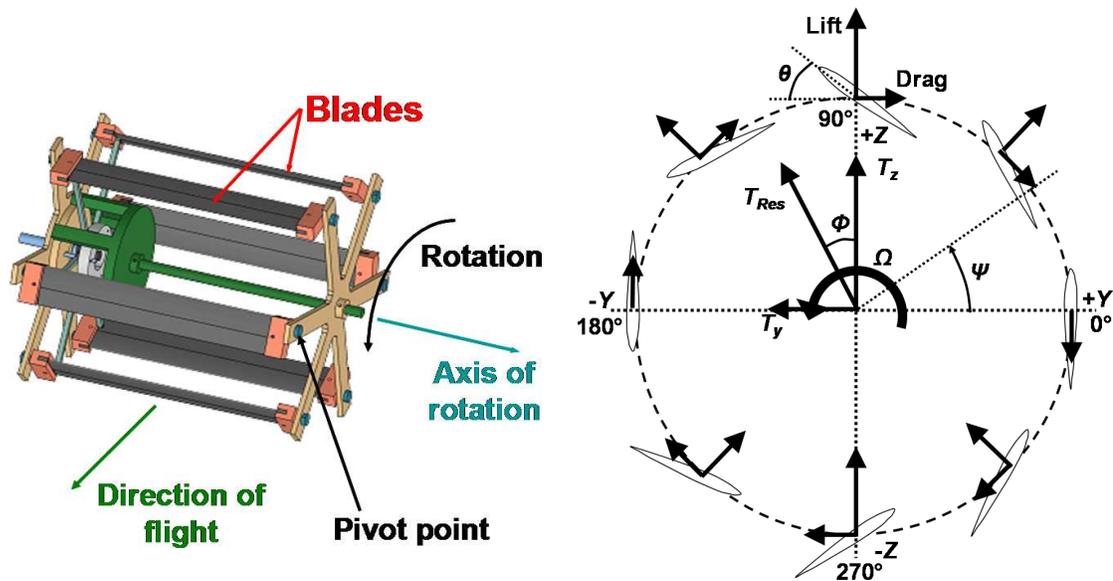
(a) Schematic of a cycloidal rotor.

(b) Blade kinematics and forces on a cycloidal rotor.

Figure 1.14: **Cycloidal rotor concept.**

many fold. Although potential for higher lift producing capability of flapping-wing ornithoptic configurations has been demonstrated for aircraft of the MAV-size and smaller, the mechanical complexity and large oscillatory inertial loads produced by such systems are barriers that remain to be overcome.

However, cycloidal rotor is still a rotary-wing concept, and therefore does not have to deal with the mechanical complexity and large oscillatory loads of a flapping concept, but can still bring in some performance improvement due to the significant unsteady effects caused by the large amplitude pitching motion of the blade.

1.3 Cycloidal-Rotor Concept

In the present study, a MAV concept based on a cycloidal-rotor (cyclorotor) system has been proposed as an alternative to the above hovering concepts. A cyclorotor (also known as a cyclocopter or cyclogyro) is a rotating-wing system (Fig. 1.14(a)) where the span of the blades runs parallel to the axis of its rotation. The pitch angle of each of the blades can be varied cyclically by mechanical means such that the blades experiences positive angles of attack at both the top and bottom positions of the azimuth cycle (Fig. 1.14(b)). The resulting time-varying lift and drag forces produced by each blade can be resolved into the vertical and horizontal directions, as shown in Fig. 1.14(b). Varying the amplitude and phase of the cyclic blade pitch can be used to change the magnitude and direction of the net thrust vector (T_{Res}) produced by the cyclorotor.

Compared to a conventional rotor, each spanwise blade element of a cyclorotor operates at similar aerodynamic conditions (i.e., at similar flow velocities, Reynolds numbers, and angles of attack), and so the blades can be more easily optimized to achieve best aerodynamic efficiency, at least in principle. Moreover, because the blades are cyclically pitched once per revolution (1/rev), unsteady flow mechanisms may delay blade stall onset and so augment the lift produced by the blades. Prior experiments have suggested that cyclorotors can reach comparable efficiencies to conventional rotor systems [28] and may also produce relatively higher values of maximum thrust. Furthermore, because the thrust vector of a cyclorotor can be almost instantaneously set to any direction perpendicular to the rotational axis,

compared to a MAV powered by a conventional rotor system a cyclorotor-based MAV may ultimately show better maneuverability and agility, which are particularly important attributes for constrained indoor flight operations.

1.4   Scientific Studies on Cyclorotors

The idea of cyclorotor is more than 100 years old, but the question of who originally invented it is open to debate. Although, the feasibility of the cyclorotor concept has been proven both theoretically and experimentally by leading aerospace researchers, there have not been any successful flying cyclogyros [29, 30]. A brief history of cyclogyros is provided in Appendix A.

Most of the attempts in the past to build a flying cyclogyro/cyclocopter (discussed in Appendix A) did not include any systematic scientific studies (theoretical or experimental) to clearly understand the physics of such a system. This was the main reason why none of these attempts succeded or in many cases did not even go beyond the design stage. This section includes most of the scientific studies that were performed on cyclorotors from 1920s to the present.

In 1920s, Professor Kurt Kirsten of the University of Washington pioneered the research on cycloidal propulsion systems both for air vehicles and marine applications [31,32]. Kirsten collaborated with Mr. W. E. Boeing and started conducting tests on the cycloidal propeller which he designed, known as the "Kirsten-Boeing" propeller. The initial success of these tests led to the establishment of the "Kirsten-Boeing Engineering Company" in Seattle (Washington) to further improve the man-

(a) Cycloplane in Popular Science magazine.

(b) Cycloplane.

Figure 1.15: **Kirsten's Cycloplane [33].**

(a) Cycloplane model in the wind tunnel.
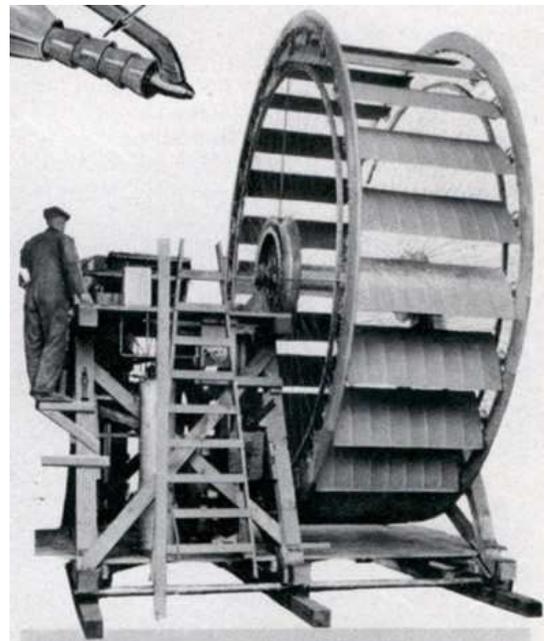
(b) Hover test rig for the full-scale cyclorotors.

Figure 1.16: **Kirsten's test setup [33].**

ufacture of "Kirsten-Boeing" propellers.

Kirsten identified that one of the main advantages of the cycloidal propeller is its ability to rotate the thrust vector to any direction around the azimuth almost instantly. The plan was to utilize the thrust vectoring ability of the cycloidal propellers for two applications, (1) three-dimensional control on an airship and, (2) to build a "cycloplane" (Figs. 1.15 and 1.16(a)) which can perform both hover and forward flight. For airship control, if the propellers are installed with their axis of rotation perpendicular to the vertical plane of the airship (Figs. 1.17 and 1.18(a)), it is then possible to orient the thrust in the desired directions to rise, descend, or move forward and backward. On the other hand, if the axis of rotation lie in the vertical plane, the airship can be driven laterally. This can improve the maneuverability of the airship to a great extent. One of the main advantages of using cycloidal propellers for airships is that the control of airship is independent of the flight speed and has very high "rudder-forces" at its disposal.

The first model built was a small propeller of 10.2 inches diameter and 5.9 inches blade span, which was tested in the wind tunnel of the University of Washington. The functioning of this experimental propeller proved very satisfactory. A larger model was then built and more accurate measurements were made at different rotational speeds and advance ratios and establised the fact that the best results depend on the ratio of the blade chord to the propeller diameter. A large airship propeller was then made as shown in Fig. 1.16(b). It had 24 blades, 4 feet 9.1 inches long and 22 inches wide, the diameter of the whole propeller being 15 feet 1.1 inches. The propeller was driven using a 400 HP Wright airplane engine, which through a
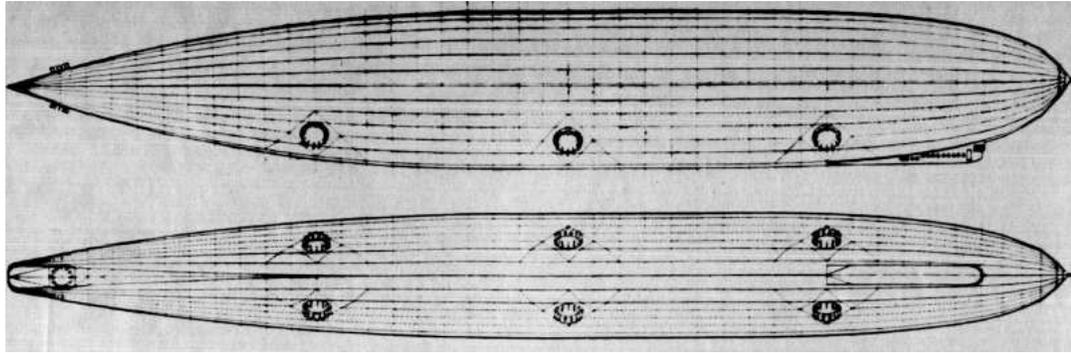
Figure 1.17: **Side view and top view of an airship installed with Kirsten-Boeing propellers [31].**

reduction gear drove the propeller at only 225 rpm. The thrust generated was about 212 lbs. Fig. 1.16(b) also shows the balance used for measuring the thrust. The hub of the propeller was made of cast aluminum. The rim was constructed out of duralumin, while steel cables were used for bracing. The blade were fabricated with a duralumin tubular axle, duralumin ribs and fabric covering.

After good results had been obtained with these experimental propellers, as regards efficiency, facility of control and quiet operation, owing to low rotational speeds, it was planned to install the Kirsten-Boeing propellers on the American airship "Shenondoah", as shown in Figs. 1.17 and 1.18(a). It can be seen that the outer rim was left off so that the blades project directly into the open air. Six main propellers were thus designed with their axis 30° to the horizontal plane. The propellers were designed for a thrust of 1800 pounds each. The total weight of the airship equipped with the Kirsten-Boeing propellers was estimated to be less than that of conventional screw propellers. Even though everything was ready, unfortunately, weeks before the installation, Shenondoah crashed and there was no
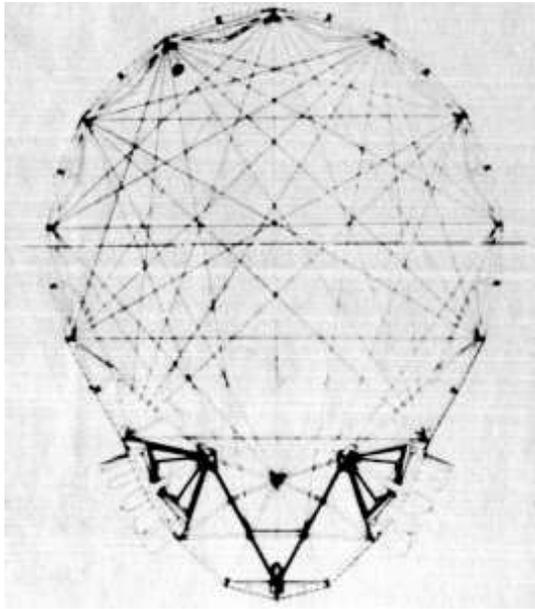
(a) Front view of the airship with Kirsten-
Boeing propellers.
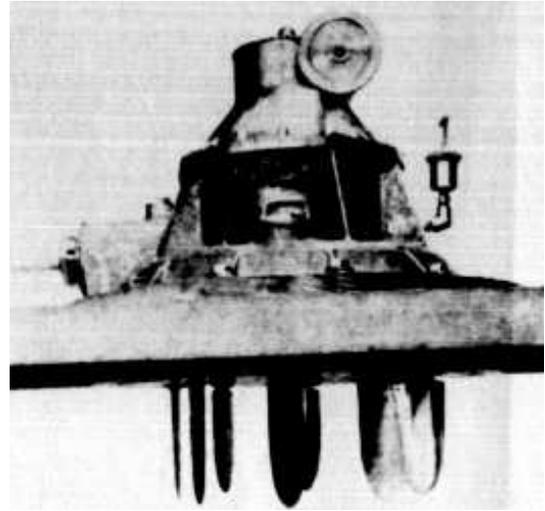
(b) Kirsten-Boeing propeller modified as a ship
propeller.

Figure 1.18: **Kirsten-Boeing cyclopropellers [31].**

other airship available to carry out the plan. This stopped the further development

of Kirsten-Boeing propellers.

In the meantime, Kirsten modified the propeller design so that they could be

used for driving boats (Fig. 1.18(b)). Three different model propellers each with 16

blades were made and installed in turn on an experimental boat. The boat propeller

required special measures to keep the water away from the driving mechanisms. The

boat made various trial trips covering a distance of about 4000 nautical miles in

both salt and fresh water, thereby demonstrating the practical utility of this kind of

propellers. After the trial trips, the propellers were tested in the naval model-testing

basin in Washington and it was found to have an efficiency of about 80% with a

slip of 20%. The boat equipped with a Kirsten-Boeing propeller requires no rudder
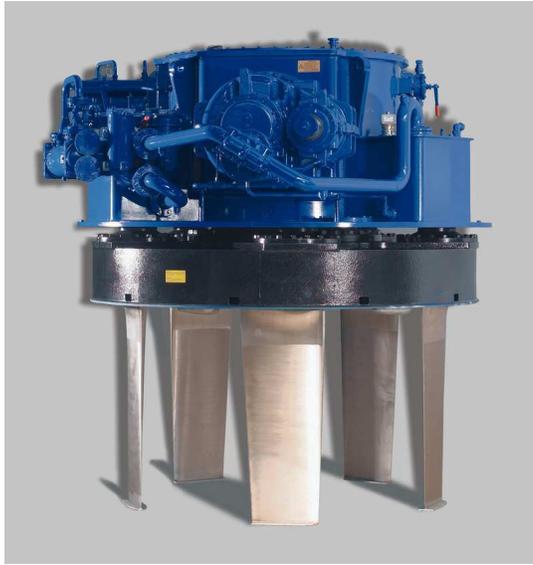
(a) Voith-Schneider propeller [34].

(b) Voith-Schneider propellers installed on a ship [35].

Figure 1.19: **Voith-Schneider propeller.**

because of the thrust vectoring ability and has exceptional maneuverability. At last, Kirsten sold his patent to Voith-Schneider Corp and they proceeded to improve the system into the Voith cycloidal propellers used today (Fig. 1.19). It should be noted that this has been the only commercial application of cycloidal propellers so far.

During the period 1924 – 1933, Swedish-French engineer Strandgren carried out numerous experiments with cyclogyro models, first in aerodynamic laboratory in Saint-Cyr and subsequently with "Lior-et-Olivier", a french aircraft manufacturer, where even real-size experiments were undertaken [36]. Experimental rotors were 5-bladed and had a diameter of 6 meters. The blades were made of duralumin and each blade had a span of 245 cm, depth of 40.8 cm and thickness of 3.8 cm and weighed 5 kgf. Strandgren also designed a cyclogyro aircraft using these rotors which was diven by a 130 hp engine placed in the fuselage (Fig. 1.20). Calculated
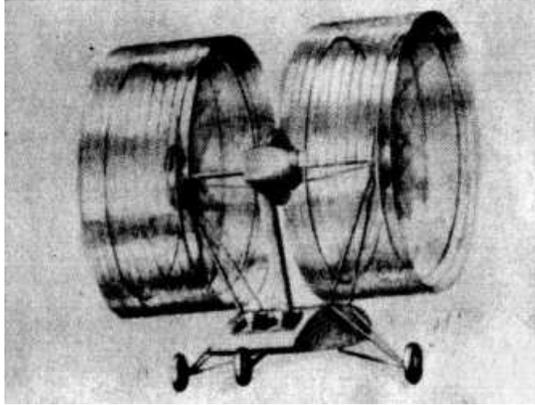
(a) Strandgren aircraft.
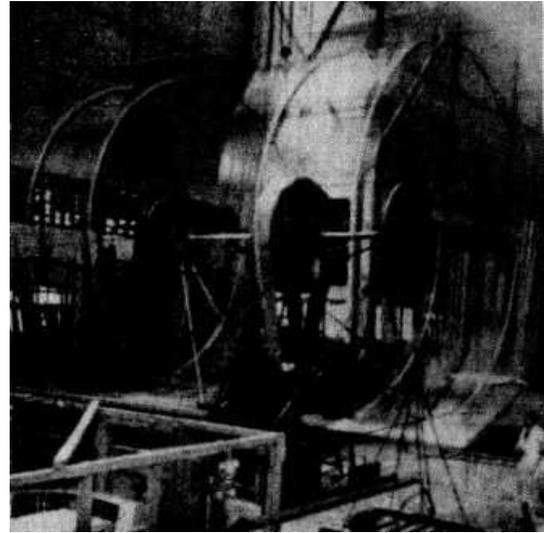
(b) Full scale test at Argenteuil (Liore et Olivier).

Figure 1.20: **Strandgren's cyclogyros [36].**

gross weight of the aircraft was about 600 kg. At a rotation speed of 120 rpm, rotors produced a lift of 800 kg. Rotors had passed a test at 180 rpm despite of some mechanical difficulties. Strandgren was granted patent to his design in 1924.

The first ever scientific analytical study of a cyclogyro was also performed by Strandgren in July 1933 [36]. He published a very simplified quasisteady aerodynamic analysis for a cyclogyro to understand how lift and propulsion are obtained on such a system. Main emphasis of this study was to evaluate the feasibility of such a concept for a flying aircraft. It was also shown, using this analysis that the pilot could have complete control of the magnitude and direction of the cyclorotor thrust by purely changing the amplitude and phasing of blade pitch kinematics.

In this analysis, based on the rotational velocity and forward velocity, the cycloidal trajectory of the blades are calculated. The instantaneous blade forces

are first calculated normal and tangential to this trajectory. Then, these forces are resolved to obtain the instantaneous forces perpendicular and parallel to the rotor forward velocity. These forces are then averaged over one revolution and multiplied with the number of blades to obtain the net rotor thrust and torque. The induced velocity was obtained using the projected area (or diametrical area) of the cylinder. Strandgren also showed the feasibility of autorotation using such an aircraft in the event of power failure. However, Strandgren never validated his analysis with experiments.

A month after Strandgren's analysis was published, in August 1933, Wheatley published a simplified aerodynamic theory, again based on a blade element momentum theory (BEMT) to predict the performance of a cyclogyro in forward flight [37]. The blade forces were assumed to be constant along the span. It was assumed that the horizontal and vertical induced velocities due to the generation of the horizontal and vertical forces were constant in magnitude throughout the rotor cylinder and was one-half the velocity increment imparted to the air in producing the horizontal and vertical forces. It was further assumed that, at low forward speeds (advance ratio $(V_\infty/\Omega R) < 0.1$), the area from which the vertical induced velocity (v_z) was calculated is that of a circle of diameter equal to the blade span (s), and at higher forward speeds, the area was assumed to be that of a rectangle of length s, and width 2R. This is equivalent to assuming that the rotor in forward flight acts like an airplane, as far as the induced velocity v_z is concerned. The horizontal induced velocity, v_x, was assumed to be derrived from the diametrical area $(2Rs)$ in all cases. The velocity at a blade section was obtained by the vector summation of the rotational

component, forward speed and the two induced velocities. The drag coefficient (C_d) was assumed to be a constant and C_l was assumed to vary linearly with α, without stall. The analysis did not include any interference effects between the blades. The time averaged thrust and power was obtained from the analysis. Since there were so many simplifying assumptions, Wheatley only expected qualitative results from this analysis.

Wheatley performed a case study using this analysis to investigate the feasibility of the cyclogyro concept for a manned aircraft of 3000 lb gross weight. From this study, he concluded that the aerodynamic principles of the cyclogyro are sound; hovering flight, vertical climb, and a reasonable forward speed may be obtained with a normal expenditure of power. Autorotation in a gliding descent is possible in the event of a power-plant failure. However, he also stated that serious structural difficulties will inhibit the practical application of these principles and the control system will be necessarily complicated mechanically, and the gyroscopic effects in the rotor could add complexities.

In 1935 Wheatley tested a 4-bladed cyclogyro rotor having a span and diameter of 8 feet, and chord of 0.312 feet in the NACA 20-foot wind tunnel (Fig. 1.21) [38]. The blade airfoil section was the NACA 0012 modified so that the mean-camber line was an arc of 9 feet radius; the mean-camber line was chosen to coincide with the blade path during a representative operating condition. The blade construction consisted of a continuous spar, a nosepiece containing a lead balance weight, wooden ribs, a metal trailing edge, and a covering of silk paper. The amplitude of the blade pitching motion was limited to a maximum of 35° by the blade pitching mechanism
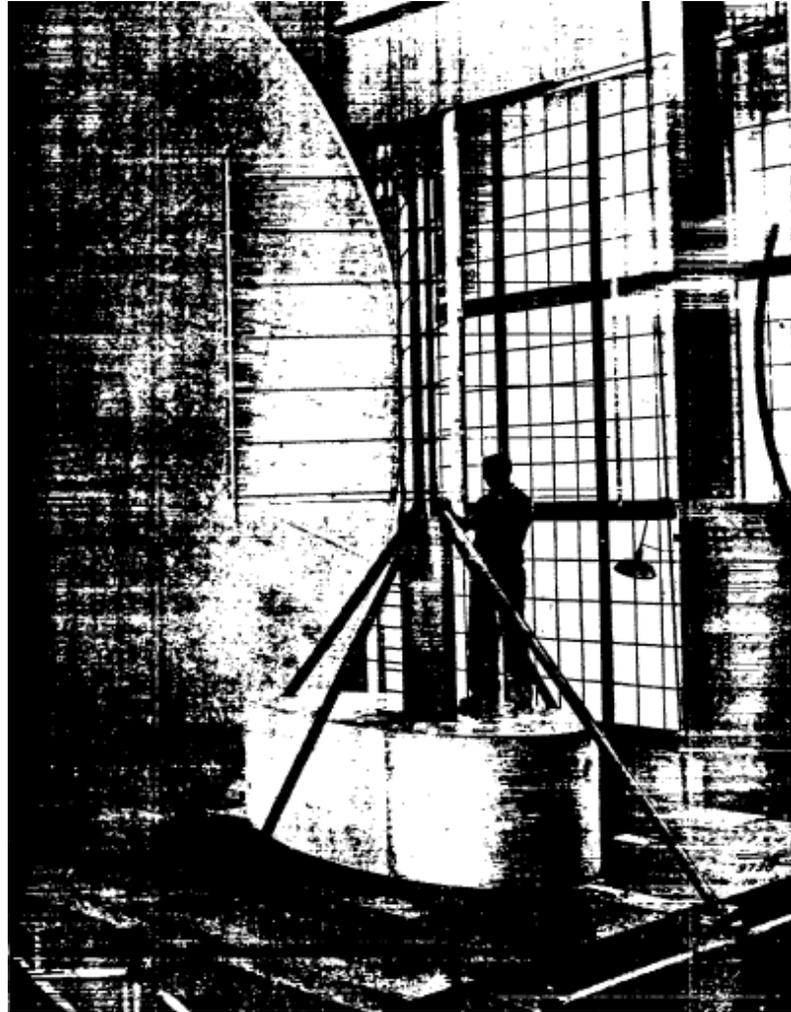
Figure 1.21: **Wheatley's experimental setup [38].**

and the pitching axis was at 25% chord location. The forces were measured using a
six-component balance.

The experimental work investigated the effect of the blade motion on the rotor
forces during the hover and forward flight conditions at several rotor tip speeds and
tunnel speeds and determined the relations between the forces generated by the rotor
and the power required for it. The advance ratio was varied from 0.2 to 0.5. A wide
range of eccentricity amplitudes and phases was used, so that the characteristics of

34

flight with and without power could be determined. Even though, the tests showed that the cyclogyro would be able to ascend vertically, fly horizontally, and glide without power, the power required for normal flight would be excessive.

The forces measured at zero tunnel speed (hover) showed that the lateral force was not zero even though the phase angle was set to give such a result. The resultant thrust was tilted at an angle 10° from the vertical for a pitching amplitude of 20°. The reason for this lateral force was explained using the Magnus effect upon the rotor shaft because of the large induced inflow produced by the rotor. For a constant advance ratio, the power required for the rotor increased much faster with lateral force (vertical force kept constant), than with vertical force (lateral force kept constant). The two variables that were varied were the amplitude and the phasing of blade pitching. In forward flight at a constant advance ratio, the vertical force was observed to be a strong function of phasing of the blade pitch and not the pitching amplitude; whereas, both the lateral force and power were strong functions of pitching amplitude and not phasing. The experimental results also showed that, even though the cyclogyro is capable of gliding flight without power, the gliding performance is very poor, the minimum vertical velocity is approximately 20 mph and increased rapidly as the horizontal speed became less that 40 mph. The miniumum gliding angle was about 25°. The power loading obtained was 6.7 lbs/hp.

The predictions obtained from Wheatley's analysis described before was compared with the experimental results. The key conclusions from that study were as follows. The value of the average blade profile-drag coeffcient (C_{D_0}) is, in reality, a function of tip-speed ratio ($\Omega R/V_\infty$) and is not constant as was assumed; the

experimental C_{D_0} rises to the unexpected value of 0.04 at a tip-speed ratio of 0.5. Consequently, the calculated power for zero rotor force is much too small. The increase in drag coefficient is similar to the increase in average drag for an airfoil oscillating in a steady freestream due to unsteady effects. Wheatley concluded this discussion by pointing out that, many of these questions now unanswered will become clear when the laws which govern the oscillating airfoils are understood. The analysis would give close agreement with the experimental results if the value of C_{D_0} were correctly chosen. The analysis was able to predict the trends correctly for the variation of vertical and horizontal forces with power. However, there was considerable differences in the actual magnitudes.

In a series of three papers spanning from 1944 to 1960 [39–41], Tanuguchi proposed an analysis based on quasi-steady aerodynamics to compute the performance of a cycloidal propeller in hover and forward flight. In this method, the total thrust and torque of the propeller were evaluated by integrating the lift and drag forces excerted on each blade section. For this, numerical values of lift and drag coefficients of the blade sections were required. In addition, an estimate of the magnitude and direction of the induced velocity at every blade section must be made. Taniguchi assumed (1) that only the longitudinal velocities induced by the trailing vortex system (i.e., those in the direction of propeller advance) contribute to the thrust and torque of the propeller, (2) that they are of constant magnitude over the length of blade, (3) that the induced velocity is not a function of the orbital position of the blade. The value of the induced velocity is obtained using momentum theory after applying a correction factor based on experimental results on a six-bladed cycloidal

propeller.

In 1961, in order to assess the validity of Taniguchi's method over a wide range of conditions, computations were carried out at the David Taylor Model Basin (DTMB) using his method [42]. The results of the DTMB computations were compared with available data from DTMB experimental investigations on 2-, 3-, and 6-bladed cycloidal propellers with blades having semi-elliptic blade planform. Good agreement was obtained between the computed and experimental values of propeller performance. However, the computations involved emperical corrections to the induced power factor (κ) and drag coefficient from the experiment. These corrections were obtained for each of the configurations tested at zero forward speed.

In addition to the validation with experiments, numerical evaluation of propeller performance characteristics were carried out over a large range of propeller eccentricity and blade solidity. Some of the key conclusions from this study were as follows. The total thrust, torque and maximum efficiency of the cycloidal propellers increase with increase in maximum blade angle. With an increase in blade solidity, the total thrust and torque increases. However, the thrust and torque of each blade and the maximum efficiency of the propeller decrease with increase in number of blades of same dimensions.

One of the most serious limitation of this method lies in the way the induced velocities are estimated; especially the assumption that only the longitudinal components contribute to propeller performance, with the assumption that the induced velocity is constant over the entire length of the blade, and finally in the fact that the induced velocity cannot be computed without resorting to determination by

(a) Cyclo-UAVs.

(b) Mockup of a cyclo-uav.

Figure 1.22: **Cyclo-UAV proposed by Bosch Aerospace [30].**

(a) Prototype cyclorotor [30].
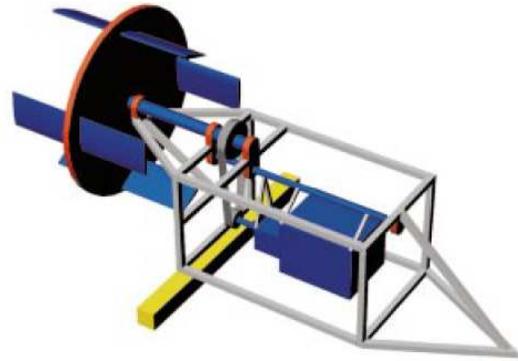
(b) Experimental setup [46].

Figure 1.23: **Bosch Aerospace cyclorotor test rig.**

experiment (empirically obtaining the induced power factor κ).

After a few decades of no research on cyclorotors, this idea was revived by Bosch Aerospace when they were awarded a SBIR in 1998, which was submitted in response to an RFP released by DoD (Navy) for an "Innovated" propulsion system for an UAV [43–45]. The proposal was to investigate the feasibility of cycloidal propulsion system for an UAV weighing 600 lbs. The mock-up of the UAV is shown in Fig. 1.22. Even though the funded project was oriented towards using this concept on a heavier-than-air UAV, later on, the cyclorotor developed was planned to be used

for airship control.

Bosch Aerospace constructed a cycloidal propeller and a test rig capable of measuring the lift, rotational speed, and torque needed by a cycloidal propeller. The cycloidal propeller and experimental rig is shown in Fig. 1.23. The test rotor used six blades with a diameter and blade span of 4 feet and blade chord of 1 foot. The blades used NACA 0012 sections. First generation blades were built with aluminum 6061 ribs welded to a main spar and covered with an aluminum 2024 skin. Since this blades had numerous structural problems, the next generation blades were constructed as one piece and consisted of a foam core, carbon woven skins, and a full length carbon spar. The blades were pitched about the c.g. axis to reduce the loads on the push-pull linkages. The central hub was CNC machined from mild steel stock. All other peripheral rotating components were machined from aircraft quality aluminum. As seen in Fig. 1.23(a), the blades also used winglets at both tips to minimize induced drag. The rotor spun upto a maximum speed of 600 rpm producing 140 lbs of thrust consuming a power of 28 HP at 25° blade pitching amplitude. During tuft testing of the cycloidal propeller, the stall commanded blade angle was determined to be approximately 32° at 500 RPM. During the operation, the cycloidal propeller was much quieter than conventional screw propellers.

Bosch aerospace in collaboration with Mcnabb of the Raspet Flight Laboratory in Mississippi State University developed a simplified unsteady aerodynamic model for a cycloidal propeller operating in hover and small forward flight speeds [46]. The model was used to support the development of the VTOL concept demonstrator vehicle which Bosch Aerospace was building. The unsteady aerodynamic analysis was

based on Garrick's formulation [47]. To include the finite span effects, 3-D corrections were applied to C_{L_α}, and induced drag was included in the drag coefficient, assuming as Oswald's efficient factor (e), which was later adjusted to match the predictions with the experiments. The velocity and the angle of attack at the blade section was calculated from the rotational speed, rotor forward velocity and the induced velocities. The induced velocities in the vertical and horizontal directions were calculated based on the net lift and thrust and a correction factor, using the rotor projected area as the actuator area. The induced velocities were assumed to be uniform across the rotor diameter. The blade interference effects were ignored in this analysis.

The force predicted by the analysis was compared with wind tunnel data produced by Wheatley in 1935 [38] and also with the results from the tests conducted in Bosch aerospace company. It was found that the estimates produced by the model agreed within 10% of Wheatley's data for the force predictions and 15% for the power predictions. Agreement between the model and the tests performed by Bosch Aerospace was within 5% for the total force and power. However, it should be noted that the value of drag coefficient (C_{d_0}) was adjusted in the analysis to match the power results. Therefore, the final value of C_{d_0} required for the power predictions to match Wheatley's experimental results was 0.07, which is quite high. Even though it could be argued that the arms of the rotating endplate and the interference effects could contribute to a portion of the measured power, it cannot explain the large discrepancy between the analysis and experiment when a realistic value of C_{d_0} is used. Historically, the underprediction of power has been a major problem starting
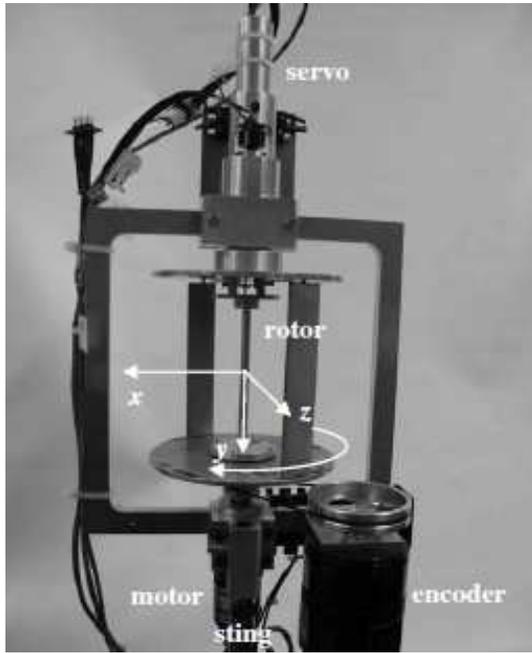
(a) Experimental setup.
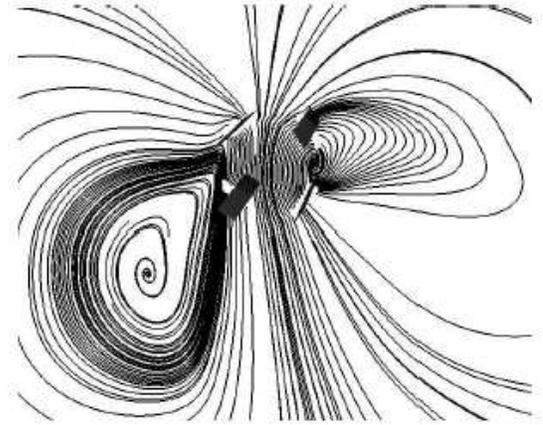
(b) CFD measured flowfield.

Figure 1.24: **Experimental and computational studies in Technion [48].**

with Wheatley's analysis, where he said it was because of the inability to model the unsteady drag on an oscillating airfoil at that time. Even in Mcnabb's model, the unsteady effects are only included in lift and pitching moment and the drag model used is still steady. This may be the reason why an unreasonably large C_{d_0} had to be used in Mcnabb's analysis to match the experimental results.

In 2003, Iosilevskii and Levy [48, 49] of the Technion University (Israel) conducted a combined experimental and numerical study of a cyclorotor operating at a blade chord Reynolds numbers of about 40,000. Experiments were carried out on an MAV-scale cyclorotor in 2-, 4- and 6-bladed configuration. The rotor had a diameter and span of 110 mm and a uniform blade chord of 22 mm. The blades used NACA 0015 airfoil section with the blade pitching axis at 45% chord. The

rotor was built with endplates at either ends of the rotor in order to minimize three dimensional aerodynamic effects on the blades. The rotor rotational speed was varied from 4000 to 6000 rpm (Reynolds number range of 34,000 – 50,000) and the blade pitching amplitude were varied continuously from 0° to 40°. The forces and moments produced by the rotor were measured using a 5-component sting balance. The rotor and the experimental rig is shown in Fig. 1.24(a).

Experimental studies showed that the resultant thrust is produced at an angle with the vertical even though the maximum angle of attack is produced in the vertical direction. This clearly showed that the thrust lags behind the blade pitch angle and the lag angle decreases as the thrust of the rotor increases. The presence of the lateral force was attributed to the Magnus effect produced by the rotor spinning in the induced flow produced by it. Rotor "stall" was apparent at angles of attack in excess of 26° for the two-bladed and 32° for the four-bladed configurations. With the induced velocity calculated based on rotor thrust and projected area, the angle of attack at stall turns out to be 8.6°. The power required to produce certain thrust is higher by about 40% than that predicted by the momentum theory based on uniform inflow velocity over the rotor projected area.

A 3-D CFD simulation was also performed on the cyclorotor. In the numerical simulation, the end plates were omitted to simplify the problem. The chord and radius have been selected so as to replicate the experimental setup; the span has been doubled to simulate the effect of endplates. All simulations were conducted using the EZNSS flow solver [50] at the reference Mach number of 0.12 and Reynolds number of 40,000, roughly corresponding to actual test conditions. Both 2- and 4-

bladed configurations have been addressed at two different pitching amplitudes.

To accommodate the geometry changes that resulted from the motion of the blades, the Chimera [51] scheme was employed. Body-fixed meshes were generated for each blade ("D"-shaped slices) and embedded in the global zone. The global mesh was extended to the distance where the interference caused by the rotor died away. The governing equations solved were the full NavierStokes equations assuming laminar compressible flow. Time integration was conducted using the implicit algorithm of Beam and Warming [52].

The average forces predicted by the CFD analysis compared well with the experimental results. In spite of the complexity of the problem, as well as replacing the end plates by doubling the span, the total force estimation error was less than 5%. Compared to the experiment, the direction of thrust led by about 10°, but captured the correct trend. The torque estimation error was less than 20% for all angle of attack modulations. The accuracy of the numerically computed integral forces provided confidence in the numerically generated flow field (Fig. 1.24(b)), which helped expose the complex aerodynamic interactions between the rotating blades.

One of the most systematic studies on cyclorotors have been performed at Seoul National University from 2003 to 2008 [28, 53–59]. This included both experimental and computational studies, as well as flight vehicle development. Numerical studies included a quasi-steady BEMT based aerodynamic model assuming linear aerodynamics and using a double-multiple-streamtube inflow model [54]. In the multiple streamtube model, the rotor is divided into a number of streamtubes, which
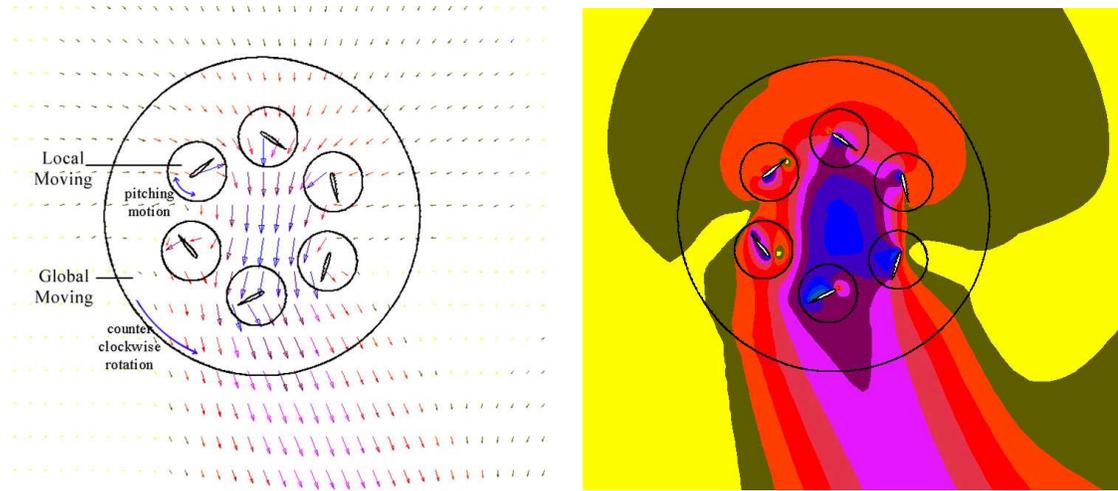
(a) Velocity vectors.

(b) Velocity contours.

Figure 1.25: **2-D CFD results from Seoul National University [28].**

intersect the rotor twice with different induced velocity values at the upstream and downstream halves. However, the analysis was only used for resultant thrust prediction. The predicted resultant thrust values correlated well with the experimental results.

A 2-dimensional CFD analysis was also performed using a commercial software, STAR-CD, to determine the aerodynamic design parameters of the cyclocopter rotor system [28, 53, 54]. The CFD analysis not only helped predict the thrust level of the cyclocopter rotor, but also helped understand the flow conditions around the rotor and the blades. To simulate the rotating and pitching motion of the blade, the moving mesh method was used in the CFD analysis. The conditions imposed on the boundary are the pressure, the no-slip wall, and the symmetry plane boundary condition. The $k-\epsilon$/low Reynolds turbulence model was applied in the CFD model, with structured and unstructured meshes. The motion of the blade in cyclorotor

can be simulated by the rotational motion of the meshes.

The forces predicted by the CFD model correlated well with the experimental results. As shown in Fig. 1.25, the flowfield obtained using CFD revealed the complex flow inside the rotor cage clearly showing that the inflow enters into the rotor normal to the upper semicircle; however, the outflow (or wake) is skewed by an angle of 20° with the vertical confirming the presence of the experimentally measured lateral force. The CFD analsyis was also used for the aerodynamic design the different cycocopter rotor systems that were built at various scales.

Detailed experimental studies were also carried out [28, 53, 54]. Most of the experimental studies were performed on a rotor with a baseline diameter and blade span of 0.8 meter and blade chord of 0.15 meter. The airfoil section used was NACA 0012. The test rotor and the experimental setup is shown in Fig. 1.26(a). During the experimental studies, the parameters varied included rotational speed, rotor diameter, number of blades and the blade pitching amplitude and phasing.

The maximum thrust from the test was 4.5 kgf, obtained using a 6-bladed rotor at a pitching amplitude of 30° at an operating speed of 450 rpm. The results showed that the thrust and power varied as the square and cube of rotational speed, respectively. The horizontal force was not zero during the tests even though the phase angle was set to be zero. The resultant force was inclined by about 20° from the desired direction when the pitching amplitude was 25°. The reason for the lateral force was attributed partly to the Magnus effect due to the rotor shaft spinning in the induced flowfield and partly due to the curvature of the induced flow in the downstream part of the rotor induced by the inner flow, which increases the

(a) Cyclorotor testing rig [28].

(b) Seoul National University 43 kg Twin-Cyclocopter UAV [56].

Figure 1.26: **Seoul National University cyclocopters.**

resultant velocity on a blade in the right side, but decreases the resultant velocity in the left side.

Even though when conventional wings operating in air, stall would occur at a very low angle of attack, the blades of the cyclorotor showed no thrust decrease until a pitching amplitude of 30°. Increase in thrust until such high pitch angles was attributed to the dynamic stall phenomenon which can happen when the blade exceeds the static stall angle and the effective angle of attack changes rapidly. There was also a rapid increase in power with pitch angle which can be again due to dynamic stall. However, for a constant thrust, power loading increased with pitching amplitude until 30°. It was observed that for a constant tip speed, the thrust produced by the rotor increased with the rotor radius. For a constant thrust, the rotor with the highest radius had highest power loading. When 2-, 3-, and 6-bladed rotors were compared at a constant thrust, the 3-bladed rotor produced the highest power loading followed by 2- and 6-bladed rotors. It was also observed that the

46

increase in thrust was not proportional to the increase in number of blades.

Seoul National University has also designed and built a range of Unmanned Aerial Vehicles (UAVs) with cycloidal blades system (cyclocopter) to evaluate the potential of cycloidal blades system for VTOL vehicle. The development of the cyclocopter was primarily focused on the hovering and low speed forward flight performance. The thrust and power were estimated by using the aerodynamic model and the 2-D CFD analysis. For the different cyclorotors that have been built, the dimension of cyclocopter rotors and the rotor design parameters for obtaining the required thrust for a given engine power was obtained through an optimization process.

The first cyclocopter UAV that was designed (Fig. 1.26(b)) composed of two main cyclorotors rotating in the same direction [53,56]. The longitudinal and lateral lengths of the cyclocopter were 1.65 m and 2.7 m, and the vehicle weighed 43 kg. The method for rotor torque compensation was to place the cyclocopter center of gravity sufficiently below and after the rotor axis so that the reaction couple between the rotor thrust and aircraft weight will cause the aircraft to seek an offset equilibrium trim position. The cyclorotors used for the UAV used 4 blades and had a diameter of 1.4 meters, blade span of 1 meter, chord of 0.15 meter and used NACA 0012 airfoil section. The designed cyclorotors could produce a thrust of 45 kgf (both rotors combined) at an operating rotational speed of 550 rpm, and a pitching amplitude of 24° the rotor consuming 11 HP. The installed engine power was 16 HP.

The rotor blade was supported at both its root and its tip to overcome centrifugal forces and the vibration problems. Along with the pitch bearing, the root

and tip of the blade are connected to hub arm by means of hinges to reduce the loadings on the blades and hub arms. The blade deformation due to centrifugal loads deteriorates aerodynamic performance of the rotor and the blade must be designed to prevent the deformation as small as possible, to sustain the centrifugal loadings, and to be light-weighted. The blades are made of composite skin, spar, and trailing stiffner. The natural frequencies of the blade were calculated for the different modes and a fan plot (Campbell diagram) was generated to check for possible resonances at the operating rotational speed. Since both the rotors were driven by the same engine through a two-stage transmission, they rotated at the same rpm. Therefore, inorder to control the cyclocopter during flight a control mechanism was designed and implemented which could change the magnitude and direction of the thrust vectors of each of the rotors independently. The magnitude of the thrust vector was changed by changing the magnitude of the offset in the pitching mechanism (this changes blade pitching amplitude) and the direction of the thrust vector was changed by changing the direction of the offset (this changes the phasing of blade pitching kinematics). The control mechanism is shown in Fig. 1.28(b). Airframe structure was designed to contain components of engine, shaft, etc., to withstand ground and flight loads and to withstand the vibratory loadings induced by the rotor. Even though the cyclocopter was build, it is not mentioned whether actual hover tests were performed even in a tethered condition.

A micro-scale cyclocopter weighing 2.6 kg was also designed and built (Fig. 1.27(a)) [57]. The design goal of this model was to take off vertically by lifting its own weight, and there was no consideration for attitude control devices such as a gyro and a servo

(a) Cyclocopter.
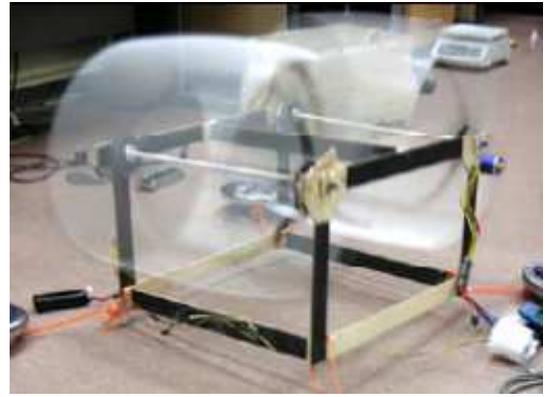
(b) Cyclocopter hovering.

Figure 1.27: **Seoul National University 2.6 kg Twin-Cyclocopter UAV [57].**

and payloads like a camera. As seen in the figure, two rotors are located in front and rear and each rotor rotates in opposite direction for the rotor torque compensation. Each of the rotors used 4 blades and had a diameter of 0.4 meter and blade span and chord of 0.35 meter and 0.05 meter, respectively. The blades used NACA 0012 sections. Each of the rotors were powered by two independent 300 watts motors. The rotors produced 3 kgf of lift at an operating speed of 1500 rpm and pitching amplitude of 26 deg. As shown in Fig. 1.27(b), this model was able to lift-off in a tethered condition.

A quad-rotor cyclocopter in the 100 kg class was also built (Fig. 1.28(a)) [57]. Aerodynamic and structural optimization was performed using a response surface methodology utilizing a 2-D CFD analysis for aerodynamic performance and NASTRAN for the blade structural analysis. Each rotor used 4 blades and had a diameter of 1.7 meter, blade span of 1.0 meter and chord of 0.22 meter. The blades used NACA 0018 airfoil section. The blade structural design includes two vertical carbon fiber spars (0/90 orientation) at 25% and 50% chord locations and

(a) Quad-Cyclocopter.
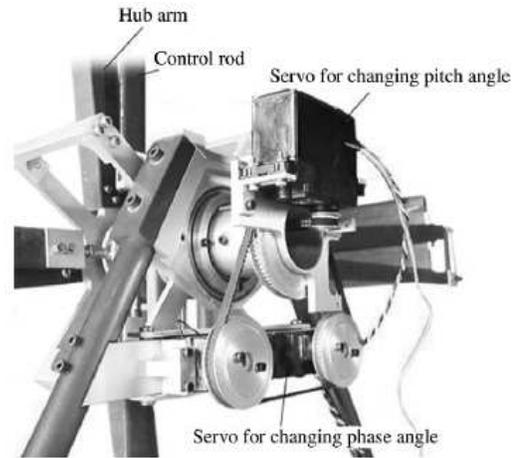
(b) Cyclocopter control system.

Figure 1.28: **Seoul National University 100 kg Quad-Cyclocopter UAV [57].**

a blade skin laminate ($\pm$ 45°). At a pitching amplitude of 25° and a rotational speed of 450 rpm, the rotors produced a thrust of 114 kgf while consuming 24.8 HP, which is about 75% of the maximum engine power. All the rotors were coupled to the same engine through a 3-stage transmission so that all the four rotors operate at the same speed. For attitude control, a servo-motor based control mechanism was developed to change the magnitude and direction of each of the thrust vectors independently (Fig. 1.28(b)). However, tethered hover tests were not performed on this cyclocopter.

A modified version of the above quad-cyclocopter was designed and built in 2008 using four rotors and having a gross weight of 12 kgf (Fig. 1.29(a)) [55]. The main differences in the new design from the previous versions of cyclocopters were elliptical blades to improve blade lift-to-drag ratio, independent electric motors for each rotor to reduce transmission complexity and weight, improved swash-plate/control mechanism design for independent control of each rotor, the ability to
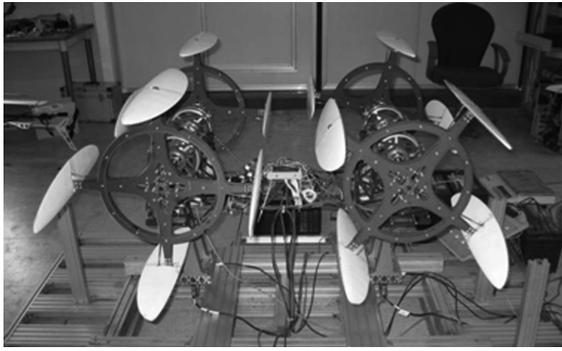
(a) Quad-Cyclocopter.
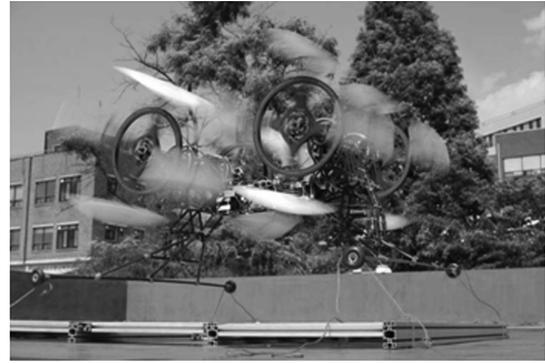
(b) Tethered hover.

Figure 1.29: **Seoul National University 12 kg Quad-Cyclocopter UAV [55].**

do independent speed control for each rotors, and the fact that all parts of the rotor blades and fuselage were manufactured out of composite material. This cyclocopter was designed through detailed CFD studies and a finite element structural analyses. Each of the rotors used four blades and had a diameter and blade span of 0.5 meter and chord of 0.105 m at the middle. The blades used NACA 0018 airfoil section. The blade construction included one circular carbon composite spar located at the 33% position from the leading edge, which acted as the pitching axis, and the control linkage was connected at the 62% position. The blade shape was formed by the skin and the ribs. The center rib was reinforced by a woven glass composite to ensure the blade can endure the highest stress value. The experimental results on the test bed gave a thrust of 157 N for the conditions of a maximum pitch angle of 25° and a rotating speed of 1100 rpm consuming 2633 watts of power. As shown in Fig. 1.29(b), the cyclocopter was capable of tethered hover even though the attitude control was unstable.

In 2006, Yu et.al performed both computational and experimental studies on

Figure 1.30: **Results from the unsteady vortex lattice analysis on the cyclorotor (National University of Singapore) [60].**

a MAV-scale cyclorotor in the National University of Singapore [61, 62]. Computational study included a 3-D Unsteady Vortex Lattice Method (UVLM), which was implemented to predict the thrust and power of a MAV-scale cyclorotor in hover [61]. UVLM is based on potential flow theory which assumes the flow to be inviscid and irrotational. However, since UVLM can deal with the blade wake, interference effects, complex blade shape and kinematics, it can enable a better understanding of the aerodynamics of cyclogyros.

The vortex rings are selected as singular elements and the blade thickness is negelected for UVLM. The vortex rings are deployed on blade surfaces and wake sheets. Wake sheet is shed from the trailing segment of the blade trailing edge vortex rings. A new wake line is added at each time step. The wake sheet rolls up with the local fluid velocity. The Neumann boundary condition is applied on each collocation point and a system of linear equations are formed. The circulation distribution on each panel can be obtained by solving these equations. The velocity

distribution can then be obtained. Then the Bernoulli function is used to calculate the forces on the wing and hence the lift, drag and torque required to drive the blade can be obtained. There can be significant blade-wake interactions for cyclorotors. However, the Biot-Savarts Law used to evaluate the induced velocity at a point due to a line vortex goes to infinity as the distance approaches zero. The remedy is to replace the singular vortex lines by the vortex line with viscous core model. The wake obtained using the UVLM analysis in forward flight is shown in Fig. 1.30.

A parametric study was performed using the UVLM analysis to understand the effect of blade pitching amplitude, planform taper ratio, blade span-to-rotor diameter ratio and winglets at blade tips on the cyclorotor performance in terms of power loading (thrust/power) at constant disk loading. The study clearly showed that moderate pitching amplitude provides the highest power loading. Blade planform taper-ratio did not have any significant effect on the power loading of the rotor. For the same disc area, the rotor with the smallest radius and highest blade span provided the highest power loading. This is because the blades with larger aspect ratio have lower induced drag. Presence of winglets decreased the power loading of the rotor.

However, the main limitation of the analysis is the lack of viscous effects. Therefore, the power obtained from the analysis is purely induced and does not include any viscous losses. Also, aerodynamic phenomena such as dynamic stall, which can play a significant role in enhancing the thrust production, is a viscous phenomenon and hence, will not be captured using this approach.

An experimental study was also performed on cyclorotors using a newly de-
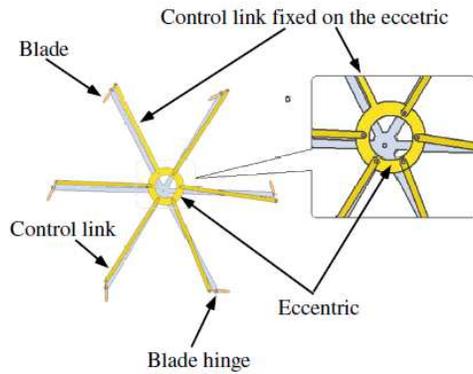
(a) 5-bar mechanism.
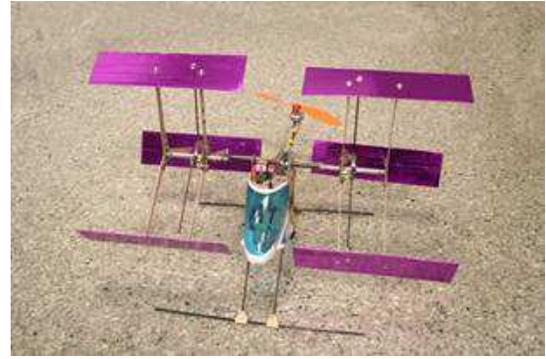
(b) Cyclocopter MAV.

Figure 1.31: **National University of Singapore cyclocopter MAV [62].**

veloped innovative 5-bar based pitching mechanism (Fig. 1.31(a)) [62]. The 5-bar based pitching mechanism was mechanically simpler compared to the traditional 4-bar based mechanisms and therefore, could be more attractive for flying vehicle applications. A MAV-scale cyclorotor was built using the new 5-bar pitching mechanism. A force balance was built to measure the thrust, lift and the torque produced by the cyclorotor. Experimental studies were performed to investigate the effect of blade airfoil section (flat plate vs. NACA 0012) and planform taper ratio, and the control linkage length, which changes the symmetry of blade pitching in the upper and lower halves of the circular blade trajectory.

The rotor used for the airfoil test was a 3-bladed design with a rotor diameter of 140 mm, blade span of 130 mm, and chord of 33 mm. The NACA blades were made out of balsa wood and the flat plate blades were made out of 1 mm thick plywood. The results showed that, for the same value of disk loading, the flat plate blades produced higher power loading than the NACA 0012 blades. The rotor used for the taper-ratio test was again a 3-bladed design with a rotor diameter of 200 mm, blade

54

span of 170 mm. The results obtained from these tests were very different from that of the static wing tests. The highest power loading was obtained for a rectangular blade (taper ratio=1) and the power loading steadily decreased as the taper ratio was decreased to 0.2. When the effect of asymmetric pitching was investigated, it was shown that the maximum power loading was obtained when the blade maximum AOA at upper cycle is a bit smaller than that at lower cycle. However, it may not be correct to come to such a conclusion because, when the different asymmetric cases were tested, the peak-to-peak angle was not kept constant.

A cyclocopter MAV was also built based on the 5-bar pitching mechanism and was capable of tethered hover (Fig. 1.31(b)). Experimental studies were used to find the cycloidal propeller with the maximum efficieny, and a cyclogyro equipped with 2 such propellers and one tail rotor was built and tested. The vehicle weighs 358 grams and is powered by two brushless electrical motors. The blades used on the propeller is a 1 mm uniform thin plate. The maximum thrust generated by the vehicle was 520–540g and this was enough lift force for the cyclogyro to hover.

In 2006, Sirohi et.al at the University of Maryland [63] performed systematic experimental parametric studies on 3- and 6-bladed micro-scale cyclorotors (diameter and span = 6 inches) (Fig. 1.32(a)) by varying the rotational speed and blade pitching amplitude. The blades used NACA 0010 section and had a chord of 1 inch. The thrust was measured using two load cells and the torque was measured using a torque cell as shown in Fig. 1.32(b). Measured thrust increased as the square of rotational speed, while power increased as the cube of rpm. No dramatic reduction in thrust was measured as blade pitch amplitude was increased up to 40°, indicating
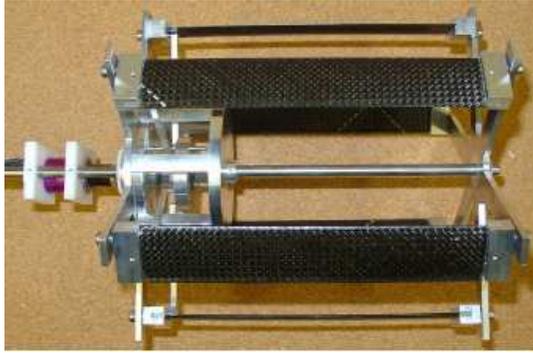
(a) Cyclorotor used for testing.
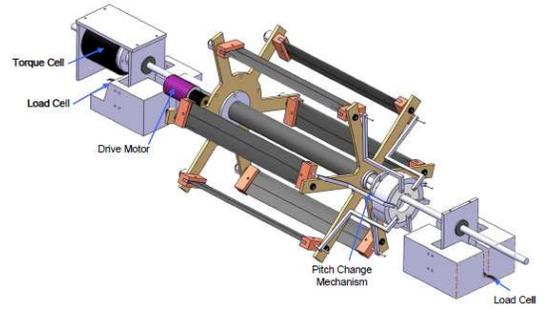
(b) Experimental setup.

Figure 1.32: **University of Maryland MAV-scale cyclorotor experiments [63].**

that dynamic stall may play a role in the operation of the cycloidal blade system. Although the six-bladed case produced greater thrust, the increase was not as great as expected, and this may be because of the increased inflow for the same rotational speed while using more blades and it is also probable that there may have been more wake interference between the blades in that case. The 3-bladed rotor had higher power loading than the 6-bladed rotor for the same thrust. Further testing on the effects of the phase angle of eccentricity on the thrust direction determined that vertical force reached a maximum at a phase lag around 15°. One main shortcoming of this work was that the rotor design was relatively heavy (weighing 450 grams), which restricted the maximum acheivable rotational speed to 1200 rpm producing only 50 grams of maximum thrust. Also, due to the heavy and bulky rotor design, the tare power was almost 75% of the total power, which led to some discrepancies in the aerodynamic power measurements.

In this study, an analytical model of a cycloidal rotor, was also developed to

Figure 1.33: **VTOL transonic aircraft with cycloidal propellers proposed by Acuity Technologies Inc [64].**

predict the magnitude and direction of thrust as well as power requirements of a cycloidal rotor in hover. By applying the motions of the pitch change mechanism, and the rotor downwash, the angle of attack of each blade may be determined. Lift and drag forces are calculated based on unsteady indicial aerodynamics assuming attached flow. Downwash is determined from a modified version of the double-multiple-streamtube model and this is used to calculate the induced angle of attack. An iterative procedure is then executed until convergence is achieved for lift and drag forces. The resulting forces from each blade are then summed to find the total vertical and horizontal forces for the rotor. When compared with experiments, the predicted thrust correlated well with the test data for lower pitching amplitudes; however, the power was overpredicted for all the cases. However, this study concluded that the cyclorotor concept can be promising at the very low Reynolds numbers typical at which MAVs operate.

In 2006 Acuity Technologies performed both experimental and 2-D CFD stud-

ies on a model cyclorotor [64]. The end goal of the project was to develop a VTOL transport aircraft using cyclorotors as shown in Fig. 1.33. The test rotors (Fig. 1.34(a)) had a diameter of 2 feet and total blade span (2 wing sections) of 5 feet and blade chord of 3 inches. The airfoil used was a modified Bell AH-1 airfoil (in turn a modified NACA 0012), which was thickened to 13.5% and cambered with the circular rotor path. The blade construction included a circular hollow carbon spar for the required bending stiffness, high density foam to maintain the required airfoil shape and a mylar skin covering the entire blade. Instead of using the conventional passive pitching mechanisms normally used on cyclorotors, in this study, individual active control of each blade was attempted using rotary actuators at the blade root in the rotating frame. It was expected that this would allow the most general form of control, including rapid pitch changes to optimize rotor performance based on considerations such as the best angle of attack profile when passing through the wake of other blades.

The force produced by the rotor in two directions are measured by two load cells and the motor torque was measured using a torque cell. At the maximum testing speed of 863 rpm (Reynolds number = 203,000), the net thrust obtained was 2.7 lbs consuming a power of 0.36 HP. At this rotational speed, the rotary actuator could acheive a maximum peak-to-peak pitch angle of 33°.

This study also performed 2-D CFD analysis of blade shapes, rotor geometry, and power requirements for a cyclogyro with a 6 ft total span and 2 ft diameter rotors. The operating Mach number was 0.1845 and Reynolds number was 266,400. NASA's Overflow-D CFD code capable on unsteady flow analysis, was used to eval-
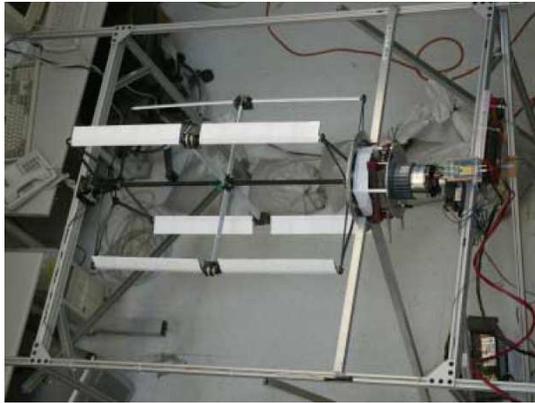
(a) Experimental setup.
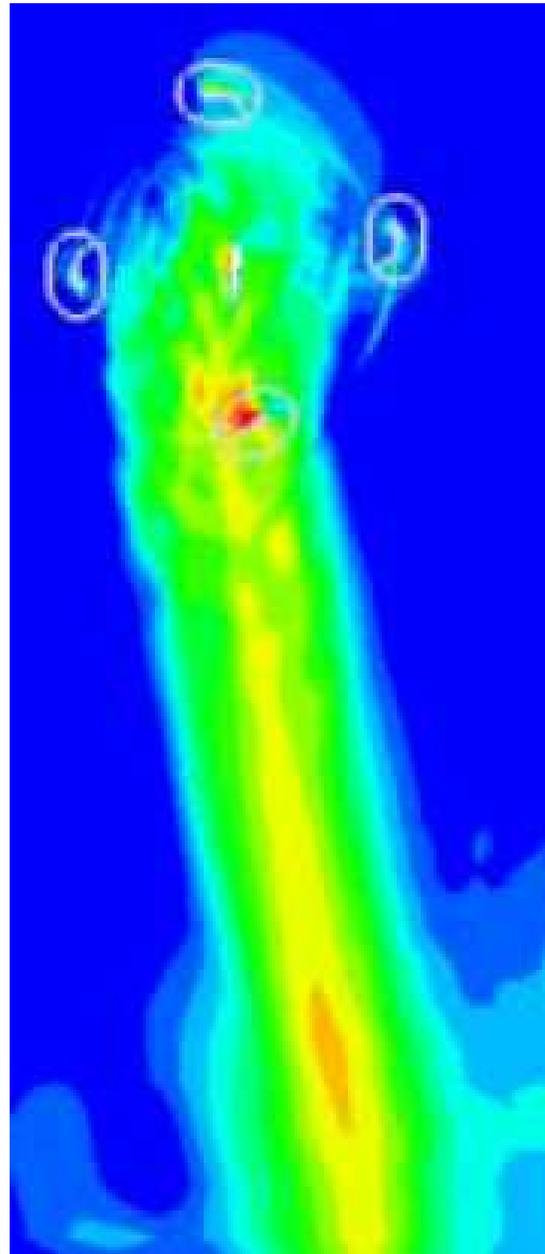
(b) 2-D CFD flow field.

Figure 1.34: **Experimental and CFD studies by Acuity Technologies [64].**

uate rotor and blade torque and power requirements. Analyses were performed for hover and also for high speed forward flight.

The analysis was used to predict the forces and torques that can be expected on the blades and drive spar fairing to identify a preliminary blade pitching kinematics that produces uniform, low vibration rotor lift and thrust in hover and forward flight. The flowfield obtained from CFD showed that the air gets pulled in from the upper semicircle around the rotor and is propelled downward, much like a propeller in static thrusting conditions. This can be seen in Fig. 1.34(b), which shows the high speed jet exiting below the rotor. Maximum velocity in the jet was approximately 0.5 times the blade speed. There was an unintended bias in the horizontal force coefficient, which happens because of the blade cutting through the jet and it suffers from increased drag in this region, which translates into a negative bias. It could be also seen that the force profile is smooth when the blade is in the upper half; however, there are significant force fluctuations as the blade passes through the downwash in the lower half.

In 2007, Siegel et.al. of the US airforce academy performed a 2-D CFD analysis to demonstrate the capability of a cycloidal propeller to utillize unsteady, dynamic lift for operation at MAV-scale Reynolds numbers [65]. The study also showed that by carefully choosing the amplitude and phasing of the blade pitching motion, both energy extraction and thrust production are shown to be achievable.

For the CFD computations, the Cobalt flow solver from Cobalt Solutions, LLC was used. In the code, the full compressible Navier-Stokes equations are solved based on the Finite Volume Formulation. The numerical method was formally second

60
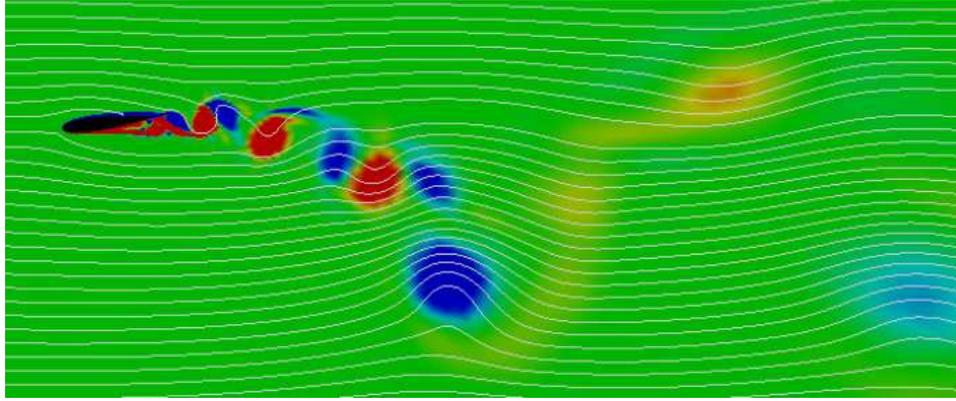
Figure 1.35: **2-D CFD flow visualization on a cycloidal propeller [65].**

order accurate in both space and time. A structured, body fitted "O" grid, was used for this investigation. The grid was locally refined near the surface to capture the boundary layer structures in detail while resolving the separated shear layer well enough to capture the large vortical structures of the detached boundary layer. The chord Reynolds number was Re=10,000; to ensure computational efficiency, the Mach number is set to M=0.1. The time step is was set at=0.25ms. Uniform flow boundary conditions at the far field were imposed using Riemann invariants. For dynamic pitching simulations, rigid body grid motion with 6 degrees of freedom was implemented in Cobalt is used.

A total of about 35 2-D cycloidal simulations were performed at different forward flight speeds (V_∞), with different combinations of frequency, radius of the foil motion, phase and pitch amplitude. Only advance ratios $(V_\infty/(\Omega R))$ less than one were considered in the present analysis. Some of the key conclusions from the study are as follows. The simulations were performed with two different airfoil sections, the NACA 0012 and NACA 0015. It was seen that the airfoil profile had

very little impact on the performance. The grid resolution study revealed that the fine grid preseved the vortices further away from the foil best, however, the grid resolution did not create significant differences in the average forces or the vortex shedding frequencies. One 3-D simulation was perfomed and the forces obtained was compared with the 2-D results. Even though there was small differences in the shedding frequencies, the forces between 2-D and 3-D results matched within a few percent.

This study also helped unravel some interesting flow physics which can enhance the cycloidal rotor thrust producing capablities. On a cycloidal rotor, as the blade moves down (left half of the circular blade trajectory) the blade is first accelerated, then decelerated in the stream wise direction. This favors early dynamic stall vortex formation, leading to an increased thrust production (Fig. 1.35). The opposite effect occurs during the upward motion (right half of the circular blade trajectory), leading to a weaker dynamic stall vortex and thus less thrust production. In addition, at the end of a motion cycle several small von Karman-type vortices are shed, which reduced thrust production.

In 2007, Hara et. al. developed a more efficient and innovative flying mechanism for cyclogyro-based horizontal axis rotorcrafts [66]. To accomplish the purpose, a new pantograph-based variable wing mechanism (Fig. 1.36) was proposed for cyclogyro-based horizontal-axis rotorcraft. As shown in Fig. 1.36, a set of pantograph-based variable wing consists of several wing segments. This mechanism is composed of two different mechanisms, a revolving slider-crank mechanism that causes revolving and reciprocating motion, and a pantograph-link mechanism that
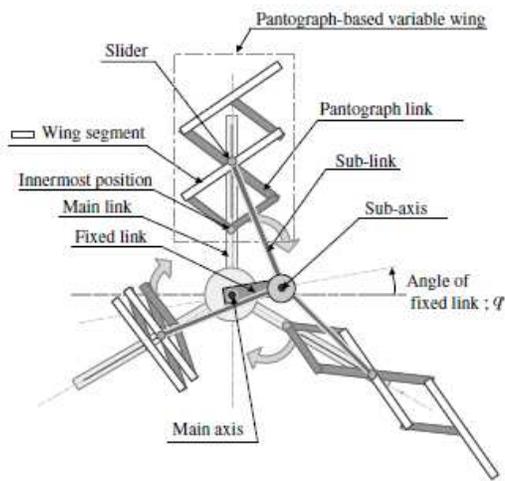
(a) Schematic of the pantoraph mechanism.

(b) Cyclorotor using the pantograph mechanism.

Figure 1.36: **Pantograph mechanism [66].**
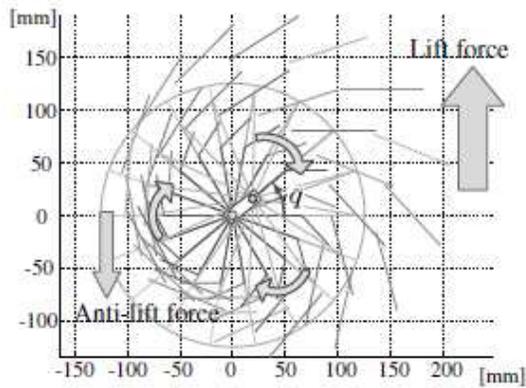
(a) Blade trajectory obtained using the pantograph mechanism.
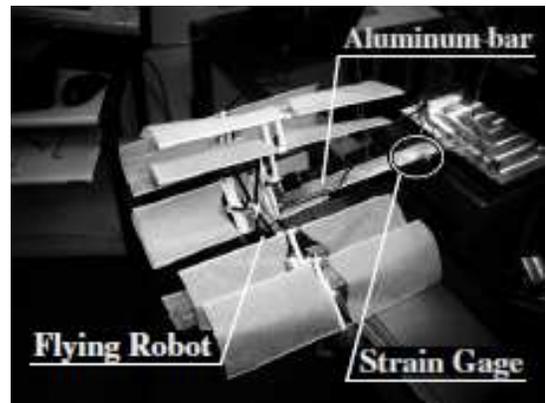
(b) Experimental setup for the lift measurement.

Figure 1.37: **Blade trajectory and experimental setup for pantograph-based cyclorotor [66].**

causes flapping motion. Because of this motions, the wing segments, located on the pantograph links like as in Fig. 1.36(a), reciprocate and swing around the center of the wing chord. The trajectory of the wings is shown in Fig. 1.37(a). In downstroke motion of the wing segments, this mechanism makes motions of expanding wings and getting high attack of angles to generate heavy drags to the upward direction. Conversely in upstroke motion, this mechanism makes motions of contracting wings and getting low angles of attack to reduce anti-lift forces directing to the downward. Due to this folding up motion of the wings, it is possible for this mechanism to have a larger wing area in a small space and to get a larger lift force.

Figure 1.36(b) shows the prototype that has been built. The rotor had 5 sets of wings with 2 wing segments for each set, the wing span was 230 mm, chord of 39 mm and the rotor weighed 245 grams. A simulation model was developed to obtain the blade pitching and flapping kinematics and the average lift and power required for the blades. As shown in Fig. 1.37(b), an experimental system was built for measuring lift forces by measuring strains of an aluminum bar with strain gages. One significant result from the experiment was that, even though the blades used were flat plates with identical trailing and leading edges, the lift produced when the rotor was rotating in clockwise direction is not same as the lift produced when the rotor was rotating in the counter-clockwise direction. This was attributed to the Magnus effect which depends on the direction of rotation. Once the rotational effect was included in the simulation, the simulation was able to capture the differences due to the sense of rotation and there was close agreement between the predition and experimental results. Rotating in counter-clockwise direction the rotor produced a
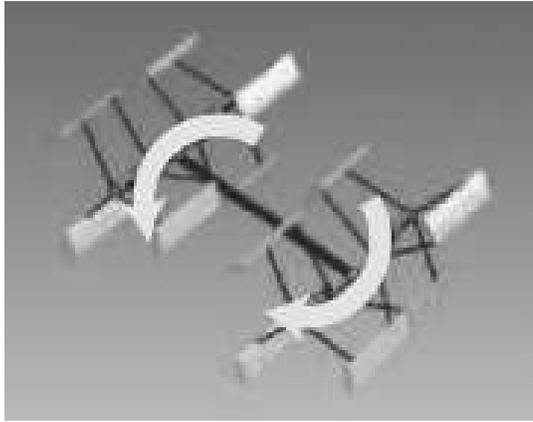
(a) Quad-Cyclocopter.
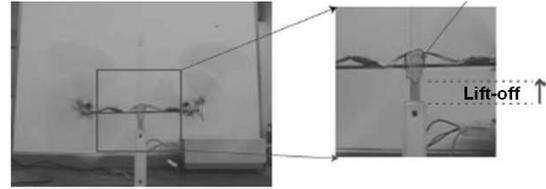
(b) Hover on the vertical guide.

Figure 1.38: **Quad-cyclocopter MAV developed by Tanaka [67].**

maximum lift force of 330 grams at 540 rpm consuming 60 watts of electrical power. An optimization study was performed using the simulation model to maximize the lift of the rotor for a given motor power by varying the blade kinematics parameters. The optimal configuration was able to acheive a payload of 210 grams showing the feasibility of a flying vehicle using this concept.

In 2007, Tanaka et. al. designed a new variable angle of attack mechanism with an eccentric (rotational) point in addition to a rotational point connecting to a motor [67]. The main feature of the mechanism with the eccentric rotational point is the ability to passively change the blade pitch angle in accordance with the blade azimuthal positions in an extremely simplified fashion so that it could be used on a flying vehicle. Experimental studies were performed on a cyclorotor model with a diameter of 0.26 meter, blade span of 0.12 meter, and a blade chord of 0.045 meter. The airfoil section used is NACA 0012. The design parameters (wing span, the number of wings, and eccentric distance) of the flying MAV are determined

through a series of experiments. The goal of the experiment was to maximize the lift produced by the rotor for a fixed motor power and thereby produce sufficient lift force for tethered flying.

Doubling the wing-span doubled the lift for the same rotational speed. Also, when the wing span of these rotors was doubled, the lift produced by the rotor for the same motor power increased by about 20%. 2- and 3-bladed cyclorotors were tested. The 2-bladed rotor was abandoned because of excessive vibrations. The 3-bladed rotor with twice the blade span produced thrust equal to 119% the weight of the vehicle at a rotational speed of 1150 rpm. Experiments were also performed to obtain the optimum eccentric distance (pitching amplitudes) for obtaining the maximum thrust for the same power.

Based on the experiments the best cyclorotor design used three double-span blades and an eccentric distance of 0.025 meter, and this rotor could generate a lift-to-weight ratio of 137.8%. A cyclocopter was designed and build using four such rotors, which was able to lift-off on a vertical guide, with power supplied from the ground as shown in Fig. 1.38.

In 2009, Nozaki et.al. conducted experimental studies on a cycloidal rotor to be used on a 20 meter airship [68]. The rotor used 3 blades with a rotor diameter of 2 meters, blade span of 1 meter, and chord of 0.3 m. The blades used NACA 0012 airfoil profile. Figure 1.39(a) shows the experimental setup for thrust measurement tests. Four sets of load cells were installed between the test bed structures and the propeller to measure thrusts in the two mutually perpendicular directions. The maximum operational speed was 480 rpm, and the blade pitching amplitude

66

(a) Prototype rotor and test setup.

(b) Cyclorotors installed on a 20 meter airship.

Figure 1.39: **Cyclorotor for airship control [68].**

was varied between $0°$ and $27°$. Consistent with the observation made by other researchers, there was a phase lag of $10°$ between the direction of resultant thrust and the direction where the maximum blade pitch angle occurs. Flowfield measurements were also made around the cycloidal rotor. Experiments were conducted to investigate the effect of adding fairings to the hub arms and winglets to the wing-tips to reduce induced drag. By adding fairings to hub arms, the power could be reduced by up to 30% at higher rotational speeds. Winglets also reduced the power by up to almost 24%, again at higher rpms.

Finally, the cycloidal propellers were installed on a 20 meter airship as shown in Fig. 1.39(b). The airship could successfully make a vertical take off and also do forward/reverse flights. Kinetic performances of the cycloidal propeller equipped airship were shown to be much maneuverable than vehicles equipped with conventional fan-type thrusters.

In 2010 Kan et.al of the University of Maryland performed 2-D and 3-D simulations of a MAV-scale cyclorotor in hover using a compressible structured overset

67
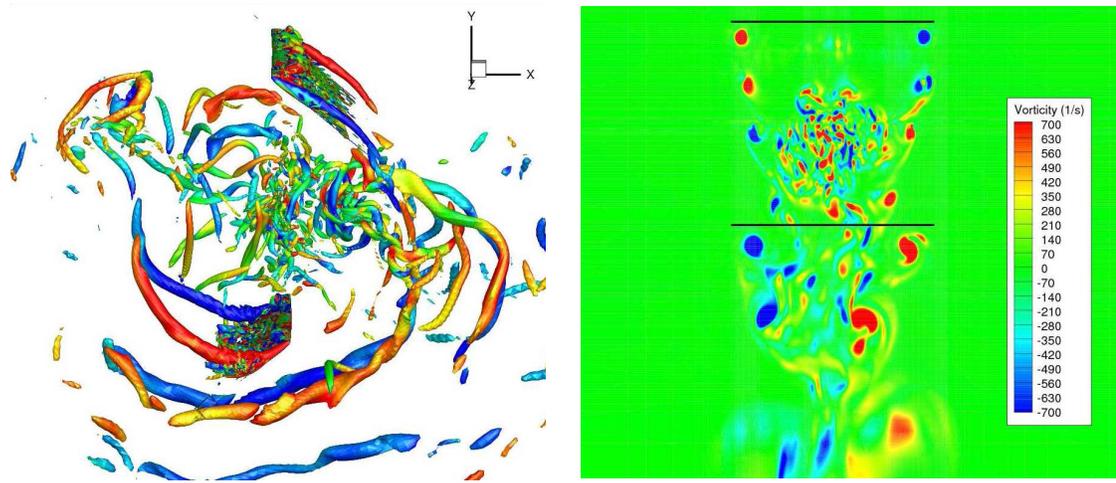
(a) 3-D Flow field inside the cyclorotor.

(b) Evolution of tip vortex.

Figure 1.40: **Results from the 3-D CFD simulation performed at the University of Maryland [69].**

Reynolds-Averaged Navier-Stokes (RANS) solver, OVERTURNS, to investigate the performance and flow physics of an MAV-scale cyclorotor [69]. The goal of the study was to develop a computational methodology to understand the complex aerodynamics of the cyclorotor.

This overset structured mesh solver uses the diagonal form of the implicit approximate factorization method with a preconditioned dualtime scheme to solve the compressible RANS equations. Computations were performed in the inertial frame in a time-accurate manner. A third-order MUSCL scheme with Roe flux difference splitting and Korens limiter was used to compute the inviscid terms, and second-order central differencing was used for the viscous terms. Due to the relatively low Mach numbers in which the cycloidal rotors operate, the inclusion of a low Mach preconditioner based on Turkels method accelerates the convergence and ensures accuracy of the solution. The Spalart-Allmaras turbulence model for RANS

closure was utilized in 3-D calculations. However, due to convergence problems with the Spalart-Allmaras model in the 2-D CFD simulation, the two-layer algebraic 0-equation turbulence model of Baldwin and Lomax was employed.

The code was validated against rotational speed and collective pitch angle sweep performance measurements; the computed results were found to provide reasonable vertical force prediction, while underpredicting sideward force and power. Even though the flow visualizations showed prominent 3-D effects, there was no significant differences between the average forces predicted by the 2-D and 3-D analysis. The maximum vertical force and aerodynamic power for the cycloidal rotor design is attained when the blade is at the lowest azimuthal position in circular blade trajectory. This is due to the virtual camber effect from blade rotation which effectively imposes a positive camber on the symmetric airfoil at the bottom of the cyclocopter cage, and a negative camber at the top. However, testing of a 4.5% camber geometric configuration to counteract virtual camber made the aerodynamic forces more symmetric in the upper and lower halves. The flowfield predicted by the 3-D CFD showed good similarity with the flow field measured using PIV. The key flow features that were observed included, two tip vortices with strength varying as the blade moved around the azimuth, a skewed wake structure confirming the lateral force, wake contraction, unsteady shedding and significant blade wake interactions (Fig. 1.40).

In 2010 Nakai et.al. conducted an experimental investigation of the flow around a cycloidal propeller [70]. Flow fields were obtained using a particle image velocimetry (PIV) system whose data acquisition was synchronized with the
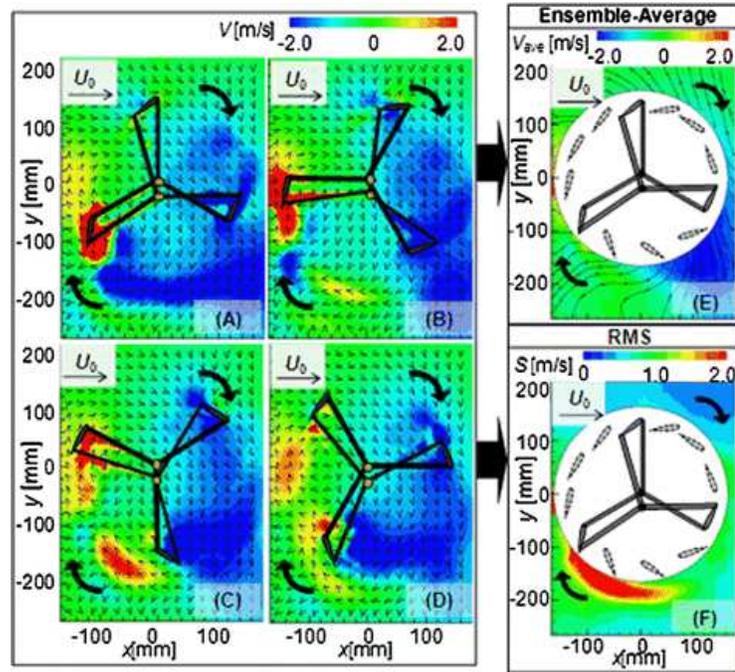
Figure 1.41: **2-D PIV measurements on a cycloidal rotor [70].**

propellers angular position. The chord-based Reynolds number was 14,000. Flow characteristics such as mean velocity, vorticity and the RMS value of velocity fluctuation were derived from the measurements. As shown in Fig. 1.41, the results demonstrated the presence of a downwash around the propeller during the generation of lift. Detailed observations around each airfoil visualized distinct vortex shedding and reattaching flow at certain phase angles of the propeller. This is the only PIV study performed on a cycloidal rotor other than the present study.

1.5   Objectives of The Current Research and Thesis Organization

As clearly seen from the literature survey, there have not been many systematic studies on cyclorotors in the past. And the studies that have been performed are

70

mostly at relatively larger scales with operating Reynolds numbers much higher than 100,000, while the MAVs operate at Reynolds number of the order of 10,000. Moreover, none of these studies were comprehensive enough to clearly lay down the design principles for an efficient, flight-capable cyclorotor. Based on the current understanding of cyclorotors, even designing such a rotor to obtain the required thrust for the vehicle to hover is a challenging task. Therefore, one of main focusses of the present study was to systematically vary the blade design and kinematics to improve the thrust producing capability of a cyclorotor at a constant rotational speed and rotor size. Once the required thrust is acheived, the next most challenging task is to increase the flight endurance of the vehicle. To this end, the achievement of a high power loading (thrust per unit power) is a key factor. A primary goal of the present work was to carefully investigate the performance of the cyclorotor concept and to examine whether its hovering efficiency could be made equal to or better than that of a conventional rotor at the micro-scale. To maximize the thrust and power loading of the present cyclorotor, a detailed experimental parametric study was performed. This forms the content of Chapter 2.

In order to design and build an efficient and flight capable cyclorotor, it is extremely important to understand the flowfield generated by such a system. The current understanding of the cyclorotor aerodynamics can be rated as qualitative, at best. Many aspects of the flow are still not completely understood. Flow field measurements can help in understanding the efficiency of such a system based on the uniformity (or otherwise) of the inflow. Obtaining an understanding of the flow inside the rotor can be useful in developing a better inflow models, which will help

in predicting the thrust and power more accurately. Chapter 3 discusses the flow field measurements that were made using the Particle Image Velocimetery (PIV) technique inside the cyclorotor-cage and the rotor-wake to better understand the aerodynamics. It should be also noted that this is the first ever flowfield measurements made on a cyclorotor at any scale.

Most of the previous studies on cyclorotors have been experimental in nature and even the computational studies that were performed were at higher Reynolds numbers ($> 100,000$). Also, all these studies were focussed on developing aerodynamic models; the effects of the blade deformations were not included while calculating the aerodynamic performance. Therefore, one of the goals of the present study is to develop a fully non-linear large deformation unsteady aeroelastic model to predict the blade loads and average performance of an MAV-scale cyclorotor. The model was validated with the test data from the present study. This forms the content of Chapter 4.

Attempts to build flight capable cyclocopters (or cyclogyros) had started since the early 20th century. Almost all these attempts were at full-scales. However, as discussed before, none of these attempts were successful in building a flying vehicle. One of the main reason for this is the fact that the structural design of a cyclorotor is more difficult than that of a conventional rotor because in a cyclorotor there is a large rotating structure which has to be designed strong enough to handle the large centrifugal loads and light enough to be used on a flying vehicle. However, today, with the breakthroughs in material technology, new fabrication techniques and high power-to-weight ratio propulsion systems, it seems feasible to build a fly-

ing cyclocopter, atleast at smaller scales. In the present work it was important to demonstrate the hover capability of this concept at a smaller scale and also develop a control strategy that can be used to stabilize and control the cyclocopter in hover. Therefore, building a hover capable cyclocopter was attempted by utilizing the understanding obtained from both experimental and analytical studies discussed in the previous chapters. Chapter 5 discusses the detailed design process and the issues encountered during the development of the two hover capable cyclocopters, the twin-rotor cyclocopter and the quad-cyclocopter and also the development and validation of the control strategy for the quad-cyclocopter. Chapter 6 outlines conclusions of this study and proposed outlines for future work.

Chapter 2

Experimental Performance Studies

2.1 Overview

As discussed in chapter. 1, cyclocopter (Fig. 2.1) is an out-of-the-box flight concept and there have not been many studies in the past to explore this idea thoroughly, atleast for flying applications. Also, most previous experiments on cyclocopters (or cyclorotors) have been at relatively larger scales [29–32, 36, 38, 43–46, 53–59, 64, 68]. Moreover, none of these studies were comprehensive enough to clearly lay out the design principles for an efficient, flight-capable cyclorotor. Based on the current understanding of cyclorotors, even designing such a rotor to obtain the required thrust for the vehicle to hover is a challenging task. Therefore, one of main focusses of the present study was to systematically vary the blade design and kinematics to improve the thrust producing capability of a cyclorotor at a constant rotational speed and rotor size.

Once the required thrust is obtained, the next most challenging tasks with any hover-capable MAV design is to increase the flight endurance of the vehicle. To this end, the achievement of a high power loading (thrust per unit power) is a key factor in determining hovering flight efficiency. None of the previous studies mentioned has carried out a comprehensive experimental parametric study to improve the perfor-mance of a cyclorotor at MAV-scale Reynolds numbers. Therefore, a primary goal
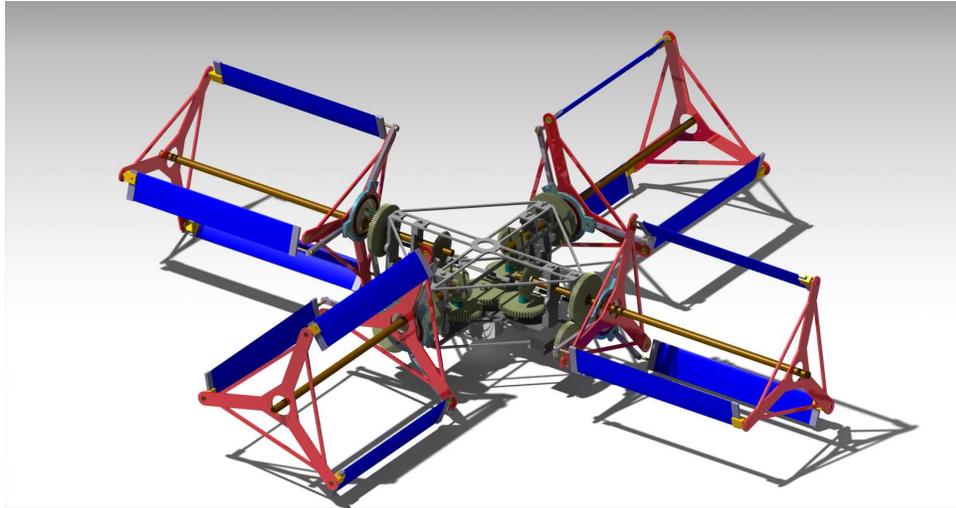
Figure 2.1: **Cyclocopter MAV design.**

of the present work was to carefully investigate the performance of the cyclorotor concept and to examine whether its hovering efficiency could be greater than that of a conventional rotor at the micro-scale. For this purpose, an experimental parametric study was performed to try to optimize the performance of a cyclorotor and to compare its power loading to that of a conventional micro-rotor when operating at the same effective disk loading.

Previous studies performed at the University of Maryland [63] included systematic experimental parametric studies on 3- and 6-bladed micro-scale cyclorotors (diameter and span = 6 inches) by varying the rotational speed and blade pitching amplitude. This study indicated that the cyclorotor concept can be promising at the very low Reynolds numbers typical at which MAVs operate. Even though this study provided lot of insights into the performance of a cyclorotor at MAV-scale Reynolds numbers, it was not very comprehensive. Moreover, it had many shortcomings such as the relatively heavy rotor design (weighing 450 grams), which restricted the maxi-

mum acheivable rotational speed to 1200 rpm producing only 50 grams of maximum thrust. Also, due to the heavy and bulky rotor design, the tare power was almost 75% of the total power, which led to some discrepancies in the aerodynamic power measurements. Therefore, it was evident that more comprehensive experimental studies have to be performed using light-weight and more realistic cyclorotors that can reach higher rotational speeds, in order to able to vault a laboratory model to a successfully working hover-capable vehicle.

As explained before, previous tests at Maryland were performed using a rigid, non-flyable bench-top test model. However, in the present work, a cyclorotor was built light enough to be potentially used on an actual flight-capable MAV. Studies were conducted to investigate the effect of the rotational speed, blade airfoil profile, blade flexibility, blade pitching amplitude (symmetric and asymmetric blade pitching), pitching axis location, number of blades with constant chord (varying solidity), and number of blades at same rotor solidity (varying blade chord). These parameters when systematically varied, identified substantial improvements in cyclorotor performance. The final performance of the optimized cyclorotor appeared significantly higher than that of a conventional rotor. Discussion of the results from these experimental studies forms the content of the present chapter.

2.2 Experimental Setup

Several experiments were conducted on MAV-scale cyclorotors (Fig. 2.2) to investigate the effects on overall performance resulting from rotational speed (rpm), num-
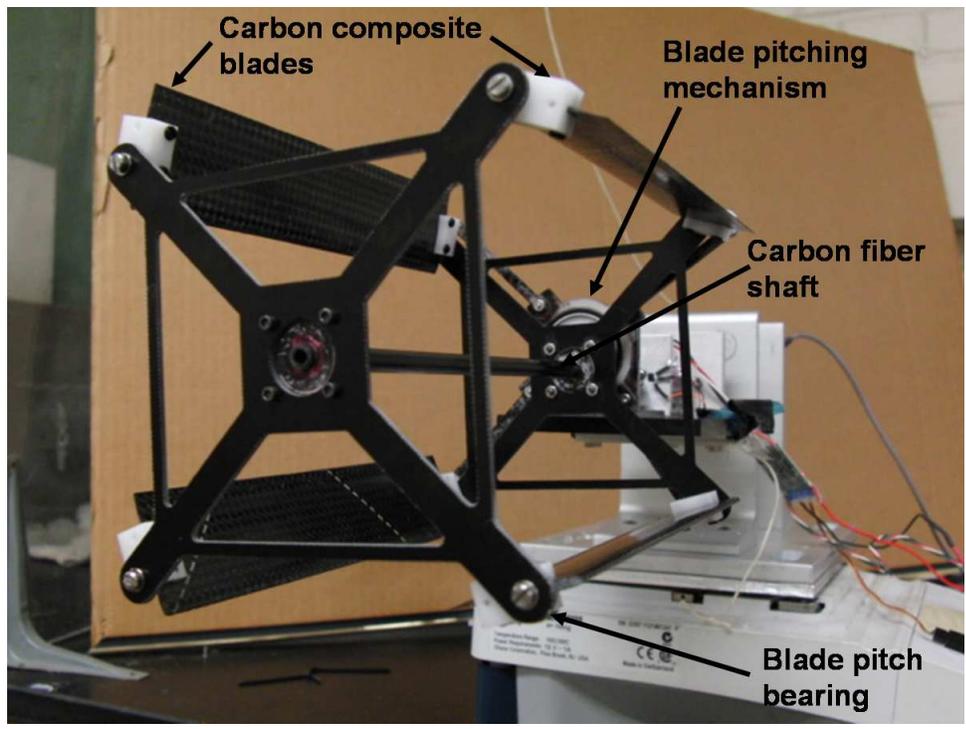
Figure 2.2: **Cyclorotor used for testing.**
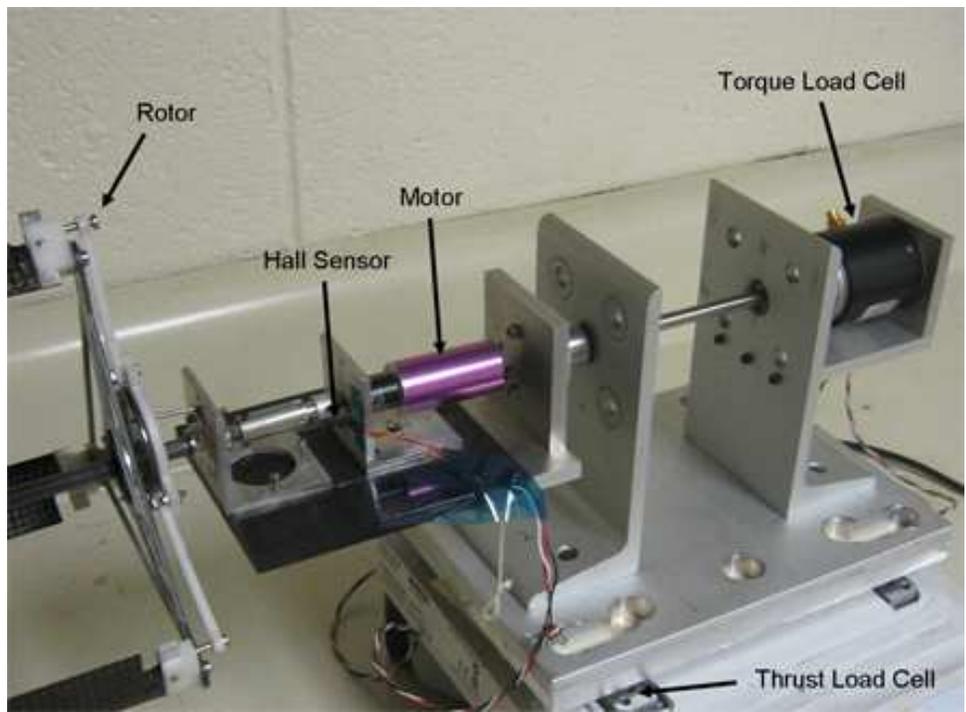
Figure 2.3: **Experimental setup.**

ber of blades (with constant and varying solidity), amplitude of blade pitch (symmetric and asymmetric pitching), blade pitching axis location, blade airfoil profile, and blade flexibility. All the rotors had a diameter of 6 inches and primarily two sets of blades were tested. The first blade set had a span of 6 inches and chord of 1 inch and the second set had a span of 6.25 and chord of 1.3 inches. The details of the design of the cyclorotors used for the performance measurements are given in Chapter 5.

A test setup (Fig. 2.3) with load cells was designed and built to measure the thrust, torque, and rotational speed of the cyclorotor. The thrust was measured with a resolution of 0.1 mN and torque with 0.175 mN-m resolution. To obtain the time-averaged thrust and torque values, the instantaneous readings were averaged over 5 seconds. The instantaneous values was acquired at 1000 samples/second, which is almost 30 times higher than the maximum speed at which the rotor was tested (2000 rpm, 33.3 Hz). A Hall-effect sensor was used to generate a 1/rev signal to measure the rotational speed. The resolution in the rotational speed measurements was ±30 rpm. The power consumption was determined from the torque and rotational speed measurements. The test data was acquired using a LABVIEW based data acquisition system. Each measurement was repeated three times and therefore, each data point is an average of these three trials. The scatter in the measurements were extremely small as shown using error bars in Figs. 2.9 to 2.11.

Measurements were taken on 2-, 3-, 4- and 5-bladed cyclorotors at blade pitching amplitudes of 25°, 30°, 35°, 40° and 45°, and for rotational speeds ranging from 400 to 2,000 rpm. The blade profile shapes that were tested included the NACA
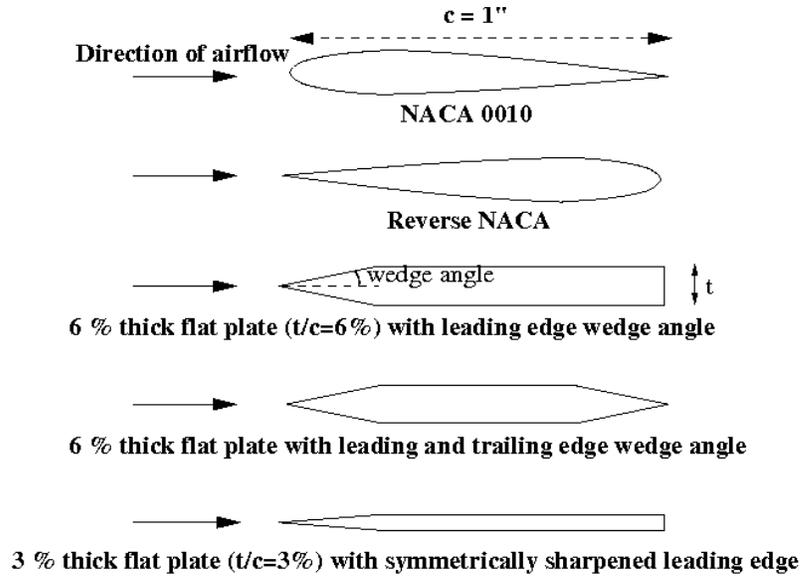
Figure 2.4: **Cross-sectional profiles of the blade sets that were tested.**

0015, NACA 0010, NACA 0006, a reverse NACA 0010 (where the trailing edge faces the flow instead of leading edge), a 6% thickness-to-chord flat plate blade with symmetric 5° leading edge wedge angle (5 deg LE), a 6% thickness-to-chord flat plate blade with symmetric 5° leading edge and trailing edge wedge angles (5 deg LE&TE), and flat plate blades with symmetrically sharpened leading edges (having 3%, 2% and 1% thickness-to-chord ratios). Figure 2.4 illustrates some of the different blade profiles.

2.3   Results and Discussion

2.3.1   Rotor Forces

The coordinate system used and the blade kinematics of the cyclorotor is shown in Fig. 2.5. The azimuthal position of the blade, Ψ, was measured counter clockwise

79
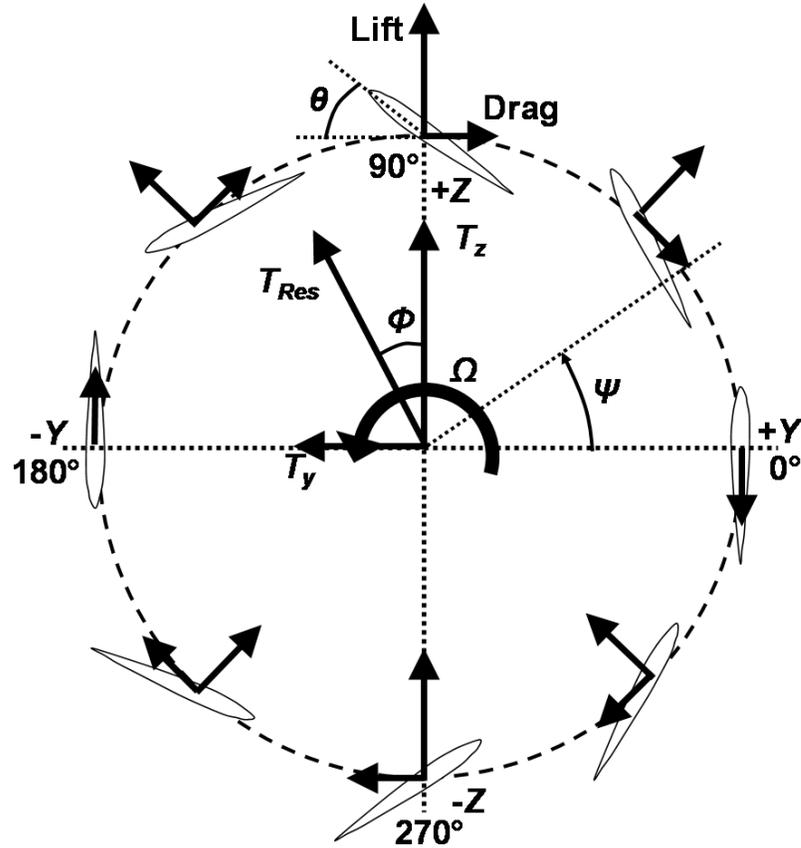
Figure 2.5: **Thrust vectors on a cyclorotor.**

from the positive Y-axis. The blade pitch angle, θ, was measured with respect to the

tangent to the circular path of the blade. The required blade pitch angle variation

was obtained using a passive four-bar based blade pitching mechanism.

Figure 2.6 shows the schematic of the passive blade pitching mechanism that

was employed to obtain the required pitching kinematics. As shown in the figure,

the blade is passively pitched using a pitch link about a point A, which forms

the pitching axis. To obtain the required kinematics, one end of the pitch link is

connected to the blade at point B, aft of the pitching axis and the other end moves

along the circumference of a disk (offset disk), which is offset from the center of the
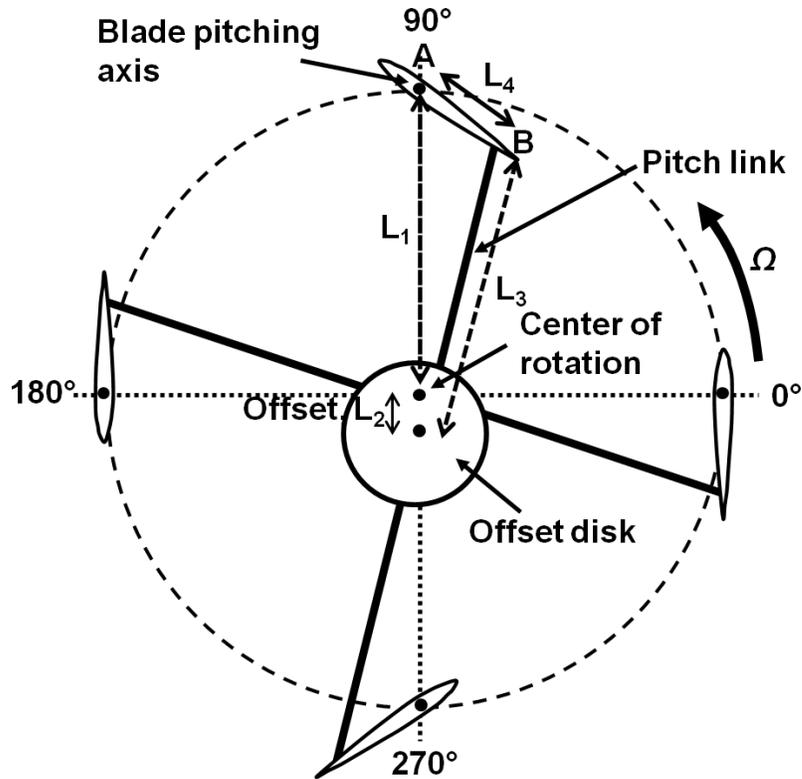
Figure 2.6: **Schematic of blade pitching mechanism.**

shaft by a distance L_2. The resulting system comprised a crank-rocker type four-bar mechanism, which could accomplish the required cyclic change in blade pitch. Notice that the blades could be set to different pitching amplitudes by changing the offset length, L_2. More details on the blade pitching mechanism are provided in Chapters 4 and 5.

Figure 2.7 shows the blade pitch angle (θ) variation for different pitching amplitudes obtained using a four-bar analysis. It can be seen that with this mechanism, the maximum blade pitch angle does not occur exactly at $\Psi=90°$ and $270°$, but with a small phase delay. Because of this phase delay, the rotor should produce a small lateral force T_y. However, the measurements showed a significant lateral force whose
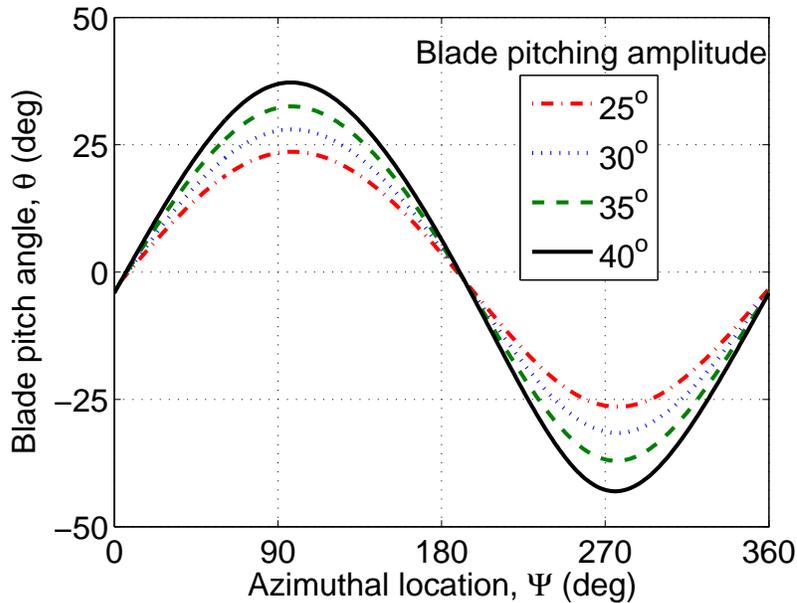
Figure 2.7: **Variation of blade pitch angle around the azimuth for different blade pitching amplitudes.**

magnitude was comparable to the vertical force T_z (Fig. 2.5). Other reasons for the lateral force could be the aerodynamic lag produced because of the unsteady aerodynamic effects, and the virtual camber effect (due to the virtue of blade kinematics), which significantly changes the behavior of the blades in the upper and lower halves, as a result the lateral forces do not cancel out. The aerodynamic lag will be explained in more detail in Chapter 4 using an unsteady aerodynamic analysis. This presence of lateral force was further confirmed by the PIV studies (discussed in Chapter 3), which showed the presence of a significantly skewed wake structure in the plane perpendicular to the axis of rotation.

In the present setup, the thrust load cell was oriented in such a way that it could only measure the forces along the Z-axis. Therefore, to measure both the
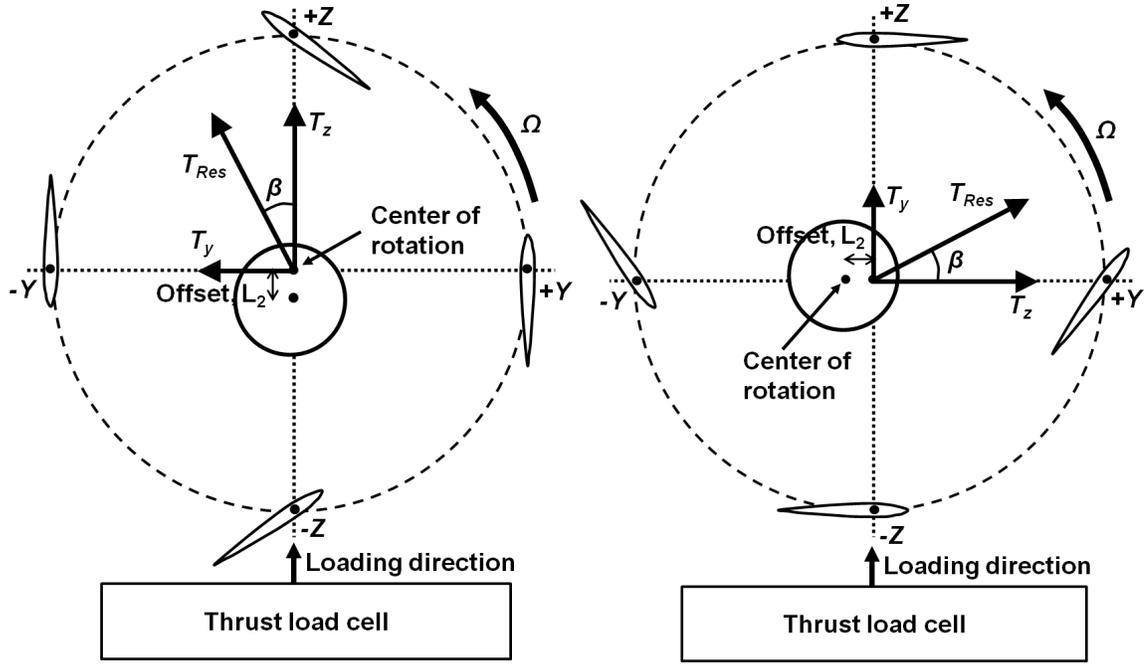
(a) 0° orientation for vertical force (T_z).   (b) 90° orientation for lateral force (T_y).

Figure 2.8: **Schematic describing the vertical (T_z) and lateral (T_y) force measurement using the experimental setup.**

vertical and lateral forces, the experimental setup was made in such a way that the whole cyclorotor assembly could be rotated along its shaft axis to any orientation along the rotational axis. Rotating the cyclorotor assembly resulted in a change in the direction of the pitching mechanism offset (L_2) as shown in Fig. 2.8. The 0° orientation of the rotor is shown in Fig. 2.8(a), which refers to the offset pointing vertically downwards (along the negative Z-axis). In this orientation the vertical force is acting along the Z-axis so that the load cell measures the vertical force (T_z). To measure the sideward force T_y, the cyclorotor setup was rotated by 90° and locked in that position as shown in Fig. 2.8(b). In this case, T_y is pointed in the Z-direction, so that its value could be measured by the load cell. The resultant
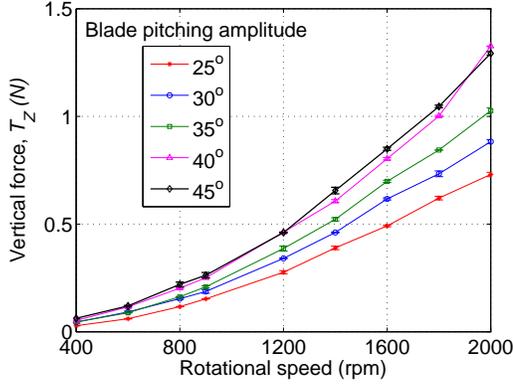
(a) Vertical force, T_z.
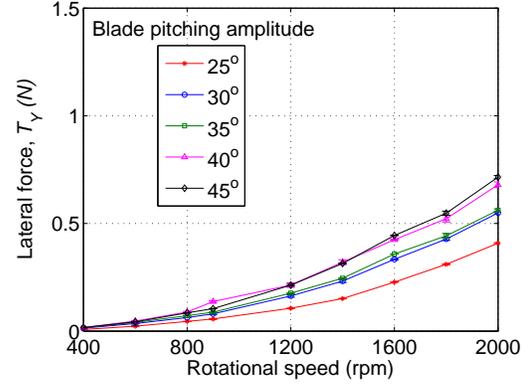
(b) Lateral force, T_y.
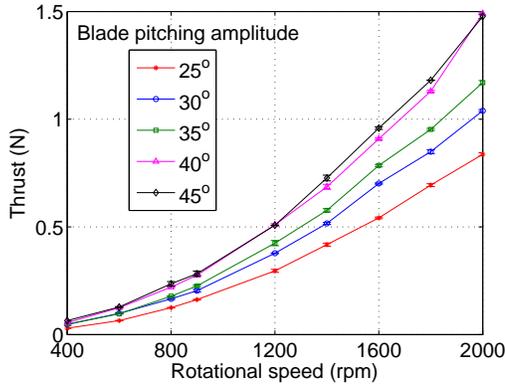
(c) Resultant thrust, T.
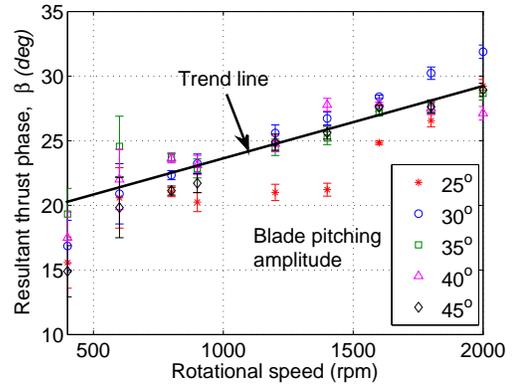
(d) Resultant thrust phasing with vertical.

Figure 2.9: **Cyclorotor forces versus rotational speed for the rotor with NACA 0010 blades at different blade pitching amplitudes.**

force, T_{Res}, was calculated from the values of T_z and T_y by using

$$T_{Res} = \sqrt{T_z^2 + T_y^2} \tag{2.1}$$

where the angle, β, made by T_{Res} to the vertical (thrust phasing, Fig. 2.5) is given by

$$\beta = \tan^{-1}\left(\frac{T_y}{T_z}\right) \tag{2.2}$$

To confirm whether the cyclorotor was producing the calculated resultant thrust at an angle with respect to the vertical, the assembly was rotated by an

angle β (so that the resultant thrust now acted along the Z-axis). The measured resultant thrust agreed well with the thrust calculated from the T_z and T_y components. Figures 2.9(a) and 2.9(b), respectively, show the variation of T_z and T_y with rotational speed when using the NACA 0010 blades operated at different blade pitching amplitudes; both force components were noted to vary with the square of the rotational speed. Figure 2.9(c) shows the variation of resultant thrust with rotational speed. Figure 2.9(d) shows the variation of the phase, β, of the resultant thrust (angle the resultant thrust vector makes with the vertical) with rotational speed, where it is apparent that β also increases with rotational speed. This outcome is an important design consideration for a cyclorotor MAV because both the magnitude and direction of the thrust vector will vary with its rotational speed. In the remainder of the current paper, the thrust refers to the resultant thrust (i.e., to T_{Res}).

2.3.2 Power Analysis

The total aerodynamic power includes the induced power, the profile power, rotational flow losses, the aerodynamic power required for cyclically pitching the blades, the profile power associated with rotating the structure of the cyclorotor (other than the blades), and the balance loses. Tare tests were carried out at different rotational speeds after removing the blades to measure the balance losses and profile power associated with the rotor structure (other than the blades). These measurements were then subtracted from the total power measurements to obtain the aerody-
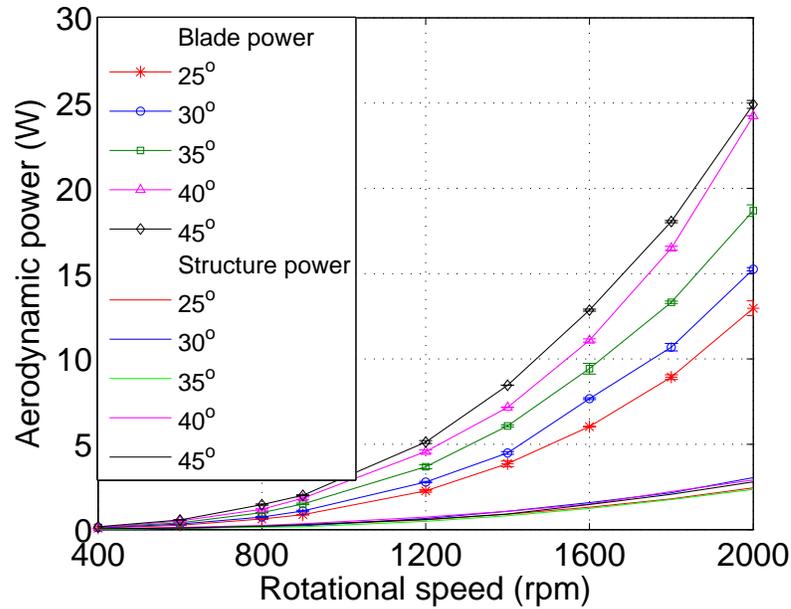
Figure 2.10: **Variation of blade and rotor-structure power with rotational speed for different blade pitching amplitudes.**

namic power required just to rotate the blades. The power breakup is shown in Fig. 2.10. Tare loses were found to constitute only around 10% of the total aerodynamic power, which was a major improvement over the previous generation of cyclorotor experiments in which such losses constituted almost 75% of the total power being measured [63].

The subsequent sections in this chapter discusses the effect of the different parameters varied on the performance of the cyclorotor in terms of thrust and power loading (thrust per unit power).
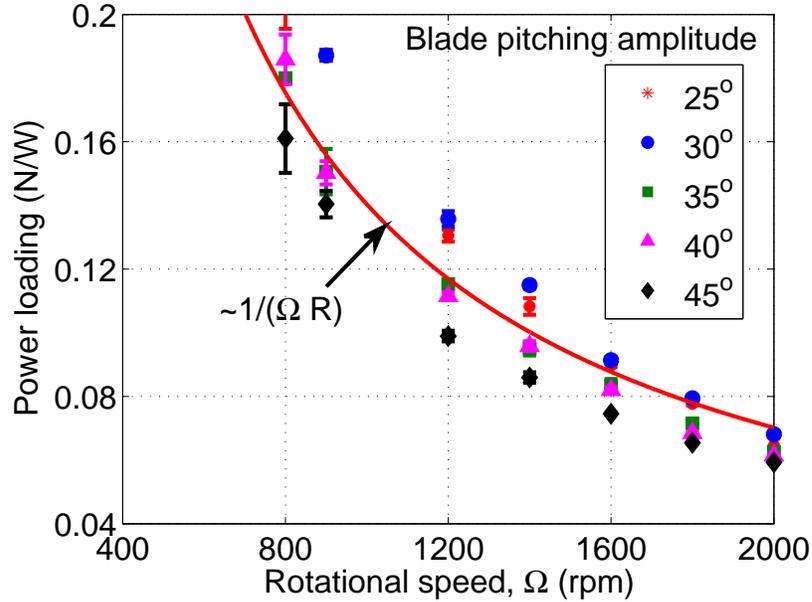
Figure 2.11: **Power loading versus disk loading for a 3-bladed cyclorotor using NACA blades at four different blade pitching amplitudes.**

2.3.3 Effect of Rotational Speed (rpm)

Operating at the optimum rotational speed is critical for maximizing the power loading (thrust/power) of a cyclorotor. Figure 2.11 shows the variation of power loading with rotational speed (Ω) for different pitching amplitudes when using the NACA 0010 blades. As expected, the measured power loading varied as $(\Omega R)^{-1}$ because thrust is a function of the square of rotational speed and power varies with the cube of rotational speed. Therefore, to maximize power loading, it is important to obtain the required thrust at the lowest rpm. The operating speed is not only important from an aerodynamic perspective, it is also the primary driver for the blade and rotor structural design because the transverse centrifugal loading on the blade varies as the square of rotational speed.
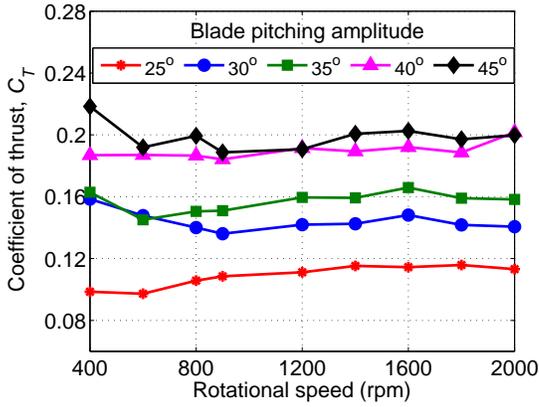
(a) NACA 0010.
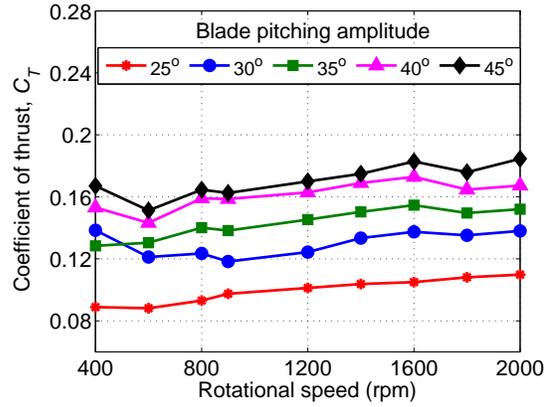
(b) Reverse NACA 0010.
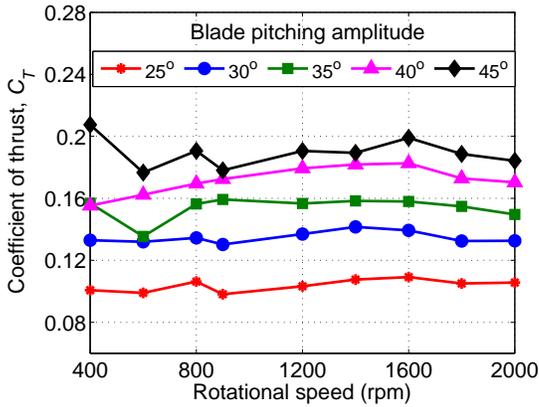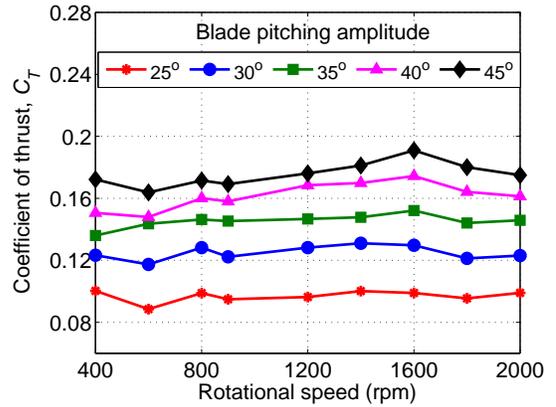
(c) 5 deg LE.

(d) 5 deg LE and TE.

Figure 2.12: **Variation of thrust coefficient (C_T) with rotational speed at different blade pitching amplitudes for different blade sections.**
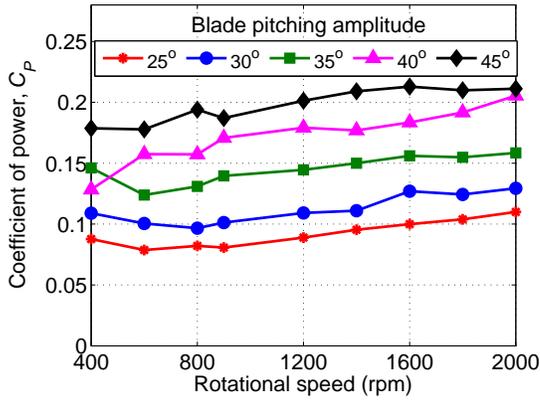
(a) NACA 0010.
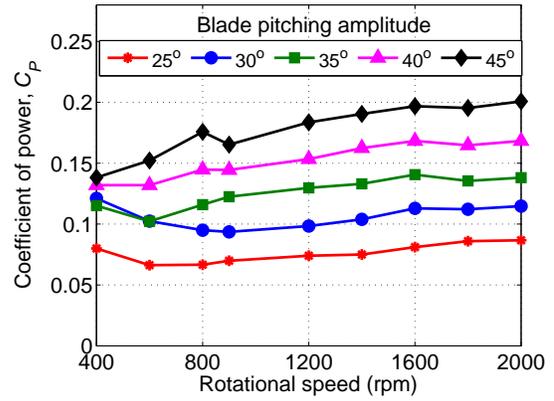
(b) Reverse NACA 0010.
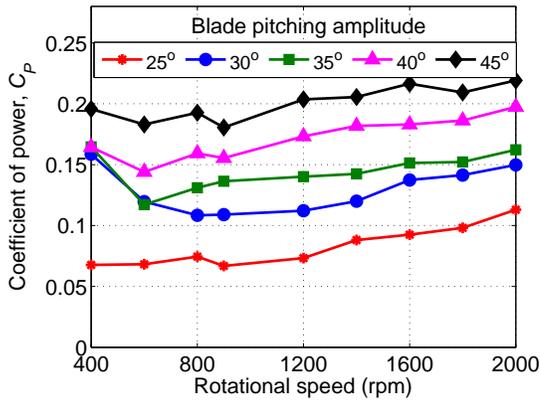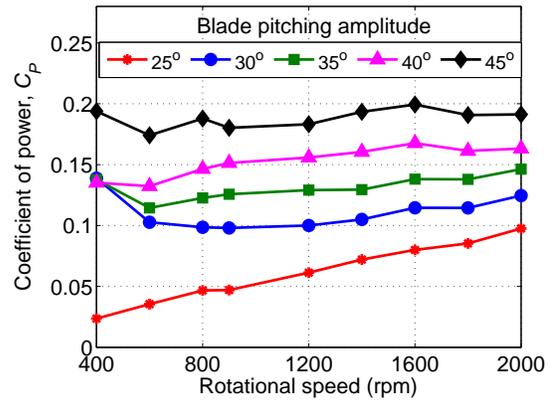
(c) 5 deg LE.

(d) 5 deg LE and TE.

Figure 2.13: **Variation of power coefficient (C_P) with rotational speed at different blade pitching amplitudes for different blade sections.**

As the rotational speed is changed from 400 rpm to 2,000 rpm, the chord Reynolds number changes by a factor of five. To see any effect of Reynolds number, the thrust and the power has to be non-dimensionlised with rotational speed. Figure 2.12 shows the variation of thrust coefficient ($C_T = T/(\rho A \Omega^2 R^2)$) with rotational speed for different blades at various blade pitching amplitudes. In all the cases, the thrust coefficient remains almost constant with rotational speed clearly showing that the thrust varies as the square of rotational speed and there are no Reynolds number effects.

Figure 2.13 shows the variation of power coefficient ($C_P = P/(\rho A \Omega^3 R^3)$) with rotational speed for different blades at various blade pitching amplitudes. Contrary to what was expected, there was a small linear increase of C_P, with rotational speed. As shown in Figure 2.13(d), the rate of increase of C_P with rotational speed was very high for the 5deg LE&TE case at 25° blade pitching amplitude.

2.3.4   Effect of Blade Pitching Amplitude (Symmetric pitching)

Operating at the optimum blade pitching amplitude is important to maximize the power loading and the thrust producing capability of the cyclorotor. The rotors were tested at blade pitching amplitudes of 25°, 30°, 35°, 40° and 45° with symmetric pitching. During symmetric pitching, the blade attains the same pitch angle at the top and bottom points of its trajectory.

Figure 2.14(a) shows the variation of thrust coefficient, C_T, with blade pitching amplitude for the five blade sets, namely, the NACA 0010, the reverse NACA 0010,

(a) Coefficient of thrust, C_T. (b) Coefficient of power, C_P.
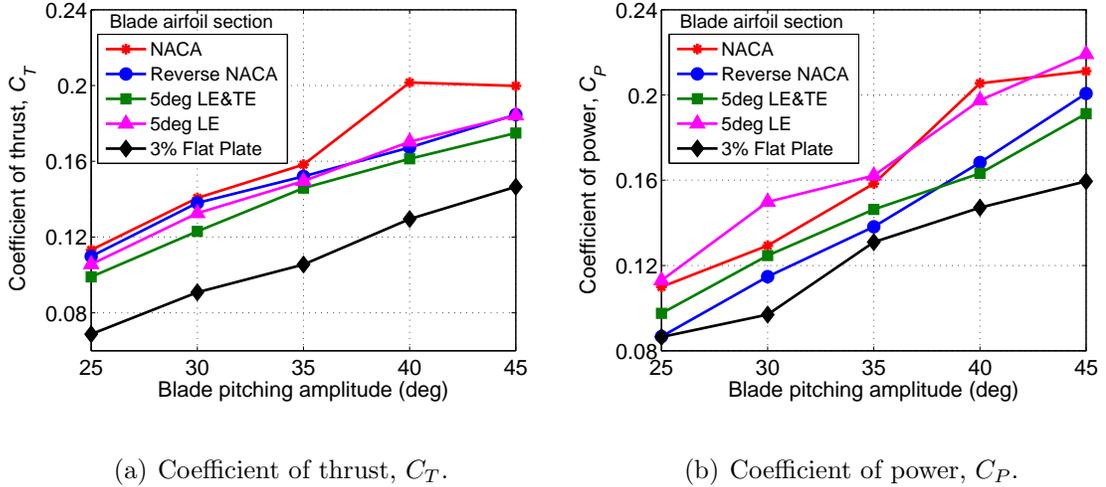
Figure 2.14: **Variation of thrust and power coefficients with blade pitching amplitude for five different blade sets at 2000 rpm.**

the 6% thickness-to-chord flat plate blade with symmetric 5° leading edge wedge angle (5deg LE), and the 6% thickness-to-chord flat plate blade with symmetric 5° leading edge and trailing edge wedge angles (5deg LE&TE), at a rotational speed of 2000 rpm. These measurements were taken on a 3-bladed, 6 inch diameter cyclorotor that had a blade span of 6 inches and chord of 1 inch. For all of the cases in Fig. 2.14(a), except for the NACA 0010 airfoil, the value of C_T was found to increase linearly with pitching amplitude from 25° to 45° without showing any signs of stall. For the NACA airfoil, the value of C_T showed a small decrease between 40° to 45° of amplitude; this is probably because the NACA 0010 airfoil had reached its maximum lift coefficient.

Figure 2.14(b) shows the variation of power coefficient, C_P, with blade pitching amplitude for the five blade sets at a rotational speed of 2000 rpm. From the results in Fig. 2.14(b), it is seen that the power coefficient increases steadily with increasing

blade pitch, confirming the absence of stall on the blades. It was significant to find that the blades remained unstalled at such large pitch angles. However, from the PIV studies (discussed in Chapter 3), it was found that the induced velocities in the wake of the cyclorotor were relatively high and were comparable to the blade section velocities resulting from rotation. Therefore, even though the pitch angle was often high, the large induced velocities decreased the effective aerodynamic angles of attack and kept them below stall. The PIV studies also showed the presence of a spilled dynamic stall vortex at the leading edge of the blades. The delay of stall to higher angles, which is a known unsteady aerodynamic mechanism of dynamic stall [71], may also occur because of the positive pitch rate of the blades.

Figure 2.15(a) shows the variation of power loading (thrust per unit power) with disk loading (thrust per unit actuator area) for the rotor using NACA 0010 blades at different pitching amplitudes. It can be clearly seen from Fig. 2.15(a), that the optimum pitching amplitude is 40°, especially for the higher disk loading conditions and the 25° pitching amplitude produced the lowest power loading. The power loadings were compared at the same disk loading instead of same thrust so that the ideal induced power remains the same. However, for all the cases discussed in Fig. 2.15(a), the same rotor was used and therefore have the same actuator area (rectangular projected area of rotor, $span \times diameter$) making the disk loading analogous to the total thrust produced. In the rest of the paper all the different test cases will be compared using power loading versus disk loading since this relationship provides a good measure of the efficiency and the thrust-producing capability of the cyclorotor.
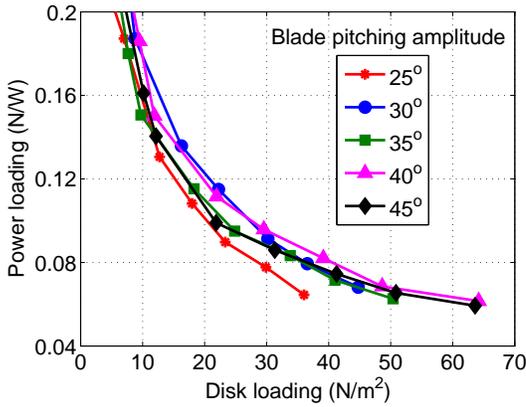
(a) NACA 0010.
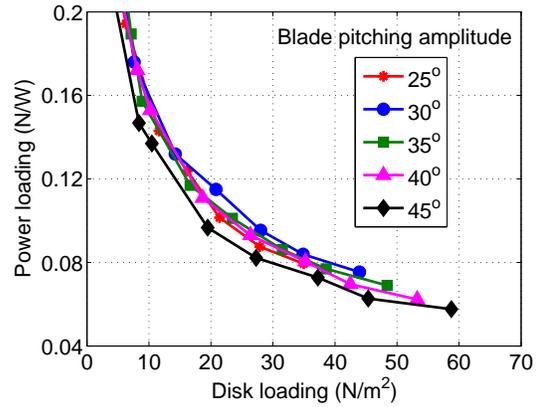
(b) Reverse NACA 0010.
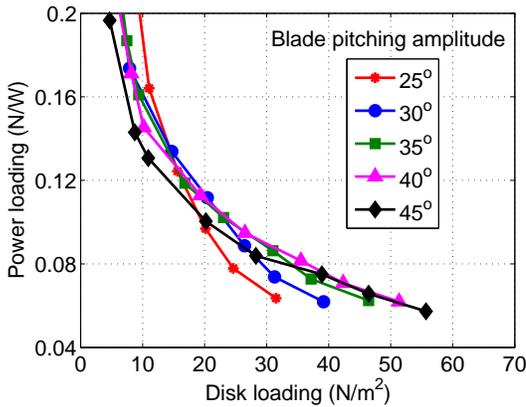
(c) 5 deg LE and TE.
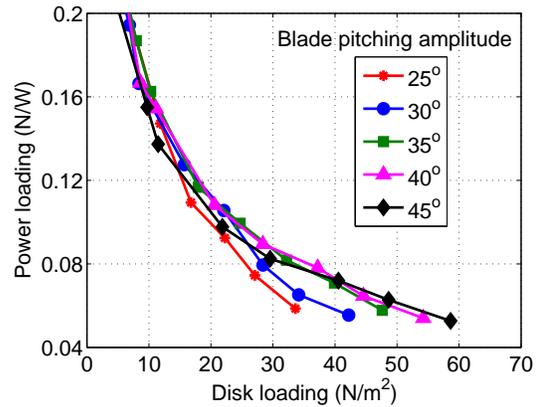
(d) 5 deg LE.

Figure 2.15: **Variation of power loading with disk loading for different blade sections at different blade pitching amplitudes.**

Figure 2.15(b) shows the variation of the power loading with disk loading for the rotor with reverse NACA 0010 blades at different pitching amplitudes. Clearly, 30° pitching amplitude produced better power loadings and 45° produced the worse power loading for all thrust conditions. For the 5° leading edge and trailing edge wedge angle (5deg LE&TE) blades (Fig. 2.15(c)), 40° pitching amplitude produced the maximum power loading at the high disk loading condition ($> 30N/m^2$) and 45° pitching amplitude produced almost the same power loading as the 40° case at extremely high disk loading conditions ($> 40N/m^2$). For the 6% thick 5° leading edge wedge angle (5deg LE) case (Figure 2.15(d)), at extremely high disk loading cases ($> 40N/m^2$), 45° pitching amplitude produced the maximum power loading for the same value of disk loading. For the cases where $DL < 30N/m^2$, 40° pitching amplitude produced the maximum power loading. Again, the 25° pitching amplitude had the lowest power loading amongst all the cases.

From the above set of tests it was evident that the efficiency and the thrust producing capability of the cyclorotor increased with pithing amplitude until a pitching amplitude of 40° for NACA 0010, reverse NACA 0010 and 6% thickness-to-chord ratio flat plate airfoil sections. However, it was important to examine if this conclusion remained true for other NACA airfoil sections. Therefore, experiments were conducted on cyclorotors using three different NACA airfoil sections, namely, NACA 0006, 0010 and 0015, at different pitching amplitudes. NACA 0010 section was again tested with the other two sections because the new blades had a chord of 1.3 inches and span of 6.25 inches. Also, these tests were peformed on 2- and 4-bladed cyclorotors, unlike the 3-bladed rotor used in the previous tests.

94
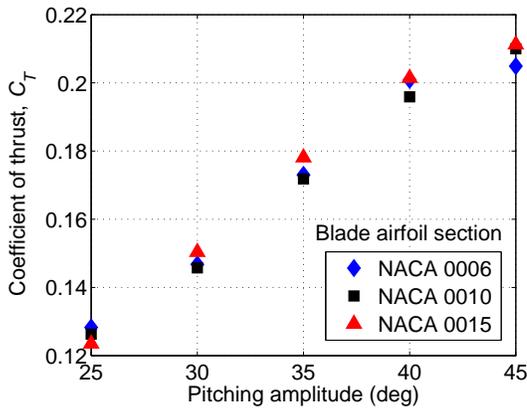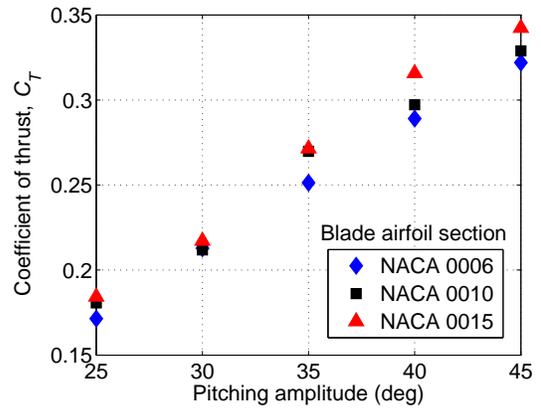
(a) 2-bladed rotor.

(b) 4-bladed rotor.

Figure 2.16: **Variation of thrust coefficient with blade pitching amplitude for 2- and 4-bladed rotors using three different airfoil sections at 1800 rpm.**
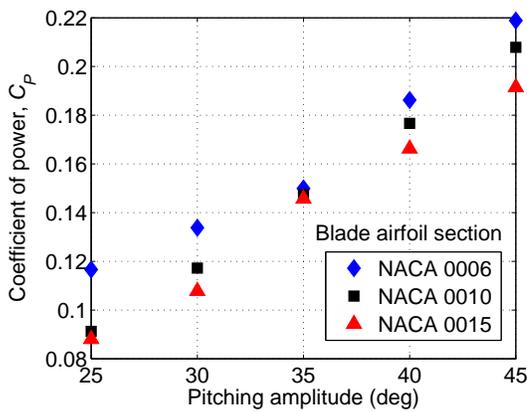
(a) 2-bladed rotor.
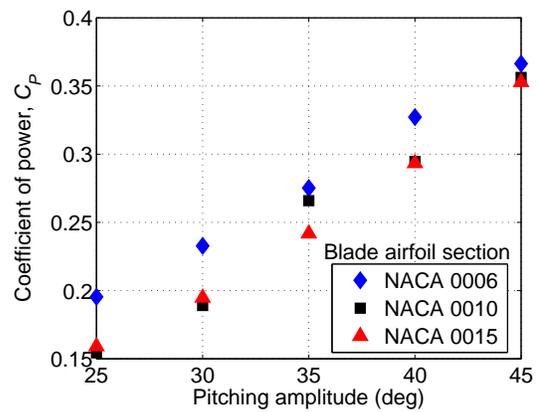
(b) 4-bladed rotor.

Figure 2.17: **Variation of power coefficient with blade pitching amplitude for 2- and 4-bladed rotors using three different airfoil sections at 1800 rpm.**

Figures 2.16(a) and 2.16(b), respectively, show the variation of thrust coefficient with blade pitching amplitude for 2- and 4-bladed cyclorotors at a constant rotational speed of 1800 rpm. The 2-bladed and the 4-bladed rotors used the blades with the same chord, hence the solidity of 2-bladed rotor is almost half of the 4-bladed rotor solidity. The primary aerodynamic differences between a 4-bladed rotor and 2-bladed rotor could be the magnitude of rotor inflow and the interference effects between the blades. For the 2-bladed rotor (Fig. 2.16(a)), similar to the 3-bladed rotor discussed before (Fig. 2.14(a)), the thrust increased linearly till 40° pitching amplitude, however, the rate of increase dropped from 40° to 45°. Again, this is probably because at 45° pitch, the airfoils might have reached closer to its maximum lift coefficient.

However, for the 4-bladed rotor (Fig. 2.16(b)), the thrust increased linearly from 25° till 45° pitching amplitude. The reason for the better performance of the 45° case on a 4-bladed rotor may be because, for a 4-bladed rotor, at the same rotational speed, the inflow is higher than that of a 2-bladed rotor because of higher thrust coefficient and therefore, the blades on a 4-bladed rotor operates at a lower aerodynamic angle of attack when compared to a 2-bladed rotor. Now, this could potentially improve blade performance if it is operating at very high pitch angles (such as 45°) close to stall. As shown in Figs. 2.17(a) and 2.17(b), the power for all the three blade sections increased steadily from 25° to 45° showing no signs of blade stall.

Figures 2.18(a) and 2.18(b), shows the variation of power loading with disk loading for 2- and 4-bladed rotors, respectively, using NACA 0006 airfoil section.

96

(a) 2-bladed rotor. (b) 4-bladed rotor.
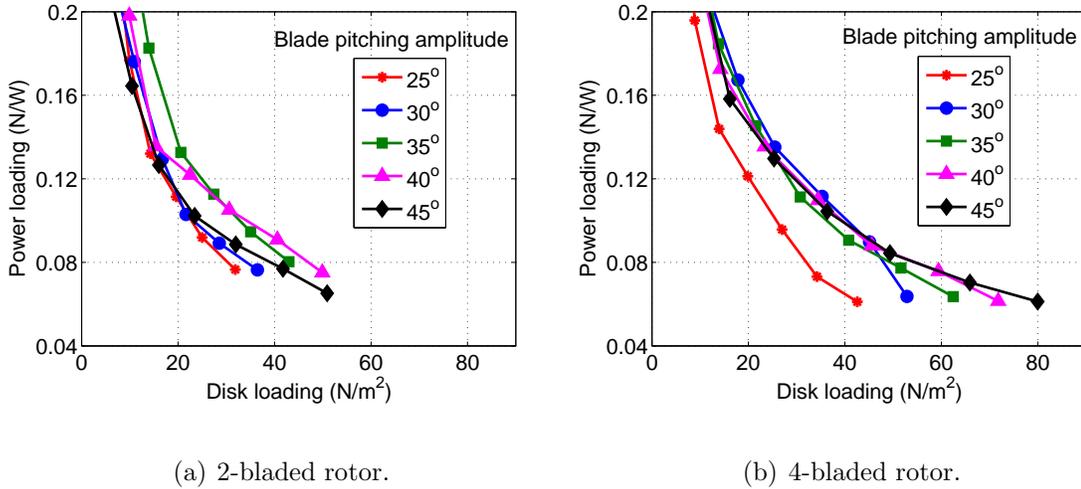
Figure 2.18: **Variation of power loading with disk loading at different blade pitching amplitudes for 2- and 4-bladed cyclorotors using NACA 0006 blades.**

From Fig. 2.18(a), it can be seen that for the 2-bladed rotor, the 40° pitching amplitude produced the maximum power loading followed by 35°, 45°, 30° and 25°. However, 45° pitching amplitude produced the maximum thrust. Unlike, the 2-bladed case, for the 4-bladed case (Fig. 2.18(b)), both the 40° and 45° pitching amplitudes had very similar power loadings, especially at higher disk loadings. Again, the 45° pitching amplitude produced the maximum thrust. 25° pitching amplitude produced the lowest power loading.

Figures 2.19(a) and 2.19(b), shows the variation of power loading with disk loading for 2- and 4-bladed rotors, respectively, using NACA 0010 airfoil section. Again, the conclusions were similar to the NACA 0006 case. For the 2-bladed rotor (Fig. 2.19(a)), the highest power loading was obtained for the 40° pitching amplitude, even though the differences in the power loading between the different

97

(a) 2-bladed rotor.   (b) 4-bladed rotor.
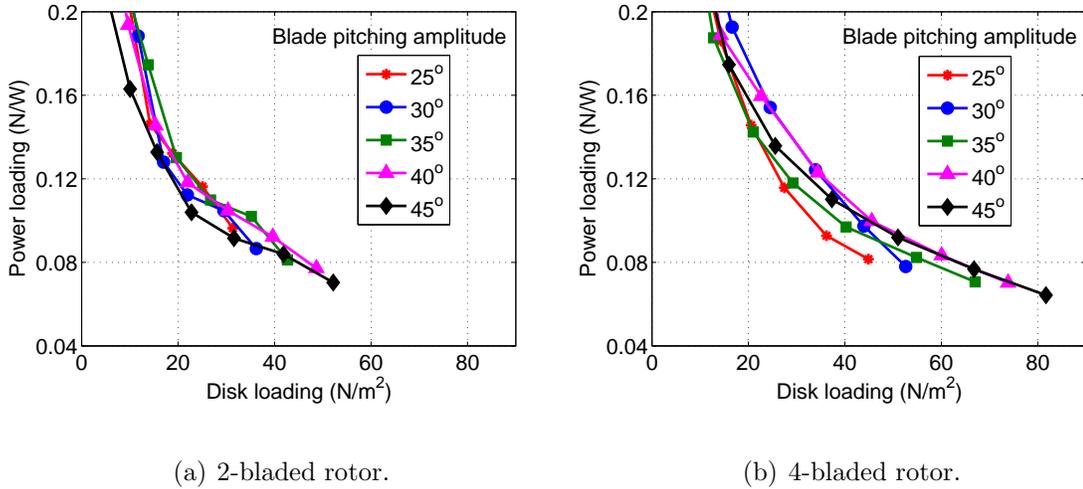
Figure 2.19: **Variation of power loading with disk loading at different blade pitching amplitudes for 2- and 4-bladed cyclorotors using NACA 0010 blades.**

pitching amplitudes were not as high as the NACA 0006 case. However, for the 4-bladed case (Fig. 2.19(b)), both 45° and 40° pitching amplitudes had similar power loadings at higher disk loadings ($> 40 N/m^2$) followed by 35°, 30° and 25°. Again, as before, in both these cases, 45° produced the maximum thrust.

Figures 2.20(a) and 2.20(b) shows power loading for the NACA 0015 blades, again for 2- and 4-bladed rotors, respectively. As in the previous cases, for the 2-bladed rotor (Fig. 2.20(a)), the power loadings were very close for the different pitching amplitudes, with 40° case producing the maximum power loading. However, for the 4-bladed case (Fig. 2.20(b)), there were significant differences in the power loadings for different pitching amplitudes. However, unlike the previous two 4-bladed cases, for the NACA 0015 blades, 40° pitching amplitude had higher power loading than 45°. The power loading for the 45° case was similar to 35° followed by
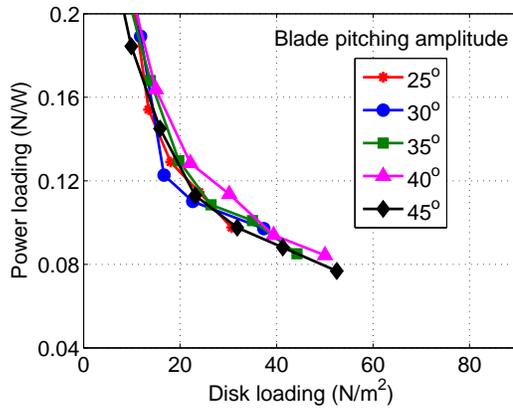
(a) 2-bladed rotor.
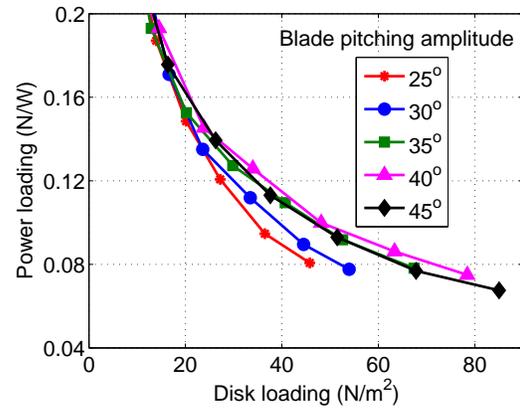
(b) 4-bladed rotor.

Figure 2.20: **Variation of power loading with disk loading at different blade pitching amplitudes for 2- and 4-bladed cyclorotors using NACA 0015 blades.**

30° and 25°.

A general observation from this part of the study was that the cyclorotor performed better when the blades were set to relatively higher pitching amplitudes. Because the power loading varies inversely with rotational speed, increasing thrust by increasing the blade section angle of attack seems more efficient than increasing the rotational speed. However, the maximum thrust that can be obtained using this approach would still be limited by the onset of blade stall, and hence will be airfoil dependent. Also, it should be noted that, at low Reynolds numbers, the profile drag coefficient is sensitive to the blade section angle of attack even before stall.
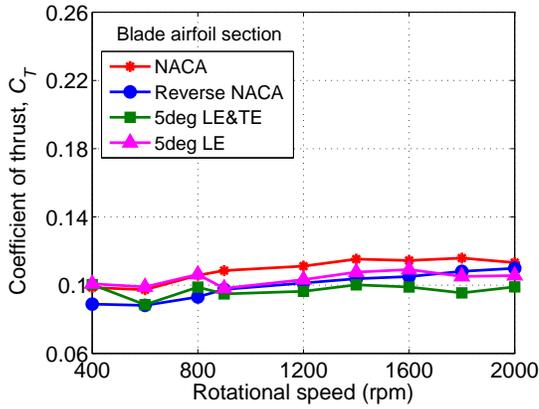
(a) Pitching amplitude=25°.
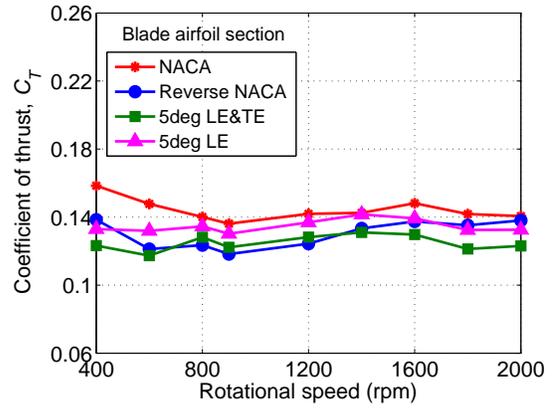
(b) Pitching amplitude=30°.
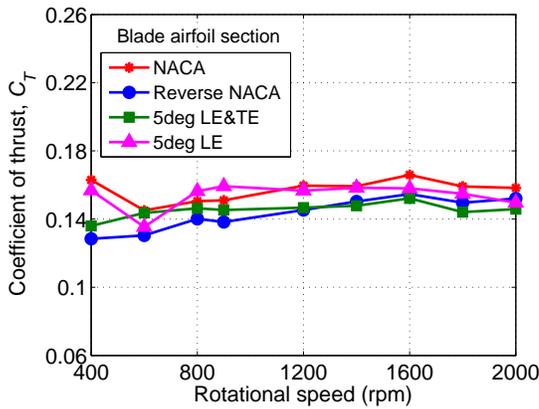
(c) Pitching amplitude=35°.
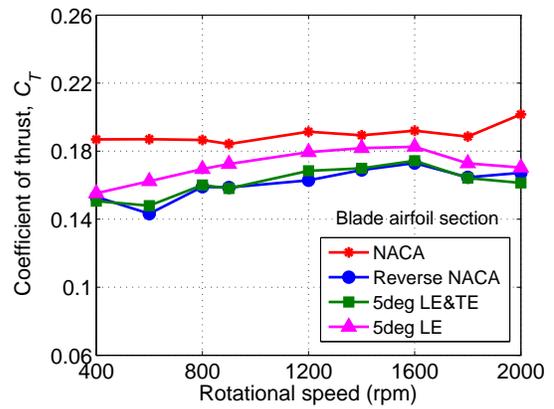
(d) Pitching amplitude=40°.

Figure 2.21: **Variation of thrust coefficient (C_T) with rotational speed for a 3-bladed cyclorotor using different blade sections at four blade pitching amplitudes.**

2.3.5 Effects of Blade Airfoil Section

Cyclorotors using blades with different airfoil sections were systematically tested at different pitching amplitudes to identify the best blade sections for MAV-scale cyclorotor applications. Previous studies on fixed-wings and rotary wings at low Reynolds numbers have shown that the thin flat plate airfoils perform better than conventional airfoils at low angles of attack and under steady conditions. However, this conclusion might not be true for a cyclorotor where the blades operate over a large angle of attack range (pitch angle range of ± 45°) under highly unsteady conditions. Therefore, the first set of tests were performed to compare a conventional NACA airfoil with different flat plate airfoils. The five blade profile shapes that were tested included the NACA 0010, a reverse NACA 0010, a 6% thickness-to-chord flat plate blade with symmetric 5° leading edge wedge angle (5deg LE), and a 6% thickness-to-chord flat plate blade with symmetric 5° leading edge and trailing edge wedge angles (5deg LE&TE). The different blade sections are shown in Fig. 2.4. These tests were performed on a 6 inch diameter, 3-bladed cyclorotor with a blade chord of 1 inch and span of 6 inches.

The results in Fig. 2.21(a) show the variation of C_T with rotational speed for the five blade sets when they were operated at 25° pitching amplitude. It can be seen that using the NACA 0010 airfoil produced maximum possible thrust from the cyclorotor at all rotational speeds. Reverse NACA and 5deg LE produced very similar thrusts, especially at higher rotational speeds. 5deg LE&TE blade produced slightly lower thrust than the rest of the blade sections at higher rpms.

Figure 2.21(b) shows the variation of thrust coefficient at 30° pitching amplitude. Again, the NACA 0010 blades produced more thrust than other blades at all rotational speeds. However, there was no significant differences between the other blade sections, even though, the reverse NACA and 5deg LE sections produced slightly higher thrust than 5deg LE&TE sections at higher rotational speeds. At 35° pitching amplitude (Fig. 2.21(c)), 5° leading edge wedge angle blades were very close to NACA in terms of thrust producing capability. Again, for the 40° pitching amplitude (Fig. 2.21(d)), the NACA blades performed better among blades in the terms of thrust followed by 5deg LE blades. Unlike, the other cases, for 35° and 40° pitching amplitudes, the reverse NACA and 5deg LE&TE blades had very similar performances.

Overall, for all the pitching amplitudes tested, even though the NACA section produced the maximum thrust, the other blade sections were very close to NACA. Therefore, from these results it can be concluded that at these low chord Reynolds numbers (less than 27,000 in this case) lift production does not actually show much sensitivity to airfoil section. In this regard, even the reverse NACA or flat plate airfoils tended to produce comparable values of thrust from the cyclorotor compared to using the baseline NACA 0010 blades.

The results shown in Fig. 2.22(a) compare the measured power loading values for the different blade sets at different disk loadings (or different thrust levels) for 25° blade pitching amplitude. Again, changing the rotational speed changed the thrust. It was interesting to see that at the highest possible disk loadings, the reverse NACA blades produced about a 25% higher power loading than when using
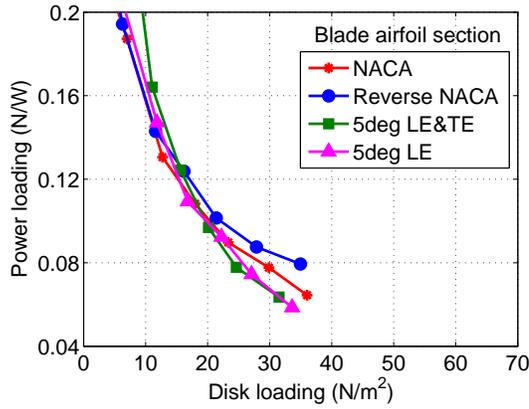
(a) Pitching amplitude=25°.
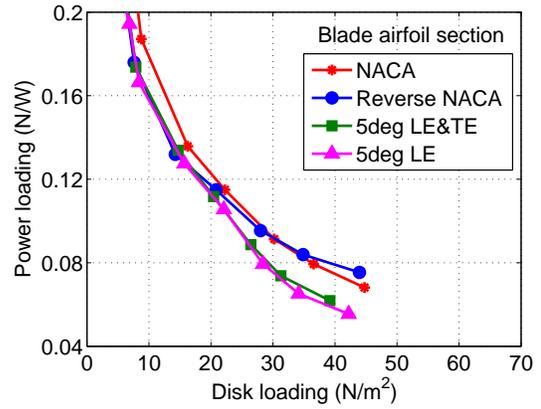
(b) Pitching amplitude=30°.
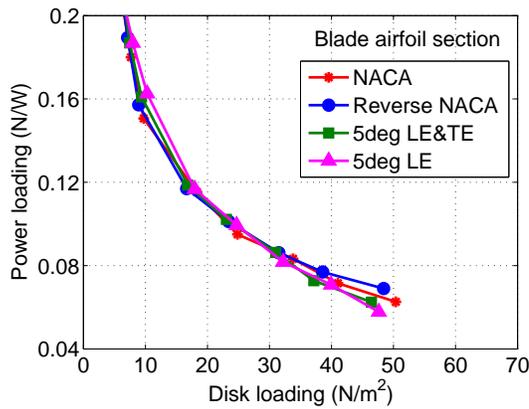
(c) Pitching amplitude=35°.
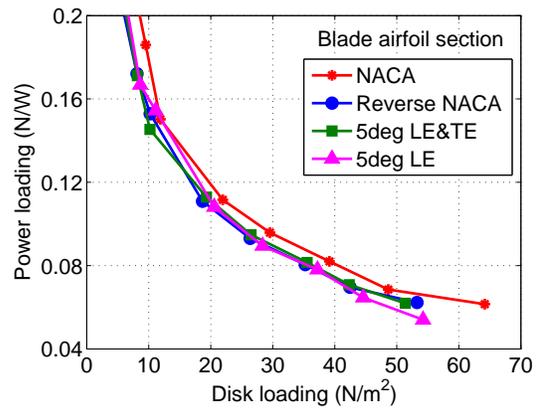
(d) Pitching amplitude=40°.

Figure 2.22: **Variation of power loading with disk loading for a 3-bladed cyclorotor using different blade sections at four blade pitching amplitudes.**

103

the baseline NACA blades. The reverse NACA blades were followed by regular NACA blades and the flat plate blades. The 5deg LE blade and the 5deg LE&TE blades had similar power loadings at all the disk loadings, even though 5deg LE&TE blades produced slightly lower thrust than the 5deg LE blades. This is because sharpening, the trailing edge decreased the power required for the 5deg LE&TE blades. Figure 2.22(b) shows the variation of power loading with disk loading for the 30° pitching amplitude. Again, in this case, the reverse NACA blades produced higher power loading than the regular NACA blades. The 5deg LE blade and the 5deg LE&TE blades had similar power loadings, which were significantly lower than the NACA blades.

Even at 35° pitching amplitude (Fig. 2.22(c)), the reverse NACA blades performed slightly better than the regular NACA blades at high disk loadings. Again, the 5deg LE blade and the 5deg LE&TE blades had very similar power loadings for all the disk loading values. At a pitching amplitude of 40° (Fig. 2.22(d)), the baseline NACA blades were found to perform better than when using the reverse NACA blades. In this case, the reverse NACA, the 5deg LE blade and the 5deg LE&TE blades had very similar power loadings.

From these results, it can be clearly seen that, even though the regular NACA blades produced the maximum thrust at all the pitching amplitudes, the reverse NACA blades had higher power loading than regular NACA blades at lower pitching amplitudes ($< 35°$). Although the 5deg LE blade was found to be better than the 5deg LE&TE blade in terms of thrust production, both blade sets produced almost the same power loading for all pitching amplitudes.
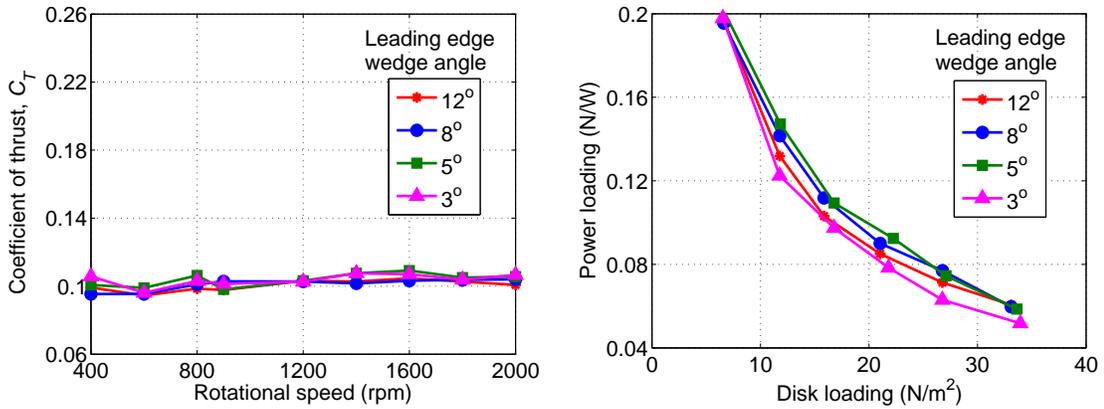
(a) Variation of thrust coefficient (C_T) with rpm.(b) Variation of power loading with disk loading.

Figure 2.23: **Performance of a cyclorotor using flat-plate blades with varying leading edge wedge angle at $25°$ pitching amplitude.**

All the flat plate airfoils tested had symmetrically sharpened leading edges. A study was performed to determine if the sharpening angle or the wedge angle at the leading edge (refer to Fig. 2.4 for the definition of wedge angle), affects the performance of a cyclorotor. Therefore, 6% thick flat plate airfoils with symmetric wedge angles of 12°, 8°, 5°, and 3° were tested at 25° pitching amplitude. Only symmetric sharpening of the blades can be used because the blades of the cyclorotor undergo periodic pitching motion and have to operate at both positive and negative angles of attack. All the blades had a chord of 1 inch and span of 6 inches. As far as the thrust is concerned, all the blades had very similar performance, as shown in Fig. 2.23(a). As shown in Fig. 2.23(b), all the blades produced very similar power loadings except for the 3° wedge angle case. The overall conclusion is that a moderate amount of leading edge sharpening (5°) produced a slightly better power loading.

Above studies proved that a conventional NACA airfoil is better than flat plate blades in terms thrust for all the pitching amplitudes and power loading for higher pitching amplitudes ($> 35°$). However, a parametric study needs to be performed to determine the optimum NACA section for the present cyclorotor. Even though low Reynolds number aerodynamic research on conventional aircraft concepts such as fixed wings and helicopters, have shown that thin airfoil sections perform better than thick sections, this has to be verified for the cyclorotor. Therfore, three different airfoil sections with different thickness to chord ratios, NACA 0006, NACA 0010 and NACA 0015, were tested on 2- and 4-bladed cyclorotors. Only symmetric airfoil sections were tested, because on a cyclorotor the blades have to operate at both positive and negative angles of attack. The blades used for these tests had a chord of 1.3 inches and span of 6.25 inches.

Figures 2.24(a)– 2.24(d) show the variation of thrust coefficient with rotational speed (rpm) for a 2-bladed rotor at 25°, 35°, 40° and 45° pitching amplitudes. From these figures, it can be seen that varying the airfoil section did not make any significant differences in the thrust producing capability of the cyclorotor. Figures 2.25(a)– 2.25(d) show the variation of power loading with disk loading for a 2-bladed rotor at four different pitching amplitudes. For the 25° pitching amplitude (Fig. 2.25(a)), both the NACA 0010 and 0015 sections had similar power loadings which was significantly higher than the NACA 0006 section at all the disk loadings. However, for the 35° pitching amplitude (Fig. 2.25(b)), all the three blade sections had very similar power loadings, even though the NACA 0015 section had slightly better performance at higher disk loadings and the NACA 0006 section produced
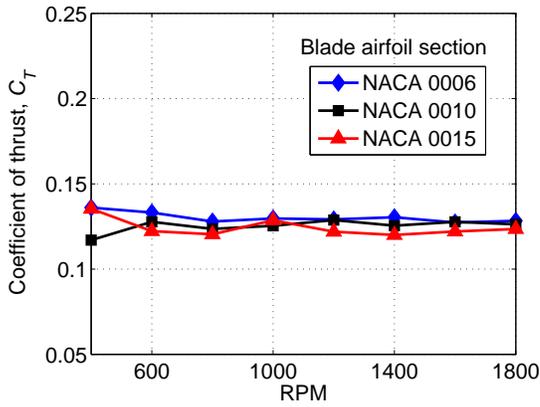
(a) Pitching amplitude=25°.
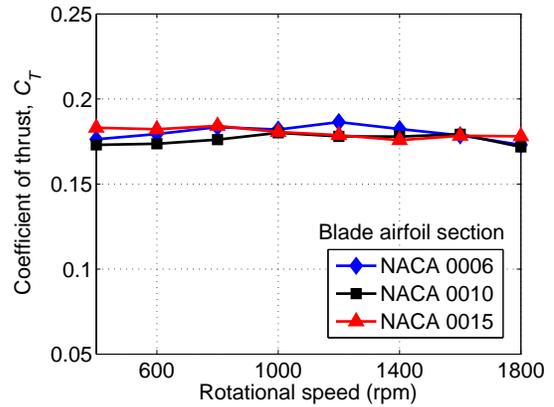
(b) Pitching amplitude=35°.
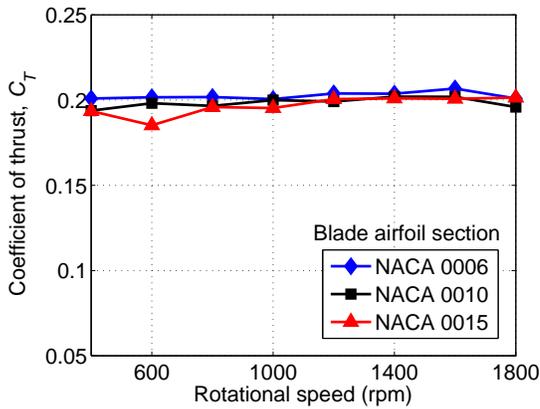
(c) Pitching amplitude=40°.
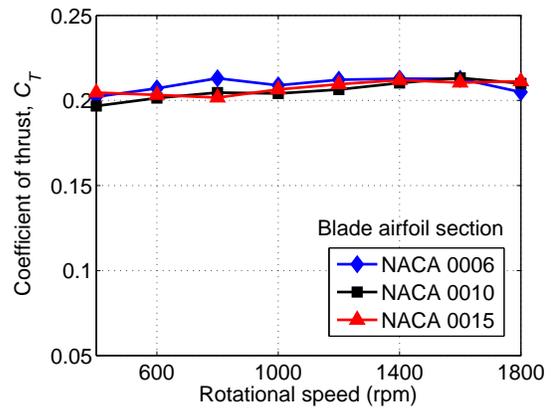
(d) Pitching amplitude=45°.

Figure 2.24: **Variation of thrust coefficient with rotational speed for a 2-bladed cyclorotor using different blade airfoil sections at four blade pitching amplitudes.**
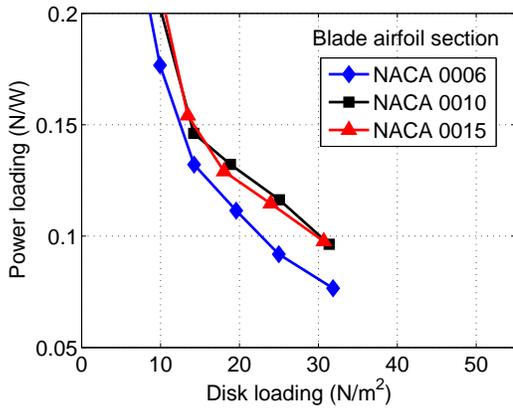
(a) Pitching amplitude=25°.
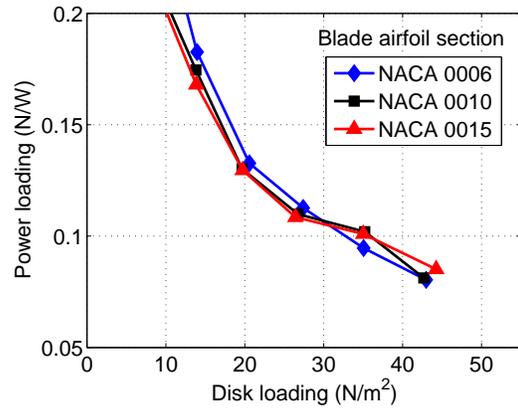
(b) Pitching amplitude=35°.
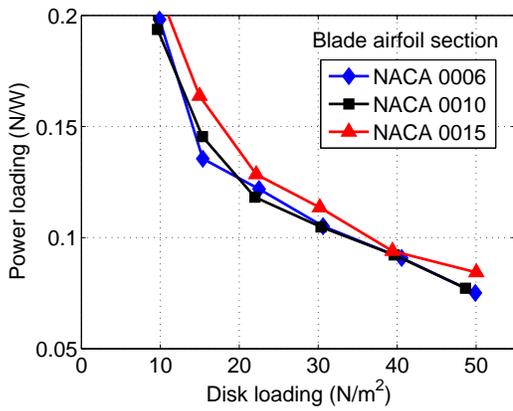
(c) Pitching amplitude=40°.
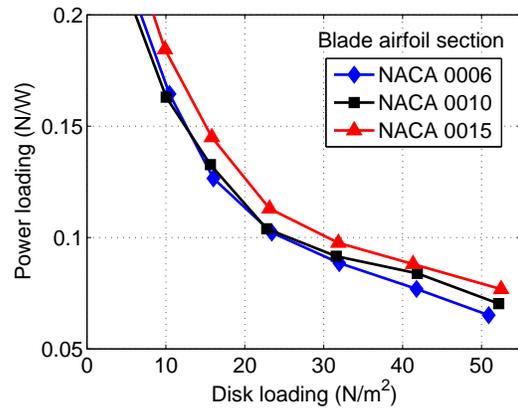
(d) Pitching amplitude=45°.

Figure 2.25: **Variation of power loading with disk loading for a 2-bladed cyclorotor using different blade airfoil sections at four blade pitching amplitudes.**

slightly higher power loading at lower disk loadings.

For the 40° pitching amplitude (Fig. 2.25(c)), the NACA 0015 section produced higher power loading compared to the other two sections at all the thrust levels. NACA 0010 and 0006 blade sections had very similar power loadings. 45° pitching amplitude (Fig. 2.25(d)) produced significant differences between all the three airfoil sections especially at higher disk loadings. The best power loading was obtained for the NACA 0015 sections followed by the NACA 0010 and 0006 sections.

Figures 2.26(a)– 2.26(d) compares the power loadings obtained using different airfoil sections on a 4-bladed cyclorotor at different pitching amplitudes. As shown in Fig. 2.26(a), for the 25° pitching amplitude case, similar to the 2-bladed case, both NACA 0015 and 0010 blades produce similar power loadings followed by NACA 0006 section which was significantly lower than the other two sections. However for the 35° case (Fig. 2.26(b)), NACA 0015 section produced the maximum power loading followed by the NACA 0010 section and then the NACA 0006 section. 40° pitching amplitude (Fig. 2.26(c)) showed the same trend as the 35° case with thicker airfoils performing better. However, for the 45° case (Fig. 2.26(d)), both NACA 0010 and 0015 sections produced very similar power loading followed by the NACA 0006 section which was slightly lower than the other two.

Even though at low Reynolds numbers, thin airfoils are expected to perform better, all the above results clearly show that NACA 0015 section consistently performed better than the thinner airfoils. Blades with NACA 0006 airfoil had significantly lower power loading than the other two blade sets. In order to understand this better, a 2-D CFD analysis was performed on the three different airfoil sections
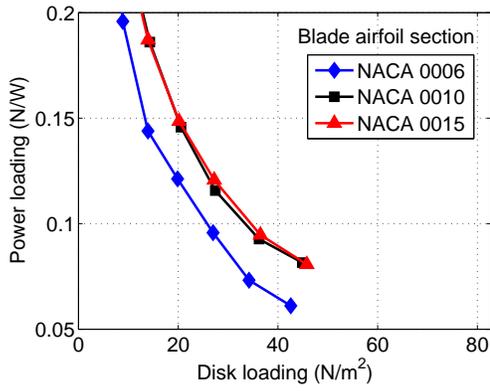
109

(a) Pitching amplitude=25°.
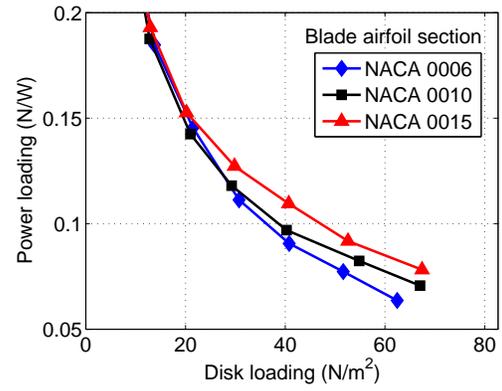
(b) Pitching amplitude=35°.
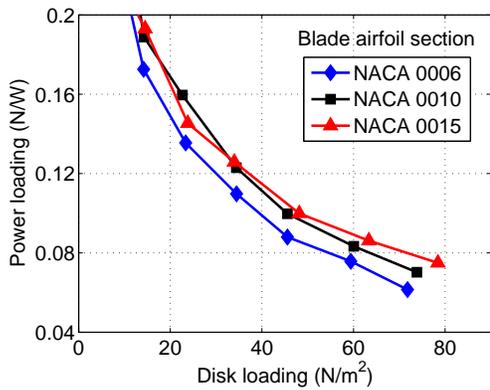
(c) Pitching amplitude=40°.
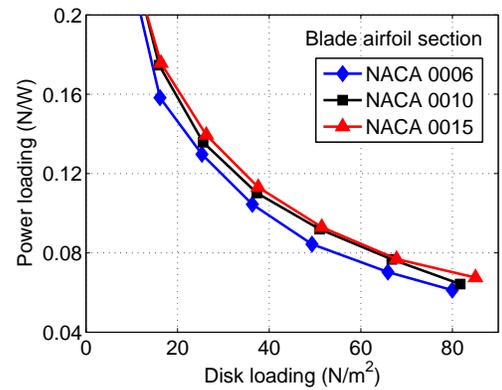
(d) Pitching amplitude=45°.

Figure 2.26: **Variation of power loading with disk loading for a 4-bladed cyclorotor using different blade airfoil sections at four blade pitching amplitudes.**

(a) Lift coefficient.
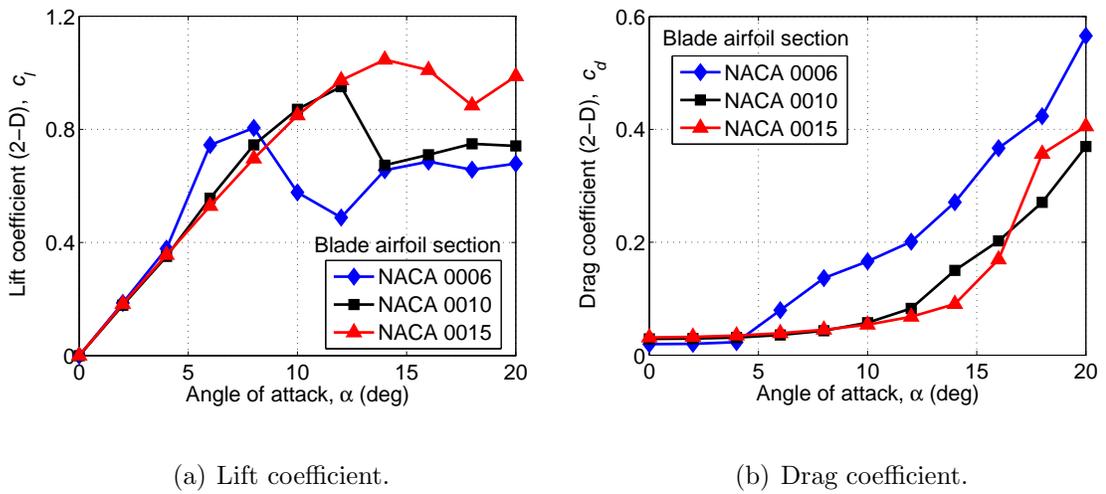
(b) Drag coefficient.

Figure 2.27: **Variation of 2-D lift and drag coefficient with angle of attack for the NACA 0015, 0010 and 0006 sections at Re = 25,000.**
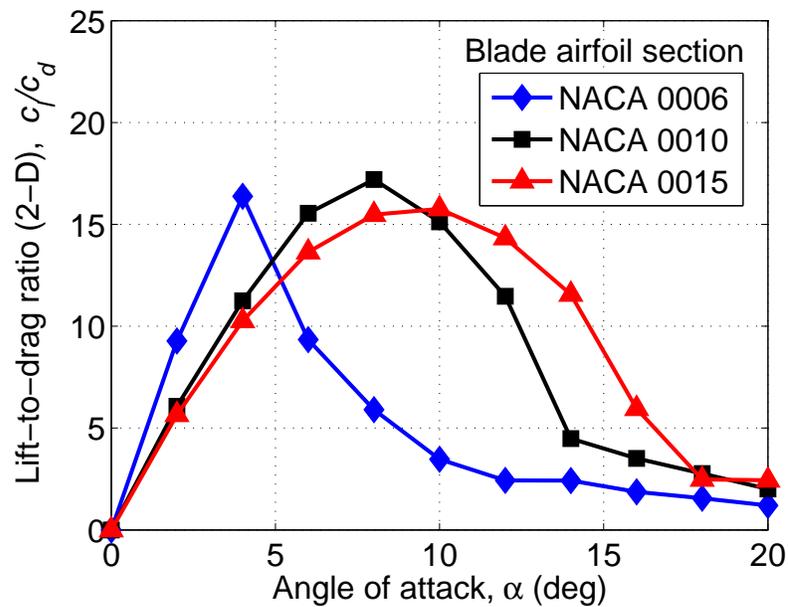
Figure 2.28: **Variation of 2-D lift-to-drag ratio with angle of attack for the NACA 0015, 0010 and 0006 sections at Re = 25,000.**

at a Reynolds number of 25,000. Figure 2.27 shows the variation of two-dimensional static lift and drag coefficient of the three different airfoil sections, with angle of attack. Figure 2.27(a) clearly shows that the static stall angle of attack and the maximum lift coefficient increases as the thickness of the airfoil is increased. As shown in Fig. 2.27(b), the drag coefficient for the NACA 006 section is lower than the NACA 0010 and 0015 sections before stall. However, the NACA 0006 section stalls before the other two sections and the post stall drag coefficient of the NACA 0006 section is much higher than the other two sections. Because of this reason, as shown in Fig. 2.28, even though the NACA 0006 section has a higher lift to drag ratio before stall, it drops much below the other two sections in the post stall regime. The same would be true for thin flat plate airfoils. However, as the airfoil thickness is increased, the higher lift-to-drag ratio is maintained over a wider range of angle of attack, despite the fact that the maximum acheivebale L/D decreases.

Therefore, for fixed wing or even rotary wing MAVs, thin airfoils may work better because the blades operate at lower angles of attack below static stall value. However, for cyclorotor applications, where the blade angle of attack varies over a large range, it is beneficial to have a more forgiving airfoil (thicker airfoils), which can maintain the high lift to drag ratio over a wider range of angle of attack.

2.3.6   Effect of Blade Flexibility

On a cyclorotor, the centrifugal forces act in the transverse direction and tend to bend and twist the blades. This is unlike a conventional rotor where the centrifugal

Table 2.1: Blade stiffness.

Properties	NACA blades	6% Flat plate	3% Flat plate	2% Flat plate
$EI(N-m^2)$	0.190	0.400	0.026	0.008
$GJ(N-m^2)$	0.252	0.122	0.010	0.004

forces act mainly parallel to the blade span. In most of the present tests, the centrifugal force resulting from blade inertia was about 20 times the aerodynamic force on the blades. For the present cyclorotor design, the blades have a pin-pin support at the ends and significant bending deformation was observed when using the thinner blades at the higher rotational speeds. As far as the torsion displacement is concerned, the blades have a fixed boundary condition at the root (from the rigid pitch link) and a free boundary condition at the tip. The pitching axis of the blade is along the 1/4-chord. Unlike NACA blades, for most of the flat plate blades, the center of gravity (c.g.) is approximately along the mid-chord, therefore, the centrifugal loading causes significant torsional deformations.

Systematic tests were performed to investigate the effects of blade bending and torsional flexibility on cyclorotor performance. The blades tested includes 1%, 2%, 3%, and 6% thickness-to-chord ratio flat plate blades with the sharpened leading edges. The overall bending and torsional stiffness (EI and GJ) of the blades, which were obtained using structural testing, are given in Table. 2.1.

Figure 2.29(a) shows the variation of thrust coefficient, C_T, with rotational speed for the four different blade sets at a 40° pitching amplitude. From a purely
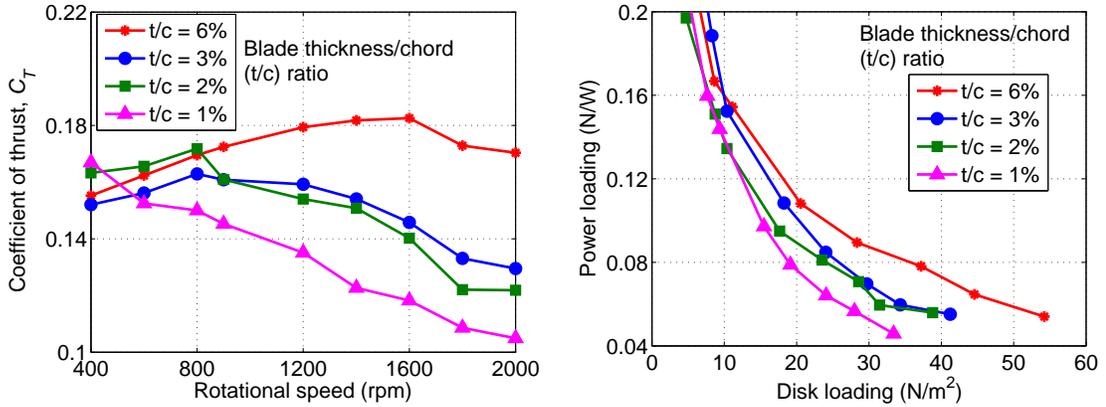
(a) Variation of thrust coefficient (C_T) with rpm.(b) Variation of power loading with disk loading.

Figure 2.29: **Performance of a cyclorotor using flat-plate blades with varying thickness-to-chord ratio at 25° pitching amplitude.**

aerodynamic perspective, little variation in thrust would be expected for these four blade sets. However, the results showed otherwise, which is because of aeroelastic effects resulting from the bending and torsional flexibility of the blades. Such a conclusion could be clearly drawn from the trends in the Figure 2.29(a), because at lower rotational speeds (< 800 rpm) all the blades produced very similar thrust values, however, the difference in the thrust levels between the different blades grew with rotational speed. This is because of the fact that the centrifugal forces and hence the deformations increase with rotational speed. Also, more flexible the blade is, lower the rpm at which the drop in C_T starts to occur. The 6% thick flat plate produced a maximum of 40% more thrust compared to the 1% thick blade, and a clear trend could be seen in the measurements. At a particular rotational speed, the lower the stiffness of the blade the lower the thrust that was produced.

The same trend held true for the power loading, as shown in Fig. 2.29(b). For
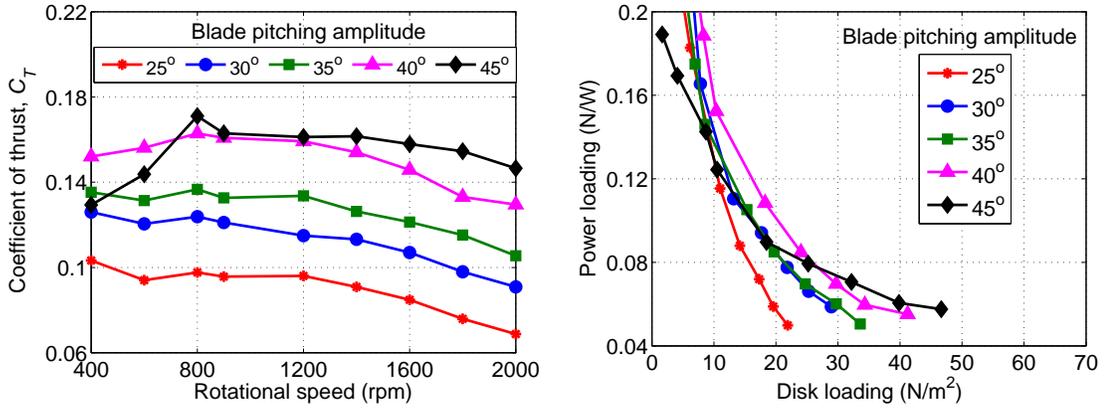
(a) Variation of thrust coefficient (C_T) with rpm.(b) Variation of power loading with disk loading.

Figure 2.30: **Performance of a 3-bladed cyclorotor using 3% thickness-to-chord ratio flexible flat plate blade section at four blade pitching amplitudes.**

the same value of disk loading (or thrust), the power loading decreased as the blades were made flexible. At the maximum value of thrust produced when using the 1% thick blade, the power loading for the 6% thick blade was almost 80% better than for the 1% thick blade. The nonlinear aeroelastic analysis that was performed on these rotors (Chapter 4) clearly showed that the reason for the drop in thrust with blade flexibility was due to the large nose-down torsional deformation produced by the centrifugal force in the upper half of the blade trajectory which is not compensated by a nose-up deformation in the lower half. This happens because the blade section c.g. is located behind the pitching axis and also becasue of the non-linear effects produced due to the large twist angles. This will be discussed in detail in Chapter 4.

The blade pitch angle affects the blade bending stiffness in the radial and

115

tangential directions and also the torsional deformations. Therefore, a flexible 3% thickness-to-chord ratio blade was tested at different blade pitching amplitudes. Figure 2.30(a) shows the variation of thrust coefficient with rotational speed at different blade pitching amplitudes. It can be seen that higher the blade pitching amplitude, lower the drop in C_T at higher rotational speeds. Figure 2.30(b) shows the variation of power loading with disk loading for the same case. Overall, 40° pitching amplitude had the best power loading. Pitching amplitudes of 45°, 35° and 30° produced very similar power loadings for the lower thrust values. However, using a pitch angle of 45° appeared to be better than the rest of the cases only for the higher thrust cases. The improved performance of the flexible blades at higher pitching amplitudes is primarily a consequence of the decrease in the blade torsional deformation with the increase in blade pitch angle, because the torsional moment produced by the centrifugal force decreases with blade pitch angle. Other reason for this could be the increase in the bending stiffness of the blade in the radial direction (i.e., in the direction of the centrifugal force) with increasing pitch angle; the contribution of lagwise bending stiffness to the blade bending stiffness in the radial direction increases with the pitch angle of the blade. The lagwise bending stiffness of all the blades tested were much higher than the flapwise stiffness.

The conclusion from these tests is that aeroelastic effects resulting from any significant blade flexibility (in either bending or torsion) deteriorates the performance of a cyclorotor. Some of the possible solutions for minimizing the blade torsional deformation without significantly increasing blade mass (and so increasing the empy weight fraction of the MAV) could be obtained by shifting the blade pitch

116

axis closer to the blade c.g. axis or by using appropriately pretwisted blades. This is beyond the scope of the present work.

2.3.7 Effect of Number of Blades (Constant Blade Chord)

From a cyclorotor design perspective, it is crucial to understand the effect of number of blades on the performance of the rotor and to determine the optimum number of blades required to produce a certain value of thrust. The first set of tests were performed using 2-, 3-, 4-, and 5-bladed rotors with the same blade chord so that the solidity of the rotors vary proportional to the number of blades used. The different rotors used are shown in Figures 2.31. The blades had a span of 6 inches and chord of 1 inch.

Figure 2.32 shows the variation of non-dimensional resultant thrust per blade (C_T/σ) with rotational speed for 2-, 3-, 4- and 5-bladed cyclorotors at four different pitching amplitudes. In Fig. 2.32(a), the experimentally measured thrust values for the 35° pitching amplitude are compared with predictions that were obtained using an aerodynamic model based on blade element momentum theory and a uniform inflow model based on the rectangular projected area (A). The aerodynamic model is discussed in detail Chapter 4. In all the cases, the thrust predictions were found to be within 10–15% of the measured values. From Fig. 2.32, it can be seen that, for all the pitching amplitudes, the 2-bladed rotor has the maximum thrust per blade, followed by the 3-, 4- and 5-bladed rotors. This is because the total thrust increases with the number of blades, which increases the inflow and thereby reduces

(a) 2-bladed cyclorotor.

(b) 3-bladed cyclorotor.
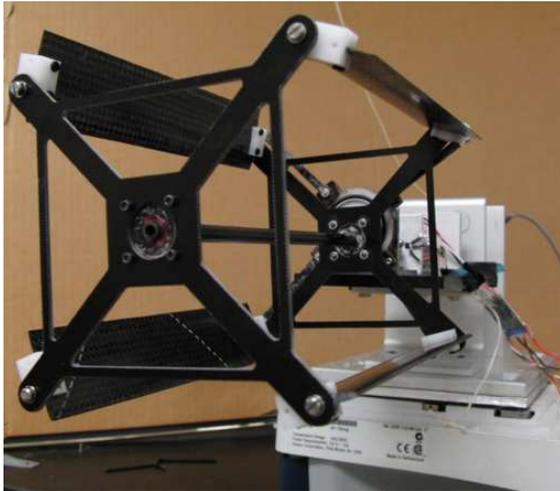
(c) 4-bladed cyclorotor.
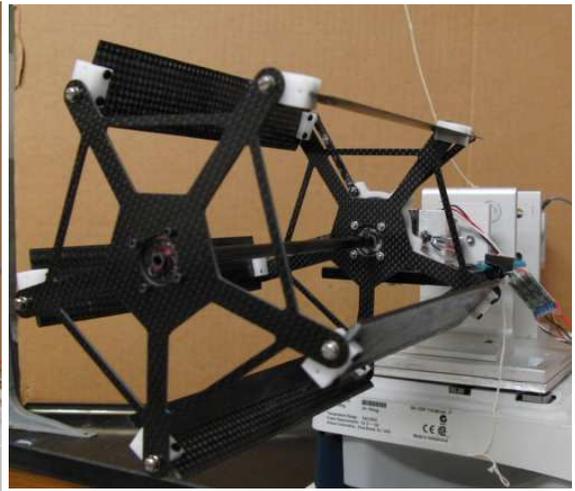
(d) 5-bladed cyclorotor.

Figure 2.31: **Different cyclorotors tested.**
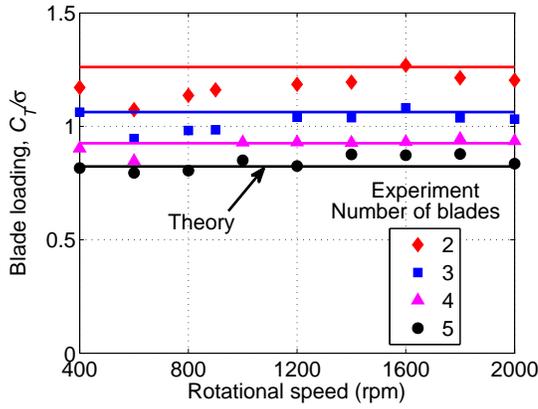
(a) Pitching amplitude=35°.
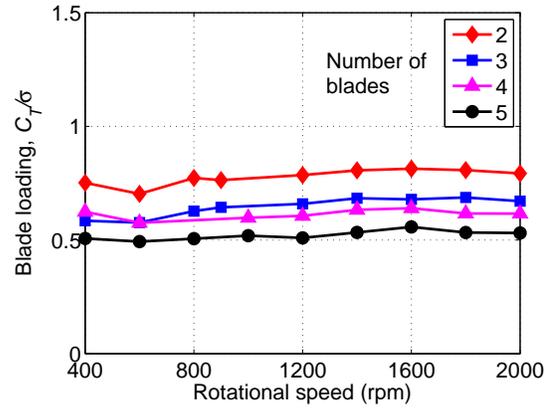
(b) Pitching amplitude=25°.
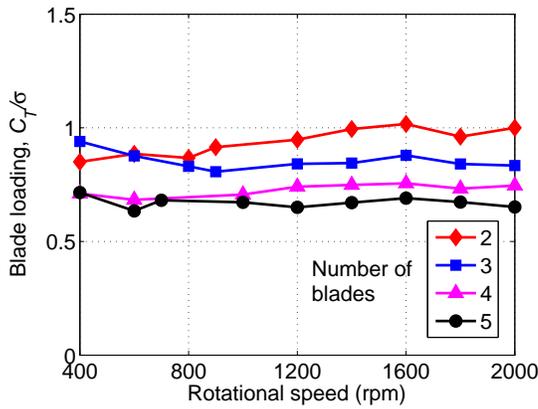
(c) Pitching amplitude=30°.
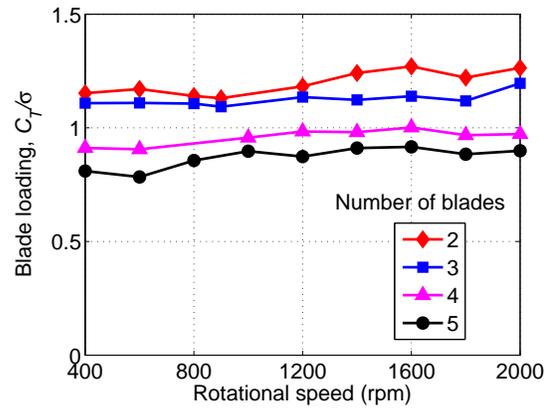
(d) Pitching amplitude=40°.

Figure 2.32: **Variation of non-dimensional resultant thrust (C_T/σ) with rotational speed (rpm) for 2-, 3-, 4- and 5-bladed cyclorotors at four different blade pitching amplitudes.**
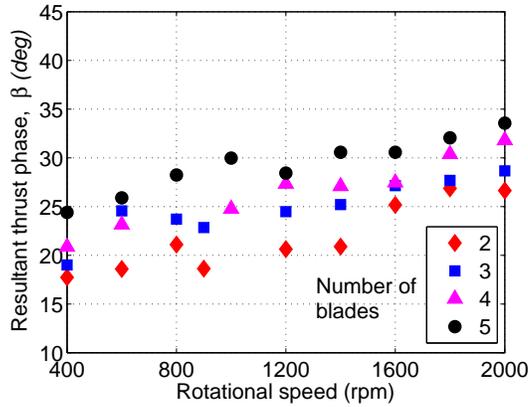
(a) Pitching amplitude=35°.
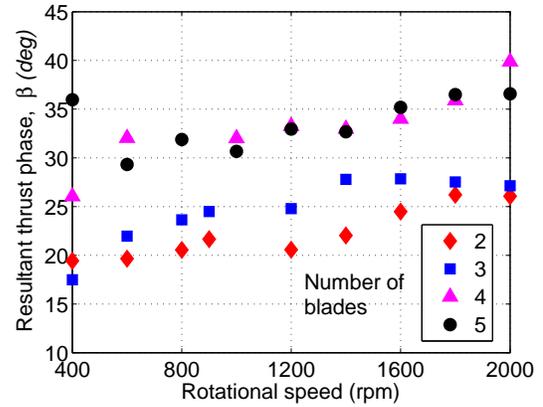
(b) Pitching amplitude=40°.

Figure 2.33: **Variation of the phasing of the resultant thrust vector (β) with rotational speed for 2-, 3-, 4-, and 5-bladed rotors at two different pitching amplitudes.**

the effective angle of attack of each of the blades. The aerodynamic model also captures this effect (Fig. 2.32(a)). The performance of the cyclorotors can also be affected by the interference between the blades, which is an effect that increases with the number of blades. However, these interference effects are not presently included in the modeling.

Another interesting observation was made on the effect of number blades on the phasing or the direction of the resultant thrust vector with the vertical (β shown in Fig. 2.5). Figure 2.33 shows the variation of β with rotational speed for 2-, 3-, 4-, and 5-bladed cyclorotors at 35° and 40° pitching amplitudes. The figures show that as the solidity (number of blades) of the rotor was increased, the tilt of the thrust vector increased because of the increased contribution from the lateral force.

Figures 2.34(a)– 2.34(d) show the variation of power loading with disk loading
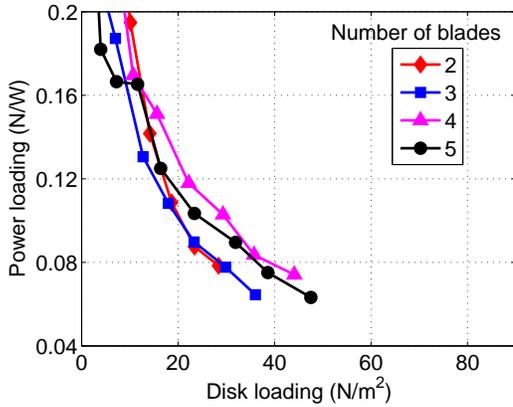
(a) Pitching amplitude=25°.
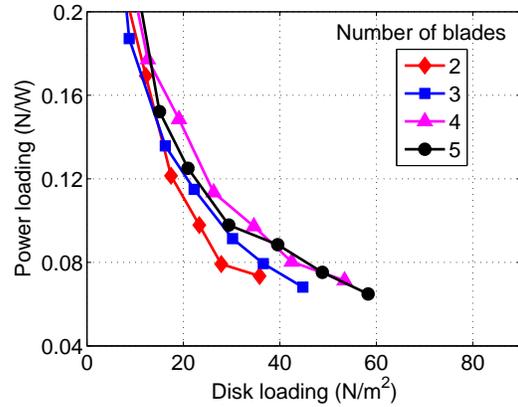
(b) Pitching amplitude=30°.
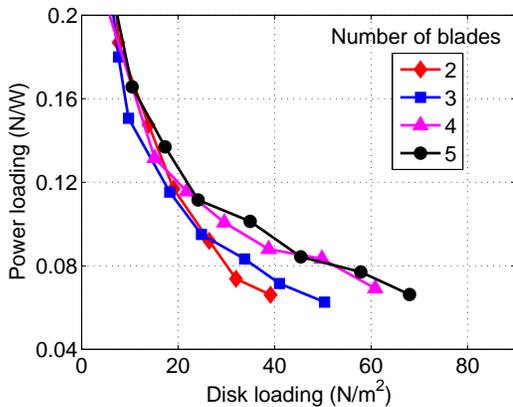
(c) Pitching amplitude=35°.
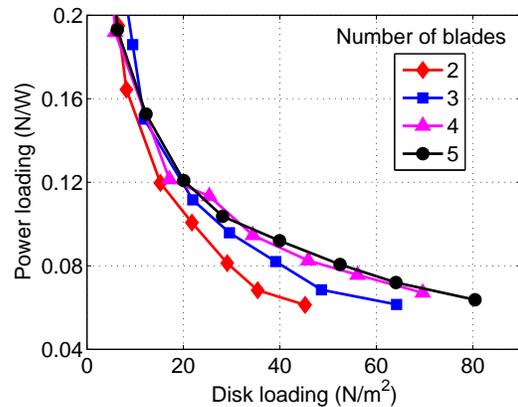
(d) Pitching amplitude=40°.

Figure 2.34: **Variation of power loading with disk loading for 2-, 3-, 4- and 5-bladed cyclorotors at four different blade pitching amplitudes.**

for different cyclorotors (2-, 3-, 4- and 5-bladed) at different blade pitching amplitudes. From the results in Fig. 2.34(a), it can be seen that at 25° blade pitching amplitude the 4-bladed cyclorotor has the best power loading for all values of disk loading, followed by the 5-, 3- and 2-bladed rotors. The power loadings of the 2- and 3- bladed cyclorotors were found to be comparable, however, they were still significantly lower than that found for the 4- and 5-bladed rotors.

For the 30° pitching amplitude case (Fig. 2.34(b)), the power loadings produced by 4- and 5- bladed cyclorotors were comparable at higher disk loading values. However, at lower disk loading values the 4-bladed rotor produced better power loading than 5-bladed rotor. At all the disk loadings, the 3-bladed cyclorotor was inferior to both the 4- and 5-bladed rotors. The 2-bladed rotor produced the lowest power loading.

For the 35° pitching amplitude (Fig. 2.34(c)), the 5-bladed cyclorotor performed better than all of the other rotors, followed by the 4-bladed, 3-bladed and 2-bladed rotors. However, it was interesting to note that for disk loading values less than 25 N/m^2, the 2-bladed rotor actually performed better than the 3-bladed rotor. For the 40° pitching amplitude case (Fig. 2.34(d)), the results showed the superior performance of the 5-bladed rotor over the 4-, 3- and 2-bladed rotors. It was interesting to see that the performance of the 5-bladed rotor improved relative to the other rotors with increasing pitching amplitude.

Figures 2.34(a) through 2.34(d) show that the rotor with higher number of blades (higher solidity) produced the better power loading for the same value of disk loading (or thrust) despite the fact that profile power increases with solidity. This is because of the fact that a rotor with higher solidity can achieve a given value of thrust at a lower rotational speed compared to a rotor with a lower solidity. To understand this further, consider two rotors with N_1 and N_2 number of blades, respectively, producing the same thrust, T. The two rotors are operating at rotational speeds of Ω_1 and Ω_2, respectively. If the two rotors are identical in all other aspects, we can

122

assume that,

$$T \propto N_1 \Omega_1^2$$

$$T \propto N_2 \Omega_2^2 \tag{2.3}$$

Therefore the ratio of the rotational speeds for the same thrust can be given as,

$$\frac{\Omega_1}{\Omega_2} = \left(\frac{N_2}{N_1}\right)^{\frac{1}{2}} \tag{2.4}$$

Since, both the rotors are producing the same thrust and have the same disk area, the induced power (P_i) can be assumed to be the same. However, the profile powers will be different and will be given as,

$$P_{0_1} \propto N_1 \Omega_1^3$$

$$P_{0_2} \propto N_2 \Omega_2^3 \tag{2.5}$$

The ratio of the profile powers is given as,

$$\frac{P_{0_1}}{P_{0_2}} = \left(\frac{N_1}{N_2}\right)\left(\frac{\Omega_1}{\Omega_2}\right)^3 \tag{2.6}$$

Substituting for Ω_1/Ω_2 in Eqn. 2.6 from Eqn. 2.4

$$\frac{P_{0_1}}{P_{0_2}} = \left(\frac{N_2}{N_1}\right)^{\frac{1}{2}} \tag{2.7}$$

This clearly shows that if all the other parameters remain the same, then

$$P_0 \propto N_b^{-\frac{1}{2}} \tag{2.8}$$

Now since the induced power remains constant, for a constant thrust, the variation of total power, P, with number of blades (N_b) follows the trend given below.

$$P \propto N_b^{-\frac{1}{2}} + constant \tag{2.9}$$

123
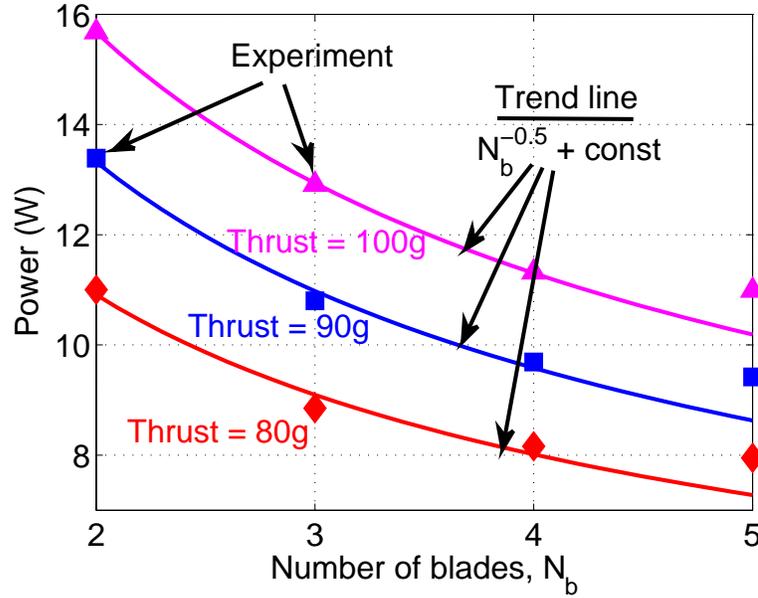
Figure 2.35: **Variation of power with number of blades for constant thrust levels.**

This clearly shows that, ideally for a cyclorotor, the power required for producing a constant thrust decreases with the number of blades. However, it is important to relate this trend to the observation from the experimental results. Therefore, the thrust and the power values measured from the experiment was interpolated to obtain the variation of power with number of blades for constant thrust levels. The results are shown in Fig. 2.35, where the trends obtained in Eqn. 2.9 is superposed on the experimentally measured power values for constant thrust levels of 80, 90, and 100 grams. It can be clearly seen that the 2-, 3-, and 4-bladed rotors followed the trend. However, for all the thrust levels, the drop in power from 4- to 5-bladed rotor, was significantly smaller than the value predicted by the trend line. This may be because of the fact that the above theory ignored the blade interference

effects which may tend to increase the power required as the number of blades are increased.

Therefore, the present study has clearly shown that there is a power benefit from increasing number of blades (solidity). As explained before, this is because that a larger solidity rotor produces the same thrust at a lower rotational speed and the decrease in the profile power because of the lower operating speed outweighs the increase in profile power due to the larger blade area. However, the foregoing results do not prove that indefinitely increasing the number of blades is a more desirable design; it only shows that power loading improves with solidity until around 0.21 is reached (4-bladed rotor), beyond which there was only a marginal improvement. The trends observed in the above results are a combined effect of both number of blades and solidity. To isolate the effect of number of blades, rotors with different number of blades would have to be tested at the same solidity by varying the chord length of the blades used on each rotor. This is discussed in the subsequent sections of the chapter.

2.3.8   Virtual Camber Effect

The virtual camber effect is introduced in order to explain some of the results in the later sections of the chapter. Virtual camber effect is an aerodynamic phenomenon commonly found in vertical axis wind turbine blades where the blades undergo an orbital motion and therefore experience a curvilinear flow. Blades subjected to a curvilinear flow behave very differently compared to being immersed in a rectilinear
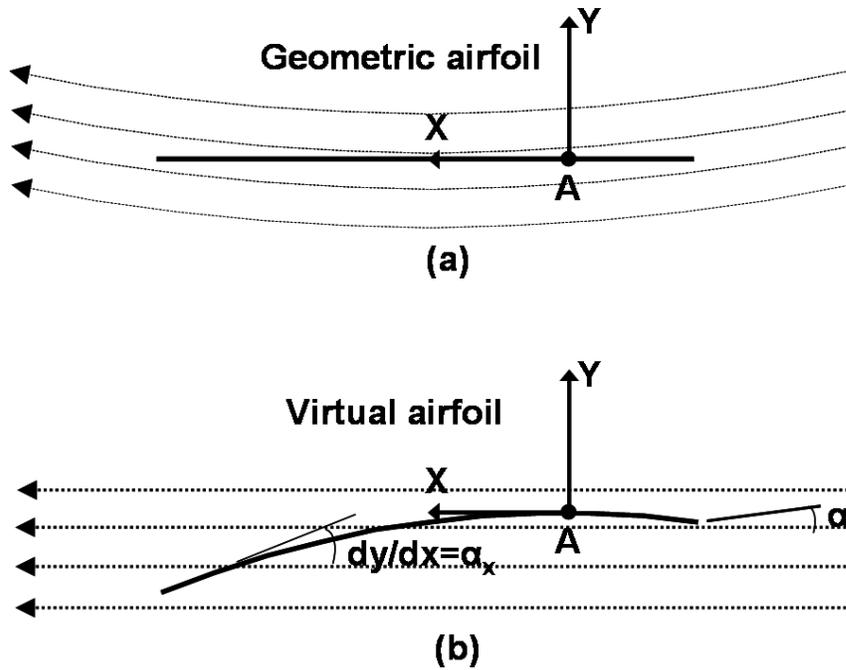
Figure 2.36: **Virtual camber in a curvilinear flow.**

flow (Fig. 2.36). In a curvilinear flow, the local velocity and angle of attack of the blade are unique at different locations on the chord. Because of this, a symmetric blade at 0° pitch angle in a curvilinear flow (Fig. 2.36(a)) can be viewed to behave like a cambered blade at an angle of incidence (α_i) in a rectilinear flow (Fig. 2.36(b)). This effect will be more pronounced with cyclorotors having large chord-to-radius ratio (c/R).

The virtual camber effect is clearly explained using Fig. 2.37 which shows a symmetric airfoil at a pitch angle of 0° at the bottom most point of the blade trajectory. Point A is the pitching axis of the blade. For the sake of explanation, resultant velocity at any location on the blade chord is assumed a function of the rotational speed (the induced velocity and the pitch rate effects are ignored). Thus, as shown in Fig. 2.37, the magnitude and direction of the resultant velocity varies
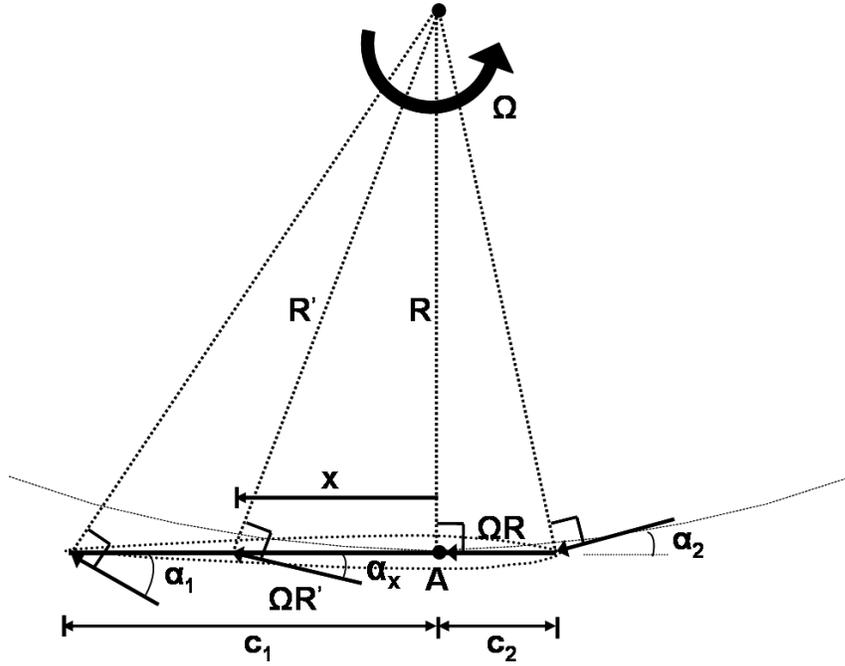
Figure 2.37: **Schematic explaining virtual camber.**

along the chord. The angle of incidence of the flow at any arbitrary location on the

chord, x, is given by $\alpha_x = tan^{-1}(x/R)$ ($\alpha_x \approx x/R$) and the velocity magnitude is

given by $\Omega R'$ where $R' = \sqrt{R^2 + x^2}$.

Now this scenario is approximately equivalent to having a cambered airfoil,

with the camber line slope (dy/dx) equal to α_x in a rectilinear flow of magnitude

ΩR as shown in Fig. 2.36(b). Figure 2.38 shows the variation of virtual camber

at different azimuthal locations for a flat plate blade pivoted at quarter chord but

with no pitching. Because of the large chord/radius ratio (c/R=0.43) of the current

rotor, there is significant virtual camber that is positive for the entire lower half

and negative for the upper half. Virtual camber should play a significant role in the

aerodynamic performance of the rotor.

The exact method of taking account of the virtual camber effect is by using

127
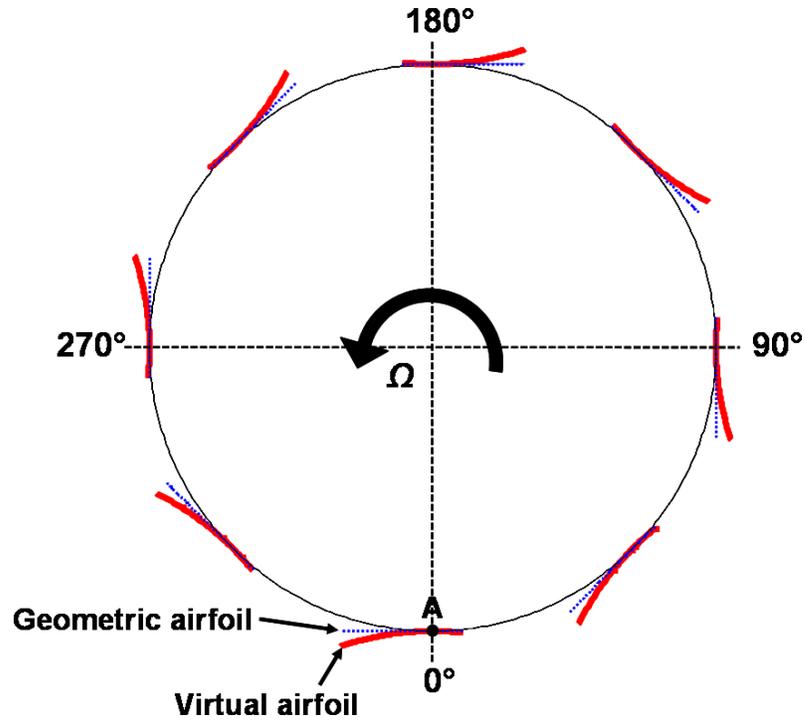
Figure 2.38: **Virtual camber at different azimuthal location for a blade pivoted at 1/4 chord and no pitching.**

a conformal mapping technique which transforms airfoils in the curved flow field to their virtual equivalents in rectilinear flow. This procedure is discussed in detail in [72] and is used to obtain the modified aerodynamic coefficients for the blade. Figure 2.39, obtained from Ref. [72], shows the variation of virtual camber and virtual incidence with chord-to-radius ratio for a NACA 0015 airfoil pivoted at the quarter chord. It can be seen that for the present rotor (c/R=0.43), the virtual camber is about 5.3% of chord and the virtual incidence is about 6.1°, which are quite significant.

For a moderate flow curvature and for attached flow, the influence of virtual camber on the aerodynamic coefficients can be accommodated by a shift in angle
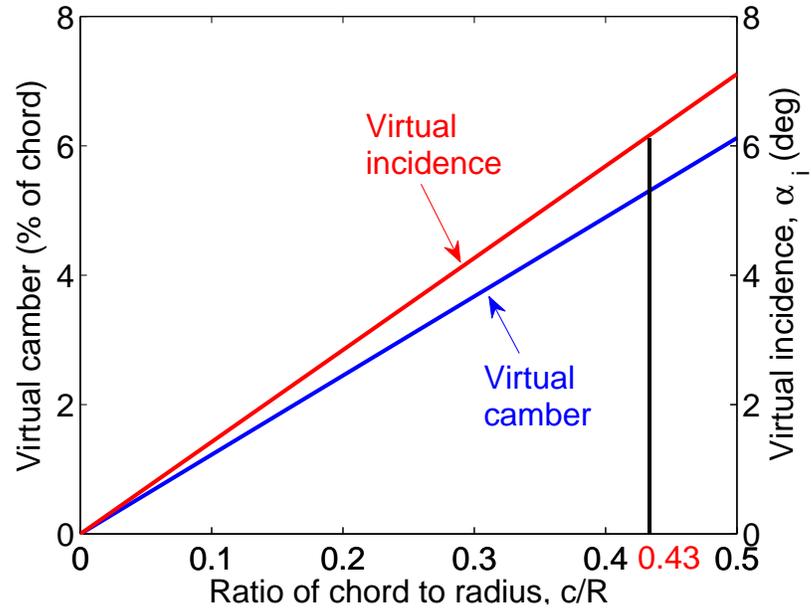
Figure 2.39: **Variation of virtual camber and incidence with chord-to-radius ratio [72].**
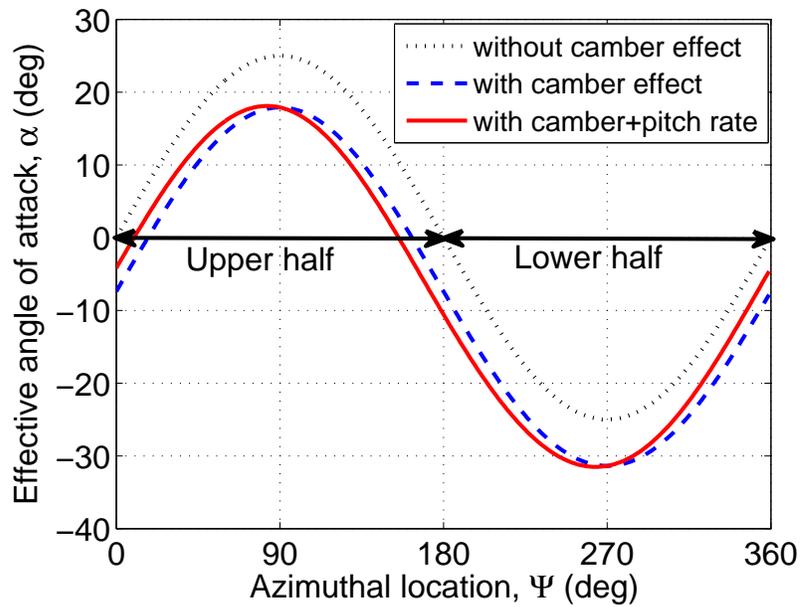
Figure 2.40: **Effect of virtual camber and pitch rate on angle of attack at 3/4-chord for a blade pitching amplitude of 25°.**

of attack [73]. Using thin airfoil theory, the strength of the circulation of a camber line with constant curvature is such that the flow at the 3/4 chord location is in the direction of the camber line. Hence, the angle of attack in the curved flow is evaluated with the flow curvature at the 3/4 chord location [74]. In the subsequent sections, the influence of virtual camber is taken into account by calculating the angle of attack at the 3/4 chord location. Figure 2.40 shows the effect of virtual camber and pitch rate on the effective angle of attack variation (without the effect of inflow) of a cyclorotor blade for a pitching amplitude of 25°. With the addition of virtual camber there is a significant shift in the angle of attack at the 3/4 chord, which can be viewed as a decrease in the effective angle of attack at the upper half and increase in the angle of attack at the lower half of the circular blade trajectory. Therefore, an asymmetric blade pitching that can acheive higher pitch angle at the top and lower pitch angle at the bottom can make the effective angle of attack variation more symmetric (in the upper and lower halves) and hence may improve the aerodynamic performance of the cyclorotor. Also, changing the pitching axis location can change the virtual camber effect which may again affect the performance of a cyclorotor.

2.3.9 Effect of Asymmetric Blade Pitching

All the tests in the previous sections were performed using a symmetric blade pitching, which means the blades have the same pitch angle at the top (Ψ=90° in Fig. 2.5) and bottom points (Ψ=270°) of the blade trajectory. However, this might not be

(a) Thrust coefficient, C_T.

(b) Power coefficient, C_P.
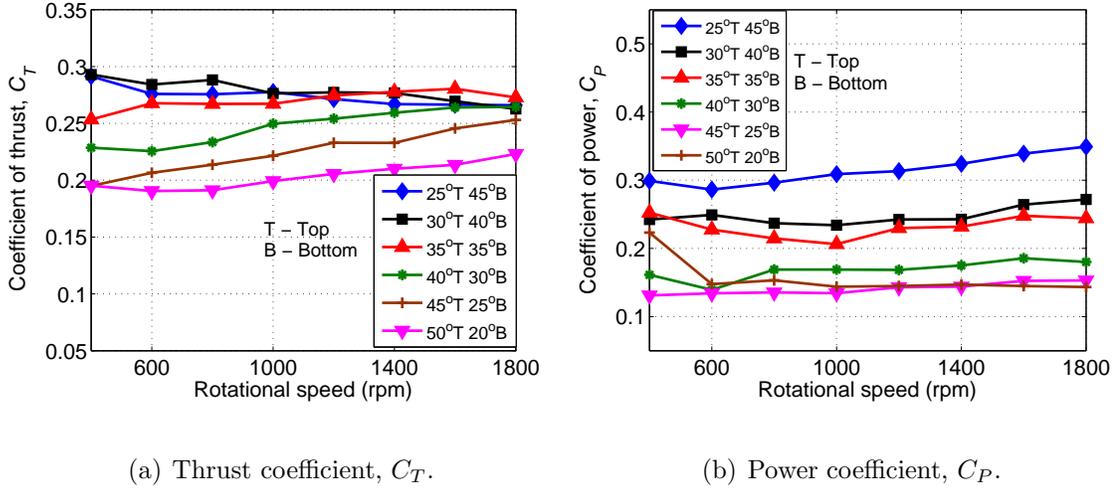
Figure 2.41: **Thrust and power for the 4-bladed cyclorotor using NACA 0015 blades with asymmetric blade pitching with a peak-to-peak pitch angle of 70° and pitching axis at 1/4 chord.**

the optimum blade kinematics considering significant virtual camber effects which is different at the upper and lower halves of the rotor (Fig. 2.38) and because of the inflow and interference effects. Therefore, tests were conducted with dissimilar blade pitch angles at the top and bottom points of the blade trajectory – asymmetric pitching. Figure 2.41 shows the variation of thrust and power for six different asymmetric cases with a peak-to-peak pitching angle of 70°. The different cases were 25° at the top and 45° at the bottom (25°T 45°B), 30° at top and 40° at bottom (30°T 40°B), 35° at top and bottom (35°T 35°B), 40° at top and 30° at bottom (40°T 30°B), 45° at top and 25° at bottom (45°T 25°B) and 50° at top and 20° at bottom (50°T 20°B). These tests were performed on 2- and 4-bladed cyclorotors with a blade span of 6.25 inches and chord of 1.3 inches.

Figure 2.41(a) shows the variation of thrust coefficient with rotational speed.
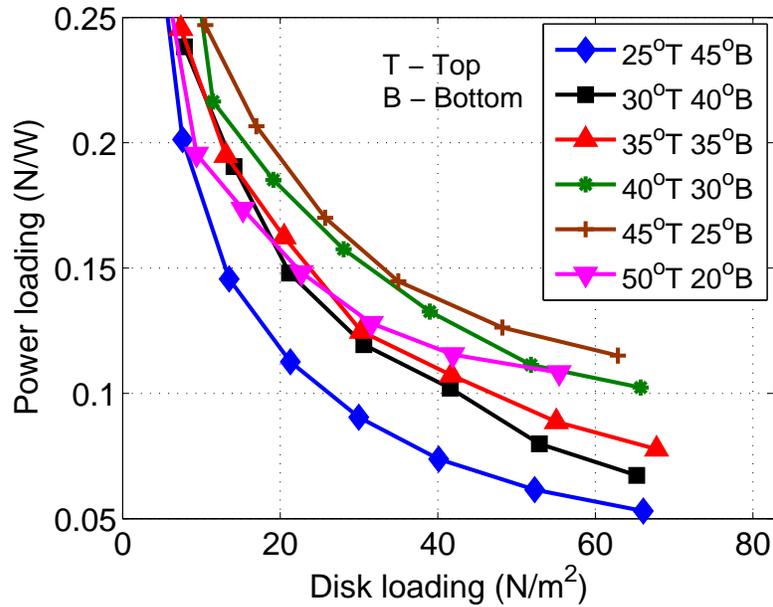
Figure 2.42: **Variation of power loading with disk loading for the 4-bladed cyclorotor using NACA 0015 blades with asymmetric blade pitching with a peak-to-peak pitch angle of 70° and pitching axis at 1/4 chord.**

For a constant rotational speed, the thrust decreased as the pitch angle at the top was increased and the pitch angle at the bottom was decreased. However, as shown in Fig. 2.41(b), the power also decreases along with thrust, as the pitch angle at the top is increased relative to the bottom. Figure 2.42 shows variation of power loading with disk loading for the same test case. It can be seen that the lowest power loading was for the 25°T 45°B case where the blades are operating at much higher pitch angle at the bottom compared to the top. However, as seen from Figure 2.42, increasing the top angle and decreasing the bottom angle improved the power loading up to 45°T 25°B and then decreased for the 50°T 20°B case probably due to blades stalling at 50° pitch angle. Therefore, the 45°T 25°B provided the

(a) Thrust coefficient, C_T.
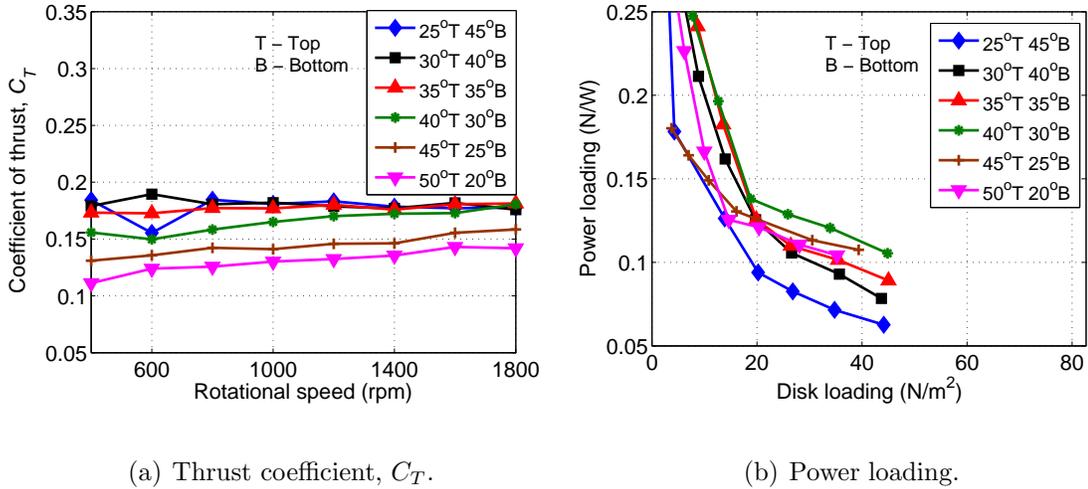
(b) Power loading.

Figure 2.43: **Thrust and power loading for the 2-bladed cyclorotor using NACA 0015 blades with asymmetric blade pitching with a peak-to-peak pitch angle of 70° and pitching axis at 1/4 chord.**

optimum blade kinematics.

Figure 2.43(a) shows the variation of thrust and power loading for the same 70° peak-to-peak pitch angle case, but using a 2-bladed rotor. The thrust and power loading followed the same trend as the 4-bladed rotor. Thrust decreased as the pitch at the top was increased relative to the bottom. The highest thrust was obtained for the 25°T 45°B case. Even though the thrust dropped, the power loading increased (Fig. 2.43(b)) as the pitch angle at the top was increased relative to the bottom till 40°T 30°B case. From the 40°T 30°B case, the power loading decreased for the 45°T 25°B case and further dropped for 50°T 20°B. It should be noted that the best power loading case for the 4-bladed was 45°T 25°B. The slight difference in optimum between the 2- and 4-bladed cases may be because of the differences in the inflow and interference effects for the two rotors.
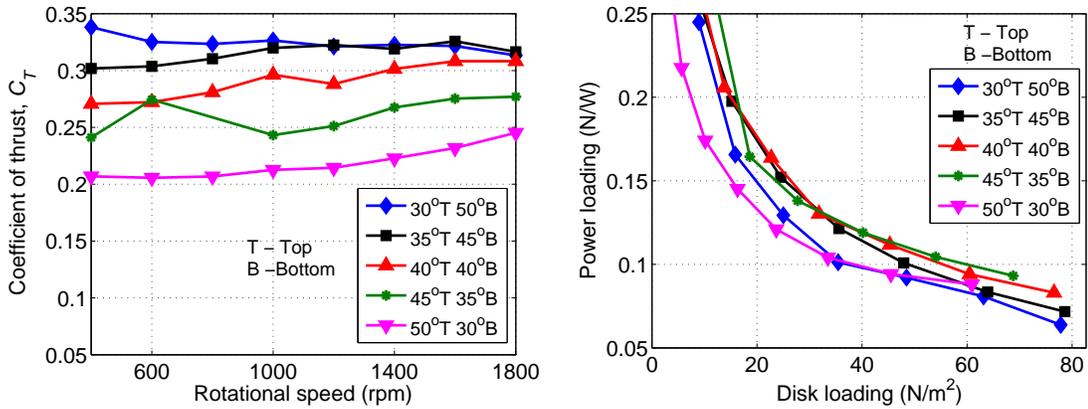
(a) Thrust coefficient, C_T.

(b) Power loading.

Figure 2.44: **Thrust and power loading for the 4-bladed cyclorotor using NACA 0015 blades with asymmetric blade pitching with a peak-to-peak pitch angle of 80° and pitching axis at 1/4 chord.**

Figure 2.44 shows the results from the asymmetric pitching tests for a total peak-to-peak amplitude of 80° on a 4-bladed rotor. The conclusons remained same as the 70° peak-to-peak case. The thrust decreased as the pitch angle at the top was increased relative to the bottom with the maximum thrust for the 30°T 50°B case. Again, the power loading improved when the top angle was increased and the bottom angle was decreased, with the optimum power loading for the case with 45° at the top and 35° at the bottom. Increasing the top angle above 45° and decreasing the bottom angle below 35° (50°T 30°B), drastically reduced the power loading. Therefore, even though the 30°T 50°B case produced the highest thrust, it had the lowest power loading. These tests clearly showed that asymmetric pitching where the pitch angle at the top is higher than the bottom proved to be better than symmetric pitching in terms of power loading.
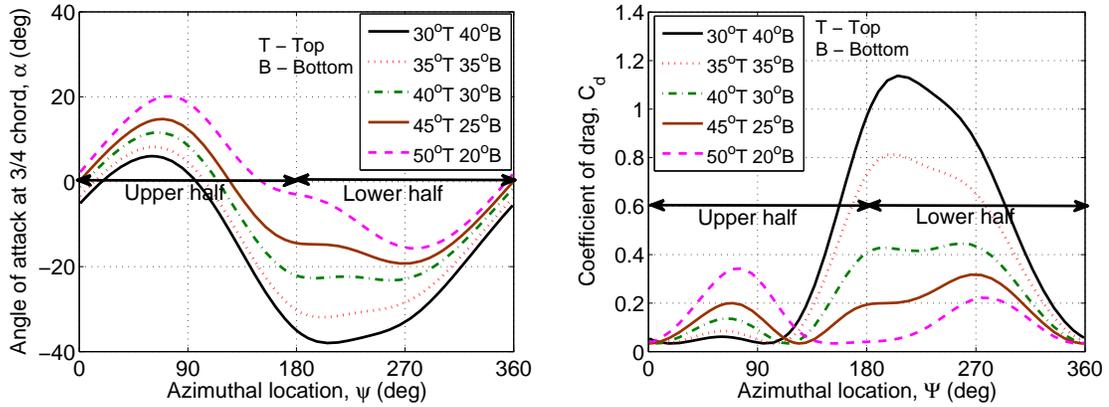
(a) Blade angle of attack at the 3/4 chord location.

(b) Blade drag coefficient.

Figure 2.45: **Variation of blade angle of attack at the 3/4 chord location and drag coefficient along the azimuth for a 4-bladed cyclorotor with asymmetric blade pitching for a peak-to-peak pitch angle of 70° and pitching axis at 1/4 chord.**

Though the improvement in power loading was clearly due to virtual camber effect, an analysis based on blade element momentum theory (BEMT) (discussed in Chapter 4) was performed to improve understanding. Figure 2.45(a) shows the variation of angle of attack at the 3/4 chord location along the azimuth for a peak-to-peak pitch angle of 70° obtained using the BEMT analysis. For the symmetric pitching case (35°T 35°B), the angle of attack in the lower half is much higher than the angle of attack in the upper half because of the virtual camber effect. As the pitch angle at the top was increased relative to the bottom, the angle of attack variation in the upper and lower halves becomes more symmetric until the 45°T 25°B case. Figure 2.45(b) shows the variation of blade drag coefficient (C_d) along the azimuth obtained using the analysis. Again, for the symmetric 35°T 35°B case,

the drag at the lower half is extremely high because of the high angle of attack and C_d varies as the square of angle of attack. As the pitch angle at the top was increased relative to the bottom, overall C_d drops drastically reducing the profile power of the cyclorotor. For the various asymmetric cases in Figs. 2.45(a) and 2.45(b), the thrust was kept constant by changing the rotational speed of the rotor. Since the thrust was kept constant, the induced power is assumed to remain the same for the various asymmetric cases. Therefore, the drop in power was caused by the drop in profile power. As the pitch angle at the bottom was decreased relative to the top, the blades operated at a lower C_d range.

2.3.10   Effect of Pitching Axis Location

For the present cyclorotor, the blade chord is comparable to the rotor radius (c/R = 0.43). Therefore, the location of the pitching axis may have a significant impact on the velocity and angle of attack at different chordwise locations on the blade, causing significantly different virtual camber/incidence effects. All the previous tests were performed with the pitching axis at the quarter-chord. A series of tests were conducted for pitching axis locations of 12.5%, 25%, 35%, 45% and 57.5% chord for a 4-bladed rotor using NACA 0015 blades and operating at a pitching amplitude of 40° (symmetric pitching). These tests were performed on a 4-bladed cyclorotor with a blade span of 6.25 inches and chord of 1.3 inches.

Figure 2.46(a) shows the variation of thrust coefficient, C_T, with the pitching axis location for different rotational speeds at a pitching amplitude of 40° (symmetric
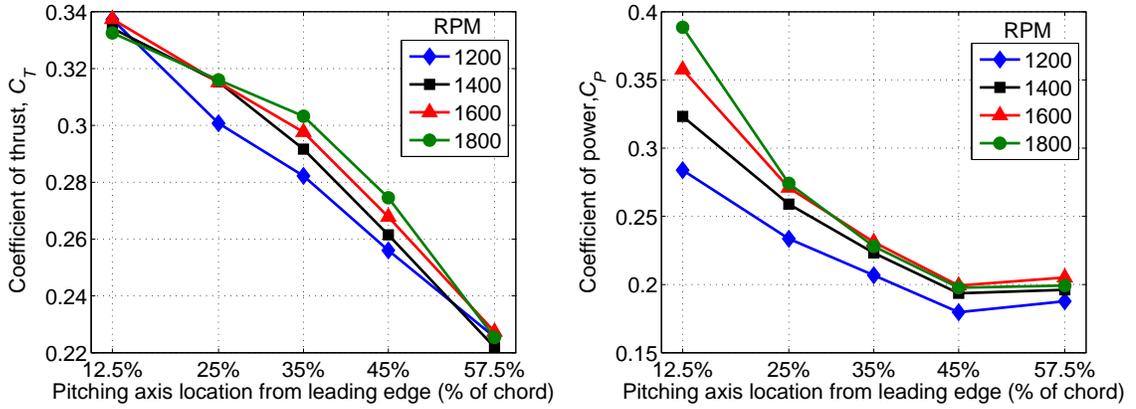
(a) Thrust coefficient, C_T.

(b) Power coefficient, C_P.

Figure 2.46: **Thrust and power coefficient versus pitching axis location at different rpms for the 4-bladed cyclorotor using NACA 0015 blades at 40° pitching amplitude.**

pitching). For all the rotational speeds, the thrust steadily decreased as the pitching axis is moved away from the leading edge. The variation of power coefficient, C_P, with pitching axis location is shown in Fig. 2.46(b). The power also decreased as the pitching axis is shifted away from the leading edge, however, at a much higher rate than the thrust. However, the power increased slightly when the pitching axis location was moved from 45% to 57.5% chord location.

To find the optimum location of the pitching axis, the variation of power loading with disk loading was plotted (Fig. 2.47(a)). Since the power decreased at a higher rate than the thrust decreased, the power loading increased as the location of pitching axis was moved away from the leading edge. At high disk loadings, the best power loading was obtained for pitching axis locations of 35% and 45% chord. However, 35% chord location produced slightly higher thrust than 45%. As
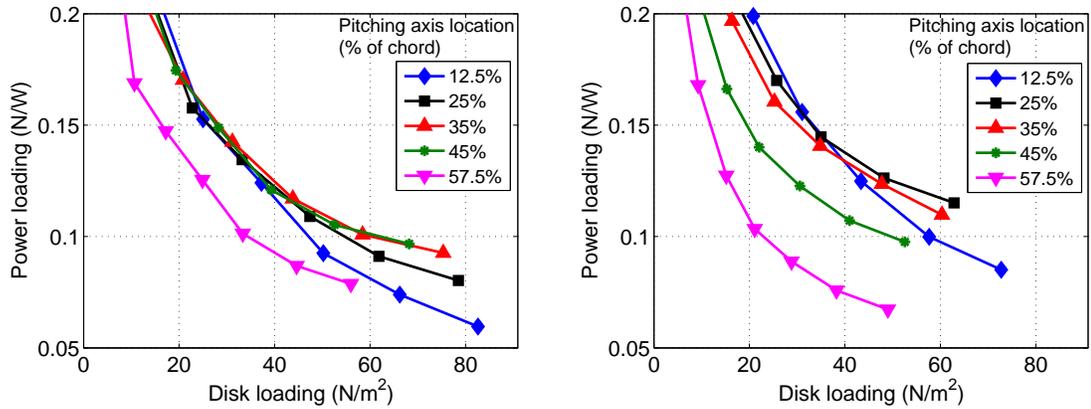
(a) 40° pitching amplitude symmetric pitching. (b) 45°T 25°B asymmetric pitching (70° pk-pk).

Figure 2.47: **Power loading versus disk loading for the 4-bladed cycloro-tor using NACA 0015 blades at 40° symmetric pitching and 45°T 25°B asymmetric pitching for different blade pitching axis locations.**

the pitching axis location was moved from 45% to 57.5% chord, the power loading dropped significantly.

Since the 45°T 25°B (70° peak-to-peak) asymmetric case with the pitching axis at quarter-chord produced the best power loading, a series of tests were conducted by varying the pitching axis location with the aim of improving the power loading further. Figure 2.47(b) shows the variation of power loading with disk loading for the 45°T 25°B case with different pitching axis locations. The power loading decreased as the pitching axis location was moved aft from 25% chord location. The power loading with pitching axis at 35% chord location was slightly lower than the 25% case. For the 45% pitching axis location, the power loading dropped significantly. For the 40° symmetric case, the best power loading was for 35% and 45% chord locations, implying that the pitching axis location for the optimum power loading

138
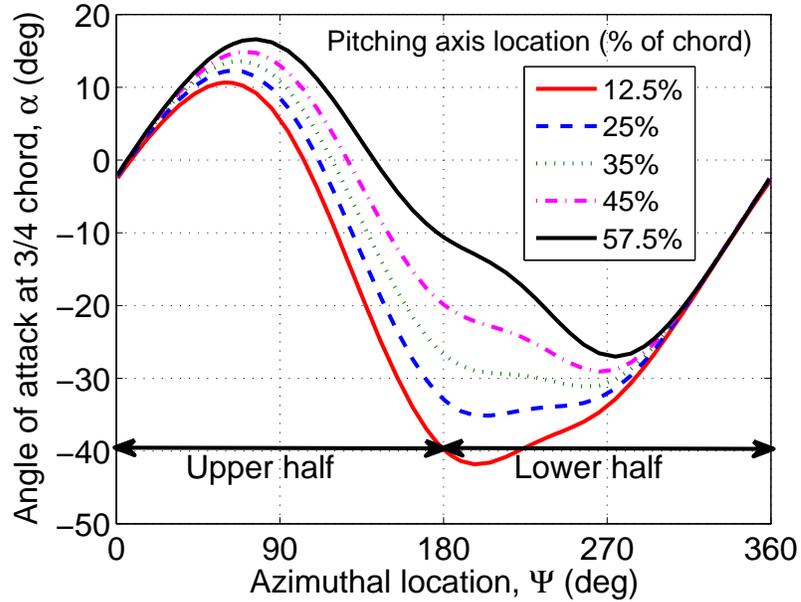
Figure 2.48: **Variation of angle of attack at the 3/4 chord for different pitching axis locations.**

is not unique but depends on the blade pitching kinematics. The other important conclusion from this study is that if the design objective is to produce more thrust at a particular rotational speed, the blade should be pivoted as close to the leading edge as possible.

The significant differences in the aerodynamic performance of the cyclorotor with the variation of pitching axis location may be due to the virtual camber effect. Figure 2.48 shows that the location of pitching axis has significant influence on the angle of attack at the 3/4 chord. As the pitching axis location is moved away from the leading edge, the angle of attack variation in the upper and lower halves become more symmetric, thereby reducing the operating drag coefficient as explained in the previous section. This can potentially reduce the profile power. However, as

Figure 2.49: **Blades with different chord lengths.**

the pitching axis is moved away from the leading edge, the thrust produced by the rotor decreases for the same rotational speed. Therefore, in order to keep the thrust constant, the rotor has to operate at higher speeds which can increase the profile power. This clearly shows that there are two opposing effects which determine the optimum pitching axis location for minimum profile power. Since the power consumed by the rotor is compared at the same thrust, the induced power is assumed to be the same.

2.3.11   Effect of Number of Blades (Constant solidity)

The study on the effect of number of blades presented in the previous section were not tested at the same solidity since all the rotors used blades with the same chord. To investigate the effect of number of blades at constant solidity ($N_b c / 2\pi R$), three

(a) Thrust coefficient, C_T.

(b) Power coefficient, C_P.
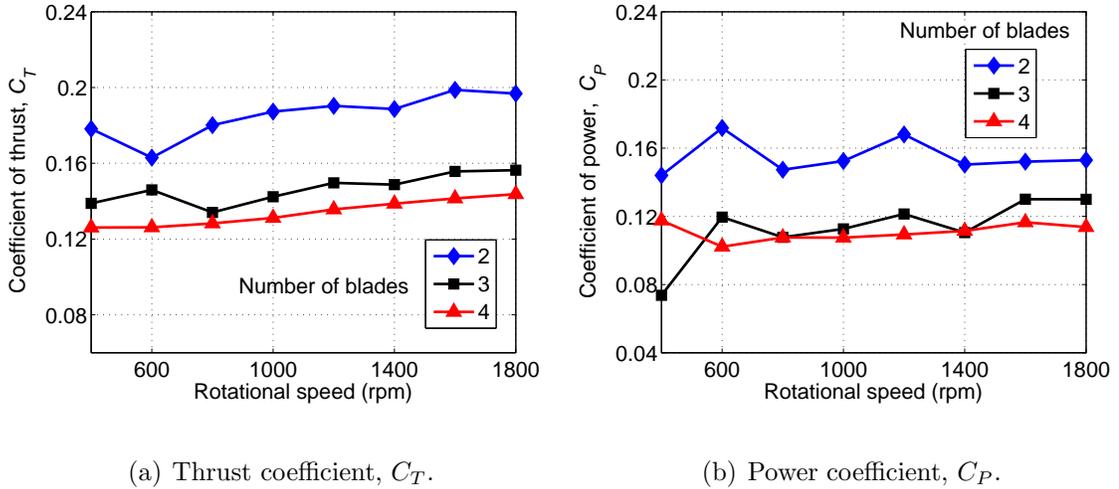
Figure 2.50: **Thrust and power coefficient versus rotational speed for cyclorotors with different number of blades (same solidity) at a pitching amplitude of 40° with pitching axis at 1/4 chord.**

sets of NACA 0015 blades with different chord lengths but same span (6.25 inches) were built as shown in Fig. 2.49. The chord lengths were 1.3 inches, 0.86 inches (2/3 of 1.3 inches) and 0.65 inches (1/2 of 1.3 inches) and were used on 2-, 3- and 4-bladed cyclorotors respectively so that all the rotors have the same total blade area and hence the same solidity because all the three rotors had the same span and diameter.

Figure 2.50(a) shows the variation of thrust coefficient (C_T) with rotational speed for the 2-, 3- and 4-bladed cyclorotors at a pitching amplitude of 40° (symmetric pitching). Although, the total blade area is the same, the 2-bladed cyclorotor produced significantly higher thrust than the 3- and 4-bladed rotors and the 3-bladed rotor produced higher thrust than the 4-bladed rotor. Also the aerodynamic power (Fig. 2.50(b)) was different for all the rotors. The 2-bladed rotor consumed
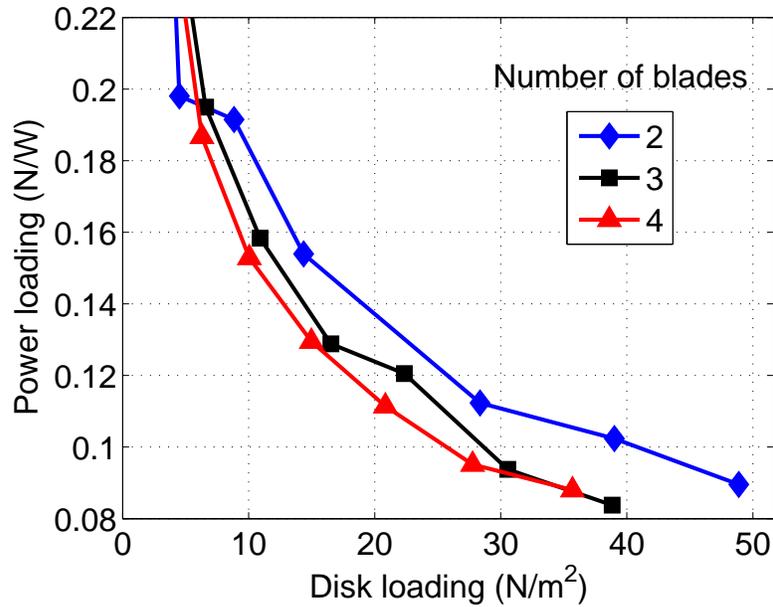
Figure 2.51: **Power loading versus disk loading for cyclorotors with different number of blades (same solidity) at a pitching amplitude of 40° with pitching axis at 1/4 chord.**

the maximum power followed by the 3- and 4-bladed rotors. As shown in Fig. 2.51, the power loadings of the three rotors differed significantly. The 2-bladed rotor produced higher power loading than the other two, followed by 3-bladed rotor which was slightly better than the 4-bladed rotor.

Fig. 2.52 shows the variation of thrust and power loading for the 25° pitching amplitude case. As before, the 2-bladed rotor produced the maximum thrust followed by 3- and 4-bladed rotors (Fig. 2.52(a)). The 3-bladed rotor was only slightly better than the 4-bladed one. The 2-bladed cyclorotor also had the highest power loading Fig. 2.52(b). However, unlike the 40° case, the 4-bladed rotor had a higher power loading than the 3-bladed one and was very close to the the 2-bladed rotor.
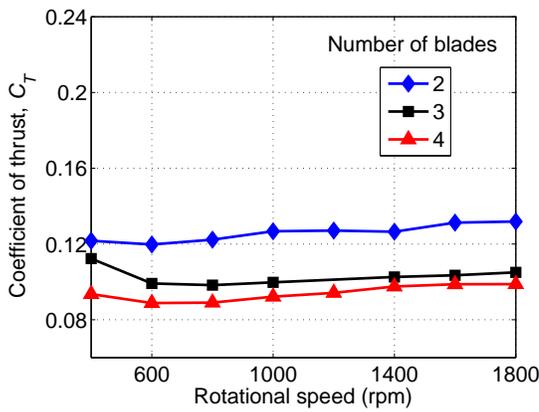
(a) Thrust coefficient, C_T.
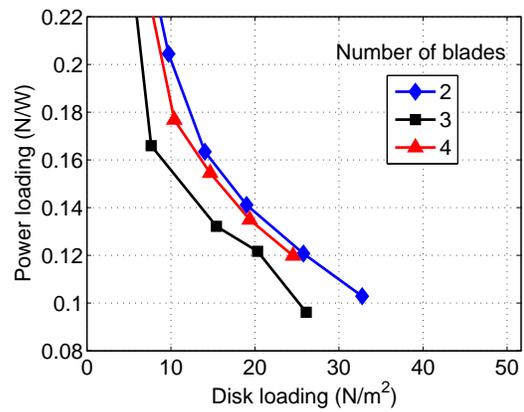
(b) Power loading.

Figure 2.52: **Thrust and power loading for cyclorotors with different number of blades (same solidity) at a pitching amplitude of 25° with pitching axis at 1/4 chord.**
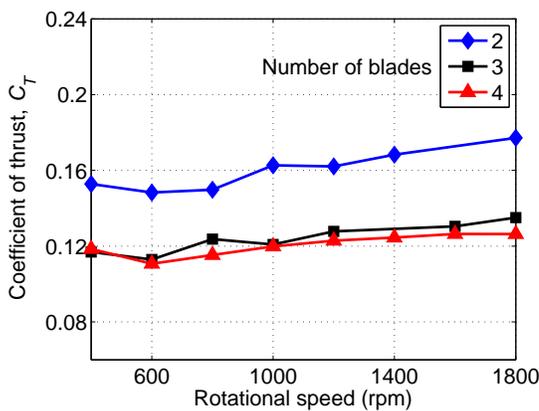
(a) Thrust coefficient, C_T.
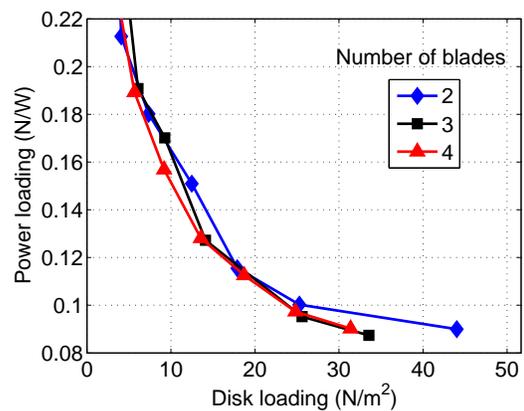
(b) Power loading.

Figure 2.53: **Thrust and power loading for cyclorotors with different number of blades (same solidity) for 45°T 35°B asymmetric pitching case with pitching axis at 1/4 chord.**

The 3-bladed cyclorotor had significantly lower power loading when compared to 2- and 4-bladed rotors.

The effect of number of blades was also investigated for an asymmetric case with 45° pitch angle at the top and 35° at bottom. As in the previous cases, the 2-bladed rotor produced significantly higher thrust than 3- and 4-bladed rotors (Fig. 2.53(a)). The 3- and 4-bladed rotors produced very similar thrusts. As shown in Fig. 2.53(b), the 2-bladed cyclorotor had slightly higher power loading than the 3- and 4-bladed rotors especially at higher disk loadings. The 3- and 4-bladed rotors had very similar power loadings.

Even with the same total blade area, the differences in the performance can be mainly attributed to the differences in virtual camber effect since the chord to radius ratio varies between the rotors. The differences can also be attributed to the interference effects which vary with the number of blades. Also, there is a significant difference in the power loading trends between 25° and 40° pitching amplitudes because the inflow and the wake interference effect is a strong function of angle of attack. The blade aspect ratio of the rotors is also different.

These tests clearly showed that for the same solidity, the 2-bladed cyclorotor has the best thrust and power loading. Also, if the design goal is to produce maximum thrust for the same total blade area, having fewer blades with larger chord is advantageous.

144
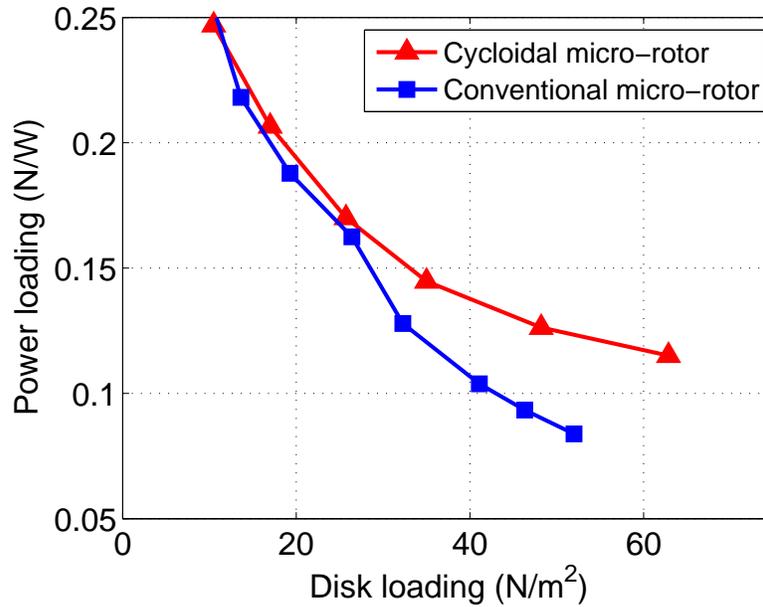
Figure 2.54: **Power loading for the cyclorotor compared with conventional micro rotor.**

2.4 Comparison to a Conventional Micro Rotor

Based on test results, the cyclorotor with the highest power loading was a 4-bladed rotor using 1.3 inch NACA 0015 blade section with an asymmetric pitching of 45° at top and 25° at bottom and the pitching axis at 25% chord. This optimized cyclorotor was compared with the performance of a conventional micro-rotor of similar actuator area (diameter=9 inches, solidity=0.137) [75] at the same disk loading (see Fig. 2.54). The power loading of the optimized cyclorotor was comparable to that of a conventional rotor at the same disk loading.

It should be noted that in this case, the conventional micro-rotor used cambered blades with rectangular planform, whereas the cyclorotor used symmetric blades, which are less efficient aerodynamically at low Reynolds numbers. Camber-

ing the cyclorotor blades such that the virtual camber effect is eliminated might improve the performance of the rotor. Therefore, the higher power loading of a cyclorotor over a conventional rotor is mainly by the virtue of the aerodynamic efficiency of the cycorotor concept.

2.5   Concluding Remarks

The present chapter discusses the systematic experimental studies that have been performed to understand and optimize the performance of a micro-scale cyclorotor in terms of thrust and power loading. Experimental parametric studies were conducted to investigate the effect of the rotational speed, blade airfoil profile, blade flexibility, blade pitching amplitude (symmetric and asymmetric blade pitching), pitching axis location, number of blades with constant chord (varying solidity), and number of blades at same rotor solidity (varying blade chord). These parameters when systematically varied, identified substantial improvements in cyclorotor performance. The following are specific conclusions derived from this work:

1. The force measurements on the cyclorotor showed the presence of a lateral force whose magnitude was comparable to that of the vertical force. The ratio of the lateral force to the vertical force (phase of the resultant force) was found to increase with increasing rotational speed and number of blades. Also, as expected, the thrust coefficient (C_T) remained constant with rotational speed proving that the thrust for a cyclorotor varied as the square of rotational speed. However, the power coeffcient (C_P), linearly increased at a very small

rate with rotational speed, especially at higher rotational speeds.

2. One of the main drawbacks of the cyclorotor was hypothesized to be the parasitic power associated with the rotor structure (endplates, linkages, etc.,), other than the blades. However, the present study showed that, if the rotor is carefully designed, this parasitic power could be as low as 10–15% of the total power.

3. The thrust produced by the cyclorotor steadily increased with pitching amplitude up to 45° without showing any signs of blade stall for all the blade airfoil sections that were tested. PIV studies (Chapter 3) showed that the absence of blade stall at such high pitch angles was because of the high induced velocities causing relatively high inflow angles, which lowered the blade angles of attack. The flow measurements also suggested a form of pitch-rate induced stall delay on the blades at high angles of attack, as well as the formation of a shed leading edge vortex similar to a dynamic stall vortex that is likely responsible for increasing the thrust.

4. Operating the cyclorotor at higher pitching amplitude also resulted in improved power loading, and this trend seemed independent of the number of blades or the blade airfoil sections that were being used. For the majority of the cases tested, the optimum pitching amplitude was observed to be 40°, even though 45° pitching amplitude always produced the maximum thrust. The reason for the higher power loading at higher pitching amplitudes is because the power loading varies inversely with rotational speed, therefore, increasing

thrust by increasing the blade section angle of attack seems more efficient than increasing the rotational speed. However, the maximum thrust that can be obtained using this approach would still be limited by the onset of blade stall, and hence will be airfoil dependent.

5. When compared to the flat-plate blades, the NACA 0010 blades produced the highest values of thrust at all blade pitching amplitudes. The NACA blades also produced higher power loading than the flat plate blades. However, the reverse NACA 0010 blades produced better power loadings at lower pitching amplitudes, even though at higher pitch amplitudes, regular NACA blades performed better. Among the three NACA sections (NACA 0006, NACA 0010 and NACA 0015) tested on the cyclorotor, NACA 0015 had the highest power loading followed by NACA 0010 and then NACA 0006. This may be because at MAV-scale Reynolds numbers, the thicker airfoils are likely to maintain a high lift-to-drag ratio over a wider angle of attack range. However, all the three NACA sections produced similar thrusts at all the pitching amplitudes

6. Using blades that were stiffer in bending and torsion produced higher thrust and power loadings than when using flexible blades because of the reduced aeroelastic effects. With the flexible blades, however, the power loading improved with an increase in blade pitch angle because a larger angle reduces the torsional moment experienced by the blade and also increases the stiffness of the blade in the direction of bending produced by centrifugal effects.

7. Power loading increased with increasing number of blades (i.e., increasing rotor

solidity) despite the fact that profile power requirements also increases with solidity. This is because that a larger solidity rotor produces the same thrust at a lower rotational speed and a decrease in the profile power because of the lower operating speed outweighs the increase in profile power due to the larger blade area. This trend remained consistent across a wide range of blade pitching amplitudes.

8. Asymmetric pitching, where the pitch angle at the top is larger than the angle at the bottom, provided a better power loading than symmetric pitching. The reason can be attributed to the virtual camber effect which tends to reduce the effective angle of attack at the top and increase the effective angle of attack at the bottom. For a total peak-to-peak pitching angle of 70°, 45° pitch angle at the top and 25° at the bottom produced the highest power loading. However, increasing the pitch angle at the bottom relative to the top increased the thrust produced at a constant rotational speed.

9. Shifting the pitching axis location away from the leading edge improved the performance, with the optimum pitching axis location being 25–35% chord depending on the blade pitching kinematics. However, the resultant thrust decreased as the pitching axis was moved away from the leading edge. Since the present rotor has a large chord-to-radius ratio, the location of the pitching axis can significantly affect the aerodynamic performance of the cyclorotor because of the virtual camber effect.

10. For a constant solidity, the rotor with fewer number of blades produced higher

thrust. 2-bladed cyclorotor had the highest power loading compared to 3- and 4-bladed rotors.

11. The power loading of the optimized cyclorotor was comparable to that of a conventional rotor when operated at the same disk loading. The optimum configuration based on all the tests was a 4-bladed rotor using 1.3 inch NACA 0015 blade section with an asymmetric pitching of 45° at top and 25° at bottom with the pitching axis at 25% chord.

Chapter 3

Particle Image Velocimetry Studies

3.1 Overview

Improving the aerodynamic performance of a cyclorotor that vaults a laboratory model to a successfully working hover-capable vehicle depends on developing a fundamental knowledge of its flow field. The current status of the aerodynamic understanding of the cyclorotor can be rated as qualitative, at best. Many aspects of the flow are still not completely understood. For example, some of the phenomena observed in Chapter 2, such as the reason behind the observed absence of blade stall, even when the blade pitch angle is set to high values, or the reason for the skewed nature of the rotor wake, are not completely understood. Flow field measurements can also expose an understanding of the efficiency of such a system based on the uniformity (or otherwise) of the inflow. Obtaining an understanding of the flow inside the rotor can be useful in developing a better inflow model, which will help in predicting the thrust and power more accurately. The present chapter discusses the flow field measurements that were made using the Particle Image Velocimetery (PIV) technique inside the cyclorotor-cage and the rotor-wake to better understand the aerodynamics. This is the first ever flowfield measurements made on a cyclorotor at any scale.

3.2 Particle Image Velocimetery (PIV) Setup

Schematics of the two PIV setups used for the measurements are shown in Fig. 3.1(a) (setup A) and Fig. 3.1(b) (setup B). The actual setup is shown in Fig. 3.2. The PIV hardware included a pulsed dual Nd:YAG laser that was operated in phase synchronization with the cyclorotor, and an articulated optical arm. The optical arm was used to locate the light sheet in the required region of interest in the flow. The laser system was capable of being pulsed at frequencies up to 15 Hz, and was synchronized to the rotational frequency by means of a Hall-effect trigger and phase-locking master timing control unit.

The flow was seeded with a mineral oil fog of sub-micron particles. The entire test area was seeded as uniformly as possible before each sequence of measurements. It should be remembered that the PIV technique actually measures the flow velocity of these seed particles, so it is essential to use small particles to prevent tracking errors but the particles must also be big enough to produce sufficient Mie scattering of the laser light. The flow images were acquired using a 2 mega-pixel resolution digital camera, which was placed orthogonal to the laser sheet. The dual lasers were fired with a pulse separation time of 10 μs. A high-speed digital frame grabber was used to acquire the resulting image pairs for analysis. For the PIV image processing, a recursive technique called a deformation grid correlation algorithm was applied to the images [76], which has been shown to be ideal for measuring the high velocity gradients found inside rotor wake flows [77].

The first setup (spanwise setup, Setup A) was used to study the trailed wake

(a) Spanwise setup (Setup-A).

(b) Chordwise setup (Setup-B).
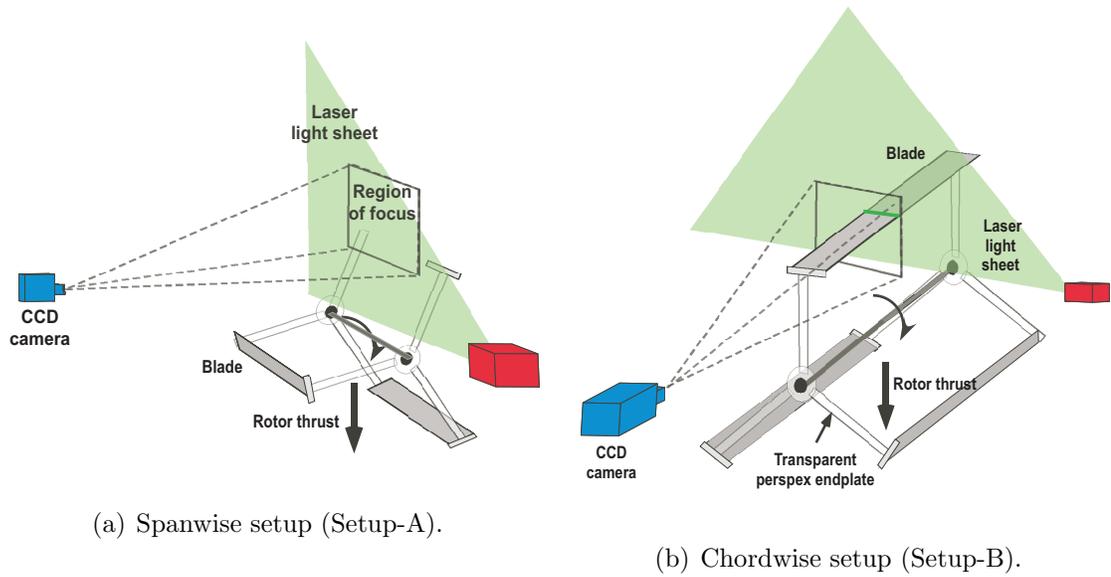
Figure 3.1: **Schematic of the PIV setup for both spanwise and chordwise measurements.**
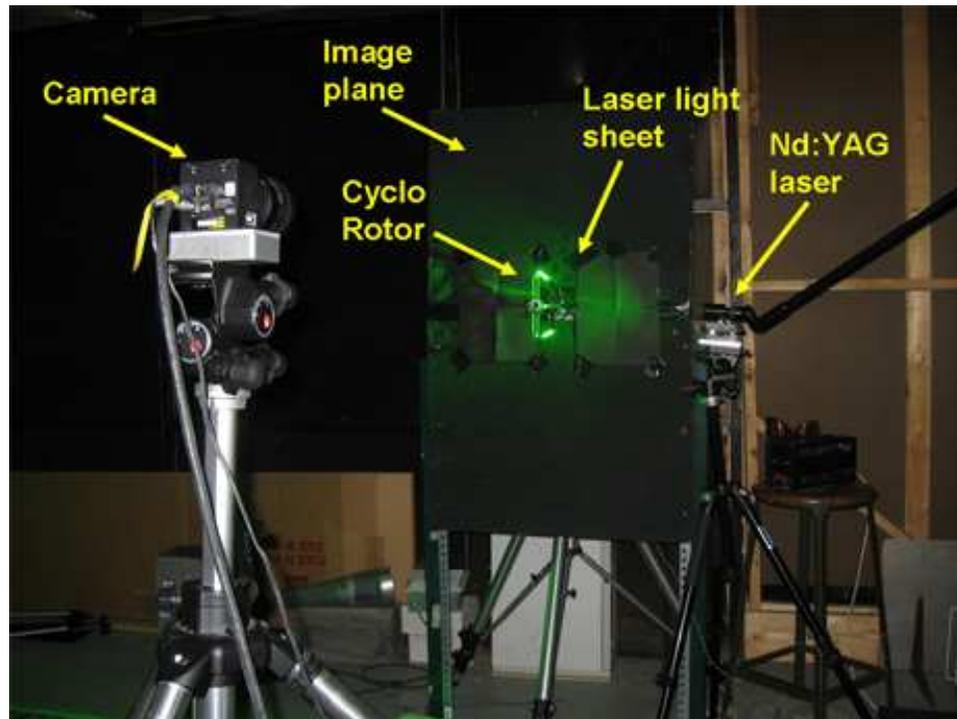
Figure 3.2: **PIV setup.**

behind the blades. The laser sheet was oriented parallel to the blade span, as shown in Fig. 3.1(a). With this setup, the spatial location of the trailed tip vortices and their strength could then be measured; this was essential for understanding the effects of the induced flow field produced by the wake. In the second setup (chordwise setup, Setup B), the positions of the laser and camera were interchanged (Fig. 3.1(b)) such that laser sheet was placed at the mid-span perpendicular to the blade and the camera placement allowed the chordwise flow velocities to be measured. With Setup B, two sets of measurements were taken. In the first set, the camera was focused on a larger region of interrogation to study the flow field inside the cage of cyclorotor as well as in the wake below it. In the second set, the camera was focused closer to the blade to examine the flow around chordwise sections. It was extremely challenging to obtain good PIV measurements inside the cyclorotor-cage because the end plates blocked optical access, and also because of the shadows cast by the individual blades. To help minimize the problem, new rotor endplates were made out of transparent Plexiglass. The PIV measurements were made on 2- 3- and 4-bladed cyclorotors at 40° pitching amplitude and a rotor speed of 1400 rpm.

3.3   PIV Results

The PIV results are discussed in two categories: (1) spanwise view where the trailing tip vortices were analyzed; (2) chordwise view where the flow inside the rotor-cage, in the wake and around the blade were studied.

3.3.1   Tip Vortex Measurements

The tip vortices trailing from the blades will affect the induced flow distribution and can play a major role in determining the overall performance of the cyclorotor. This can be expected based on the observations of a conventional rotor wake [78]. These vortices are even more important at low Reynolds numbers because of their larger relative size in the flow and the wider influence of their induced flow fields compared to the dimensions of the blade chord [79].

The spanwise wake and tip vortex measurements were made using Setup A (Fig. 3.1(a)). These measurements were made on a 3-bladed cyclorotor. The camera was focused on the lowest blade and in the wake below it. Because each blade of the cyclorotor has two free tips, a pair of counter rotating tip vortices were produced, as shown in Fig. 3.3. Furthermore, unlike conventional rotors where the root of the blade experiences very low velocity, the blades of a cyclorotor have nominally the same velocity along their entire span. The results in Figs. 3.4(a)–3.4(f) shows the evolution of both tip vortices. In these figures, the distances are nondimensionalized by the blade span and the velocities by the rotational velocity of the blade, respectively. The data in the figures shows the phase-averaged flow velocity vectors superimposed on the vorticity contours for several wake ages. Notice that 0° wake age corresponds to the alignment of the laser light sheet with the trailing edge of the blade as the blade reaches its lowest most point in its cycle. The measurements were performed at 6 different wake ages, namely, 30°, 45°, 60°, 75°, 90° and 105°. Because there are three blades, after 120° the flow structures become

155
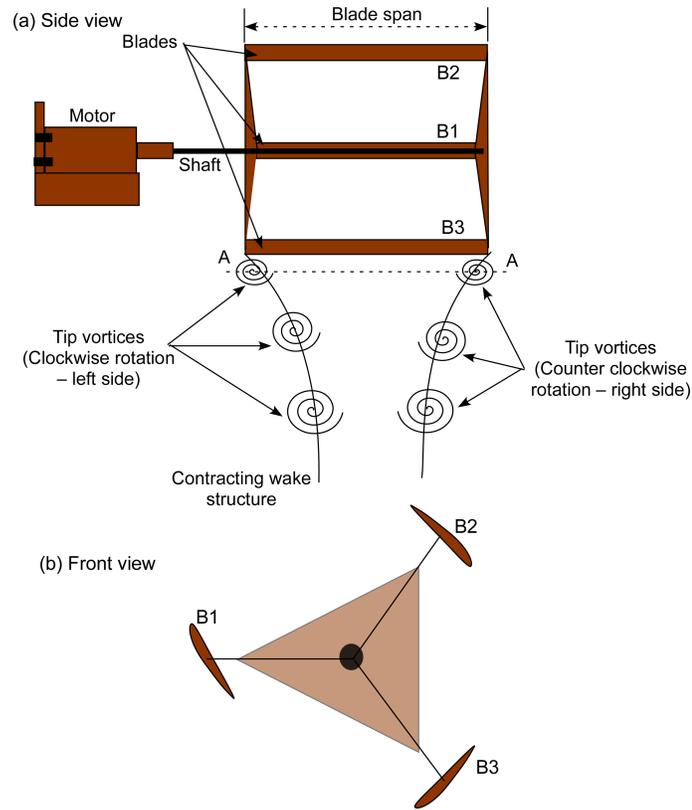
Figure 3.3: **Schematic showing the evolution of the tip vortices.**

repeated.

The results in Fig. 3.4(a) show the vorticity contours at 30° of wake age. The trailing vortices from the right and left blade tips can be seen. Adjacent tip vortices on the same side are at 120° of wake age apart, which is the phase angle between the blades. As expected, the left and right tip vortices have opposite values of circulation. Because the entire blade operates at the same sectional speed, and because all the blade sections are set at the same pitch angle, the initial expectation is that the left and right tip vortices should have almost the same strength. However, for all the wake ages (Figs. 3.4(a)– 3.4(f)) it can be seen that the right tip vortex (at blade tip) is somewhat stronger than the left one (at blade root); this outcome
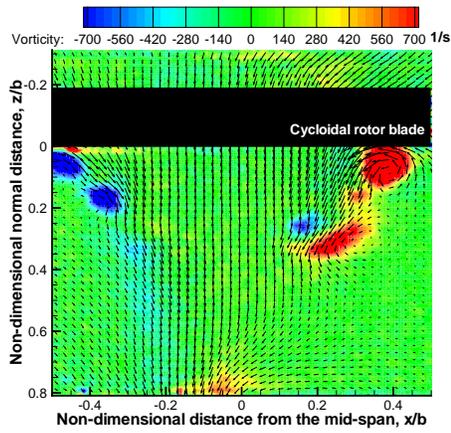
(a) Wake age, $\zeta = 30°$.
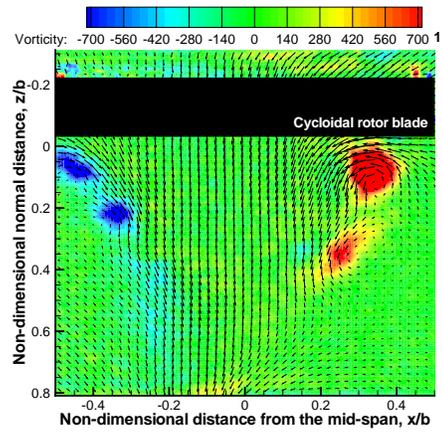
(b) Wake age, $\zeta = 45°$.
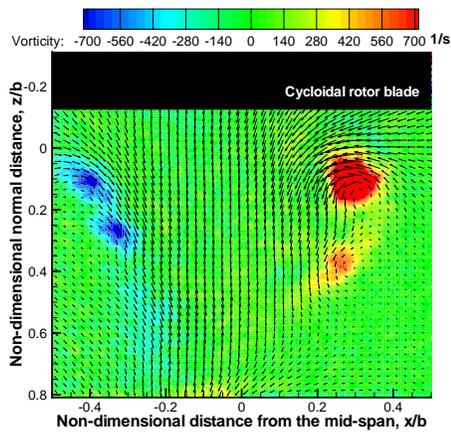
(c) Wake age, $\zeta = 60°$.
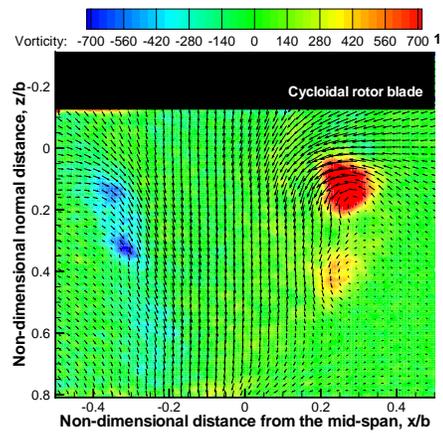
(d) Wake age, $\zeta = 75°$.
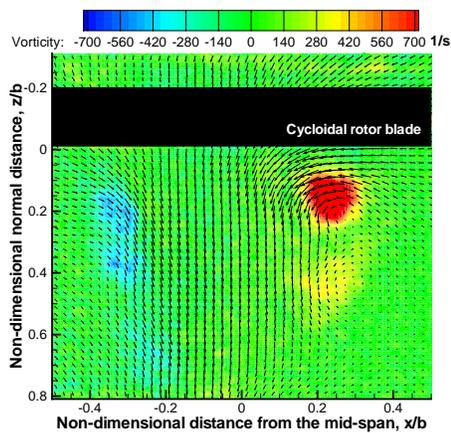
(e) Wake age, $\zeta = 90°$.
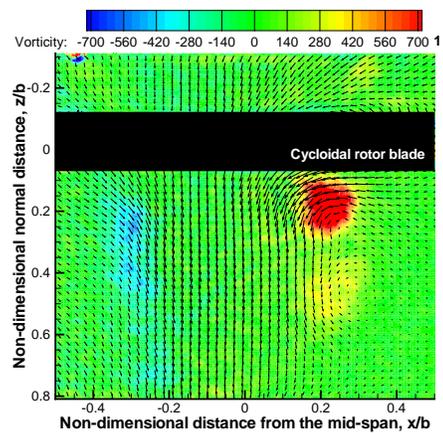
(f) Wake age, $\zeta = 105°$.

Figure 3.4: **PIV measurements showing the presence of a pair of tip vortices from either side of the cyclocopter blade,Wake age, $\zeta = 30°$ to $105°$.**
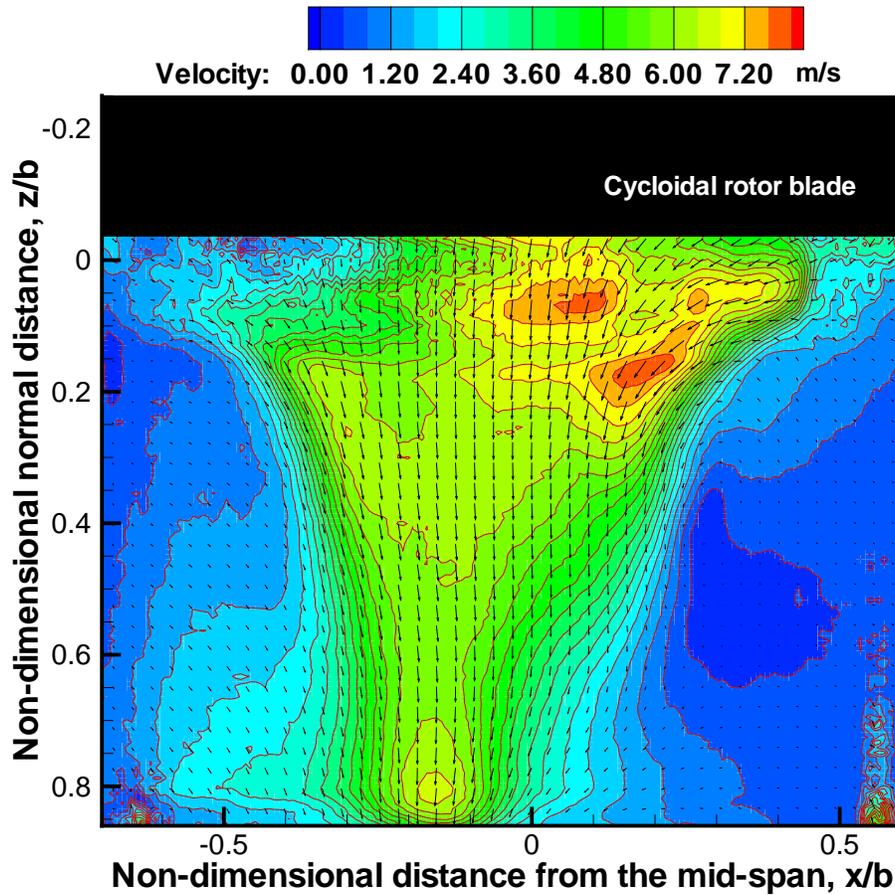
Figure 3.5: **Time averaged velocity measurements showing the wake contraction of the cyclorotor.**

can be attributed to the dissimilar blade attachments at the root and tip of each blade.

Figures 3.4(b)– 3.4(f) (45° to 105° of wake age) show the downward axial convection of the tip vortices. It can also be seen that as the vortices convect downwards in the flow they gradually spin down and diffuse. The results in Fig. 3.5 show the time-averaged flow field in the wake of the cyclorotor where the color contours represent absolute velocity. A very distinct slipstream boundary can be
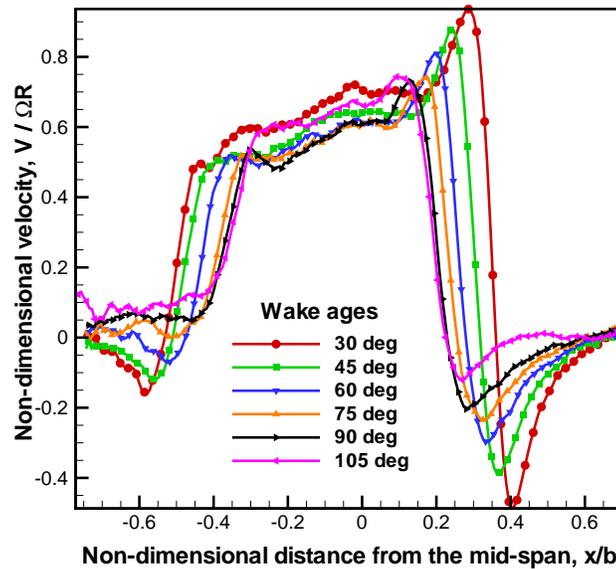
Figure 3.6: **Velocity profiles across the rotor wake by taking the sections across the tip vortices at all the six wake ages.**

seen in this case. Because the cyclorotor produces considerable thrust, a firmly contracting wake structure is an expected result.

The results in Fig. 3.6 show the variation of the swirl velocity along a section (Section AA as shown in Fig. 3.3) across the wake. As the wake age increases, the core sizes of the both the left and right tip vortices increase and the peak swirl velocity decrease, which is consistent with viscous and turbulent diffusion [80]. An important observation here is the relatively high induced velocities that are seen inside the wake; the induced velocities are seen to be (on average) 60 to 70% of the rotational velocity of the blade, which leads to relatively large induced angles of attack at the blade elements which lowers the angles of attack and might explain why the blades do not stall even at high pitch angles.

3.3.2 Chordwise View

The PIV setup B (Fig. 3.1(b)) was used to obtain the velocity measurements in the plane of the rotor and perpendicular to the blade span. The measurements were made on 2-, 3- and 4-bladed cyclorotors, the results being shown in Figs. 3.7 through 3.9. Figures 3.7(a) through 3.7(d) show the phase-averaged velocity vectors (resultant velocity) inside and around the 2-bladed rotor with a pitching amplitude of 40° at four different wake ages, namely, 0°, 30°, 120°, and 150°. A wake age of 0° corresponds to the alignment of the laser light sheet with the trailing edge of the blade when the blade reaches the lowest point in its cycle. Because there are two blades, after 180° the flow structures are repeated. The color contour on each figure and the vector length shows the magnitude of the resultant velocity. Spurious vectors that were produced by reflections from the blades were all removed.

Flow field measurements for the 4-bladed case (40° pitch amplitude) were performed for wake ages of 0°, 20°, 40°, 60°, 75° and 90°. For the 4-bladed rotor, the flow repeats after 90°. Figure 3.8 shows the time-averaged flow field of all these cases. In these figures, the distances are non-dimensionalized by the blade span and the velocity is normalized by blade velocity. The key observation from the PIV measurements is the large region of rotational flow inside the rotor. This result, coupled with the fact that the lower half of the rotor is operating in the wake of the upper rotor, can account for some of the energy loss.

The rotational flow also creates an asymmetry of the inflow about the Z-axis, as can be seen in Figs. 3.7(a) through 3.8 (skewed wake structure), which is

160
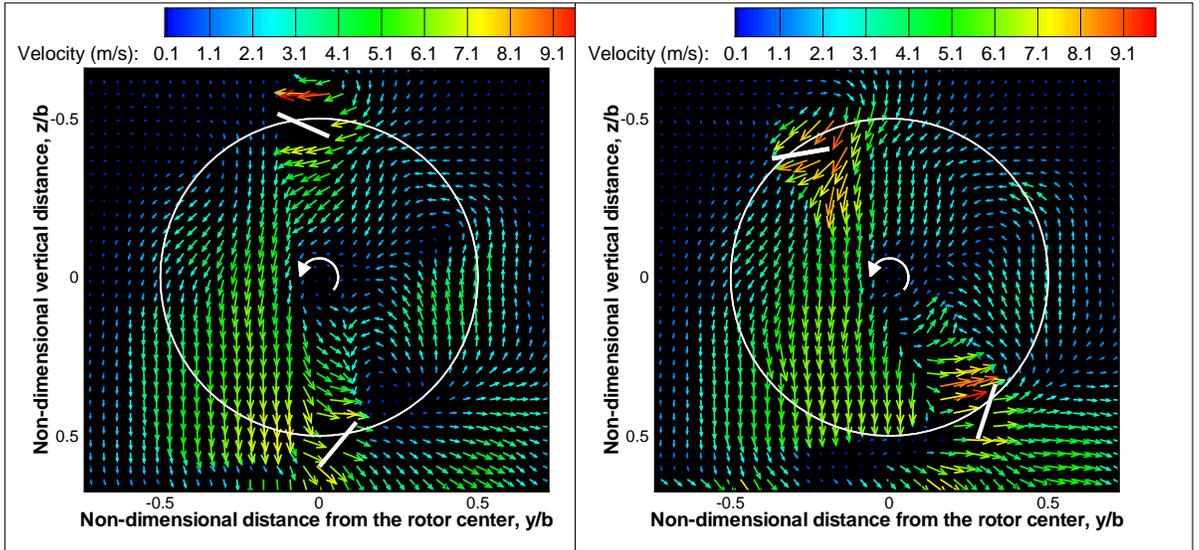
(a) Wake age, $\zeta = 0°$.

(b) Wake age, $\zeta = 30°$.
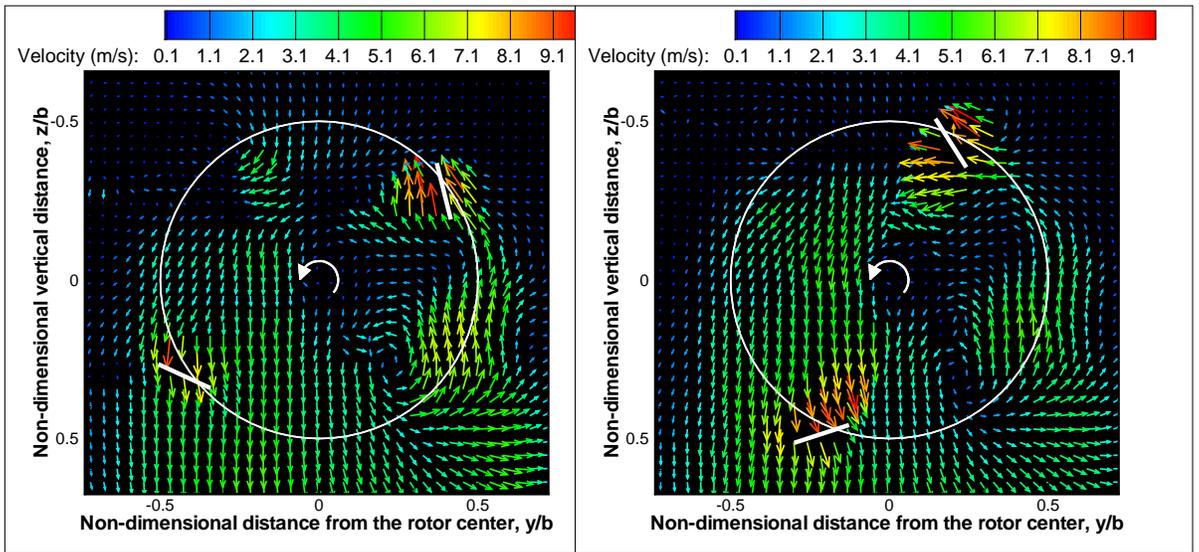
(c) Wake age, $\zeta = 120°$.

(d) Wake age, $\zeta = 150°$.

Figure 3.7: **PIV measurements showing the flow field inside the 2-bladed cyclorotor from wake age, $\zeta = 0°$ to $\zeta = 150°$**
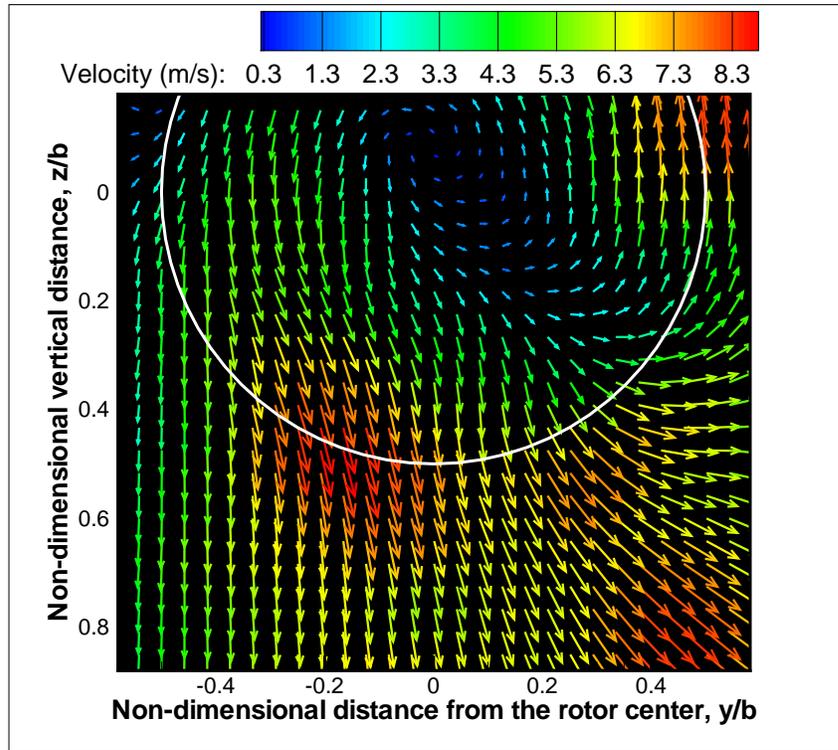
Figure 3.8: **Time averaged velocity measurements showing the flow field inside the 4-bladed cyclorotor.**

consistent with the sideward force measured during the performance tests. The relative complexity of the flow inside the rotor-cage also emphasizes the need for a more detailed inflow model or for a computational fluid dynamics based model to capture the flow physics and accurately predict the performance of a cyclorotor.

For a cyclorotor there is a relatively high amplitude (25° to 45°) 1/rev cyclic pitching motion associated with the blade along with its angular rotation. This is an ideal condition for the development of a leading edge vortex, helping to delay lift stall to a higher angle of attack. To capture the leading edge vortex on the blade in detail, the camera and laser sheet were moved to focus on a blade when it reached its maximum pitch angle. It can be seen from the results in Fig. 3.9 that the PIV
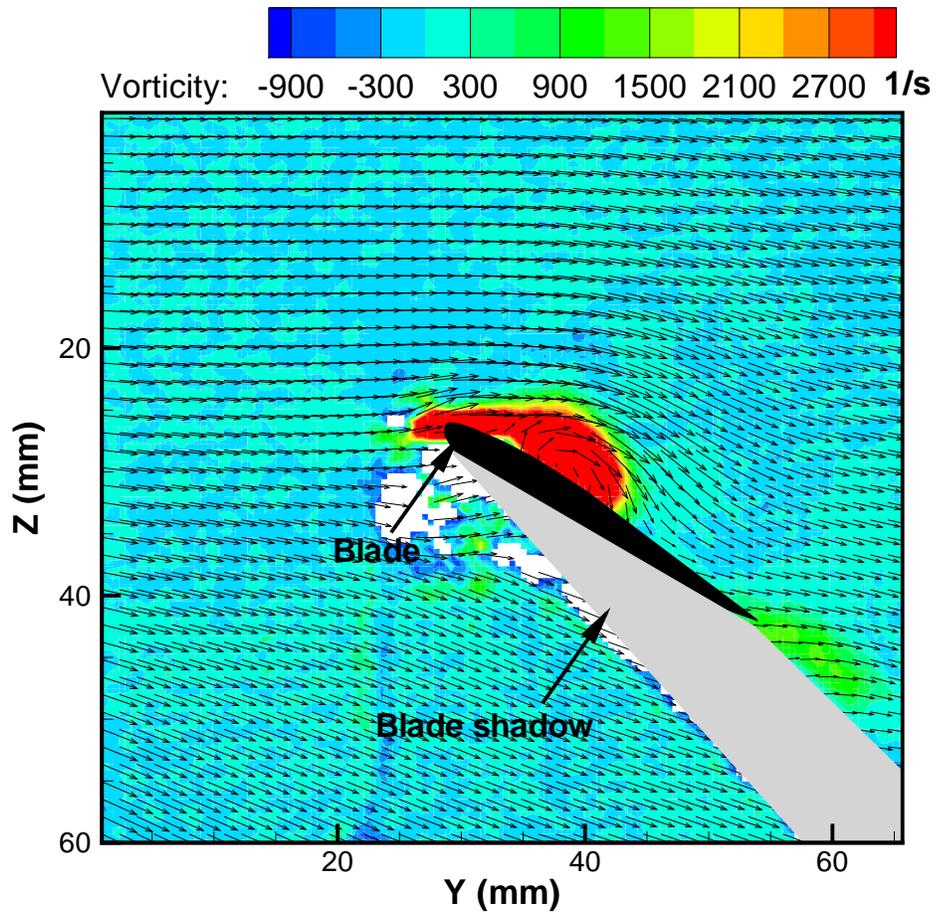
Figure 3.9: **PIV measurements showing the leading edge vortex on top of the blade.**

measurements have indeed resolved a leading edge vortex on the blade. Clearly, this vortex must play some additional role in enhancing lift on the blades, and may be a phenomenon that is associated with the normal operation of a cyclorotor.

3.3.2.1 Thrust from Momentum Balance

The thrust produced by the cyclorotor can also be obtained by computing the change in momentum of the flow passing through a control volume surrounding the rotor.
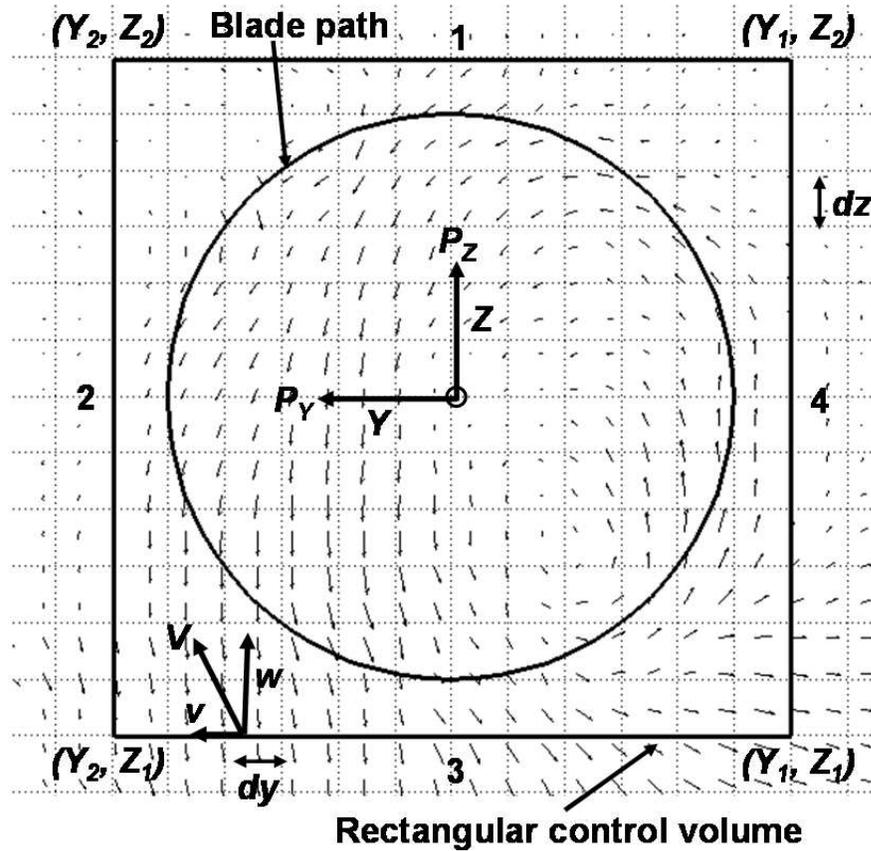
Figure 3.10: **Schematic showing the procedure used to obtain sectional thrust from a momentum balance at a given spanwise location.**

For the present study, a rectangular control volume was used and the net vertical and sideward thrust components were measured from the total momentum flux flowing into the control volume compared to the total momentum flux flowing out. However, the size of the control volume has to be large enough to capture the momentum change in the entire flow field.

The schematic in Fig. 3.10 shows the procedure used for this computation. The first rectangular loop completely encloses the rotor, i.e., the circular blade path of the rotor is within the loop. In the second step, the length of the rectangular loop

164

was increased by Δx (one node in the PIV grid) on all four sides. Subsequent loops increased their length by Δx on all four sides relative to the previous loop. This procedure was continued until the thrust values were converged. The net vertical and sideward thrusts were obtained by numerically evaluating the momentum change across all four sides of the rectangular loop using the velocities measured in the flow field by PIV.

The net horizontal (P_Y) and vertical momentum (P_Z) per unit span through horizontal sides 1 and 3 (Fig. 3.10) is given by

$$P_Y = \int_{Y_1}^{Y_2} \rho V v \, dy$$
$$P_Z = \int_{Y_1}^{Y_2} \rho V w \, dy \tag{3.1}$$

where

$$V = \sqrt{v^2 + w^2} \tag{3.2}$$

and the mass flow rate per unit span across the sides is given by

$$\dot{m} = \int_{Y_1}^{Y_2} \rho V \, dy \tag{3.3}$$

The net horizontal (P_Y) and vertical momentum (P_Z) per unit span through vertical sides 2 and 4 is given by

$$P_Y = \int_{Z_1}^{Z_2} \rho V v \, dz$$
$$P_Z = \int_{Z_1}^{Z_2} \rho V w \, dz \tag{3.4}$$

The horizontal (T_Y) and vertical (T_Z) components of thrust per unit span are then

given by

$$T_Y = (P_{Y_3} - P_{Y_1}) + (P_{Y_4} - P_{Y_2})$$

$$T_Z = (P_{Z_3} - P_{Z_1}) + (P_{Z_4} - P_{Z_2}) \tag{3.5}$$

respectively, where P_{Z_i} and P_{Y_i} denote the momentum of the fluid per unit span through the ith side, in Z and Y directions respectively.

However, this calculation gives only the thrust produced per unit length of the blade at the mid-span location because the PIV measurements were only made at 50% blade span. To obtain the total thrust produced by the rotor, an elliptical lift distribution was assumed along the blade span. The vertical, sideward and resultant thrust values computed using the PIV agreed within 15% of the values obtained from the balance measurements.

3.3.2.2 Wake Integration and Profile Drag

The momentum deficit approach can be used to estimate the sectional drag by comparing the momentum upstream and downstream of the blade section. By using the continuity equation , the equation for the drag is given by [81],

$$D = \frac{1}{2}\rho \int_{-\infty}^{\infty} U_{T_2}(U_{T_1} - U_{T_2})ds \tag{3.6}$$

where the subscripts 1 and 2 denote the upstream and downstream locations relative to the blade section, respectively. Here the quantity $(U_{T_1} - U_{T_2})$ is the decrease in flow velocity, which when multiplied by the mass flux, ρU_{T_2}, gives the decrement in momentum per unit time in the drag direction.
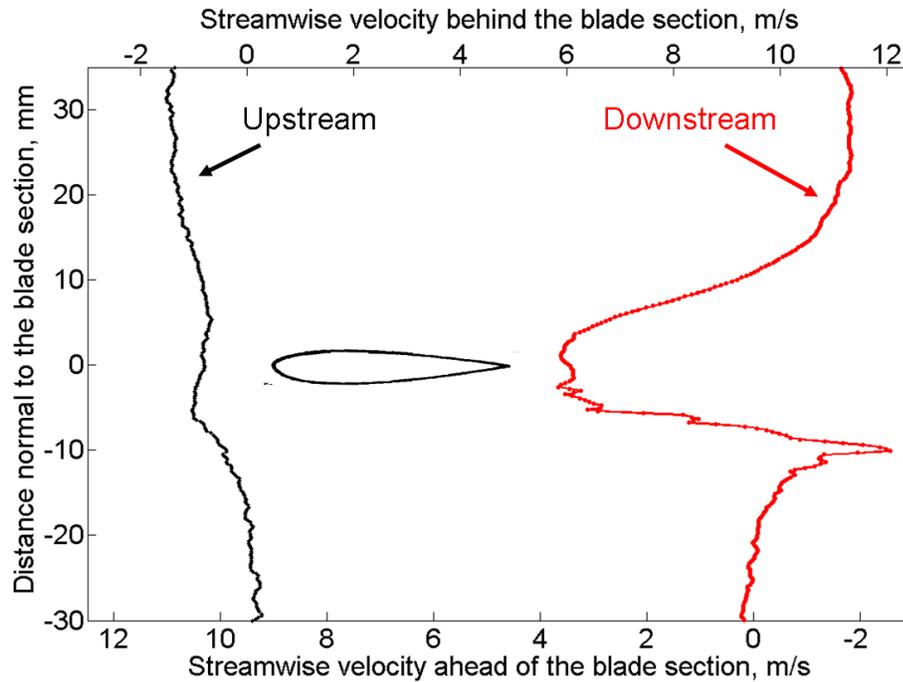
Figure 3.11: **Velocity deficit behind the cyclorotor blade at the mid-span location at 270° azimuthal location.**

Figure 3.11 shows the reduction in the flow velocity behind the rotor blade that was obtained from the PIV measurements for the 270° azimuthal location. The coefficient of drag (c_d) for the blade section computed at the 270° azimuthal location (blade pitch angle of 40°) was 0.09 which is a typical value at these Reynolds numbers at such high angles of attack [17].

3.4   Concluding Remarks

Two sets of PIV measurements, spanwise and chordwise measurements were performed to understand the flowfield of the cycloidal rotor. These studies helped answer some of questions that arouse during the performance measurements dis-

cussed in Chapter 2. Following are the specific conclusions derrived from the PIV studies.

1. The cyclorotor was shown to generate relatively high values of thrust even at extremely high blade pitch angles. PIV measurements showed that the blades experienced relatively high inflow velocities, which lowered the angles of attack. The flow measurements also suggested a form of pitch-rate induced stall delay on the blades at high angles of attack, as well as the formation of a leading edge vortex shed similar to a dynamic stall vortex that is likely responsible for increasing the thrust.

2. The spanwise PIV measurements showed the presence of two contra-rotating tip vortices from the two blade tips which convected downwards in a contracting wake pattern.

3. The presence of a sideward force on the cyclorotor was found to be of a magnitude comparable to that of the vertical force. The ratio of the sideward force to the vertical force (phase of the resultant force) was found to vary with rotational speed. A significantly skewed downstream wake structure in the cross-plane was also found from the PIV measurements, which confirmed the existence of the sideward force.

4. A momentum balance performed using the flow field measurements helped to quantify the vertical and sideward forces produced by the cyclorotor. The estimated momentum values showed good agreement with the force measurements made using load balance. The drag coefficient of the blades was also

computed using the momentum deficit approach, and the computed C_d values correlated well with the typical airfoil values for these low Reynolds numbers.

5. The PIV measurements showed that the flowfield inside the cyclorotor-cage was far from uniform and there were significant rotational flows inside the rotor cage, which coupled with the influence of the upper wake on the lower half of the rotor can account for some energy losses inside the cyclorotor.

Chapter 4

Aeroelastic Modeling

4.1 Overview

This chapter describes and validates the aeroelastic model which has been developed to predict the blade loads and the average thrust of a MAV-scale cycloidal rotor with sufficient accuracy so that it could be used for routine design calculations. This model have been also used to obtain a fundamental understanding of cycloidal rotor aeroelasticity and hence explain some of the different behaviors/trends that were observed during the experimental studies discussed in Chapter. 2.

Most of the previous studies on cyclorotors have been experimental in nature [29–32, 36, 38, 43–45, 53–59, 64, 68]. One of the initial analytical studies on cyclorotors was performed by Wheatley [37, 38] in 1930s, and it focused on the development of a simplified aerodynamic model which was validated against wind tunnel measurements. However, the analysis showed poor agreement with the experimental measurements. McNabb [46] developed an unsteady aerodynamic model of a cyclorotor, and the predictions were found to correlate well with the measurements. More recently, Kim et. al. [53, 57–59] developed a quasi-steady aerodynamic model for a cyclorotor and a parallel analysis was conducted using CFD to help predict the aerodynamic characteristics.

However, all these studies were performed on large-scale rotors at Reynolds

numbers of the order of 10^5 or higher. The only low Reynolds number computational studies were conducted by Iosilevskii and Levy [48,49] and Yang et al. [69]. Iosilevskii and Levy [48, 49] performed a 2-D CFD investigation of a cyclorotor operating at blade chord Reynolds numbers of about 40,000. This CFD study helped expose the complex aerodynamic interactions between the rotating blades, which also showed good agreement with the measured time-averaged forces. Yang et al. [69] conducted a 3-D CFD study of the same cycloidal rotor used in the current study. When compared with the experimental results, the CFD predictions matched reasonably well for the vertical force, while the lateral force and power were underpredicted. Velocity field obtained from the CFD study exhibited good correlation with the PIV results in capturing essential flow features. The study also revealed a very complex flowfield with significant shedding from the blades and a high level of blade-vortex interaction and wake skewness.

Since all these studies were focussed on developing aerodynamic models, the effects of the blade deformations were not included while calculating the aerodynamic performance. However, the experimental studies have shown that at higher rotating speeds, the cycloidal rotors experience large inertial (mostly centrifugal force) and aerodynamic forces causing significant bending and torsional deformation especially for flexible blades. These deformations play a crucial role in the aerodynamic performance of the cycloidal rotor both in terms of thrust and power as shown in Fig. 4.1. It can be clearly seen that the average thrust produced by the cyclorotor reduces as the bending and torsional stiffness of the blade is decreased. Therefore, the effect of deformations cannot be neglected for the evaluation of the performance of the

171
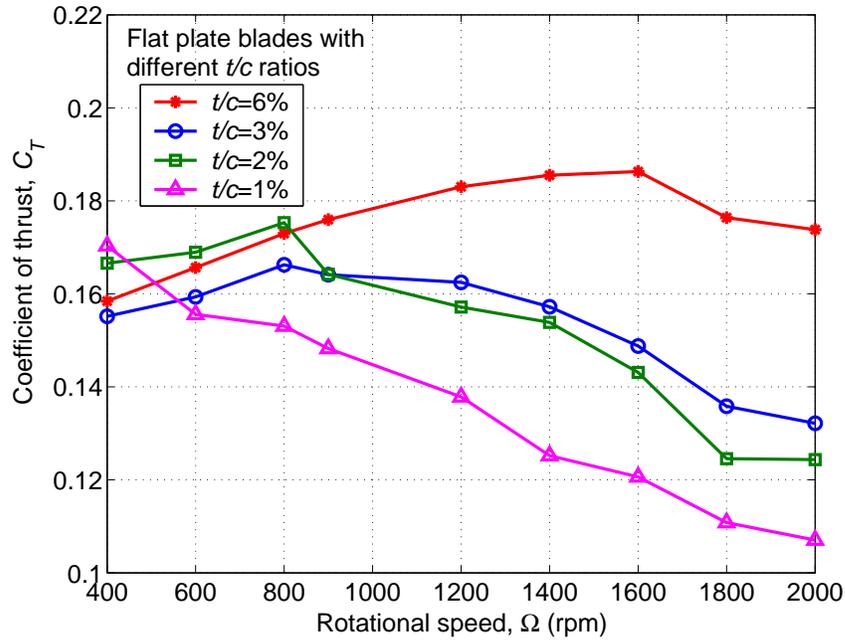
Figure 4.1: **Effect of flexibility on cyclorotor thrust coefficient** (C_T).

cyclorotor. This clearly shows the need of a refined aeroelastic model to predict the performance of the cyclorotor, which is the focus of the current chapter.

The structural modeling of the cyclorotor blade is performed using two parallel approaches, (1) second-order non-linear finite element analysis for a beam undergoing radial bending, tangential bending and twisting motions and, (2) multibody based analysis (using software MBDyn) including the same degrees of freedom, but using a fully-nonlinear geometrically exact beam model suitable for extremely flexible blades that undergo large displacements. Even though for the moderately flexible blades, the finite element model was able to predict the deformations accurately, for the extremely flexible blades, a fully-nonlinear model based analysis is important to predict the deformations correctly.

A blade element based aerodynamic model using an unsteady attached flow

formulation (thin airfoil theory) is used in the present analysis. Unsteady aerodynamics formulation uses indicial aerodynamics based on Wagner function and Duhamel's superposition principle to obtain the circulatory lift and moment for arbitrary variations in angle of attack. The unsteady aerodynamic model is implemented with two different inflow models, single streamtube and a double-multiple streamtube inflow model, which will be explained in the chapter.

The current chapter discusses the aeroelastic model of the rotor in detail. The independent validations of the structural and aerodynamic models are discussed. Towards the end of the chapter the average thrust predictions from the aeroelastic model is validated with experimental measurements discussed in Chapter 2 for both moderately flexible and extremely flexible blades.

4.2   Analysis Methodologies

In the present study, two completely independent aeroelastic models have been developed to predict the performance of the cyclorotor. The first model uses a structural model based on second-order non-linear finite element analysis for a beam undergoing radial bending, tangential bending and torsional degrees of freedom along with an unsteady aerodynamic model and two different inflow models, single streamtube and double-multiple streamtube (D-MS) model. The steady blade periodic response is obtained using a finite element in time approach. However, this model can be only used for moderate blade deformations. Therefore, a second model was developed using a fully non-linear structural model (using MBDyn) and it can
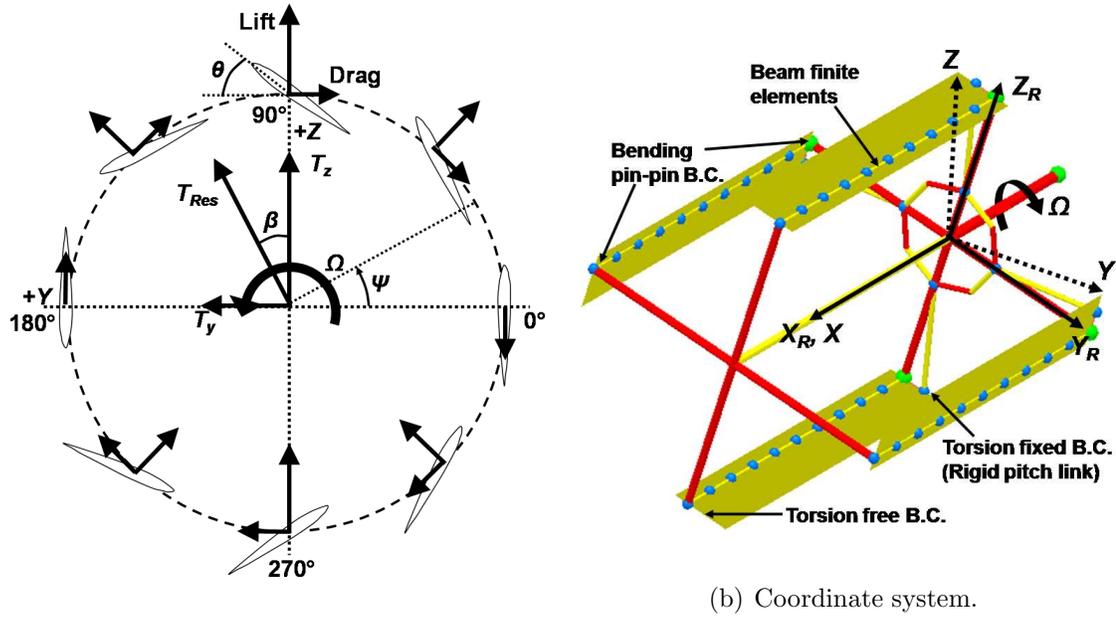
(a) Blade kinematics and forces.

(b) Coordinate system.

Figure 4.2: **Cyclorotor blade kinematics, forces and coordinate system definition.**

handle large deformations. The aerodynamic formulation is same as the previous model except that it uses a state space formulation for the unsteady loads calculation. For the remainder of the paper, the first model will be referred to as the FEM analysis and the second model as MBDyn.

4.3 FEM-Based Aeroelastic Analysis

4.3.1 Rotor structural model

The cyclorotor blades are modeled as non-linear, isotropic Euler-Bernoulli beam undergoing radial bending (flap, w), tangential bending (lag, v) and elastic twist (ϕ) deformations. The blade coordinate system is shown in Fig. 4.2 and the definitions of radial bending, tangential bending and torsional deformations are shown

174

in Fig. 4.3. The coupled flap-lag-torsion equations are based on Ref. [82] and can handle moderate deformations since the model includes geometric non-linearities up to second order. Each blade is modeled using 10 finite elements undergoing radial bending, tangential bending and torsional degrees of freedom. The cyclorotor blades were assumed to have a pin-pin boundary conditions for bending and a fixed-free boundary condition for torsion (Fig. 4.2(b)). Torsion has a fixed boundary condition at the root because the pitching linkages are assumed to be rigid. In the present study, three different blades were analyzed, which included a baseline NACA 0010 blade, 6% thickness-to-chord ratio (t/c) flat plate blade, and 3% t/c flexible flat plate blade. All the blades had uniform chord of 1 inch and span of 6 inches. Detailed structural testing was conducted to obtain the bending and torsional stiffness (EI_y (flapwise), EI_z (chordwise) and GJ (torsion)) of the blades. The structural properties of the different blades are provided in Table 4.1. The equations of motion for the blade are developed using Hamilton's principle [83]. To obtain the steady blade periodic response the governing partial differential equations are first transformed into modal space using rotating coupled natural modes and then solved using finite element method in time [83].

4.3.2 Inertial force formulation

Figures 4.2(b) and 4.3(a) shows the coordinate system and the definition of the inertial forces on a cycloidal rotor. Let the position of an arbitrary point on the

(a) Forces
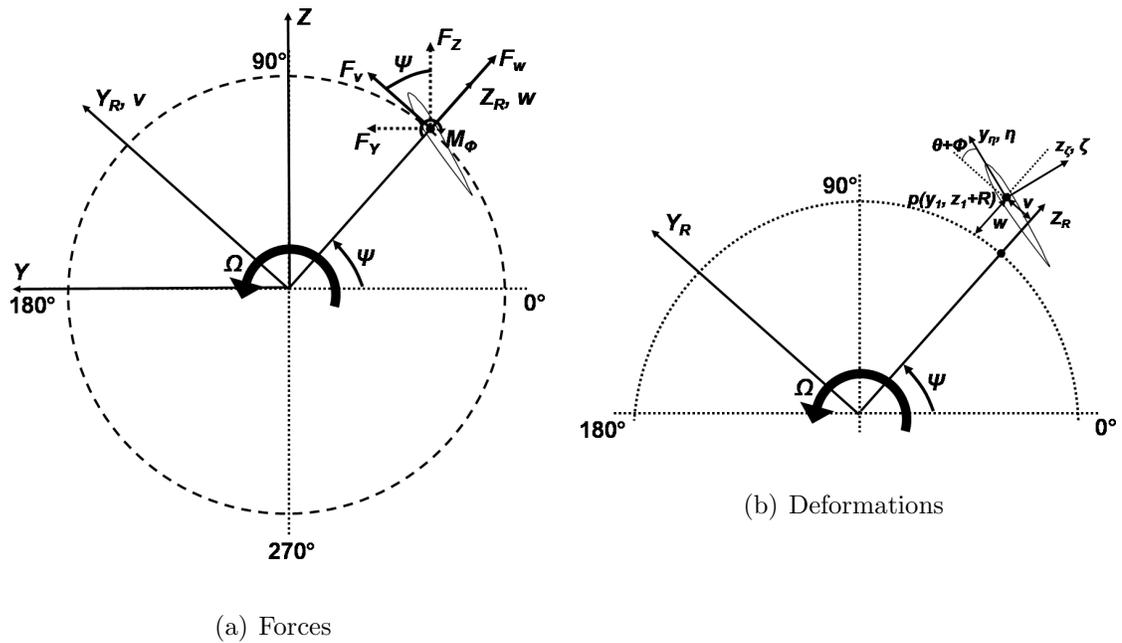
(b) Deformations

Figure 4.3: **Definition of forces and deformations on a cyclorotor.**

Table 4.1: Blade structural properties

Blade	EI_y	EI_z	GJ	m	c.g location from LE
Baseline NACA 0010	0.19	2.9	0.25	0.025	40%c
6% flat plate	0.40	102	0.12	0.061	50%c
3% flat plate	0.026	29	0.01	0.022	50%c

deformed beam be given by the position vector $\bar{r}$ which is given by:

$$\bar{r} = x_1\hat{i} + y_1\hat{j} + (z_1 + R)\hat{k}, \tag{4.1}$$

where $\hat{i}$, $\hat{j}$ and $\hat{k}$ are the unit vectors along along the rotating undeformed coordinate system (X_R, Y_R, Z_R). x_1, y_1 and z_1 can be expressed as

$$x_1 = x - v'(y_1 - v) - w'(z_1 - w),$$

$$y_1 = v + (y_1 - v),$$

$$z_1 = w + (z_1 - w), \tag{4.2}$$

and

$$y_1 - v = \eta\cos\theta_1 - \zeta\sin\theta_1,$$

$$z_1 - w = \eta\sin\theta_1 + \zeta\cos\theta_1, \tag{4.3}$$

$$\theta_1 = \theta + \hat{\phi}. \tag{4.4}$$

Now, the velocity vector, $\bar{V}_b$ is given as:

$$\bar{V}_b = \frac{\partial\bar{r}}{\partial t} + \bar{\Omega} \times \bar{r}, \tag{4.5}$$

where

$$\bar{\Omega} = -\Omega\hat{i}, \tag{4.6}$$

and

$$\frac{\partial\bar{r}}{\partial t} = \dot{x}_1\hat{i} + \dot{y}_1\hat{j} + \dot{z}_1\hat{k}. \tag{4.7}$$

For the present blades $\eta = e_g$ and $\zeta = 0$, where e_g is the chordwise location of the blade c.g. ahead of the elastic axis. For instance, if the blade elastic axis is at

177

1/4-chord and the blade c.g. is at 1/2-chord, then $e_g = -0.25c$.

$$\dot{x}_1 = -(\dot{v}' + w'\dot{\theta}_1)e_g \cos\theta_1 - (\dot{w}' - v'\dot{\theta}_1)e_g \sin\theta_1, \tag{4.8}$$

$$\dot{y}_1 = \dot{v} - e_g \sin\theta_1\dot{\theta}_1, \tag{4.9}$$

$$\dot{z}_1 = \dot{w} + e_g \cos\theta_1\dot{\theta}_1, \tag{4.10}$$

$$\bar{V}_b = V_{bx}\hat{i} + V_{by}\hat{j} + (V_{bz})\hat{k}, \tag{4.11}$$

$$V_{bx} = -(\dot{v}' + w'\dot{\theta}_1)e_g \cos\theta_1 - (\dot{w}' - v'\dot{\theta}_1)e_g \sin\theta_1, \tag{4.12}$$

$$V_{by} = \dot{v} - e_g \sin\theta_1\dot{\theta}_1 + \Omega(w + e_g \sin\theta_1 + R), \tag{4.13}$$

$$V_{bz} = \dot{w} + e_g \cos\theta_1\dot{\theta}_1 - \Omega(v + e_g \cos\theta_1). \tag{4.14}$$

Now the acceleration of the point (x_1, y_1, z_1) on the blade is given by:

$$\bar{a}_b = \frac{\partial^2 \bar{r}}{\partial t^2} + \bar{\Omega} \times (\bar{\Omega} \times \bar{r}) + 2\bar{\Omega} \times \frac{\partial \bar{r}}{\partial t}, \tag{4.15}$$

$$\frac{\partial^2 \bar{r}}{\partial t^2} = \ddot{x}_1\hat{i} + \ddot{y}_1\hat{j} + \ddot{z}_1\hat{k}, \tag{4.16}$$

$$\ddot{x}_1 = -e_g \cos\theta_1(\ddot{v}' + w'\ddot{\theta}_1 + \dot{w}'\dot{\theta}_1) + (\dot{v}' + w'\dot{\theta}_1)e_g \sin\theta_1\dot{\theta}_1$$
$$-e_g \sin\theta_1(\ddot{w}' - v'\ddot{\theta}_1 - \dot{v}'\dot{\theta}_1) - (\dot{w}' - v'\dot{\theta}_1)e_g \cos\theta_1\dot{\theta}_1, \tag{4.17}$$

$$\ddot{y}_1 = \ddot{v} - e_g \sin\theta_1\ddot{\theta}_1 - \dot{\theta}_1^{\,2}e_g \cos\theta_1, \tag{4.18}$$

$$\ddot{z}_1 = \ddot{w} + e_g \cos\theta_1\ddot{\theta}_1 - \dot{\theta}_1^{\,2}e_g \sin\theta_1. \tag{4.19}$$

From eqns 4.15 – 4.19, the inertial forces in the radial (F_w^I), tangential (F_v^I) and torsion (M_ϕ^I) direction are given as:

$$F_w^I = -m[\ddot{w} + e_g \cos\theta_1\ddot{\theta}_1 - \dot{\theta}_1^{\,2}e_g \sin\theta_1 - \Omega^2(w + e_g \sin\theta_1 + R) - 2\Omega(\dot{v} - e_g \sin\theta_1\dot{\theta}_1)], \tag{4.20}$$

178
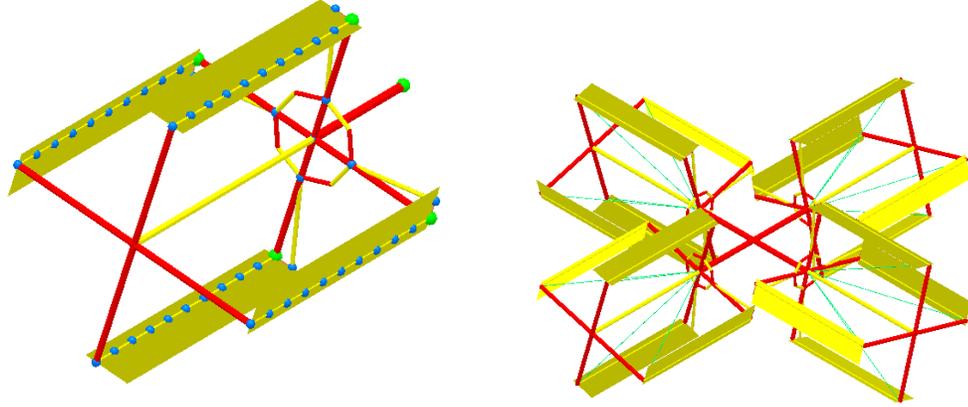
Figure 4.4: Multibody models.

$$F_v^I = -m[\ddot{v} - e_g \sin\theta_1 \ddot{\theta}_1 - \dot{\theta}_1^2 e_g \cos\theta_1 - \Omega^2(v + e_g \cos\theta_1) + 2\Omega(\dot{w} + e_g \cos\theta_1 \dot{\theta}_1)], \quad (4.21)$$

$$M_\phi^I = -me_g[-\ddot{v}\sin\theta_1 + \ddot{w}\cos\theta_1 - 2\Omega(\dot{w}\sin\theta_1 + \dot{v}\cos\theta_1)$$

$$-\Omega^2 \cos\theta_1(w + R) + \Omega^2 \sin\theta_1 v] - I_0\ddot{\theta}_1. \quad (4.22)$$

4.4 Multibody Model

In modeling a non-conventional system, such as the cyclorotor, the multibody approach appears attractive because it provides the opportunity to build hierarchically models of increasing complexity. This attribute has been exploited in this work, where first of all an aeroelastic model of a single blade has been realized and validated, then the same blade has been used to model 2-, 3-, 4-, and 5-bladed rotors. Subsequently, the model complexity was increased through an addition of a kinematically exact model of the blades 1/rev pitching mechanism. Within the multibody formalism, the latter has been added using the elements of the joints library to reproduce the actual joints of the pitching mechanism.

A multibody model of the cyclorotor has been realized using the general-

179

purpose open-source multibody simulation software MBDyn. MBDyn provides the availability of many working elements, together with the possibility to add new elements. In the present work, this possibility has been exploited to add some aerodynamic features fundamental for the cyclorotor modeling, such as the unsteady aerodynamics model based on indicial aerodynamics and the inflow models for this unconventional rotor.

4.4.1 The multibody solver MBDyn

MBDyn is a software intended to model generic multidisciplinary problems, characterized by exact constrained rigid body dynamics, deformable components, simplified aerodynamics, and vehicle controls. It solves Initial Value Problems (IVP) in form of Differential-Algebraic Equations (DAE),using a family of multistep L-stable integration algorithms.

The dynamics of the rigid bodies is written in term of Newton-Euler equations, constrained using Lagrange's multipliers. The equations of motion of all the unconstrained nodes can be summarized as:

$$\mathbf{M}\dot{\mathbf{q}} = \mathbf{p} \tag{4.23}$$

$$\dot{\mathbf{p}} = \mathbf{f}\left(\mathbf{q}, \dot{\mathbf{q}}, \mathbf{p}, t\right),$$

where $\mathbf{q} \in \mathbb{R}^n$ summarizes the n coordinates of the system, $\mathbf{M} \in \mathbb{R}^{n \times n}$ is the mass matrix, $\mathbf{p} \in \mathbb{R}^n$ summarizes the momentum and momenta moments and $\mathbf{f} : \mathbb{R}^{3n+1} \mapsto \mathbb{R}^n$ summarizes the generic forces, possibly depending on the configuration of the system.

When the system is subjected to kinematics constraints, the c constraint equations $\phi(\mathbf{q}, t) : \mathbb{R}^{n+1} \mapsto \mathbb{R}^n$ are added to Eqs. 4.23 using Lagrange's multipliers, resulting in:

$$\mathbf{M}\dot{\mathbf{q}} = \mathbf{p} \qquad (4.24)$$

$$\dot{\mathbf{p}} + \phi_{/\mathbf{q}}^T \boldsymbol{\lambda} = \mathbf{f}(\mathbf{q}, \dot{\mathbf{q}}, \mathbf{p}, t)$$

$$\phi(\mathbf{q}, t) = \mathbf{0}.$$

Eqs. 4.24 express the dynamics of a system constrained by holonomic rheonomic constraints in form of implicit DAE:

$$\mathbf{g}(\dot{\mathbf{y}}, \mathbf{y}, t) = \mathbf{0}, \qquad (4.25)$$

where $\mathbf{y} = \left[\mathbf{q}^T, \mathbf{p}^T, \boldsymbol{\lambda}^T\right]^T$ summarizes all the variables in Eqs. 4.24. The DAE is solved using original multistep integration algorithms described in Ref. [84].

4.4.2 Structural modeling

The cycloidal rotor's blades are modeled using 5 three-nodes beam elements. MB-Dyn implements an original non-linear finite-volume geometrically exact beam formulation, described in Ref. [85]. This beam model can simulate large node displacements that arise when the blade is very flexible and the rotor speed is high.

The blade is constrained in two points: a spherical hinge at the blade root and a spherical hinge free to move along the blade span at the tip. The blade pitch is imposed in two different ways:

1. Ideal kinematics: the desired pitch angle is directly imposed to the blade root,
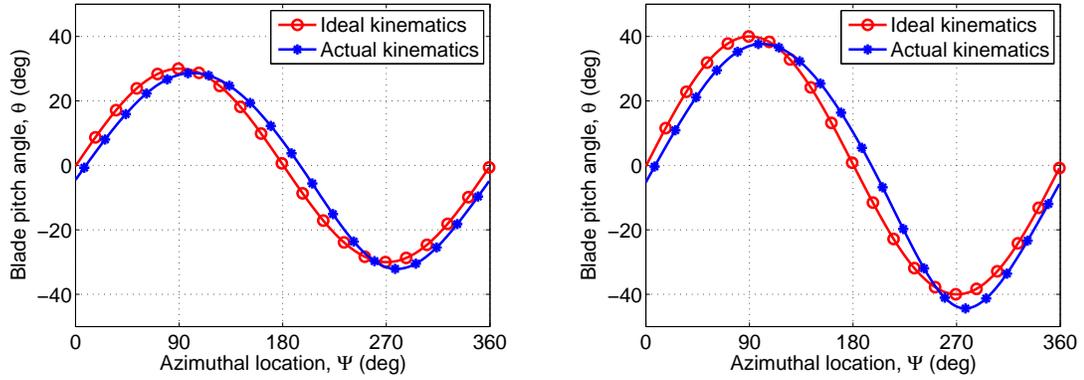
(a) Pitching amplitude=30°.

(b) Pitching amplitude=40°.

Figure 4.5: **Actual versus ideal blade pitch kinematics.**

so it is possible to have an arbitrary relationship between the pitch angle θ and the blade azimuth ψ.

2. Actual kinematics: the actual pitching mechanism is modeled in order to obtain the actual pitch angle. In this case the relationship $\theta = f(\psi)$ is fixed and depends only on the mechanism geometry.

Figure. 4.5 shows the comparison of the ideal harmonic blade pitching kinematics with the actual kinematics obtained using MBDyn for 30° and 40° blade pitching amplitudes. In the FEM analysis, the actual blade kinematics was included using a four-bar based blade kinematics analysis. One key characteristic to note in Fig. 4.5 is the phase delay in the actual kinematics with respect to the ideal kinematics and this may be one reason for the lateral force production.

As explained in the previous section, MBDyn solves initial value problems, so a dynamics simulation with a fictitious initial transient starting from a null rotor speed is performed to obtain the final periodic solution.

4.5 Aerodynamic Modeling

Flowfield studies have clearly shown that the cycloidal rotor blades operate in a complex 3-D aerodynamic environment characterized by unsteady effects resulting from the large amplitude blade pitching at significant reduced frequencies ($k \approx 0.18$). A high fidelity modeling tool such as CFD would be required to capture all these effects with sufficient accuracy. However, in the present study, the goal is to develop a reduced-order model that can predict the blade loads and average rotor performance with sufficient accuracy so that it could be used for routine design calculations. Therefore, a blade element based aerodynamic model using an unsteady attached flow formulation (thin airfoil theory) is used. Unsteady aerodynamics formulation uses indicial aerodynamics based on Wagner function and Duhamel's superposition principle to obtain the circulatory lift and moment for arbitrary variations in angle of attack. It should be noted that the use of Wagner function is an approximation for the present problem since the wake from the trailing edge of the airfoil is not planar.

It is important to justify the use of an attached flow formulation without a stall model when the blades are pitching at high amplitudes. First of all, none of the previous experiments have showed any evidence of blade stall until a pitching amplitude of 40°. One reason for this is the large induced velocities, as measured in the rotor wake using PIV, which clearly shows that the actual aerodynamic angle of attack is much lower than the pitch angle. Another reason could be the fact that the unsteady effects normally delay the stall to higher angle of attacks. Therefore,
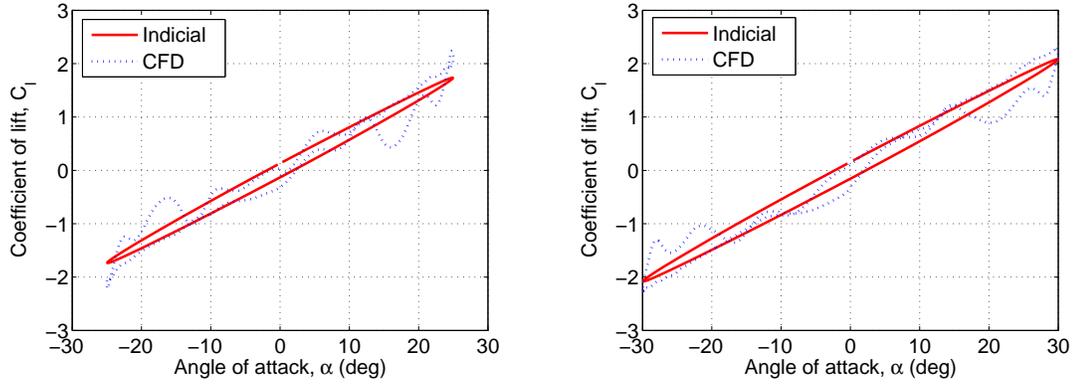
(a) Blade pitching amplitude=25°.   (b) Blade pitching amplitude=30°.

Figure 4.6: **Comparison of lift coefficient (C_l) from attached indicial model with 2-D CFD results for a NACA 0010 airfoil pitching in freestream, Re=25,000, reduced frequency, k=0.18.**

to understand the role of unsteady aerodynamics on the lift produced by an airfoil at these low Reynolds numbers, a 2-D CFD analysis was performed on an airfoil pitching in a uniform freestream. The airfoil was harmonically pitched in a uniform freestream at a reduced frequency of 0.18 and Reynolds number = 25,000. Figure 4.6 show variation of C_l with α for NACA 0010 airfoil predicted using 2-D CFD for pitching amplitudes of 25° and 30°. It was interesting to see that at these low Reynolds numbers, even at such high pitching amplitudes, the dynamic stall was extremely weak and this was mainly because of the continuous shedding of vorticity from the airfoil leading edge (evident from the local dips in C_l curve), instead of vorticity accumulation at the leading edge and shedding as a strong dynamic stall vortex as expected in conventional dynamic stall case at high Reynolds numbers. Because of this reason, as shown in Fig. 4.6, the attached flow indicial aerodynamics formulation with a C_{l_α} of 5.2 is able to predict the average behavior satisfactorily,

(a) Uniform inflow.

(b) Double-Multiple Streamtube (D-MS) in-
flow.
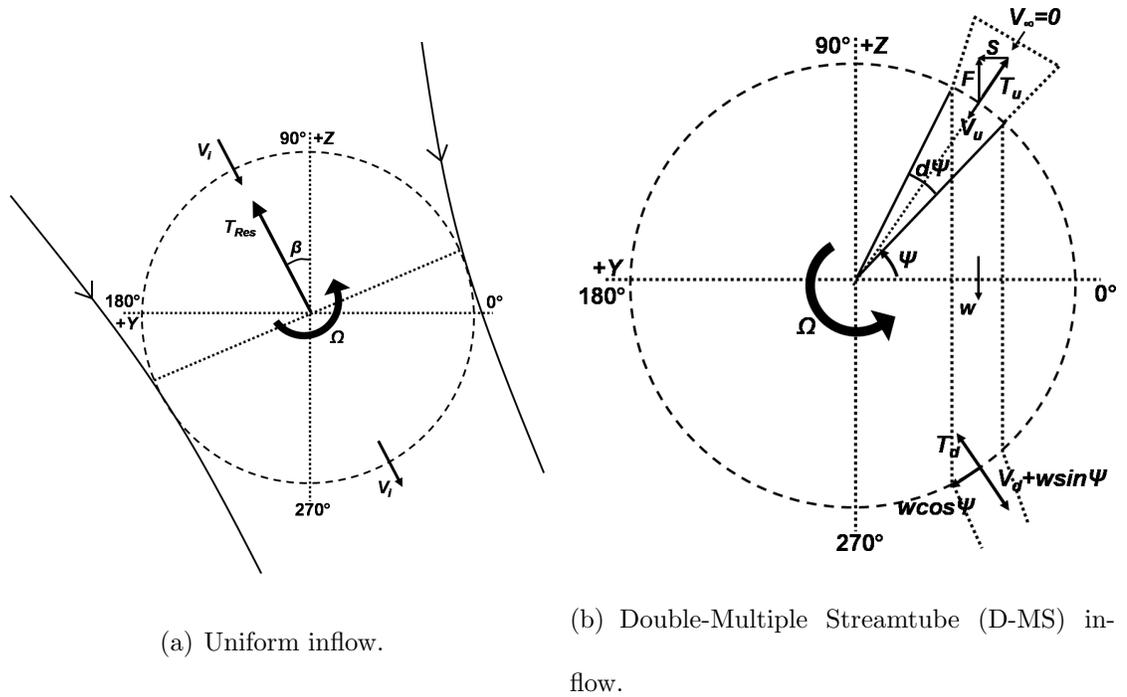
Figure 4.7: **Schematic of the inflow models.**

which might be sufficient to predict the average forces correctly. However, it should
be noted that this is an approximation and a better way of modeling this would be
by using a dynamic stall model such as the Leishman-Beddoes model [71].

4.5.1   Inflow model

An accurate inflow model is the key to predicting the aerodynamic loads on the
cyclorotor. Two different inflow models based on momentum theory are examined in
the present study, (1) a single streamtube model where the entire rotor is immersed
in a single streamtube as shown in Fig. 4.7(a), and (2) a double-multiple streamtube
(D-MS) model developed in Ref. [54], where the rotor is divided into number of
streamtubes and also the influence of the upper half of the rotor on the lower half
is taken into account (Fig. 4.7(b)). The double multiple streamtube model is a

modified version of the flow model used for the analysis of Darrieus vertical axis wind turbines [86]. From the PIV measured flowfield it could be seen that the flow inside the cyclorotor is extremely complicated and neither of these models may be able to represent the flowfield accurately. However, it should be noted that since these momentum theory based models are based on Newton's laws, they may be able to predict the average thrust correctly.

4.5.1.1 Single streamtube inflow model

Even though, based on the PIV measured flowfield, a momentum theory based uniform inflow model might not appear to be suitable for a cyclorotor. For the single streamtube inflow model, the magnitude of the inflow is calculated as

$$v_i = \sqrt{\frac{\kappa T}{2\rho A}} \tag{4.26}$$

The direction of the inflow is updated in each iteration based on the direction of the resultant thrust (β) as shown in Fig. 4.7(a). The correction factor for the inflow, κ was assumed to be 1.15.

4.5.1.2 Double-Multiple Streamtube (D-MS) inflow model

In the multiple streamtube model, the rotor is divided into a number of streamtubes, which intersect the rotor twice with different induced velocity values at the upstream and downstream halves as shown in Fig. 4.7(b). At the two points of intersection of each streamtube with the blade path, the blade swept area ($Rd\psi$) acts as infinitesimally thin actuator surfaces, across which the rotor imparts axial

186

momentum into the flow. In the present formulation, this 2-D inflow model has to be used at each spanwise location of the blade since the angle of attack of the blade and hence the lift produced varies along the span due to elastic blade twist.

In the upstream half, the flow enters the rotor in the radial direction and bends due to the pressure forces ($\bar{S}$) from the adjacent streamtube so that the streamtube becomes vertical. The bending of the streamtube is also important to maintain the symmetry of the flow inside the rotor. It is also assumed that the freestream pressure is attained at some point inside the rotor and the velocity at that point is taken as the wake velocity (w) for the upstream actuator surface. The wake velocity forms the freestream velocity to the downstream actuator surface. Based on the mass, momentum and energy conservation in the streamtube, the wake velocity can be expressed in terms of the upstream induced velocity as:

$$w = \frac{2v_u}{\sin \Psi}, \tag{4.27}$$

where

$$v_u = \sqrt{\frac{dT_u \sin^2 \Psi}{2\rho R d\Psi}} \tag{4.28}$$

For the downstream half of the rotor:

$$dT_d = 2\rho R v_d \sqrt{w^2 + 2wv_d \sin \Psi + v_d^2} d\Psi \tag{4.29}$$

The above equation has to be iteratively solved to obtain the inflow v_d in the downstream half. $dT_{u,d}$ is obtained from the blade element analysis and is given by

$$dT_{u,d} = \bar{F}_w^A \left(\frac{N_b d\Psi}{2\pi} \right) \tag{4.30}$$

187
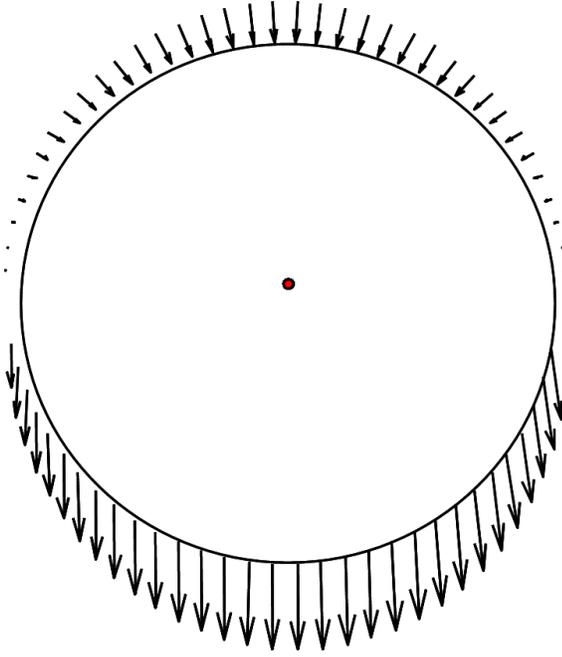
Figure 4.8: **Typical inflow distribution obtained using the double-multiple streamtube model.**

where $\bar{F}_w^A$ is the aerodynamic force in the radial direction which will be derived later in the paper using blade element analysis. Equation 30 is derived based on the assumption that for a cyclorotor with N_b blades, each of these N_b blades spends $(d\Psi/2\pi)$ time in each streamtube. A typical inflow distribution obtained using the double-multiple streamtube model is shown in Fig. 4.8.

4.5.2   Calculation of blade aerodynamic loads

First step in the calculation of the blade aerodynamic forces is the calculation of section angle of attack. The angle of attack of a blade segment is due to two components: the wind velocity and the blade velocity at the 3/4 chord location. The general expression for the resultant velocity at a spanwise station, x, in the
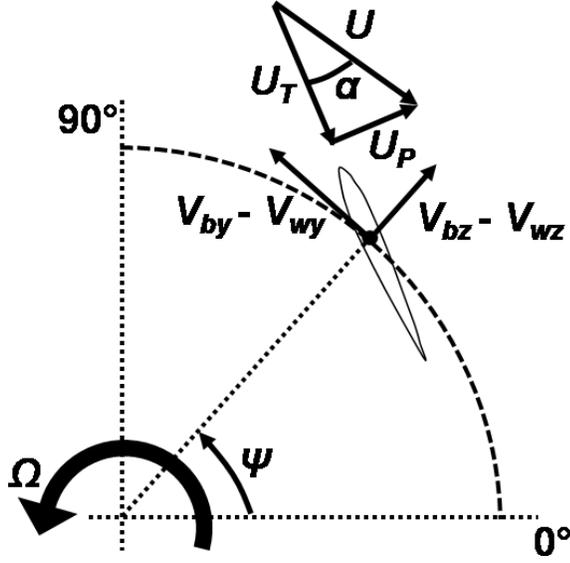
Figure 4.9: **Schematic showing the velocities used in the aerodynamics formulation.**

rotating undeformed frame is given by (Fig. 4.9):

$$\bar{V} = -\bar{V}_w + \bar{V}_b,$$
(4.31)

where $\bar{V}_w$ is the wind velocity contribution from rotor inflow and $\bar{V}_b$ is the blade velocity relative to the hub fixed frame resulting from blade rotation and blade motion:

$$\bar{V}_w = V_{wx}\hat{i} + V_{wy}\hat{j} + V_{wz}\hat{k}.$$
(4.32)

For the uniform inflow model:

$$V_{wx} = 0,$$

$$V_{wy} = -v_i \cos{(\Psi - \beta)},$$

$$V_{wz} = -v_i \sin{(\Psi - \beta)}.$$
(4.33)

For the multiple streamtube inflow model upstream half:

$$V_{wx} = 0,$$

$$V_{wy} = 0,$$

$$V_{wz} = -v_u, \tag{4.34}$$

and for the downstream half:

$$V_{wx} = 0,$$

$$V_{wy} = -w \cos \Psi,$$

$$V_{wz} = w \sin \Psi + v_d. \tag{4.35}$$

The blade velocities V_{bx}, V_{by} and V_{bz} are given in Eqns. 4.12–4.14. However, since the blade velocities are calculated at 3/4-chord, the distance e_g is replaced by η_r, where η_r is the position of the 3/4-chord location ahead of the blade pitching axis. For instance, if the blade is pitching at 1/4-chord, $\eta_r = -0.5c$.

$$V_{bx} = -(\dot{v}' + w'\dot{\theta}_1)\eta_r \cos\theta_1 - (\dot{w}' - v'\dot{\theta}_1)\eta_r \sin\theta_1,$$

$$V_{by} = \dot{v} - \eta_r \sin\theta_1 \dot{\theta}_1 + \Omega(w + \eta_r \sin\theta_1 + R),$$

$$V_{bz} = \dot{w} + \eta_r \cos\theta_1 \dot{\theta}_1 - \Omega(v + \eta_r \cos\theta_1). \tag{4.36}$$

The resultant blade velocity at a spanwise location, x, can be written in the rotating undeformed coordinate system as:

$$\bar{V} = V_x \hat{i} + V_y \hat{j} + V_z \hat{k} = (V_{bx} - V_{wx})\hat{i} + (V_{by} - V_{wy})\hat{j} + (V_{bz} - V_{wz})\hat{k}. \tag{4.37}$$

190

However, the blade section loads are calculated using the resultant velocity and aerodynamic angle of attack in the rotating deformed blade coordinate system:

$$
\begin{bmatrix} U_R \\ U_T \\ U_P \end{bmatrix} = T_{DU} \begin{bmatrix} V_x \\ V_y \\ V_z \end{bmatrix},
\tag{4.38}
$$

where U_R, U_T and U_P are the velocities in the deformed frame (Fig. 4.9) and T_{DU} is the transformation matrix from undeformed to deformed frame:

$$
T_{DU} = \begin{bmatrix} 1 - \frac{v'^2}{2} - \frac{w'^2}{2} & v' & w' \\ -v' \cos\theta_1 - w' \sin\theta_1 & \left(1 - \frac{v'^2}{2}\right)\cos\theta_1 - v'w' \sin\theta_1 & \left(1 - \frac{w'^2}{2}\right)\sin\theta_1 \\ v' \sin\theta_1 - w' \cos\theta_1 & -\left(1 - \frac{v'^2}{2}\right)\sin\theta_1 - v'w' \cos\theta_1 & \left(1 - \frac{w'^2}{2}\right)\cos\theta_1 \end{bmatrix},
\tag{4.39}
$$

$$
\alpha = \tan^{-1}\left(\frac{U_P}{U_T}\right),
\tag{4.40}
$$

$$
U = \sqrt{U_T^2 + U_P^2}.
\tag{4.41}
$$

Wagner function based indicial aerodynamics is used to include the unsteady effects [71, 87]. In this formulation, the angle of attack variation over time is discretized as a series of step inputs. The airload response to each step input is calculated using semi-empirical indicial response functions. The response depends on the pitch and pitch rate of each step input. Once the indicial response is known, the unsteady loads to arbitrary changes in angle of attack can be obtained through the superposition of indicial aerodynamic responses using the Duhamel's integral. The circulatory part of the lift coefficient, C_l^c, in response to an arbitrary variation in angle of attack can now be written in terms of Wagner function ($\phi(s)$) as:

$$
C_l^c(t) = C_{l_\alpha}\left(\alpha(0)\phi(s) + \int_0^s \frac{d\alpha(\sigma)}{ds}\phi(s - \sigma)d\sigma\right),
\tag{4.42}
$$

191

$$s = \frac{2}{c} \int_0^t U dt. \tag{4.43}$$

The approximate expression for Wagner function for incompressible flow is given by:

$$\phi(s) \approx 1 - A_1 e^{-b_1 s} - A_2 e^{-b_2 s}, \tag{4.44}$$

where $A_1 = 0.165$, $A_2 = 0.335$, $b_1 = 0.0455$ and $b_2 = 0.3$. The circulatory component of the lift has contribution from both angle of attack (α) and pitch rate (q). For an incompressible flow, the same Wagner function can be used for both α and q. The Duhamel's integral is solved in a recursive fashion and the effective unsteady angle of attack (α_e) and effective pitch rate (q_e) which has the time history effects because of the shed wake is given as:

$$\alpha_e = \alpha - X_\alpha(s) - Y_\alpha(s), \tag{4.45}$$

$$q_e = q - X_q(s) - Y_q(s), \tag{4.46}$$

where $X_\alpha(s)$, $Y_\alpha(s)$ are the deficiency functions for the angle of attack, α, and $X_q(s)$, $Y_q(s)$ are the deficiency functions for the pitch rate, q, which are obtained numerically using one step recursive formulas given below:

$$X_\alpha(s) = X_\alpha(s - \delta s)e^{-b_1 \Delta s} + A_1 \Delta \alpha_s,$$

$$Y_\alpha(s) = Y_\alpha(s - \delta s)e^{-b_2 \Delta s} + A_2 \Delta \alpha_s. \tag{4.47}$$

$$X_q(s) = X_q(s - \delta s)e^{-b_1 \Delta s} + A_1 \Delta q_s,$$

$$Y_q(s) = Y_q(s - \delta s)e^{-b_2 \Delta s} + A_2 \Delta q_s. \tag{4.48}$$

The sectional lift coefficient includes the contribution from both circulatory and non-circulatory components:

$$C_l = C_l^c + C_l^{nc}, \tag{4.49}$$

The circulatory and non-circulatory components of lift are expressed as:

$$C_l^c = C_{l_\alpha}\alpha_e + \frac{1}{2}C_{l_\alpha}q_e,$$

$$C_l^{nc} = \frac{\pi}{2U}c\dot{\alpha} - \frac{\pi}{4}\left(\frac{c}{U}\right)^2 a\ddot{\alpha}. \tag{4.50}$$

For the present formulation, since the pitching axis is at 1/4-chord, a=-0.5. As explained in previous section, 2-D C_{l_α} obtained from the CFD analysis is 5.2. However, for the present analysis, finite span corrections have been applied to the 2-D C_{l_α} value as shown below (Eqn. 4.51) to obtain the C_{l_α} for the present blades. Twice the aspect ratio is used for the finite span correction to account for the blade attachment and end-plates which partially covers the blade tips.

$$C_{l_{\alpha finite}} = \frac{C_{l_{\alpha 2D}}}{1 + \frac{C_{l_{\alpha 2D}}}{2AR\pi}}. \tag{4.51}$$

Sectional profile drag is given by:

$$C_{d_0} = d_0 + d_1\alpha + d_2\alpha^2. \tag{4.52}$$

Based on the 2-D CFD study, the static C_{d_0} values for a NACA 0010 airfoil at 25,000 Reynolds number could be approximately expressed using $d_0 = 0.0334$, $d_1 = 0$ (symmetric airfoil) and $d_2 = 2.511$. The total drag, C_d, is given as the sum of profile (C_{d_0}) and induced drag (C_{d_i}) components:

$$C_d = C_{d_0} + C_{d_i}, \tag{4.53}$$

where C_{d_i} is given as:

$$C_{d_i} = \frac{C_l^2}{\pi 2ARe}. \tag{4.54}$$

In the present analysis the Oswald's efficiency factor, e is assumed to be 0.85. As, explained before, twice the aspect ratio is used to account for the fact that the blade tips were partially covered. The normal (F_n^A) and chordwise (F_c^A) forces are given as:

$$F_n^A = 0.5\rho U^2 c(C_l \cos \alpha + C_d \sin \alpha), \tag{4.55}$$

$$F_c^A = 0.5\rho U^2 c(C_l \sin \alpha - C_d \cos \alpha), \tag{4.56}$$

In the present formulation, spanwise flow is ignored and therefore the force in the spanwise direction, $F_x^A = 0$. Aerodynamic forces in the undeformed rotating blade coordinate system is given by:

$$\bar{F}^A = F_u^A \hat{i} + F_v^A \hat{j} + F_w^A \hat{k}, \tag{4.57}$$

where

$$\begin{bmatrix} F_u^A \\ F_v^A \\ F_w^A \end{bmatrix} = T_{DU}^T \begin{bmatrix} F_x^A \\ F_c^A \\ F_n^A \end{bmatrix}. \tag{4.58}$$

The aerodynamic forces in the non-rotating inertial frame, F_Z^A and F_Y^A are given by:

$$F_Z^A = F_w^A \sin \Psi + F_v^A \cos \Psi, \tag{4.59}$$

$$F_Y^A = -F_w^A \cos \Psi + F_v^A \sin \Psi. \tag{4.60}$$

194
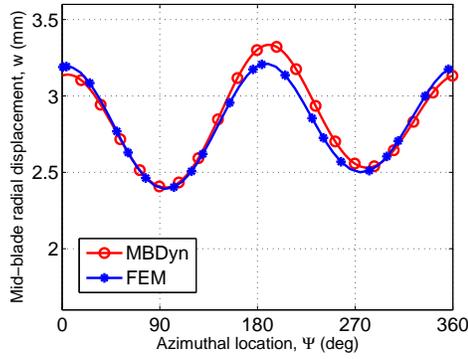
(a) Mid-beam radial bending deformation (w) for NACA 0010 blades at 30° pitching amplitude.
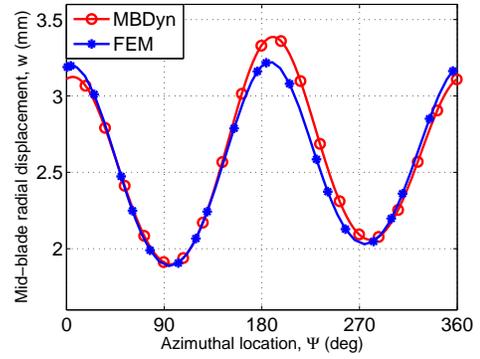
(b) Mid-beam radial bending deformation (w) for NACA 0010 blades at 40° pitching amplitude.
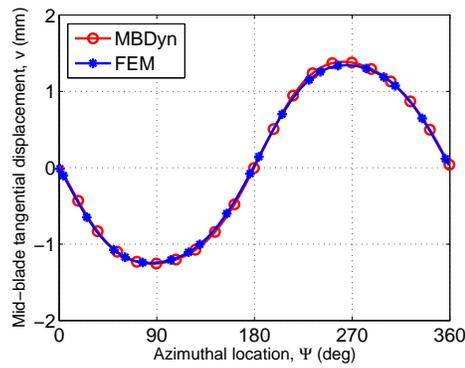
(c) Mid-beam tangential bending deformation (v) for NACA 0010 blades at 30° pitching amplitude.
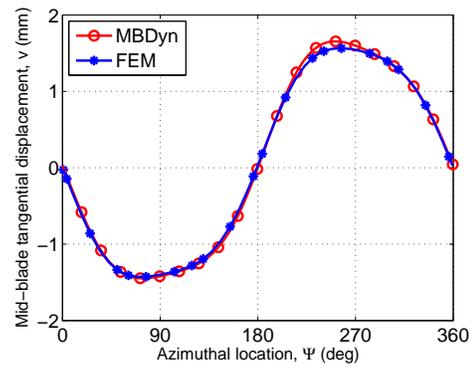
(d) Mid-beam tangential bending deformation (v) for NACA 0010 blades at 40° pitching amplitude.
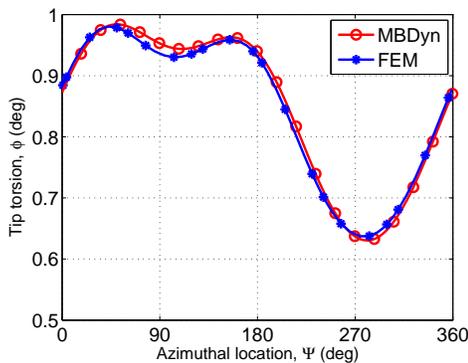
(e) Tip torsional deformation (ϕ) for NACA 0010 blades at 30° pitching amplitude.
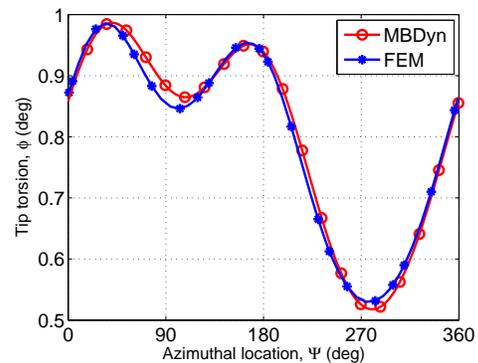
(f) Tip torsional deformation (ϕ) for NACA 0010 blades at 40° pitching amplitude.

Figure 4.10: **Comparison of FEM and MBDyn blade deformations with inertial loads for the baseline NACA 0010 blades at 2000 rpm.**
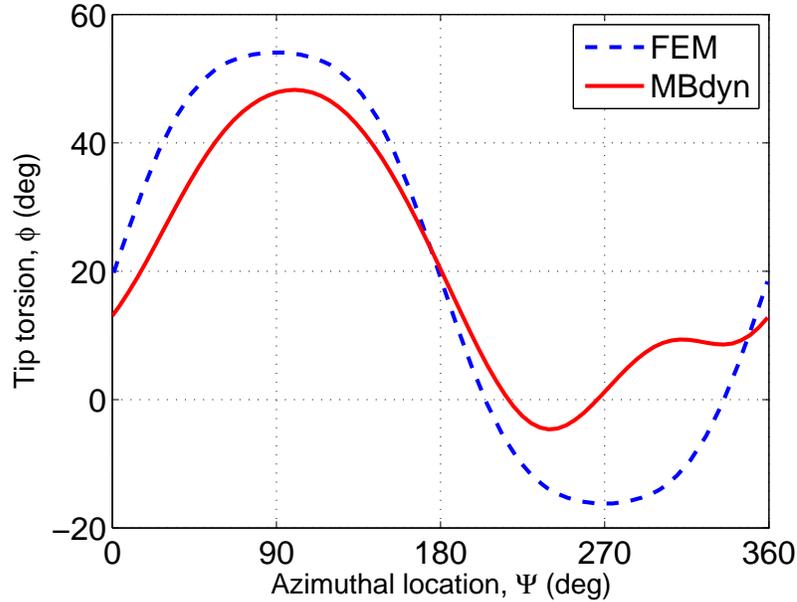
Figure 4.11: **Comparison of FEM and MBDyn blade tip twist with inertial loads for 3% t/c flexible blades at 2000 rpm.**

4.6 Validation of the Structural Model and Inertial Force Formulation in the FEM Analysis

The structural model along with the inertial forces in the FEM analysis have been validated by comparing the deformations predicted by the FEM analysis with the results obtained from MBDyn (multibody model) due to only inertial forces for moderate deformations as shown in Figs 4.10(a) to 4.10(f). The results are obtained for the baseline NACA 0010 blade at a rotational speed of 2000 rpm with harmonic blade pitching. Figures 4.10(a), 4.10(c) and 4.10(e) respectively show results for mid-beam radial bending deformation, tangential bending deformation and tip twist for a pitching amplitude of 30°. In figures 4.10(b), 4.10(d) and 4.10(f), results are shown

for a pitching amplitude of 40°. Overall, there is a good agreement between two sets of results. Figure 4.11 shows the comparison of tip twist for the flexible blades (3% flat plate blade) at a pitching amplitude of 40° and 2000 rpm. As shown in the figure, the tip twist was extremely high (almost 40° in the upper half) and there is a discrepancy between the FEM analysis and MBDyn. Therefore, for such large deformations, the FEM model with second order non-linearity is not able to predict the deformations accurately. This clearly shows the need for a fully nonlinear beam modeling tool such as the one available in MBDyn in order to be able to accurately predict the performance of extremely flexible blades.

4.7 Validation of the Aerodynamic Model

Since only the average forces were measured during the experiments, the force predictions obtained from a 3-D CFD study [69] was used to validate the instantaneous forces from the unsteady aerodynamic model based on the two different inflow models: (1) single streamtube, and (2) double-multiple streamtube (D-MS) model. For validation studies, rigid blades (no deformations) were used in both CFD and the present analysis so that the aerodynamic model can be validated independent of the structural model. Figures 4.12(a) and 4.12(b), respectively, shows the comparison between CFD, single streamtube and multiple streamtube models for the instantaneous vertical (T_z) and lateral aerodynamic forces (T_y) in the inertial frame produced by a single blade on a 2-bladed cyclorotor at a pitching amplitude of 35°. The forces predicted by the multiple streamtube model show better agreement with CFD pre-
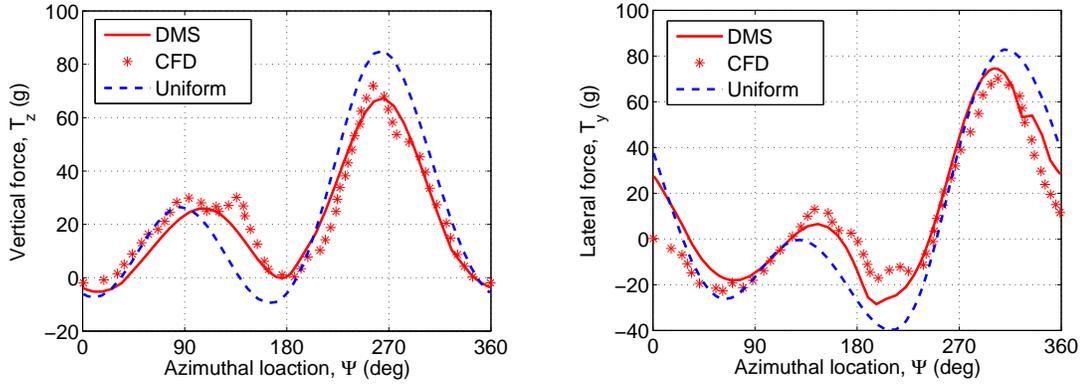
(a) Vertical force, T_z (b) Lateral force, T_y

Figure 4.12: **Comparison of the instantaneous vertical (T_z) and lateral (T_y) aerodynamic forces in the inertial frame due to a single blade with 3-D CFD results at a pitching amplitude of $35°$ for a 2-bladed rotor with rigid blades using uniform inflow and double-multiple streamtube (D-MS) inflow models.**

dicted forces in the case of both vertical (T_z) and lateral forces (T_y). The single streamtube model underpredicts T_z in the upper half of the blade trajectory and overpredicts in the lower half. In the case of lateral force (T_y), the single streamtube model overpredicts the forces in both upper and lower halves of the rotor. The lower accuracy of the single streamtube model when compared to the multiple streamtube model may be due to the fact that the single streamtube model does not include the azimuthal variation of inflow nor the effect of the induced flow from the upper half of the rotor on the lower half.

The other interesting characteristic to note from the time history of the vertical force (Fig. 4.12(a)) is that, even though the blade pitch angle is identical at the top most ($\psi=90°$) and bottom most ($\psi=270°$) points of the blade trajectory, the vertical
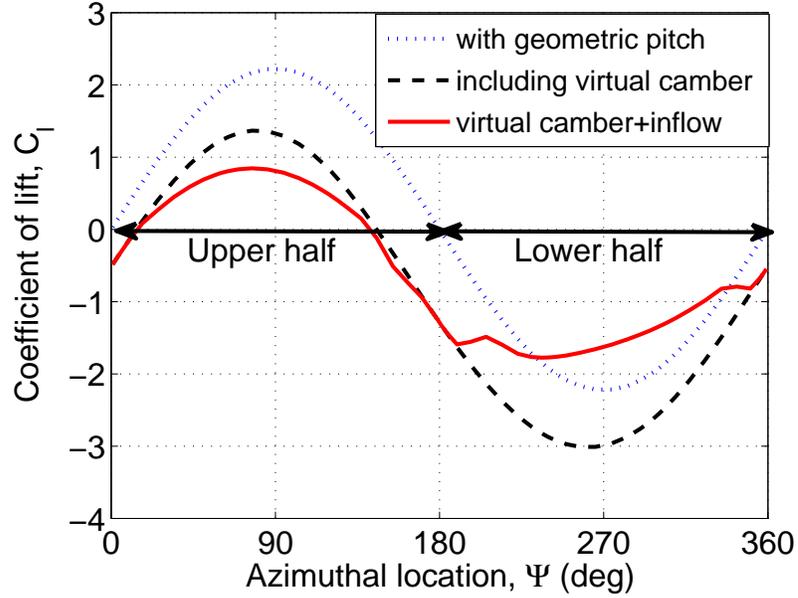
Figure 4.13: **Effect of virtual camber effect and inflow on the blade lift.**

force (T_z) at the top most point is almost half of that at the bottom. Even if there is an effect of the wake from the upper half on the lower half, it should only decrease the angle of attack at the bottom half and thereby decrease the vertical force. However, the opposite is happening because of the virtual camber effect caused due to the flow curvature, which will reduce the effective C_l in the upper half and increase the C_l in the lower half as explained in Chapter 2 [72]. The virtual camber effect will be taken into account if the angle of attack is calculated at 3/4-chord location [74]. Figure 4.13 clearly shows the effect of virtual camber and inflow on the lift variation of the blades. The dotted line in the figure shows the variation of lift coefficient of the blade calculated based on pure geometric pitch angle. Because of the large chord-to-radius ratio (c/R=0.33) of the present cyclorotor, when the virtual camber effect is included, there is a downward shift of the curve (dashed line), increasing
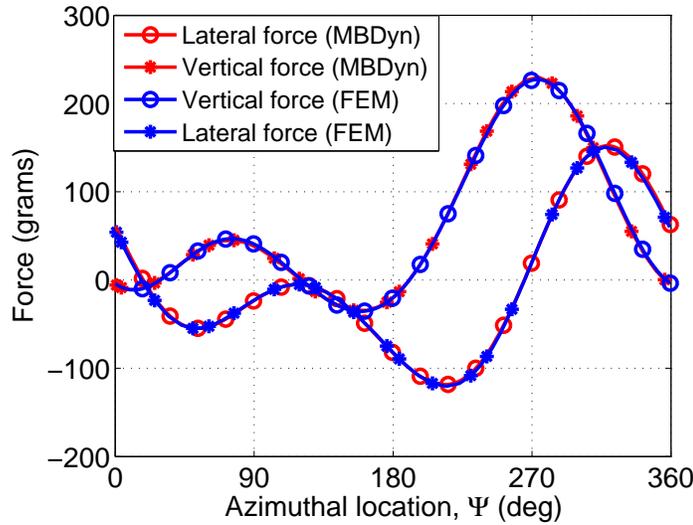
Figure 4.14: **Comparison of the instantaneous vertical (T_z) and lateral (T_y) aerodynamic forces for a 1-bladed rotor operating at 30° pitching amplitude (harmonic pitching) using NACA 0010 blade.**

the magnitude of the lift in the lower half and decreasing the lift in the upper half. Inclusion of the inflow effect (solid line) using the double-multiple streamtube model, tries to reduce the lift in the lower half since it operates in the wake of the upper half. Even then, it can be clearly seen that the magnitude of the lift coefficient is much higher in the lower half compared to the upper half. This is the reason for the higher vertical thrust in the lower half compared to the upper half. From figures 4.10(a) to 4.10(f) it can be seen that even for the relatively stiff, NACA 0010 blades, there was a small difference in bending and torsional deformations between FEM and MBDyn predictions. Now, the next step was to investigate whether these small differences in deformations can cause significant differences in the aerodynamic forces and also to validate the aerodynamic models in the FEM analysis and MBDyn. Figure 4.14

200

clearly shows that even with the small differences in the deformation predictions, the aerodynamic forces match quite well. However, this is not true for the flexible 3% flat plate blades because the deformations predicted by MBDyn and the FEM analyses are significantly different.

4.8   Effect of Aerodynamics on Blade Deformation

Understanding the contribution of aerodynamic forces to the blade deformation is the key in deciding whether a coupled aeroelastic analysis is required to accurately predict the blade aerodynamic loads; or it is acceptable to obtain the deformations based on only inertial loads (primarily centrifugal force) and provide it as prescribed deformations to the aerodynamic model. This understanding is of great significance while performing a CFD-CSD analysis where each iteration is computationally intensive. Figures 4.15(a) to 4.15(f) show the variation of mid-blade radial bending (w), mid-blade tangential bending (v) and tip twist (ϕ) about the azimuth due to inertial loads and combined inertial and aerodynamic loads for the 3% flexible flat plate blade and for NACA 0010 blade at 40° pitching amplitude. These results were calculated using MBDyn with single streamtube inflow aerodynamic model. It can be clearly seen from the figures that for both the blades, even though the deformations were primarily driven by the inertial forces, the addition of aerodynamic forces brought in significant differences especially for radial bending and torsional deformation. However, for the stiffer NACA 0010 blades, since the deformations themselves are significantly small, the effect of these deformations on aerodynamic
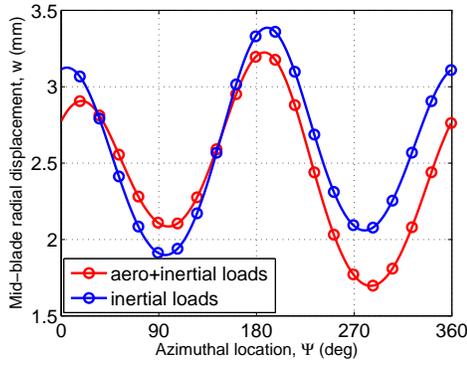
(a) Mid-beam radial bending deformation (w) for NACA 0010 blades.
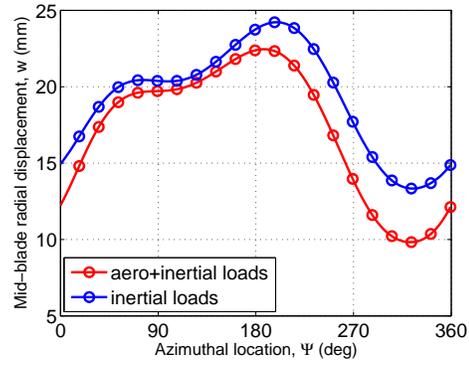
(b) Mid-beam radial bending deformation (w) for 3% blades.
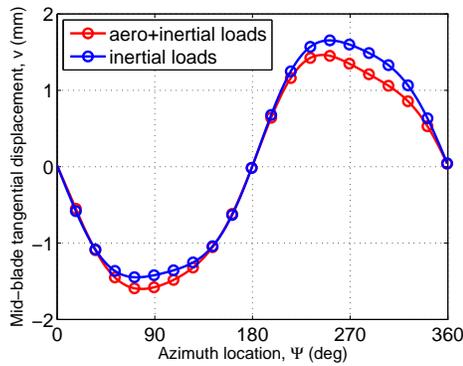
(c) Mid-beam tangential bending deformation (v) for NACA 0010 blades.
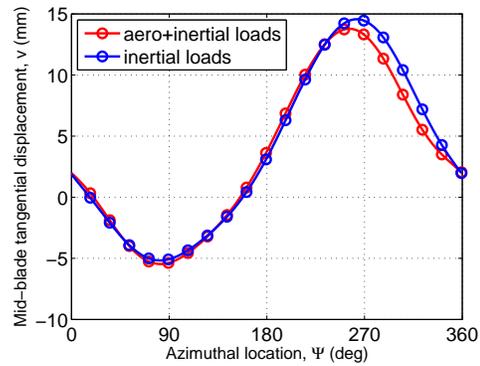
(d) Mid-beam tangential bending deformation (v) for 3% blades.
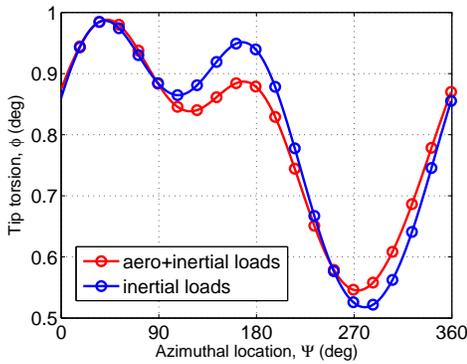
(e) Tip torsional deformation (ϕ) for NACA 0010 blades.
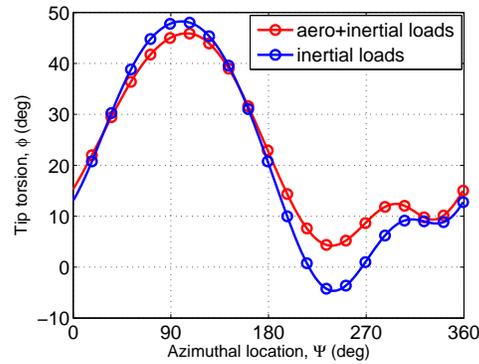
(f) Tip torsional deformation (ϕ) for 3% blades.

Figure 4.15: **Comparison of blade deformations with and without aerodynamic loads for the baseline NACA 0010 blades and 3% flat plate blades at 40° pitching amplitude and 2000 rpm.**

forces are minimal. This clearly demonstrates that a coupled aeroelastic analysis is required in order to be able to predict the blade aerodynamic loads accurately, especially for flexible blades.

4.9 Effect of Unsteady Aerodynamics

Since the blades are operating at a moderately high reduced frequency ($k \approx 0.18$), the unsteady aerodynamic effects can have a significant effect on the blade loads. However, the most significant effect of the unsteady aerodynamics is in creating a phase lag in the development of aerodynamic forces which contributes to the lateral force. Figure 4.16 compares the predicted average vertical and lateral force with quasi-steady and unsteady aerodynamic model for 30° harmonic blade pitching. It can be clearly seen that the unsteady effect produced higher lateral forces compared to the quasi-steady model. Also, the vertical force drops slightly with the inclusion of unsteady aerodynamics.

4.10 Validation of the Aeroelastic Models

The two aeroelastic models: (1) Nonlinear FEM, and (2) MBDyn, were validated using the experimental results discussed in Chapter. 2. The model was validated for 2- and 3-bladed cyclorotors over a range of rotational speeds from 400 rpm to 2000 rpm and pitching amplitudes ranging from 25° to 40°. As discussed before, the blades used in the validation studies included a relatively stiffer baseline NACA 0010 blade and two flat plate blades which had thickness-to-chord ratios of 6% and
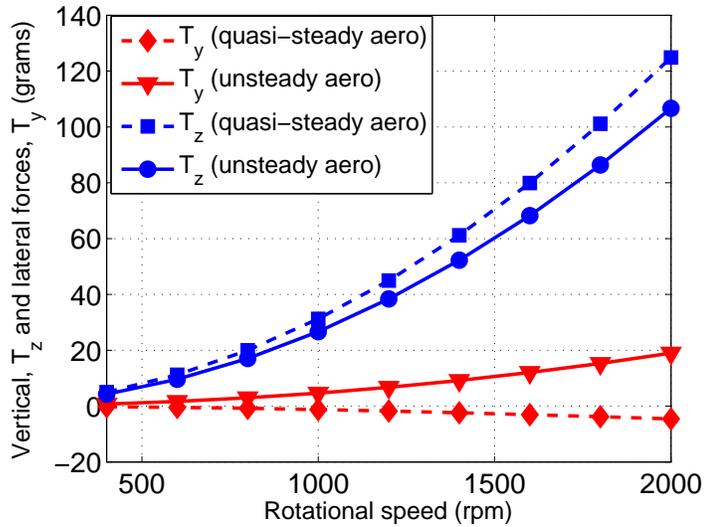
Figure 4.16: **Comparison of the average vertical (T_z) and lateral (T_y) forces with quasi-steady and unsteady aerodynamics for a 3-bladed rotor operating at 30° harmonic pitching.**

3%. All the blades had a chord of 1 inch and span of 6 inches. The validation studies were performed using the actual blade pitching kinematics in the model.

4.10.1 NACA 0010 blades

For the NACA 0010 blades, as shown in Figs. 4.10(a) to 4.10(f), the deformations predicted by both the FEM analysis and MBDyn were in good agreement. Moreover, the elastic deformations were small and therefore it did not have a significant effect on the blade aerodynamic loads. Therefore, it should be noted that, for these blades, the differences between the predicted and measured forces are driven by the inaccuracies in aerodynamic modeling, and not because of the inaccurate prediction of the blade deformations. It was also shown that using the same aerodynamic
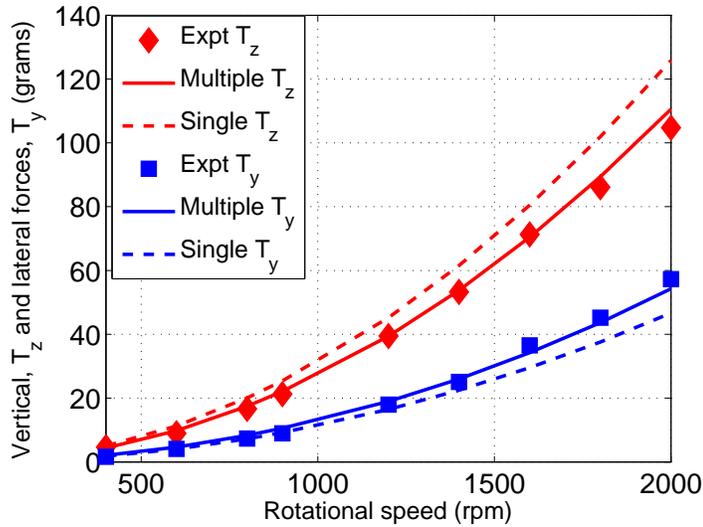
Figure 4.17: **Comparison of the predicted average vertical (T_z) and lateral (T_y) forces obtained using the two different inflow models with experimental data for a 3-bladed rotor using baseline NACA blades at 35° pitching amplitude.**

model, both FEM and MBDyn predicted identical blade loads for the NACA 0010 blades (Fig. 4.14). Therefore, it would be more useful to compare average force predictions from the aeroelastic models based on two different inflow models with the experimentally measured forces.

Figure 4.17 shows the validation of T_z and T_y for a 3-bladed rotor operating at a pithing amplitude of 35° obtained using the two different inflow models. It can be clearly seen that for this particular case, the multiple streamtube model is predicting both the vertical and lateral force accurately. The single streamtube model is over-predicting the vertical force, and underpredicting the lateral force. Figures 4.18(a) and 4.18(b) show the validation of average vertical (T_z) and lateral (T_y) forces for
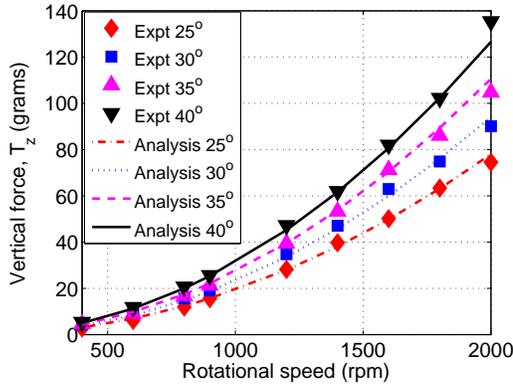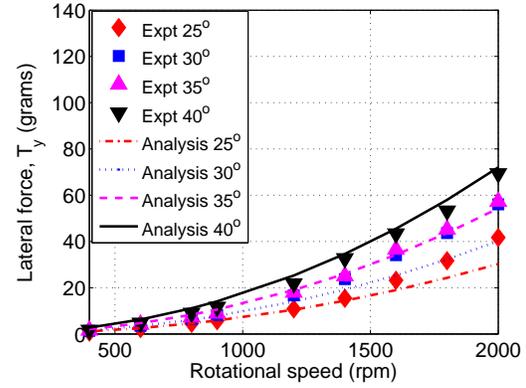
(a) Vertical force, T_z (b) Lateral force, T_y

Figure 4.18: **Comparison of the predicted average vertical force (T_z) and lateral force (T_y) obtained using multiple streamtube model with experimental data for a 3-bladed rotor using baseline NACA blades.**

the 3-bladed cyclorotor at pitching amplitudes of 25°, 30°, 35° and 40° obtained using the multiple streamtube model. From Fig. 4.18(a) it can be clearly seen that the multiple streamtube model is able to predict T_z very accurately for all the pitching amplitudes. The lateral force prediction (Fig. 4.18(b)) also correlated well with the experimental data for 35° and 40° pitching amplitudes; however, it underpredicted for the 25° and 30° cases. Figure 4.19 shows the validation of resultant thrust, T, for a 3-bladed rotor operating at a pithing amplitude of 35° obtained using the two different inflow models. It can be clearly seen that the multiple streamtube model is predicting the resultant thrust accurately, while the single streamtube model is slightly overpredicting the thrust. As explained before, this may be due to the fact that the single streamtube model is not accounting for the effect of the wake from the upper half on the lower half and therefore, the blades operate at a higher angle of attack at the lower half producing more lift. Figure 4.20(a) shows the validation

206
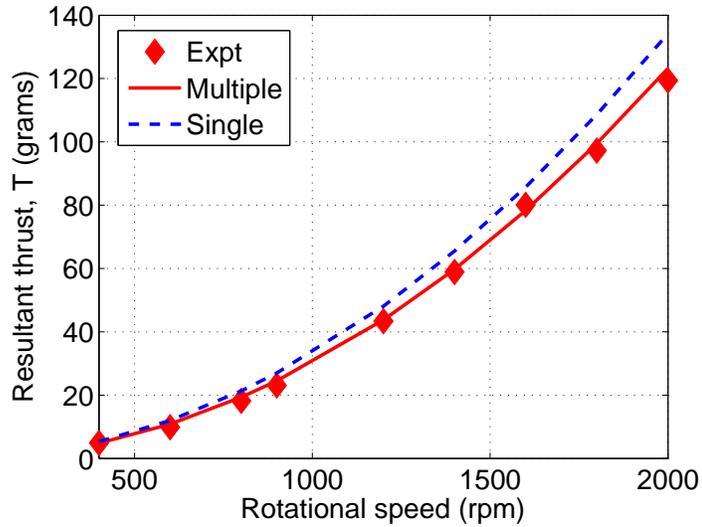
Figure 4.19: **Comparison of the predicted average resultant thrust obtained using the two different inflow models with experimental data for a 3-bladed rotor using baseline NACA blades at 35° pitching amplitude.**

of the average resultant thrust (T) obtained using the multiple streamtube model for a 3-bladed rotor at blade pitching amplitudes of 25°, 30°, 35° and 40°. It can be clearly seen that the predictions obtained using the multiple streamtube model correlates very well with experimental data for all the pitching amplitudes. Figure 4.20(b) shows the validation of the single streamtube predictions for the same case. However, as explained before, there is a slight overprediction of the resultant thrust when the single streamtube model is used. Figures 4.20(c) and 4.20(d) shows the resultant thrust validation for multiple and single streamtube models for a 2-bladed rotor at different blade pitching amplitudes. Again, as in the 3-bladed case, the multiple streamtube model predicted the thrust accurately, whereas, the single streamtube model overpredicted the thrust slightly.
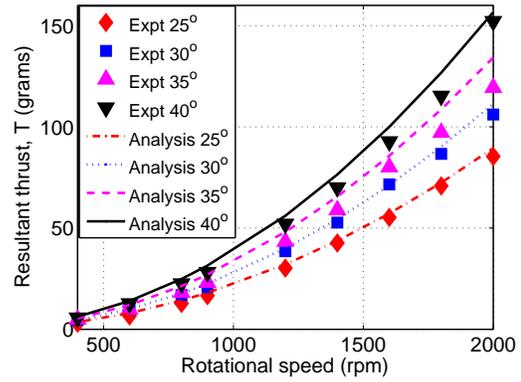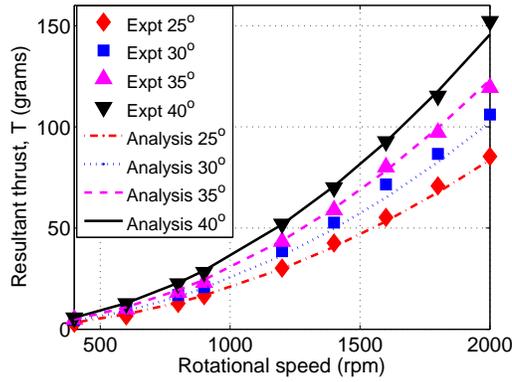
(a) Multiple streamtube model, 3-bladed rotor.   (b) Single streamtube model, 3-bladed rotor.
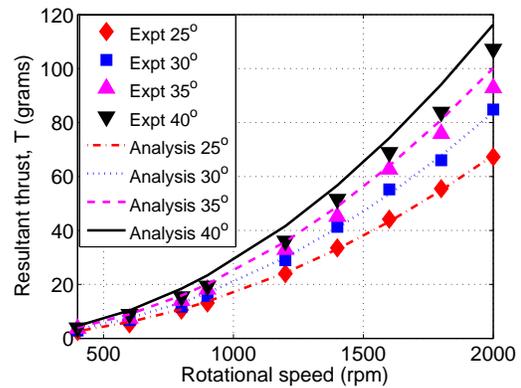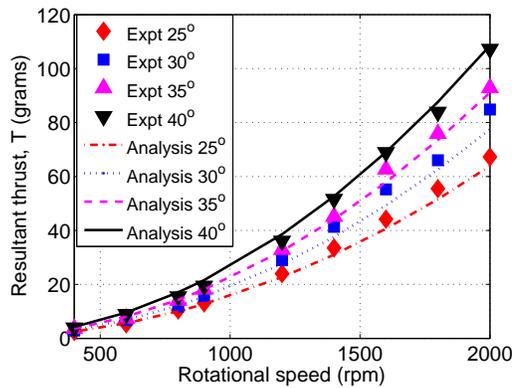
(c) Multiple streamtube model, 2-bladed rotor   (d) Single streamtube model, 2-bladed rotor

Figure 4.20: **Comparison of the predicted average resultant thrust (T) obtained using single and multiple streamtube models with experimental data for 2-bladed and 3-bladed rotors using baseline NACA blades.**

A key conclusion from the above study is that even though both the inflow models predicts the magnitude of the resultant thrust reasonably well, the multiple streamtube model proved to be slightly better than the single streamtube model. However, from a cyclocopter design point of view, predicting both magnitude and the phasing of the resultant thrust (β, Fig. 4.2(a)) is very important. Accurate prediction of the phase would require accurate prediction of both vertical and lateral forces. As shown before, the multiple streamtube model is able to predict the vertical force correctly for all the cases; however the lateral force was underpredicted for lower pitching amplitudes. Using, the single streamtube model the phase predictions were incorrect for most of the cases.

4.10.2   Flexible flat plate blades

As explained before, experimental studies (discussed in Chapter. 2) have clearly shown that the thrust producing capability of the cyclorotor degrades as the blades are made flexible. This aspect is investigated in this section using flexible 3% thickness-to-chord ratio flat plate blade and a relatively stiff 6% thickness-to-chord ratio blades. The structural properties of the blades are given in Table 4.1.

Earlier, it was shown that for the relatively stiff NACA 0010 blade, the resultant thrust was predicted with sufficient accuracy with either of the aerodynamic models. However, since the blades were relatively stiff, it was more of an aerodynamic problem. However, for the flexible blades, it is a highly coupled aeroelastic problem and the accurate prediction of both structural deformations and aerody-

209
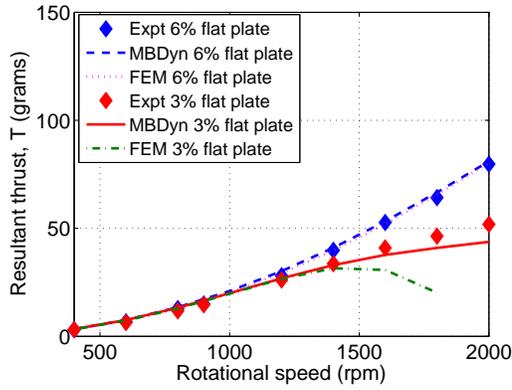
(a) Blade pitching amplitude=25°
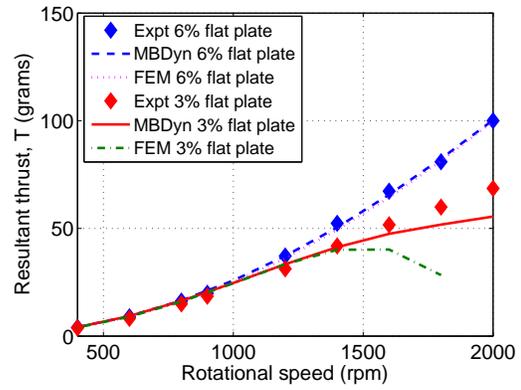
(b) Blade pitching amplitude=30°
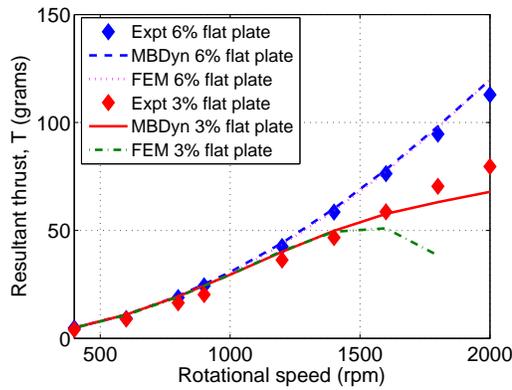
(c) Blade pitching amplitude=35°
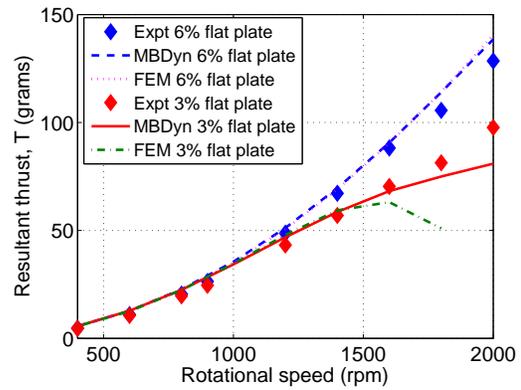
(d) Blade pitching amplitude=40°

Figure 4.21: **Comparison of the predicted average resultant thrust with experimental data for 6% and 3% flat plate blades.**

namic forces (with the effect of deformations) is important for the accurate prediction of the rotor thrust. Both FEM analysis and MBDyn analysis using a single streamtube model was used for the flexible blade validations. Single streamtube model was used because inflow converegence was hard to attain for most of the flexible blade cases using the multiple streamtube model.

Figure 4.21 shows the comparison of the resultant thrust predictions with experimental results for the moderately flexible 6% flat plate blade and the extremely

flexible 3% blade at pitching amplitudes of 25°, 30°, 35° and 40°. It can be concluded that the drop in thrust for the 3% flexible blade seen in the experimental results at higher rotational speeds is predominantly due to the blade deformations because both the 6% and 3% blades produced very similar thrust at lower rotational speeds where the centrifugal forces are small. From the figures, it can be seen that for the relatively stiff 6% flat plate blade, the predictions from the FEM analysis and MBDyn were very similar and they compared well with the experimental data. Where as, for the 3% flat plate blade, as expected, both FEM and MBDyn predictions were very similar at lower rotational speeds (< 1400 rpm), however, at higher speeds, the thrust predicted by FEM was much lower when compared to MBDyn. The reason for this is the overprediction of torsional deformations by the FEM analysis as shown in Fig. 4.11. This clearly shows that the second-order nonlinear model in the present FEM analysis is not adequate for predicting the performance of such flexible blades at higher rotational speeds. When compared to the experimental results, the MBDyn model is able to predict the forces accurately at lower rotational speeds, however, there is a slight underprediction above 1200 rpm. However, the MBDyn predictions are signifcantly better than the FEM predictions and also, MBDyn accurately captures the trend in the variation of thrust for the 3% blade.

Figure 4.22 shows the comparison of vertical and lateral force predictions from MBdyn with experimental results for the 6% and 3% blades. Figure 4.22(a) compares the vertical force prediction with the experimental measurements for a 3-bladed rotor at 30° pitching amplitude. Again, it can be seen that for the 6% blade, the predictions were very accurate. However, for the 3% blade, the model is able
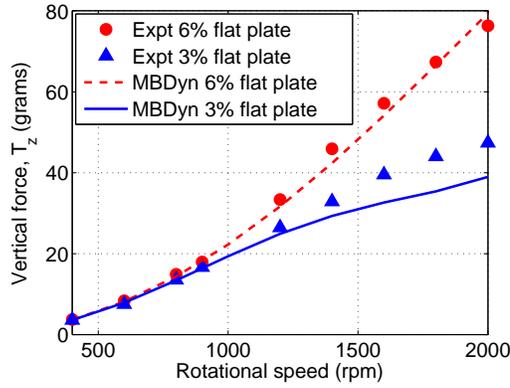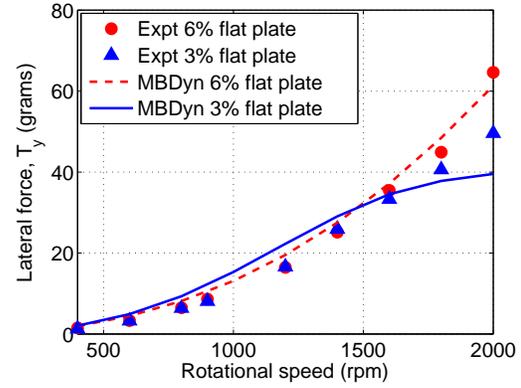
(a) Vertical force, T_z (b) Lateral force, T_y

Figure 4.22: **Comparison of the predicted average vertical (T_z) and lateral (T_y) force with experimental data at a pitching amplitude of $30°$ for a 3-bladed rotor using 6% and 3% flat plate blades.**

to predict the vertical force accurately at lower rotational speeds, however, there is an underprediction at higher rpms. However, the model accurately captures the trend in the variation of vertical force for the 3% blade. Figure 4.22(b) compares the predicted lateral forces with measured values for the same case. Again, it can be clearly seen that the predictions for the 6% blade are good. However, for the flexible 3% blade, even though the predicted values are close to the experimental values, the lateral force is overpredicted at lower rotational speeds, and underpredicted at higher rotational speeds. One reason for the inaccurate prediction of the thrust using MBdyn at higher rotational speeds is the fact that the deformations increase with rotational speed and hence their contribution to the blade aerodynamic loads increases. Therefore the ability to predict deformations accurately and to include their influence in the aerodynamic forces becomes important. The underprediction in thrust may be attributed to the overprediction of deformations at higher speeds
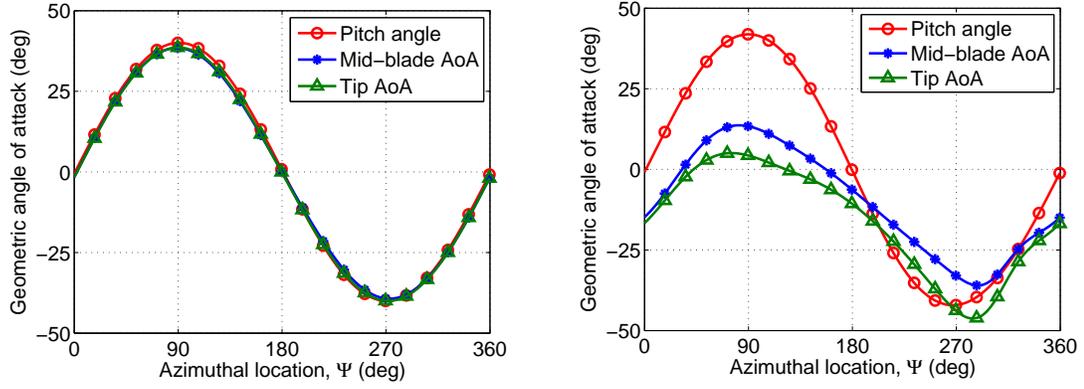
(a) Geometric angle of attack $(\theta + \hat{\phi})$ for the baseline NACA 0010 blade.

(b) Geometric angle of attack $(\theta + \hat{\phi})$ for the 3% flexible flat plate blade.

Figure 4.23: **Variation of Geometric angle of attack $(\theta + \hat{\phi})$ at the tip and mid-span for $40°$ pitching amplitude.**

or the inaccuracies in including the effect of deformations on aerodynamic loads. However, the overall prediction for the flexible 3% blade is quite satisfactory considering the fact that the blades are undergoing large deformations (blades twist up to $40°$ at the tip for 2000 rpm (Fig. 4.11)).

In order to understand the reason for the drop in thrust for flexible blades, it is important to look at the geometric angle of attack $(\theta + \hat{\phi})$ of the blades with the effect of twist included in it. Figures 4.23(a) and 4.23(b) and shows the variation of geometric angle of attack of the blades $(\theta + \hat{\phi})$ at the mid-span and tip for the baseline NACA 0010 blade and also the flexible 3% blades for a pitching amplitude of $40°$ at 2000 rpm. It should be noted that these are geometric angles and therefore do not have the effect of inflow. As shown in Fig. 4.23(a), for the baseline NACA 0010 blades, the twist is significantly small and the geometric angles of attack are not very different from the prescribed pitch angles. However, this is not true for the

flexible 3% thickness-to-chord ratio blades (Fig. 4.23(b)). From Fig. 4.23(b) it can be clearly see that for the flexible 3% blade, the drop in thrust at higher rotational speeds is due to the large nose-down twist in the upper half ($\Psi = 0°-180°$), which significantly decreases the geometric angle of attack. However, there is a small nose-up twist in the lower half ($\Psi = 180°-360°$) especially at the tip, however, this is much smaller than the nose-down twist in the upper half and is not sufficient to compensate for the loss of lift in the upper half and this effectively decreases the net force.

4.11 Concluding Remarks

The objective of the present work was to develop a refined aeroelastic model that can accurately predict the blade loads and average thrust of a MAV-scale cycloidal rotor. The analysis followed two parallel approaches: (1) second-order non-linear beam finite element analysis with moderately large radial bending, tangential bending and torsional deformation and, (2) multibody based analysis, based on MBDyn applicable for large deformations. Both the analyses used unsteady aerodynamics assuming attached flow. Two different inflow models, single streamtube, and double-multiple streamtube (D-MS) were investigated. The analysis was also used to understand the effect of blade flexibility, unsteady aerodynamics and blade kinematics on the cyclorotor performance. The following are specific conclusions drawn from this study:

1. When compared to the experimental measurements, the present analysis was

able to predict the magnitude of the resultant thrust vector with sufficient accuracy over a wide range of rotational speeds, pitching amplitudes, number of blades and even for an extremely flexible blade. However, the direction of the resultant thrust vector was not predicted with the same accuracy in all the cases.

2. The multiple streamtube inflow model predicted the instantaneous forces and average thrust more accurately than the single streamtube inflow model. The single streamtube model slightly overpredicted the resultant thrust for most of the cases.

3. Significantly high virtual camber effect was identified for the present rotor which effectively increased the blade lift in the lower half and decreased the lift in the upper half of the blade trajectory. Including the virtual camber effect in the analysis proved to be crucial in an accurate prediction of the blade loads.

4. The key reasons for the lateral force production was identified to be the mechanical lag in the actual blade kinematics (easily modeled within the multibody approach) and the aerodynamic phase lag brought about by the unsteady aerodynamics. Another parameter that had a significant influence on the magnitude of the lateral force (with minimal influence on the vertical force) is the drag model used for the blades. Without the contribution from the induced drag, the lateral force was always underpredicted when compared with test data.

5. Even though the deformations were dominated primarily by inertial forces, aerodynamic forces also had significant influence on them. This clearly shows the need for a coupled aeroelastic analysis for predicting the blade loads on a cyclorotor with flexible blades.

6. FEM analysis with moderatley large deformation model was unable to predict accurately the deformations and hence blade loads for the 3% thickness-to-chord ratio flexible blades. However, MBDyn was able to predict the thrust accurately for flexible blades at lower rotational speeds ($<$ 1200 rpm) but slightly underpredicted at higher rotational speeds. The underprediction may be attributed to the overprediction of structural deformations. Another reason could be the inaccuracies in the accounting for the effect of deformations in blade aerodynamics forces.

7. The key reason for the lower thrust while using flexible blades was identified to be the reduction in geometric pitch angle due to the large nose down torsional deformation of the blades in the upper half of the circular blade trajectory which is not compensated by the nose-up blade deformation in the bottom half as expected. Also, the study showed that a fully nonlinear large deformation analysis is required to predict the deformations accurately for very flexible blades.

Chapter 5

Cyclocopter Design

5.1 Overview

Till this point the focus has been on understanding and improving the aerodynamics of an isolated cyclorotor through experimental and analytical studies. To this end, chapter. 2 focussed on the systematic experimental studies to understand and hence optimize the performance of the cyclorotor. Chapter 3 discussed the PIV studies performed to understand the key flow phenomena involved. Chapter 4 dealt with the aeroelastic analysis which helped improve the understanding of the cyclorotor thrust production mechanisms and also design better rotors. However, all these studies would only be significant if a flying vehicle could be build using this new concept, especially considering the fact that there are no existing flight capable cyclocopters.

Figure 5.1: **Schroeder cyclogyro built in 1930s [29].**

Attempts to build flight capable cyclocopters (cyclogiros) had started since the early 20th century [29–32, 36, 88]. Almost all these attempts were at full-scales. One of the cyclogyros build in 1930s by Schroeder is shown in Fig. 5.1 [29]. However, as discussed in Chapter 1 and Appendix A, none of these attempts were successful in building a flying vehicle. One of the main reason for this is the fact that the structural design of a cyclorotor is more difficult than that of a conventional rotor because in a cyclorotor there is a large rotating structure which has to be carefully designed to be strong enough to handle the large centrifugal loads and light enough to be used on a flying vehicle. Moreover, unlike a conventional rotor, on a cyclorotor blade, the centrifugal force acts in the transverse direction and therefore the blade design has to be stiff enough to limit transverse bending and torsional deformations. The need for high bending and torsional stiffness resulted in heavy blades due to the lack of high strength-to-weight ratio materials at that time. Now, the weight of the blades increased the rotor structure weight because they had to be strong enough to handle the high centrifugal loads produced by the heavy blades and this resulted in cyclorotors which was considerably heavier than their conventional counterparts. These structural design issues were exacerbated because all the early attempts were made at larger scales. Because of these problems, building a flight capable vehicle using the cyclorotor concept seemed close to impossible at that time.

However, today, with the breakthroughs in material technology, new fabrication techniques and high power-to-weight ratio propulsion systems, it looks feasible to build a flying cyclocopter, atleast at smaller scales. The only hover capable (tethered hover) cyclocopter, other than the one built in the present study was de-
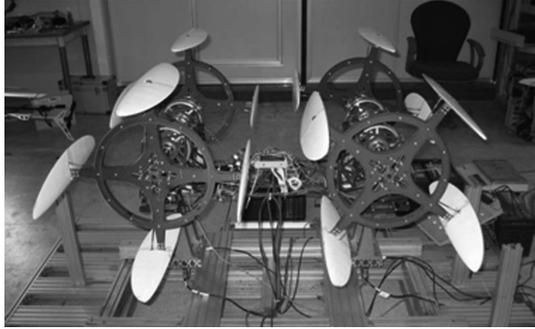
(a) Seoul National University cyclocopter.
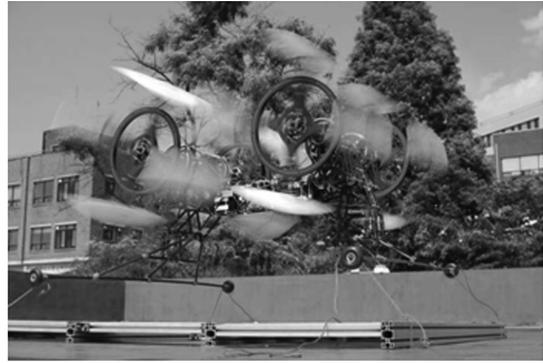
(b) Tethered hover.

Figure 5.2: **Quad-cyclocopter developed in Seoul National University [55].**

veloped in Seoul National University in 2008 [55]. This vehicle was a four-rotor design and weighed 10 Kgs (Fig. 5.2(a)). Even though tethered hover could be acheived (Fig. 5.2(b)), the vehicle was not controllable. Therefore, at this point there is no cyclocopter which can do a stable untethered hover.

In the present work, it was important to demonstrate the hover capability of this concept at a smaller scale and also develop a control strategy that can be used to stabilize and control the cyclocopter in hover. Therefore, building a hover capable cyclocopter was attempted by utilizing the understanding obtained from both experimental and analytical studies discussed in the previous chapters. The first half of this chapter discusses the detailed design process and the issues encountered during the development of the two hover capable cyclocopters, the twin-rotor cyclocopter and the quad-cyclocopter. The second half deals with the development and validation of the control strategy for the quad-cyclocopter.
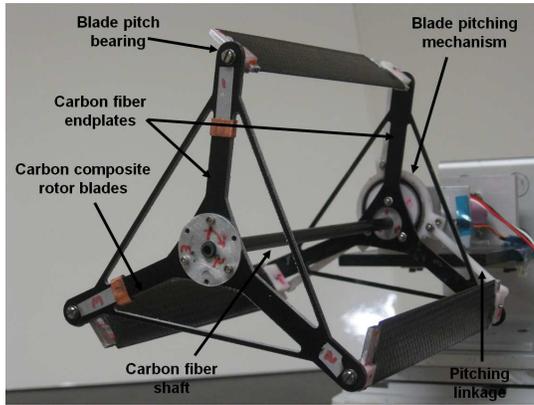
(a) Rotor used on the twin-cyclocopter.

(b) Rotor used on the quad-cyclocopter.

Figure 5.3: **Cyclocopter rotors.**

5.2 Cyclorotor Design

The main challenge in the cyclocopter design was to design the cyclorotor with the lowest possible weight and mechanical complexity. Figure 5.3(a) shows the cyclorotor system which was used on the twin-cyclocopter. The rotor used three blades with a span and radius of 0.152 meters (0.5 ft) and a chord of 0.0254 meter (0.0833 ft). However, the rotor used on the quad-cyclocopter (Fig. 5.3(b)) had a 4-bladed design with a blade span of 0.159 meters (0.52 ft) and a chord of 0.033 meter (0.1083 ft). Both the rotors used NACA 0010 blades. The rotor blades used on the twin- and quad-cyclocopters are shown in Fig. 5.4. The reason for two different rotor designs being used on two cyclocopters had to do with the optimum rotor that was present during the time frame when each of these vehicles were built. This happened because both these vehicles were built before the experimental parametric studies were completed.
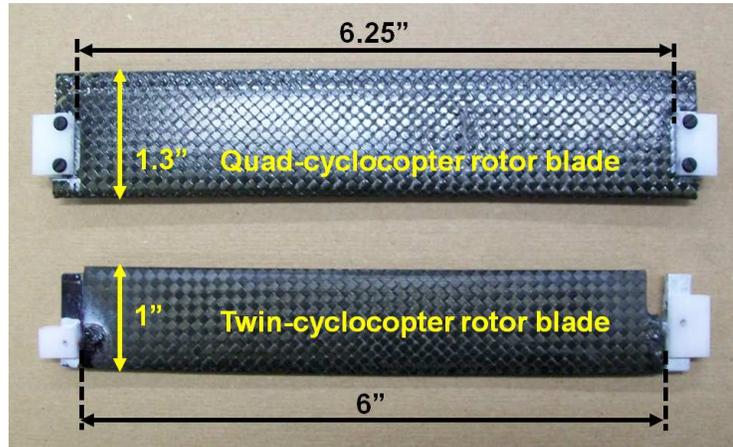
Figure 5.4: **Twin- and Quad-cyclocopter rotor blades.**

5.2.1 Blade Design and Fabrication

Structural design of the blades is the key to an efficient cyclorotor. It was shown in chapter. 2 that the flexibility of the blades significantly degrades the performance of a cyclorotor. Experimental studies also ruled-out flat-plate blades because thin flat plates (2–3 layers of carbon prepreg) made with carbon composite laminates were extremely flexible, even though they were easy to fabricate compared to a blade with conventional airfoil cross-section. Thicker flat plate blades (6–7 layers of carbon prepreg) proved to be stiff, however turned out to be three times as heavy as a conventional airfoil blade. The goal was to make blades which are light and also structurally stiff enough to withstand the high centrifugal forces. Therefore, the blades were fabricated using a single layer $\pm 45°$ carbon composite prepreg wrapped around a foam core. Foam core helped maintain the required airfoil shape for the blades and also increased the separation between the upper and lower carbon layers and thereby increased the bending stiffness. The closed cross-section and $\pm 45°$ fiber
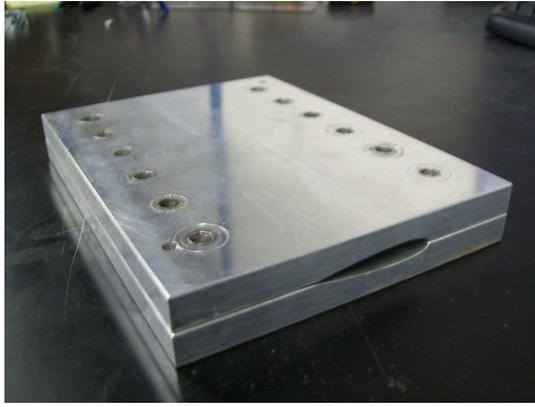
(a) Blade mold.
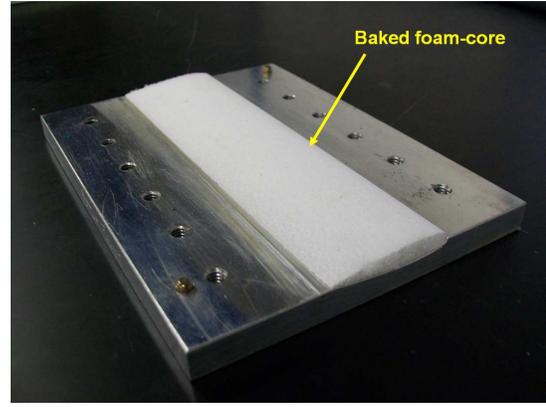
(b) Baked foam core inside the mold.
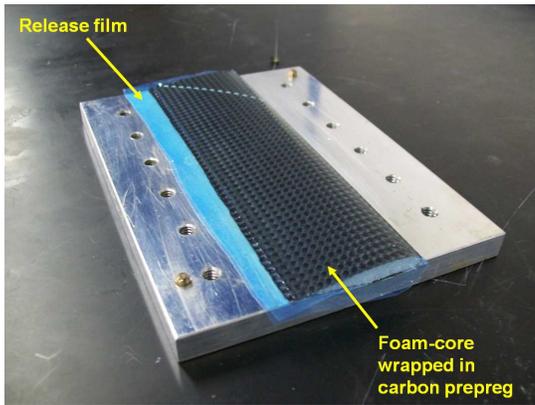
(c) Prepreg wrapped around foam core

(d) Final finished blade

Figure 5.5: **Steps involved in the carbon composite blade fabrication process.**

orientation increased the torsional stiffness. A symmetric NACA 0010 airfoil was used for the baseline blades because the airfoil sections must operate efficiently at both positive and negative angles of attack on a cyclorotor. The airfoil profile had to be chosen such that the blade is thick enough to resist the centrifugal loads.

Different steps involved in the blade fabrication are shown in Fig. 5.5. To fabricate different blades discussed in Chapter 2, six different blade mold sets were fabricated out of aluminum. One of the blade molds is shown in Fig. 5.5(a). The first

(a) Aluminum root insert.
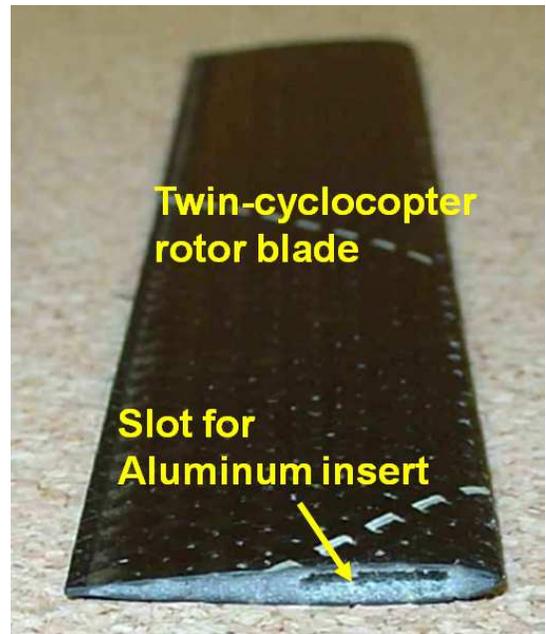
(b) Blade design.

Figure 5.6: **Twin-cyclocopter blade design.**

step involves cutting a rectangular foam piece to the right dimensions and sanding it into an approximate airfoil shape to fit the mold. The foam piece has to slightly bigger than the mold so that it will be compressed to the right shape when the mold is closed. The foam is then baked in the mold at 350°F for a duration of 75 minutes. After this process, the foam core takes the shape of the blade mold which was then filed to correct blade dimensions (Fig. 5.5(b)). Pre-impregnated carbon fiber and the releasing tape was then wrapped around the foam core and inserted in the mold (Fig. 5.5(c)), which is cured for 75 minutes at 250°F and then for 135 minutes at 350°F. The blade is then removed and sanded to the correct dimensions. Figure 5.5(d) shows a finished blade.

Although somewhat labor-intensive, this design provides a light-weight blade capable of resisting the considerable transverse centrifugal forces inherent to the

223
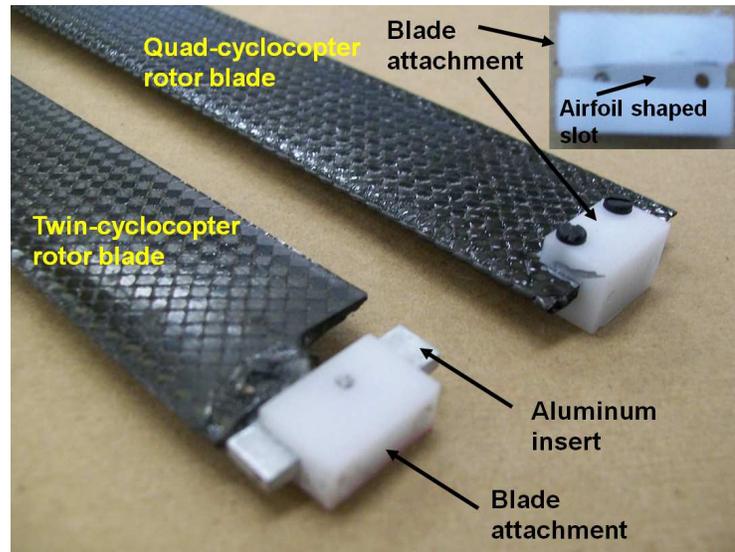
Figure 5.7: **Blade attachments on twin- and quad-cyclocopter rotor blades.**

cyclorotor. For the first generation blades (1" chord, twin-cyclocopter blade), an aluminum extension was inserted into each end of the blade (Fig. 5.6) which fits in a blade attachment at each end of the blade as shown in Fig. 5.7. This allowed the blades to easily be removed from the rotor. However, the aluminum inserts were slightly heavy and increased the centrifugal forces transferred to the rest of the rotor structure. Therefore, the blades used on the quad-cyclocopter did not use these aluminum inserts and used sightly different blade attachments as shown in Fig. 5.7. The blade attachment was made such that the blade tips fit perfectly in the airfoil shaped slot which is further secured by screws passing through the blade. The new design decreased the blade weight and also proved to be a more secure way of holding the blades at higher rotational speeds.

As shown in Fig. 5.3(a), other than the blades, the main structural elements of the cyclorotor design consisted of two carbon fiber end-plates to which each of the

blades were attached. The blades were pitched about two pitch bearings on the root and tip end-plates, respectively. The end-plates were also connected to each other by a hollow carbon fiber shaft, which rotated about two bearings at the root end. Previous tests on a prototype cyclorotor system [63] had shown that its mechanical power losses constituted almost 75% of the total power consumption. Therefore, extreme care was taken while building the new cyclorotor to reduce sources of friction and mechanical interference.

The first generation cyclorotor (3-bladed rotor used on twin-cyclocopter) as fabricated had a mass of only 78 grams (0.172 lbs), and was carefully balanced to minimize vibrations. The structural design went through several iterations to reach the stage where the cyclorotor could successfully operate at a speed of up to 2,000 rpm without any mechanical concerns. At 2,000 rpm and a 40° pitching amplitude, the cyclorotor was shown to produce 150 grams of thrust, which was enough for the twin-rotor cyclocopter to hover when using two such rotor systems. However, the current generation cyclorotor (4-bladed design used on quad-cyclocopter) weighed 95 grams and produced 195 grams of thrust at 1800 rpm and 40° pitching amplitude.

5.2.2 Blade Pitching Mechanism

For the cyclorotor concept to be used on a flying vehicle, it is important to design a simplified, light-weight blade pitching mechanism. The mechanism devised for achieving the required cyclic blade pitch was entirely passive. Therefore, the only power penalty incurred in its operation was the frictional losses associated with
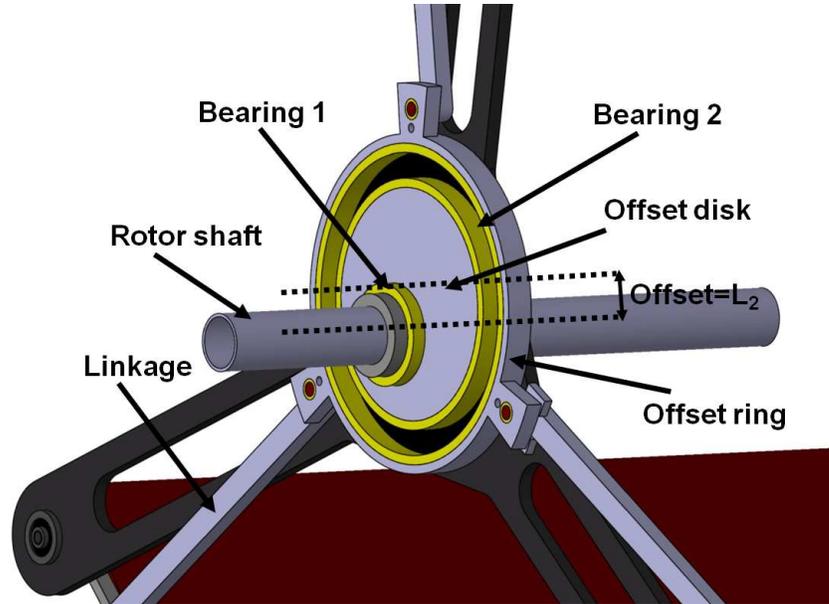
Figure 5.8: **Passive blade pithching mechanism.**
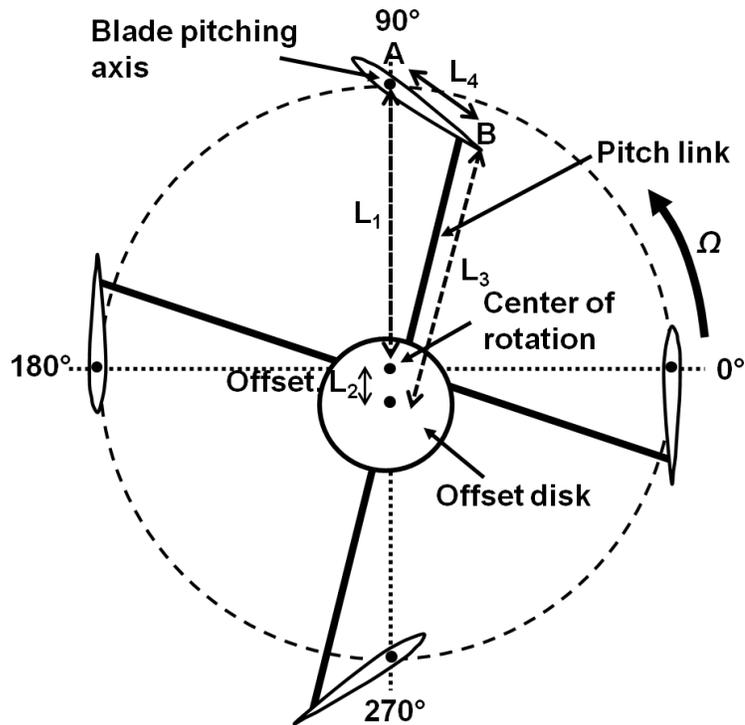
Figure 5.9: **Schematic showing the blade pitching mechanism.**

(a) High pitching amplitude.

(b) Low pitching amplitude.
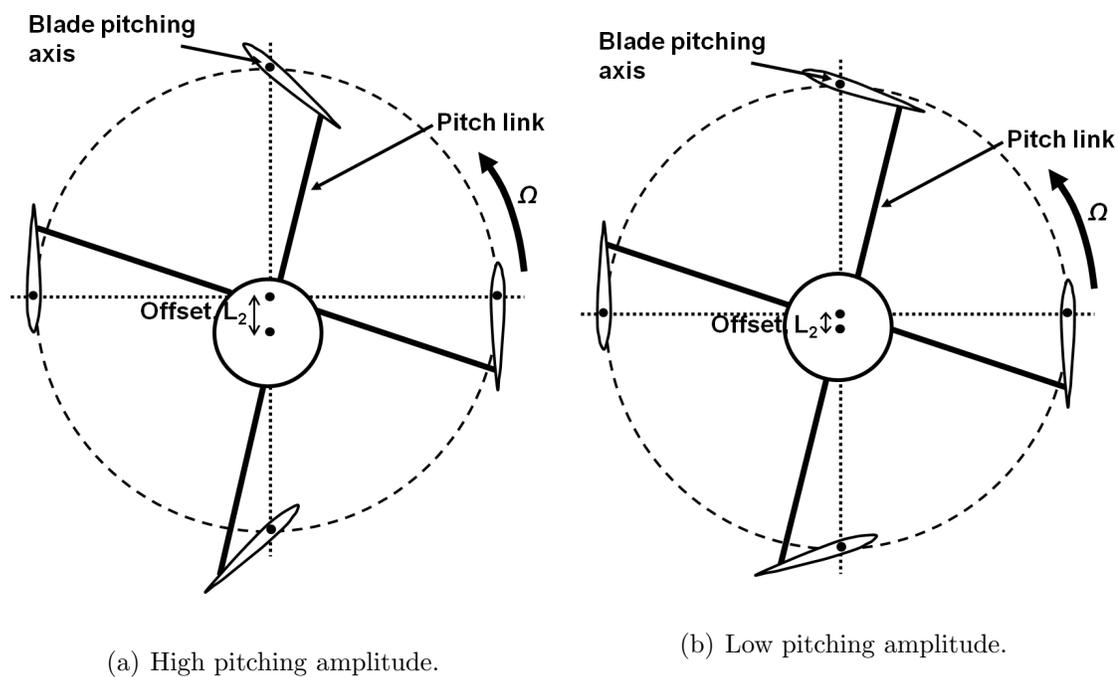
Figure 5.10: **Varying the blade pitching amplitude.**

the moving components. The blade pitching mechanism consisted mainly of two bearings, as shown in Fig 5.8. These bearings were installed such that there was an offset, L_2, between their axes (Figs. 5.8 and 5.9). The pitch linkages were connected to the offset ring, which was installed around bearing number 2. The other end of each linkage was connected to the blade at point (B) aft of the blade-pitching axis (A) (see Fig. 5.9). The resulting system comprised a crank-rocker type four-bar mechanism, which could accomplish the required cyclic change in blade pitch. Notice that the blades could be set to different pitching amplitudes by changing the offset length, L_2. This magnitude of the offset changed the blade pitching amplitude and thereby the magnitude of the thrust produced by the cyclorotor (Fig. 5.10). The direction of the thrust vector could be changed by varying the offset direction (i.e., the rotation of the offset disk as shown in Fig. 5.11). The azimuthal variation of the

227

(a) Vertical thrust.

(b) Anticlockwise thrust vectoring.
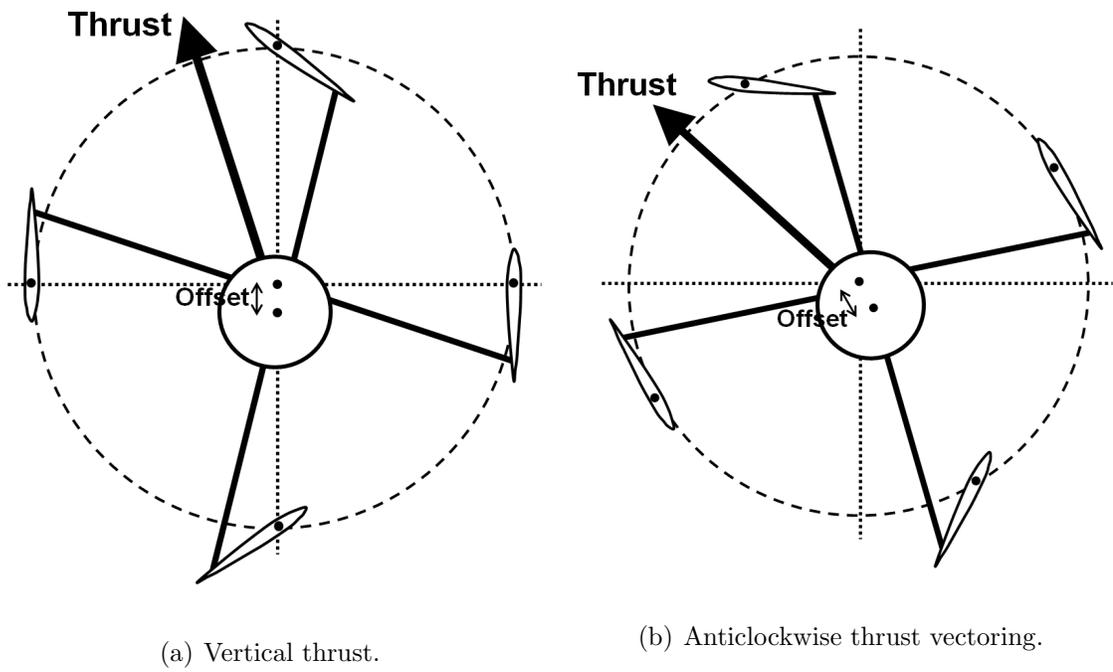
Figure 5.11: **Varying the phasing of blade pitch (thrust vectoring).**
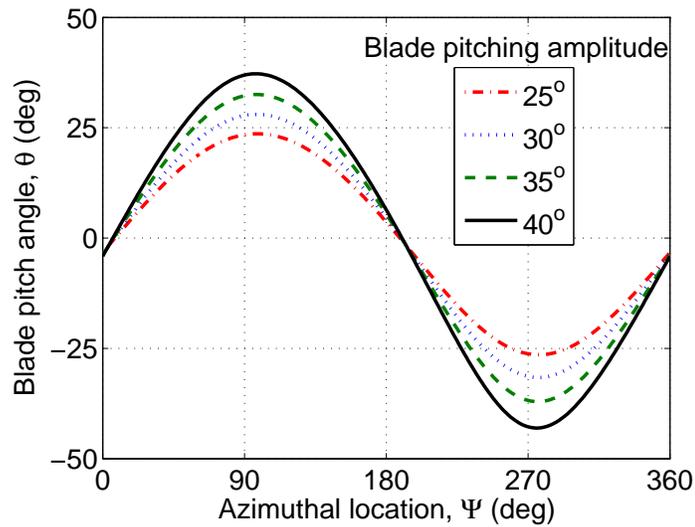
Figure 5.12: **Variation of blade pitch angle along the azimuth.**

blade pitch angle (i.e., the geometric angle of attack) that was obtained by using the four-bar analysis for different pitching amplitudes is shown in Fig. 5.12.

5.3 Twin-Rotor Cyclocopter

After the first set of experimental parametric studies was performed, a twin-rotor cyclocopter was designed and built (Fig. 5.13) to prove the flighworthiness of the concept. Therefore, the rotors used on the twin-cyclocopter was the best configuration at that point and not the final optimized design. As seen in the figure, the vehicle has two contra-rotating 3-bladed cyclorotors which operate at pitching amplitude of 40°. The overall dimensions of the vehicle are 15" X 6" X 6" and weighs 280 grams. Each rotor has a span and diameter of 6 inches with a blade chord of 1 inch. The rotors were spun in opposite directions using separate outrunner motors (rated for 75 watts) allowing independent control of rotor speeds. The transmission comprised of a set of bevel gears with a gear ratio of 5:1 allowing the motors to operate at 10,000 rpm, which is close to their peak efficiency rpm. At the operating rotational speed of 2000 rpm, both the rotors produced a total thrust of 300 grams. The rotors are powered from the ground and the vehicle is installed on a low-friction vertical slider. If the thrust produced by the rotors is more than the weight of the vehicle, it can lift off, with all the other degrees of freedom constrained. Figure 5.14 shows the vehicle hovering on the slider. However, the control techniques for a twin-rotor cyclocopter are extremely challenging and this led to the development of a quad-rotor cyclocopter which will be discussed in the subsequent
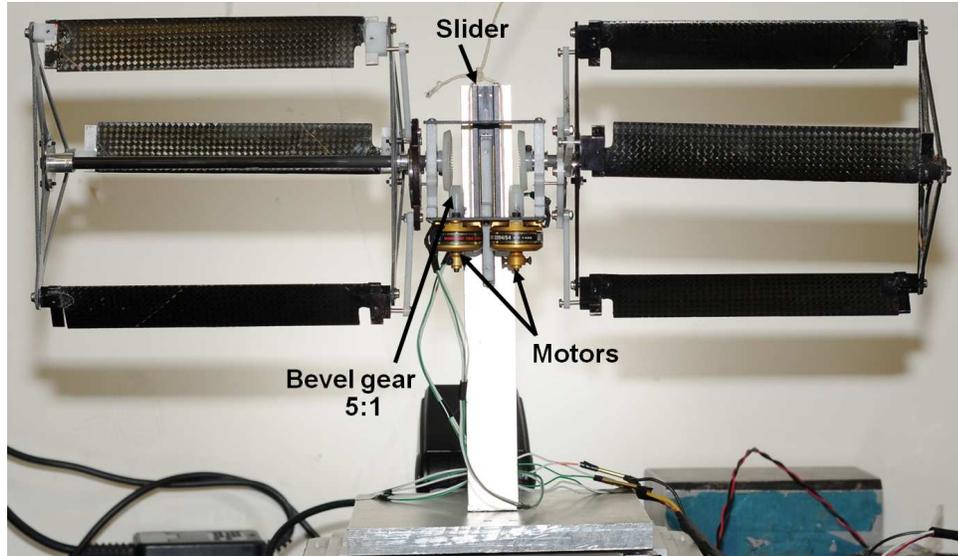
Figure 5.13: **Twin-rotor cyclocopter.**
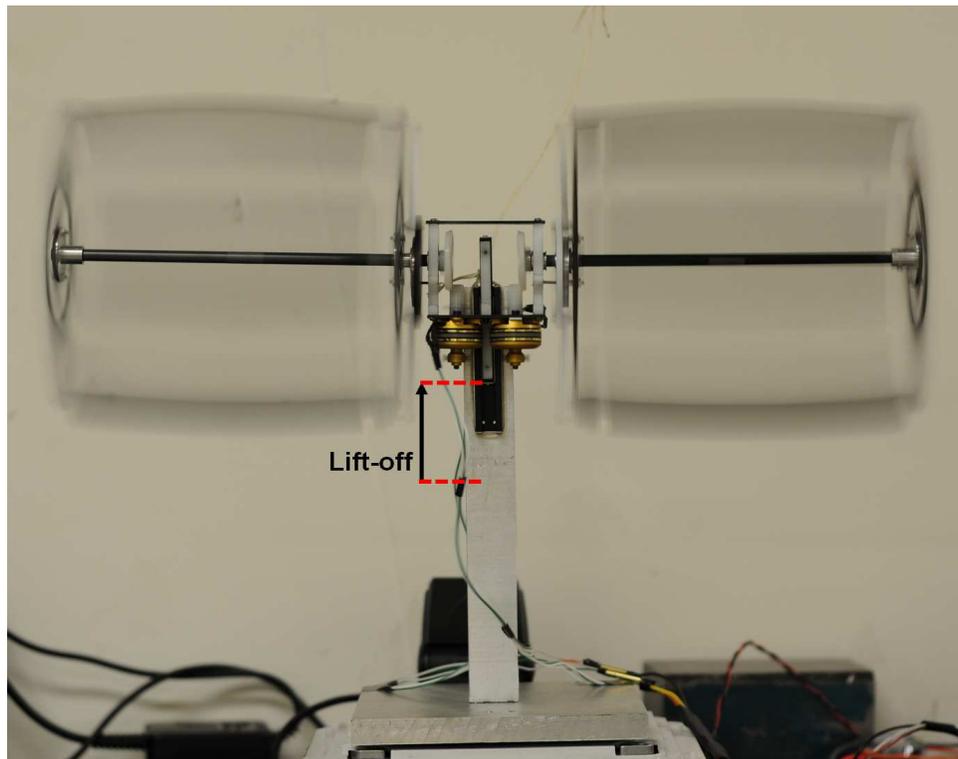
Figure 5.14: **Tethered hovering of the twin-rotor cyclocopter.**
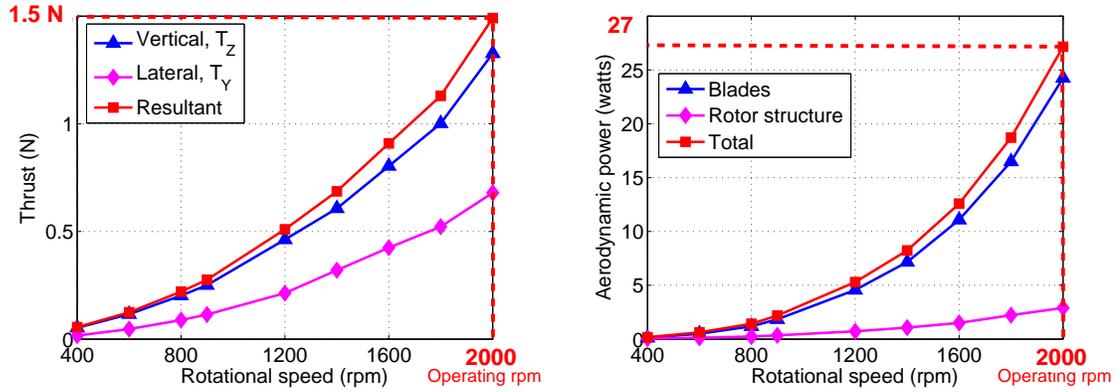
(a) Variation of thrust with rotational speed.

(b) Variation of power with rotational speed.

Figure 5.15: **Aerodynamic performance of the twin-cyclocopter rotor.**

sections.

The performance of the rotor used on the twin-cyclocopter is given in Figs. 5.15 and 5.16. Figure 5.15(a) shows the variation of vertical, sideward and resultant thrust produced by the rotor, with rotational speed. From the variation of the vertical and sideward forces with rotational speed, it can be inferred that both the magnitude and the direction of the thrust vector changes with rotor speed and at the operating rpm the resultant thrust is inclined at an angle of 30° with the vertical. The direction of the offset in the rotors' pitch changing mechanism was rotated by 30° such that the resultant thrust acted in the vertical direction for the vehicle to hover.

One of the drawbacks of the cyclorotor compared to a conventional rotor could be the parasite power associated with the rotor structure other than the blades (such as endplates, linkages, blade attachments, etc.,). This was described as tare power in Chapter 2. Even though in Chapter 2, the power loading was calculated based on just the blade power, from a vehicle perspective, it is important to look at the

231
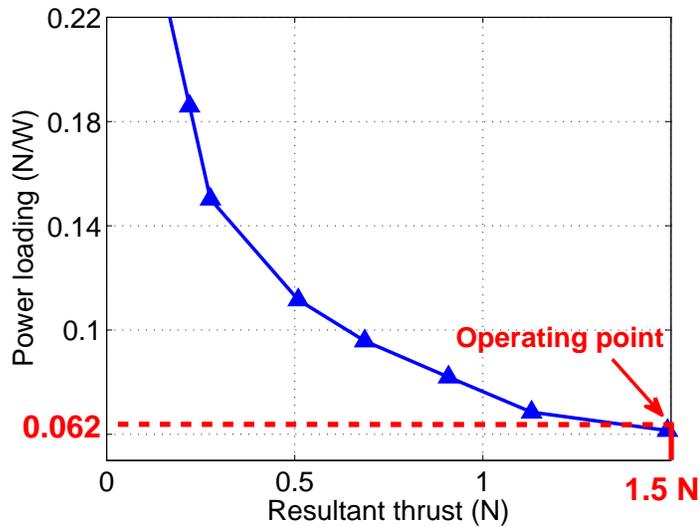
Figure 5.16: **Variation of power loading with thrust for the twin-cyclocopter rotor.**

total power required to spin the rotor. Therefore, power measurements were taken without the blades to obtain the power required to rotate just the rotor structure. Figure 5.15 shows the power breakup for the cyclorotor. It can be seen that the rotor structure power was only 10% of the total power. The variation of aerodynamic power loading with thrust is given in Figure 5.16. At the operating thrust of 1.5 N (per rotor), the power loading of the rotor was 0.062 N/W (10.4 lbs/hp).

5.4 Quad-Rotor Cyclocopter

From the control perspective, a quad-rotor cyclocopter may be easier to stabilize and control in hover and may be even more maneuverable as compared to a twin-rotor cyclocopter. A quad-rotor cyclocopter was designed and built as shown in Fig. 5.17. The rotor used on the quad-cyclocopter had a diameter of 6 inches and used four

Table 5.1: Quad-Cyclocopter weight breakdown.

Component	Weight (g)	% Total
Rotors (combined)	385	47.6%
Structure	225	27.8%
Motor and controller	95	11.7%
Li-Po battery	75	9.3%
Electronics	29	3.6%
Total	**809**	**100%**

blades with pitching amplitude of 40° (symmetric pitching). The blades have NACA 0010 airfoil section with a chord of 1.3 inches and span of 6.25 inches. This rotor design is different from the one used on the twin-cyclocopter because some more experimental parametric studies were performed after the twin-cyclocopter was built and it was seen that a 4-bladed rotor design with a higher chord/radius ratio had superior performance in terms of both thrust and power loading. The all-up weight of the vehicle is 809 grams. The component weight-breakup of the cyclocopter is given in Table 5.1. The vehicle has a dimension of 2 feet (rotor tip-to-tip) and a height of 1.2 feet.

Unlike the twin-cyclocopter where the rotor speeds were independently controlled using two separate motors, in the quad-cyclocopter, all the rotors were mechanically coupled to a single outrunner motor (rated 250 watts) through a two-stage transmission such that all the rotors opertated at the same rpm (Fig. 5.17). The
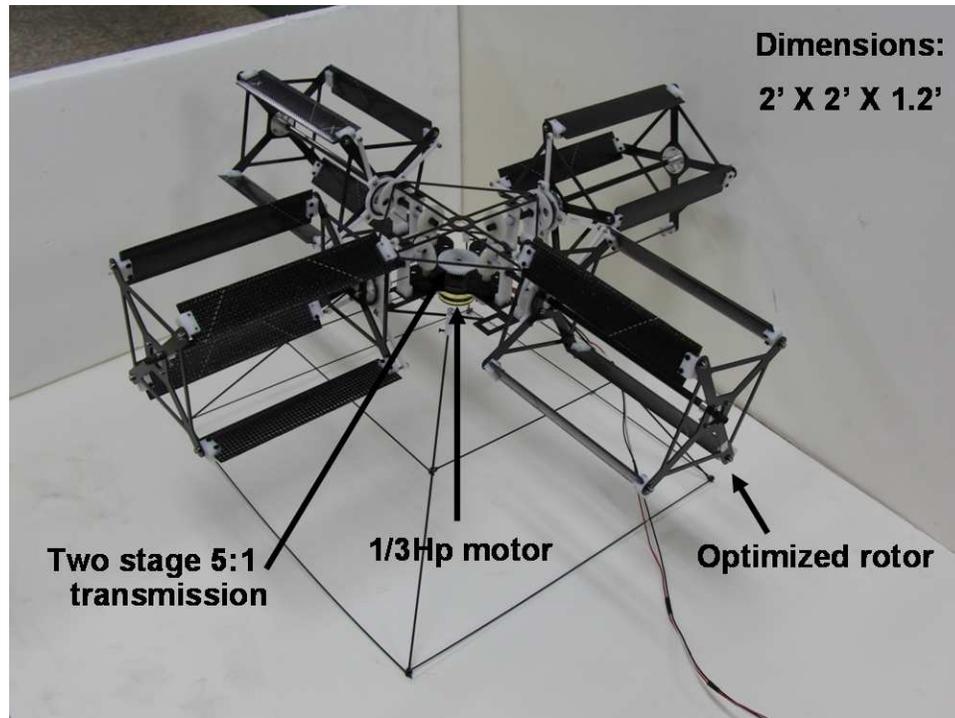
Figure 5.17: **Quad-rotor cyclocopter.**

Figure 5.18: **Tethered hovering of the quad-rotor cyclocopter.**
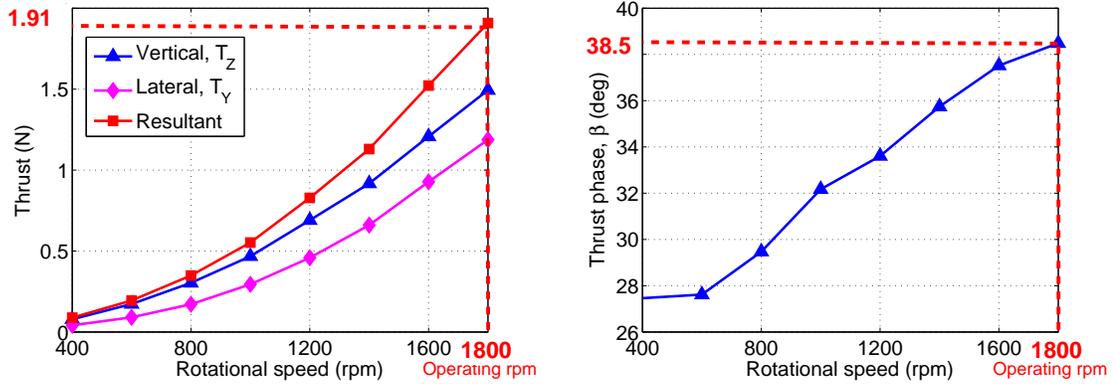
(a) Variation of thrust with rpm.   (b) Variation of thrust phasing with rpm.

Figure 5.19: **Magnitude and phasing of the resultant thrust for the quad-cyclocopter rotor.**

overall gear ratio of 5:1 is chosen because at the operating rotor rpm of 1800, the motor operates at 9000 rpm which is close to its peak efficiency rpm. Using a bevel gear arrangement, the opposite rotors are rotated in opposite directions and as a result are expected to produce zero rolling or pitching moment. As shown in Fig. 5.18, the cyclocopter is capable of tethered hover.

The performance of the rotor used on the quad-cyclocopter is given in Figs. 5.19–5.20. Figure 5.19(a) shows the variation of vertical, sideward and resultant thrust produced by a single rotor, with rotational speed and Fig. 5.19(b) shows the variation of the phasing of the resultant thrust vector (β, direction of the resultant thrust vector with respect to vertical) with rotational speed. It can be seen that the direction of the thrust vector also changes with rotational speed which makes it difficult to control a quad-cyclocopter through independent rpm control. Since the phase angle (β) was 40° at the operating rpm, for the vehicle to hover, the offset on the pitching mechanism was rotated by 40° so that the thrust vector is now verti-

235
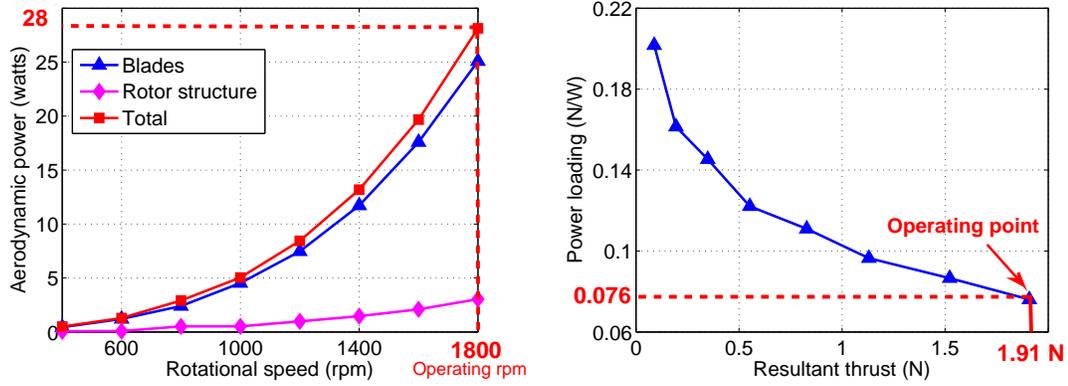
(a) Variation of power with rotational speed.

(b) Variation of power loading with thrust.

Figure 5.20: **Power and power loading for the quad-cyclocopter.**

cal. At the operating RPM of 1800, each rotor produced around 1.91 N of thrust. Figure 5.20(a) shows the breakup of aerodynamic blade and structure power. As before, the structure power is only 10% of the total power. The variation of power loading of each of the rotor with thrust is given in Fig. 5.20(b). At the operating thrust, the power loading is about 0.076 N/W (12.7 lbs/hp).

Since tethered hover was achieved, the next step would be to develop a control strategy for the quad-cyclocopter. Since, independent rpm control is not possible on the present quad-cyclocopter, the attitude control strategy will be through the independent vectoring of each of the four thrust vectors.

5.5 Attitude Control of Quad-Rotor Cyclocopter

Possible control strategy for the cyclocopter is by using the thrust vectoring capability of the rotors because all the rotors rotate at the same rpm. As explained in the previous section, ideally cyclorotors are capable of 360° thrust vectoring because
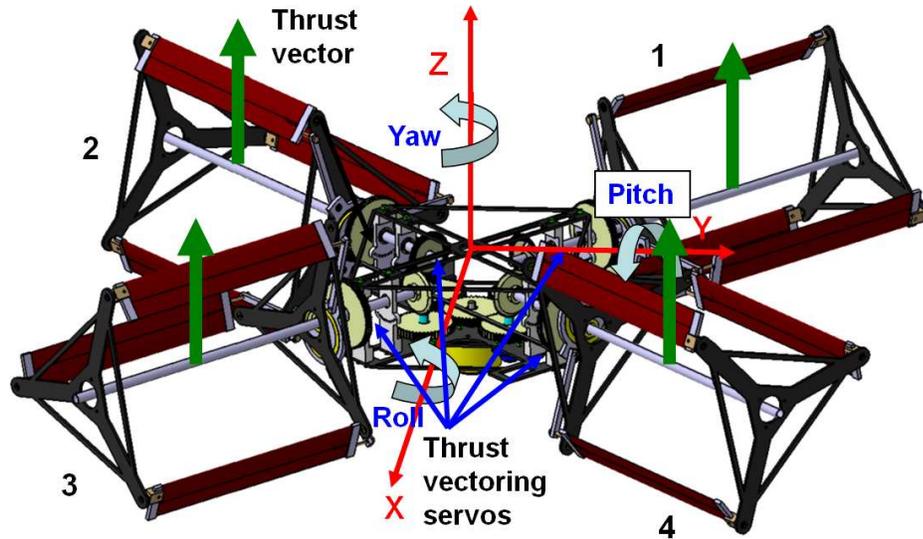
Figure 5.21: **Definition of pitch, roll and yaw for the quad-cyclocopter.**

of its unique pitch changing mechanism. Since there is no control over the pithing amplitude, the magnitude of the thrust can be changed by simultaneously changing the rpm of all the four rotors.

5.5.1   Attitude Control Strategy

The control strategy and the pitch and roll axes were defined such that the pitch, roll and yaw controls are not coupled. Figure 5.21 shows the pitch, roll and yaw axes of the cyclocopter. The roll and pitch axes are oriented at an angle of 45° with the rotor shaft axes. In the figure, rotors are numbered from 1 to 4. For simplicity of explanation, it is assumed that all the four rotors are identical and therefore produce the same thrust since they rotate at the same rpm. Therefore, when the vehicle is trimmed in hover all the thrust vectors have to be vertical as shown in Fig. 5.21. Now, to produce a yawing moment, the thrust vectors of two of the opposite rotors
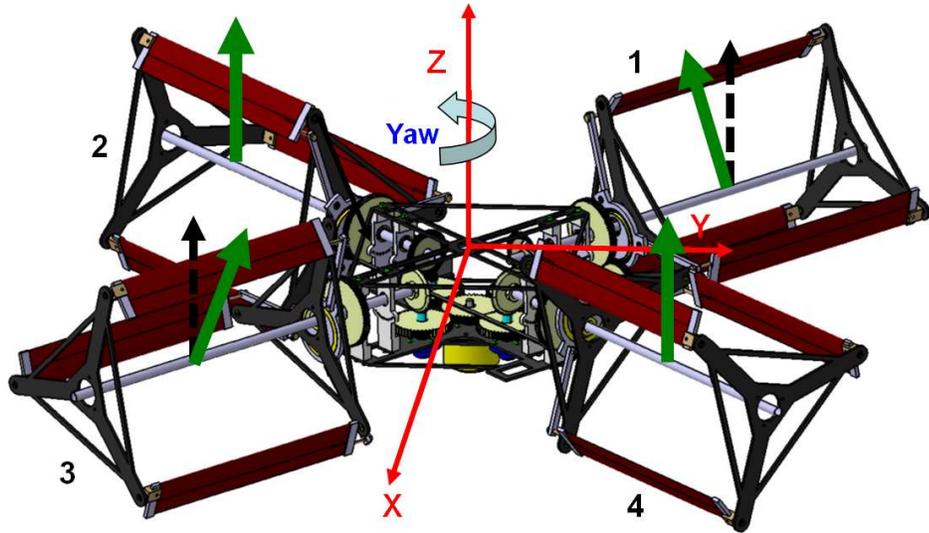
Figure 5.22: **Yaw contol scheme.**

have to be rotated in the opposite directions as shown in Fig. 5.22, where thrust vectors of rotors 1 and 3 are rotated in the opposite directions. The same effect can be produced by rotating 2 and 4. As shown in Fig. 5.23, to obtain a positive rolling moment, the thrust vectors of rotors 2 and 3 are tilted towards each other so that the vertical component of the thrust in that sector drops and the vehicle rolls to the left (as seen in the figure) without causing any pitching or yawing. Now, to obtain a negative rolling moment, the thrust vectors of rotors 1 and 4 are tilted towards each other. Since this is an axisymmetric vehicle, pitch control is same as the roll control. The main advantage of this control strategy is that the pitch, roll and yaw controls are decoupled.

As explained in the previous section on pitch mechanism design (Fig. 5.11), the thrust vector can be rotated by changing the offset direction in the pitch changing mechanism. In the present vehicle this is implemented using a servo and gear

238
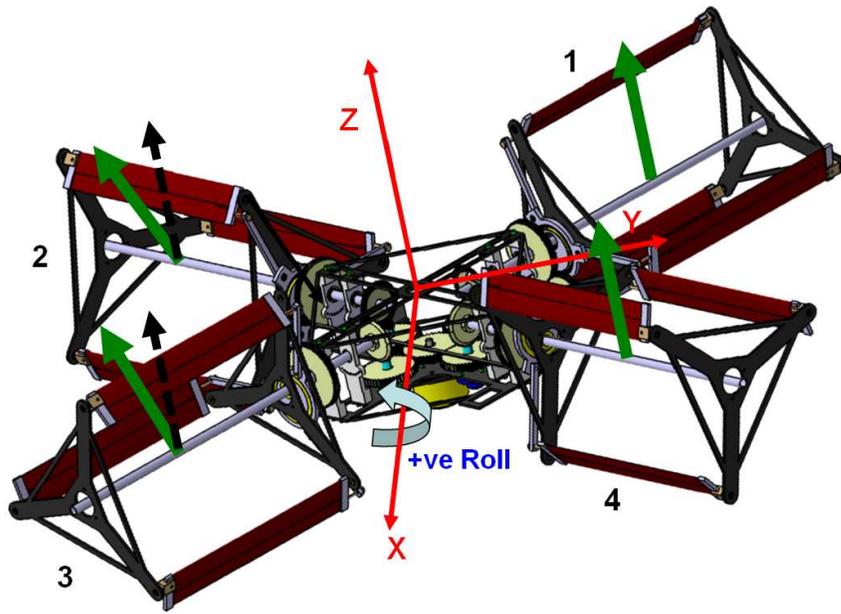
Figure 5.23: **Positive roll.**
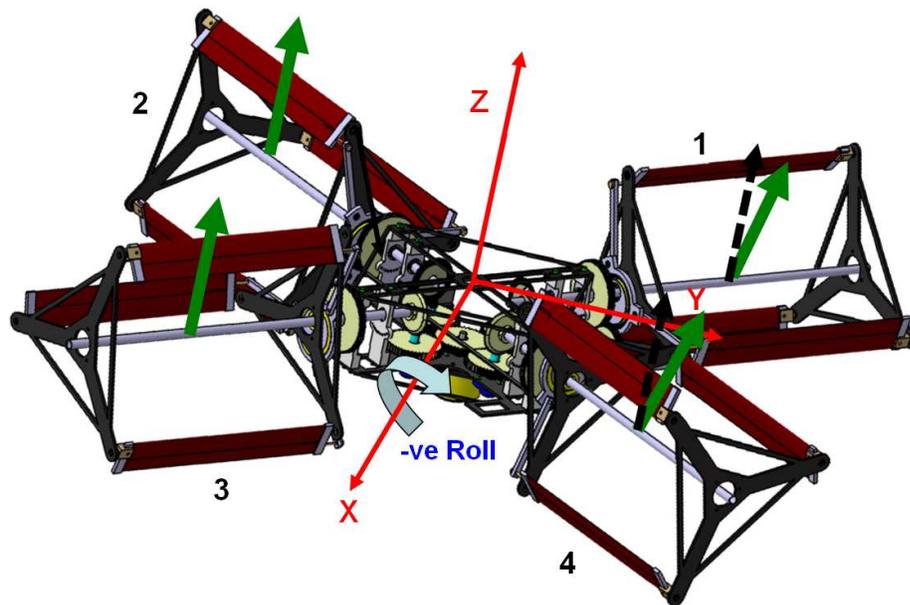
Figure 5.24: **Negative roll.**
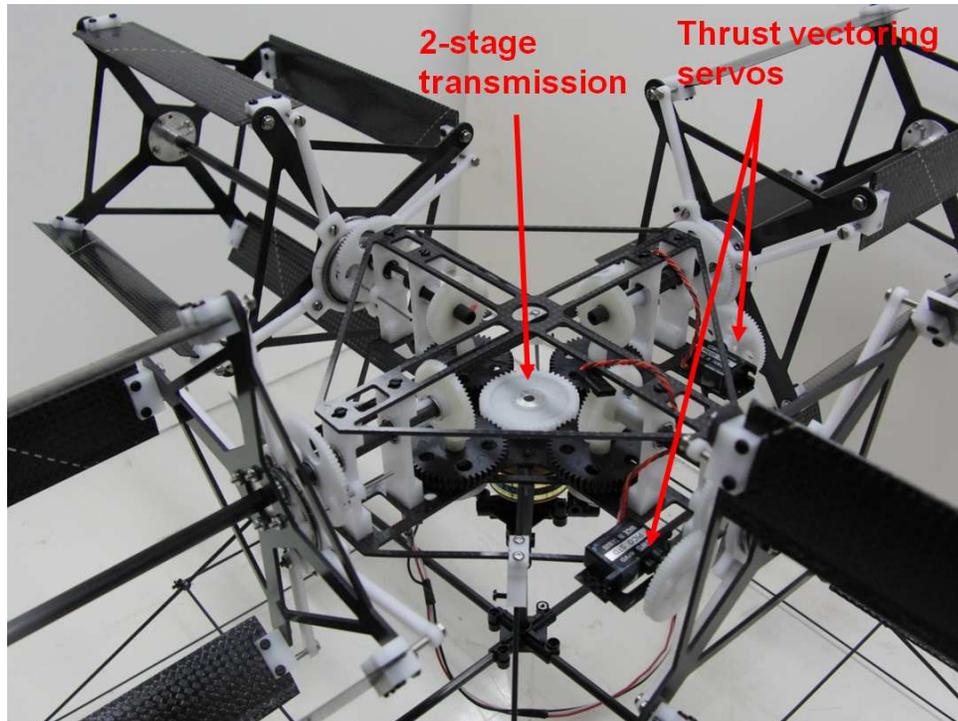
Figure 5.25: **Thrust vectoring servos on the quad-cyclocopter.**
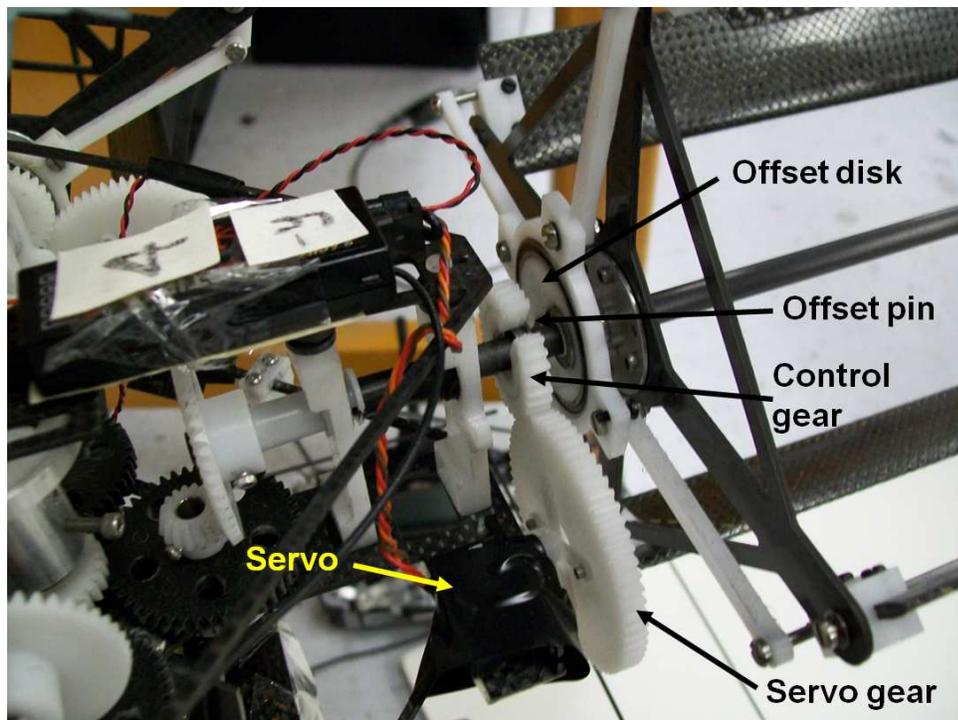
Figure 5.26: **Close-up of the thrust vector control mechanism.**

arrangement as shown in Figs. 5.25 and 5.26. As shown in Fig. 5.26, the servo gear rotates the control gear, which is mounted on the rotor shaft. A bearing is installed between the control gear and the shaft to prevent the control gear from rotating with the shaft. The control gear is connected to the offset disk through an offset pin so that rotation of the control gear rotates the offset disk, which in turn changes the direction of the offset which changes the phasing of the blade pitch variation and thereby rotates the thrust vector. The servo used is a GWS Pico Sub-Micro servo with a total swivel angle of 60°. A gear ratio of 1:2 is used between the servo gear and control gear so that when the servo rotates by 60° the control gear rotates by 120°. This gives +/-60° of thrust vectoring which is not possible to attain on any conventional rotary-wing aircraft unless the entire rotor is tilted. However, acheiving thrust vectoring on a cyclorotor is far easier than tilting the entire rotor and this ability can be utilized to improve the maneuverability of the cyclocopter.

5.6 Validtaion of the Control Strategy

Once the control strategy was formulated, the next step was to implement and validate this strategy on the quad-cyclocopter. The experimental setup and telemetry used for this study is described below.

5.6.1 Gimal-Stand Setup

To accurately simulate free flight conditions for attitude dynamics, the cyclocopter was mounted on a gimbal stand (Fig. 5.27), where the gimbal was located exactly
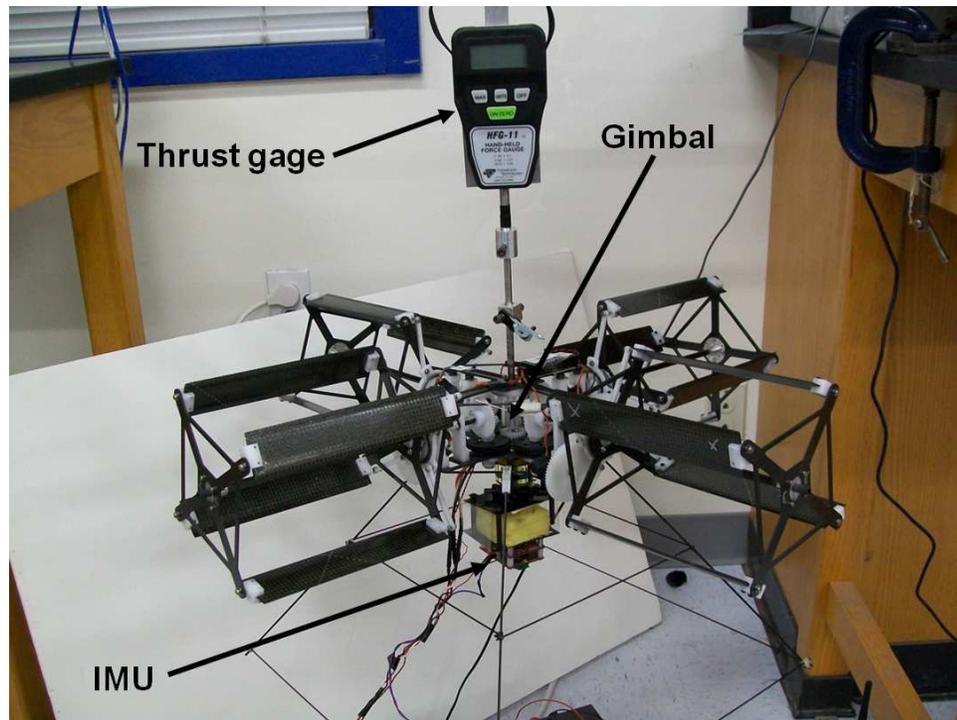
Figure 5.27: **Quad-cyclocopter mounted on the gimbal stand.**

at the center of gravity of the vehicle. The gimbal-setup provided the pitch, roll and yaw degrees of freedom to the cyclocopter while constraining all the translational degrees of freedom. This also allowed safe testing without the risk of damaging the vehicle. A thrust gage was installed on the gimbal so the thrust generated by the cyclocopter could be recorded (Fig. 5.27). The attitude of the vehicle was measured using an onboard six degree of freedom inertial measurement unit (IMU). The IMU uses one microelectromechanical (MEMS) based tri-axis accelerometer, two rate gyros, and two magnetometers to provide sensory feedback. It weighs approximately 30 grams and has an input voltage of 5 Volts provided by a power supply. A 10 bit Analog-to-Digital Converter (ADC) reads the sensor outputs and integrates the data serially. The measurements are transmitted to a ground station
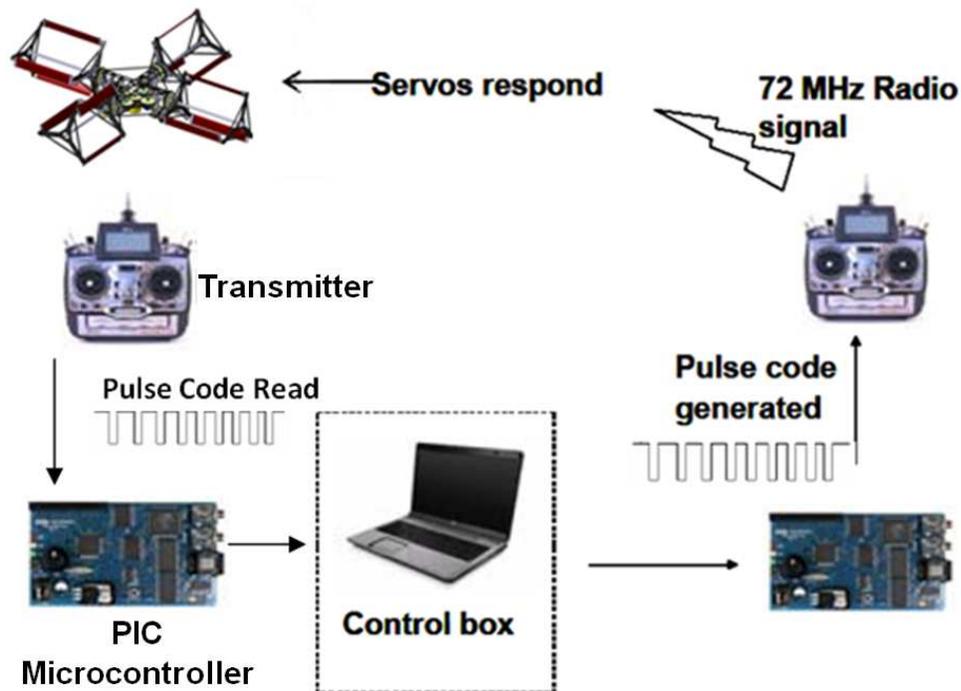
Figure 5.28: **Avionics and telemetry.**

via wireless Bluetooth at a rate of 200 Hertz. The ground based PC processes and filters the data to ascertain the vehicles states.

5.6.2 Avionics and Telemetry

The present control strategy for the quad-rotor cyclocopter is designed keeping in mind that a human pilot should be able to control it (open-loop control), using no computer augmented feedback control system. Therefore, it is important to reduce the number of controls to just four stick commands, which are pitch, roll, yaw and throttle and also decouple the pitch, roll and the yaw control. Computer will be only used to mix the servo commands (mix electronically) so that when the pilot gives a control input (pitch, roll or yaw), the appropriate servos are actuated.

Telemetery used in the present control system, is shown in Fig. 5.28. The pitch, roll, yaw, and thrust commands given by the human pilot on a radio transmitter are serially integrated by a Programmable Interface Controller (PIC) microcontroller and sent to the ground station (PC) for processing. The ground station reads the serial data and converts the pitch, roll, and yaw commands into specific signals corresponding to the movement of the four servos controlling the angle of each rotors thrust vector. The radio transmitter receives the servo control signals via the PIC microcontroller where they are converted to a Position Pulse Modulated (PPM) signal. An onboard radio receiver uploads the PPM signals determining the servo movement. The radio transmitter is connected to the microcontroller through the transmitters trainer channel.

Mixing the different channels could have been also done using the transmitter, however, most of the state of the art transmitters can only mix two channels at a time which is not sufficient for controlling the cyclocopter. One of the other advantages of using the present telemetry system is that, since the pilot stick inputs are transferred to the computer, the time history of the pilot control inputs could be recorded, which is very important for understanding the dynamics of the vehicle. Also, with the present strategy it it not difficult to move from an open loop to a closed loop control.

5.6.3 Results from the Validation Study

The next step was to perform systematic tests on the gimbal setup discussed in the previous section (Fig. 5.27) to validate the control strategy. The goal of this study was to provide the vehicle with pitch, roll and yaw control inputs and measure the vehicle dynamics (pitch, roll and yaw) and thereby validate the control strategy. The vehicle dynamics was measured using the 6-DOF Inertial Measurement Unit (IMU) mounted on the vehicle and was transmitted to the computer via bluetooth. For these tests, the servo commands are directly sent from the computer to the respective servos through the radio transmitter. The telemetry and avionics used were discussed in the previous section. Both the servo positions and the IMU data are time-stamped so that it is possible to relate the vehicle dynamics with the control inputs (servo angles). Now, since the direction of the thrust vectors are directly proportional to the servo position, it is possible to relate the dynamics of the vehicle with the orientation of thrust vector of each of the rotors.

As shown in Fig. 5.29(a), when the offset is perfectly vertical (corresponds to servo angle $= 0°$), the resultant thrust vector makes an angle, β_{trim}, with the vertical. Therefore, in order to trim the vehicle in hover, the the offset disk has to be rotated by β_{trim} as shown in Fig. 5.29(b), such that the resultant thrust vector is vertical. This is done using the servo arrangement as explained before (Fig. 5.26). However, since all the rotors are not exactly identical on the actual vehicle, it was observed that the trim servo angles are not exactly same for all the four cyclorotors. Fig. 5.30(a) shows the vehicle pitch, roll and yaw rate (measured by the IMU) after

(a) Servo angle $= 0°$.   (b) Servo angle $= \beta_{trim}^{\circ}$.
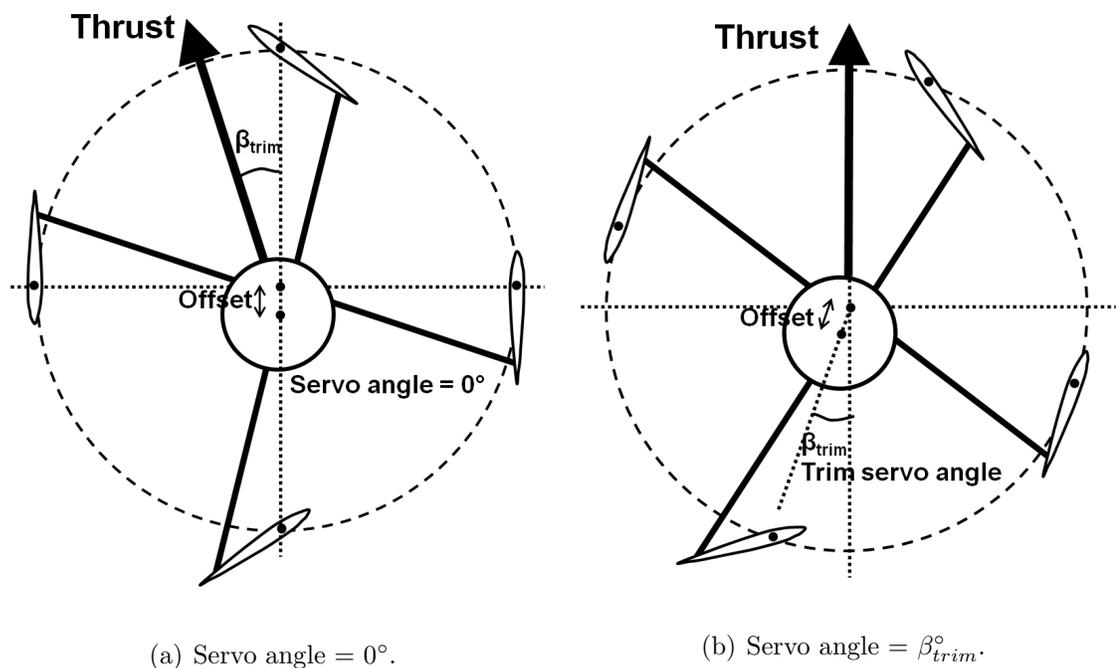
Figure 5.29: **Vertical thrust vector.**

the vehicle is trimmed on the gimbal stand at a thrust of 150 grams. As expected, the pitch and roll angles, and yaw rates are almost zero. Fig. 5.30(b) shows the four servo angles (β_{trim}) when the vehicle is trimmed. All the trim angles were very close to 40°.

After the vehicle was successfully trimmed, the next step was to generate pitch, roll and yaw motions using the control strategy described before (Figs. 5.23– 5.22). Yaw degree of freedom was first attempted. A yawing moment could be provided to the vehicle by simultaneously tilting the thrust vectors of rotors 1 and 3 or rotors 2 and 4 in the opposite directions as shown in Fig. 5.22. Ideally, either of these should produce the same yaw rate. Figure. 5.31 shows the variation of yaw rate with the servo angle (or thrust vector tilt with vertical) for tilting vectors 1, 3 and vectors 2, 4. As expected, the yaw rate increases linearly with the servo angle and both the

246
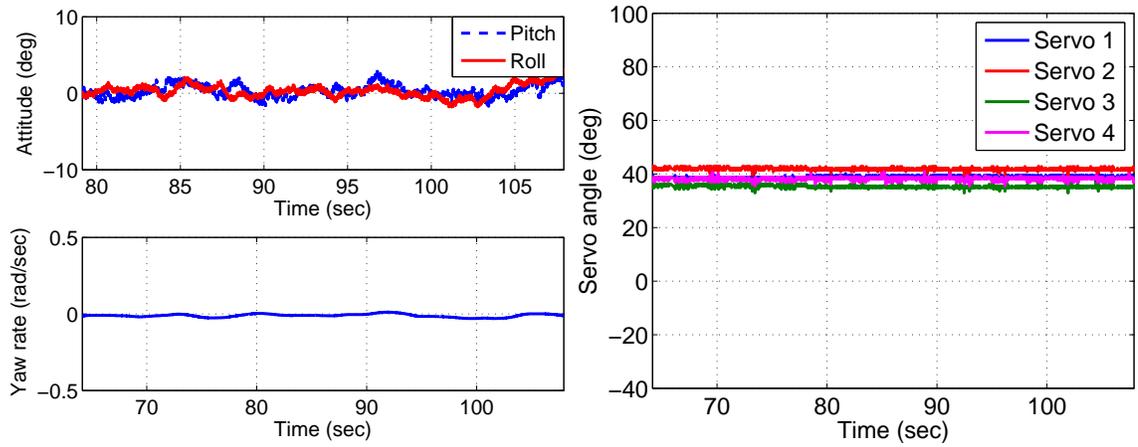
(a) Vehicle pitch, roll attitude and yaw rate.

(b) Servo angles to trim the vehicle.

Figure 5.30: **Vehicle attitude and servo positions for vehicle trimmed at Thrust = 150 grams.**
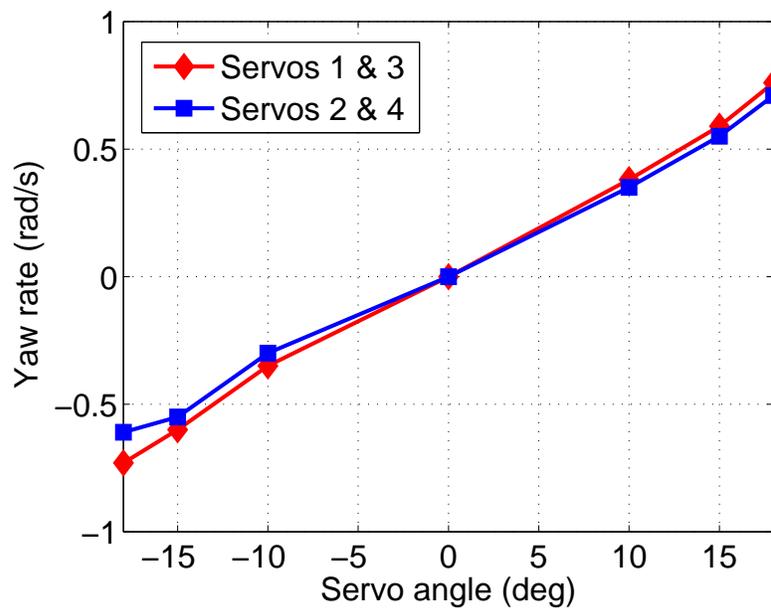
Figure 5.31: **Variation of yaw rate with servo angle.**

strategies produced identical yaw rates. Also it should be noted that that tilting the thrust vectors in the opposite directions produced similar yaw rates, but in opposite directions.

Once the yaw strategy is validated, the roll and pitch motions were attempted. As shown in Fig. 5.23, to generate a positive rolling moment, the servos 3 and 2 are rotated such that the thrust vectors 3 and 2 are tilted towards each other. And to generate negative rolling (Fig. 5.24), the thrust vectors 1 and 4 are rotated towards each other using servos 1 and 4. Positive and negative rolling demonstrated on the gimball stand is shown in Fig. 5.32. The time history of control inputs (servo angles) and the IMU measured pitch and roll angles for the positive and negative rolling cases are shown in Figs. 5.33 and 5.34, respectively. It can be seen that when the servos 3, 2 and servos 4, 1 are moved, the vehicle undergoes a pure roll motion without much change in the pitch attitude. This also proves that using this control strategy pitch and roll are uncoupled. The maximum pitch/roll motion allowed by the gimball setup was +/- 8°.

Similarly, to generate a positive pitching moment, the servos 4 and 3 are rotated such that the thrust vectors 4 and 3 are tilted towards each other. And to generate negative picthing, the thrust vectors 2 and 1 are rotated towards each other. The time history of control inputs and the pitch and roll angles for the positive and negative pitching cases are shown in Figs. 5.35 and 5.36, respectively. It can be seen that when the servos 4, 3 and 2, 1 are moved, the vehicle undergoes a pure pitch motion without much change in the roll attitude again showing that the control strategy is uncoupled. The results from these tests clearly show that

248
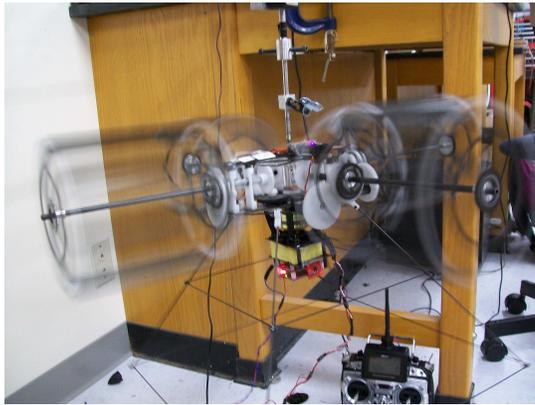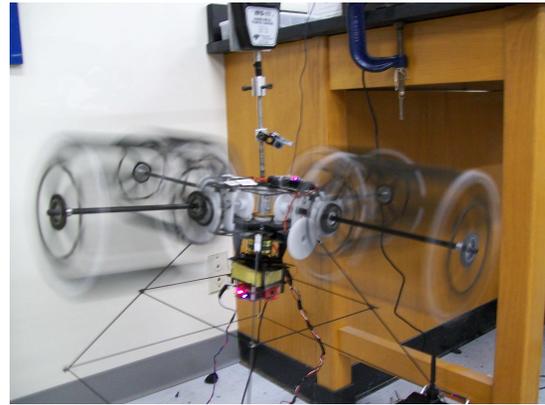
(a) Positive roll.

(b) Negative roll.

Figure 5.32: **Demonstration of positive and negative roll on the gimball setup.**
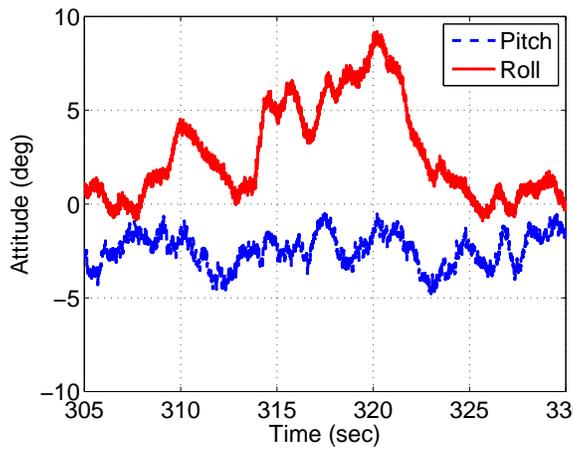
(a) Vehicle pitch, roll attitude.
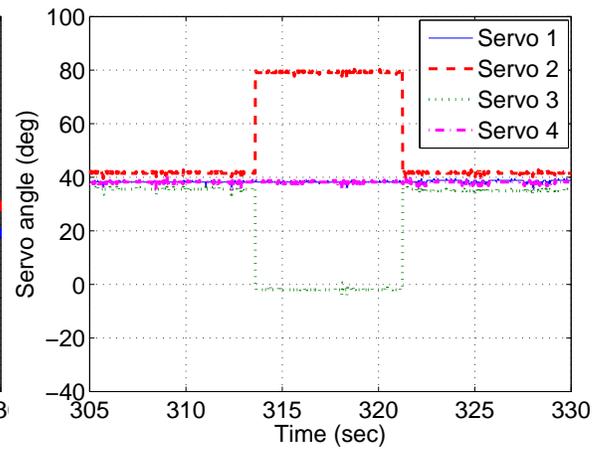
(b) Servo angles for positive roll.

Figure 5.33: **Vehicle attitude and servo positions during positive roll.**
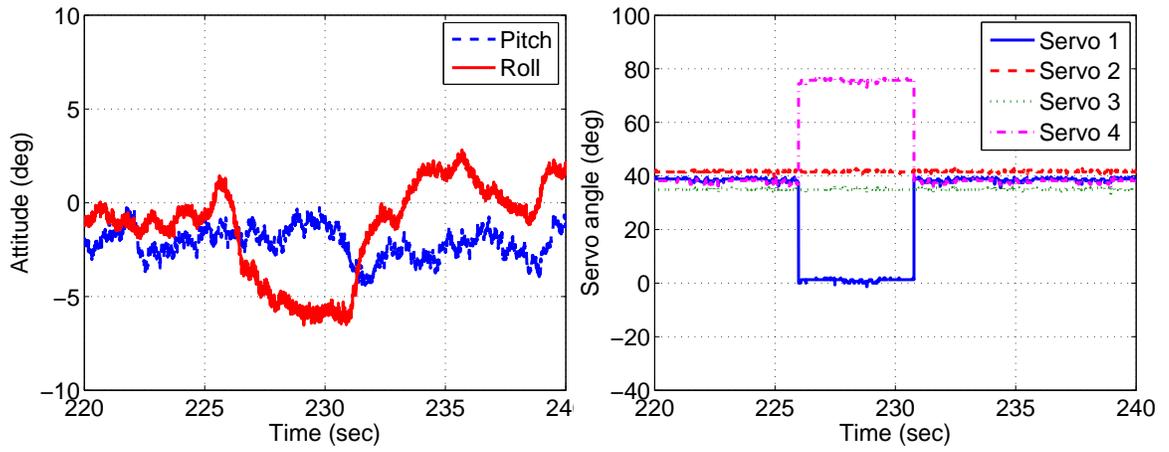
(a) Vehicle pitch, roll attitude.

(b) Servo angles for negative roll.

Figure 5.34: **Vehicle attitude and servo positions during negative roll.**
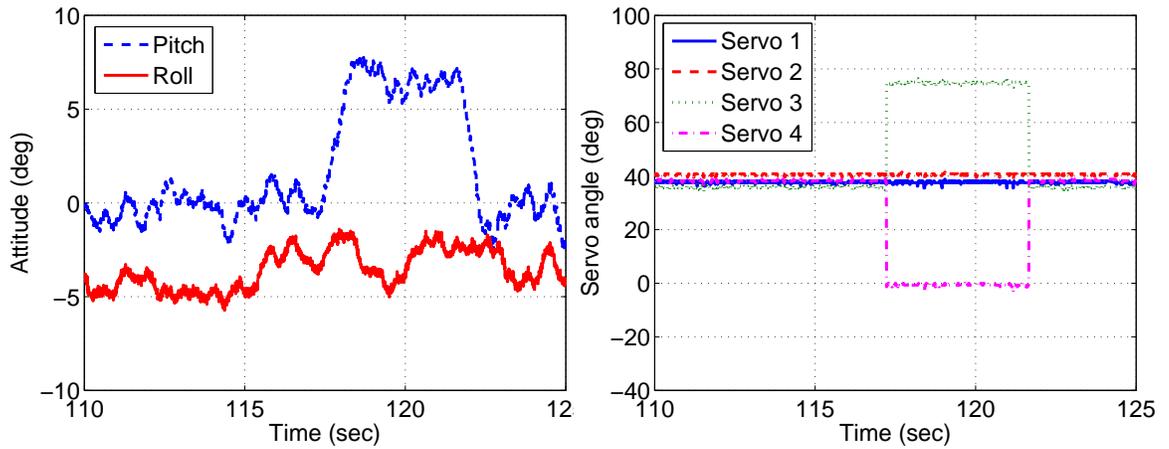
(a) Vehicle pitch, roll attitude.

(b) Servo angles for positive pitch.

Figure 5.35: **Vehicle attitude and servo positions during positive pitch.**

250

(a) Vehicle pitch, roll attitude. (b) Servo angles for negative pitch.
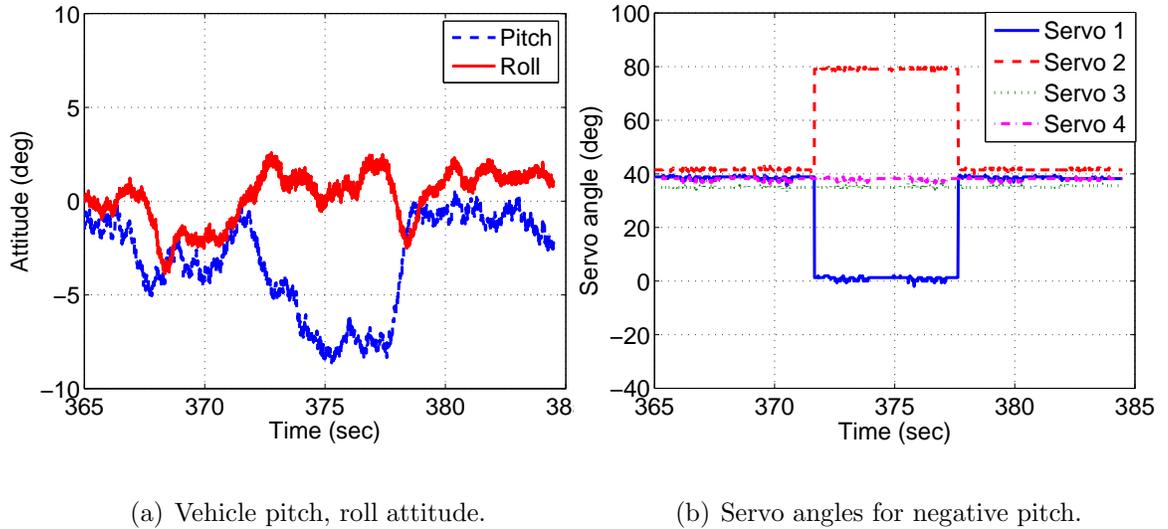
Figure 5.36: **Vehicle attitude and servo positions during negative pitch.**

it is possible to trim and control the cyclocopter in hover by using just thrust vectoring and without individual rpm control. However, adding individual rpm control could definitely improve the maneuverability of the vehicle with the cost of added complexity to the control system.

5.7 Concluding Remarks

The objective of the task discussed in this chapter was to demonstrate the flight capability of the cyclocopter concept through tethered hover and also to develop and validate a control strategy (using thrust vectoring) that can be used for the attitude control of such a vehicle. However, performing controlled, stable untethered hover is beyond the scope of the present work. Given below is the summary and some of the specific conclusions drawn from this study:

1. A twin-rotor cyclocopter (weighing 280 grams) was designed and built. The

cyclocopter was capable of tethered hover on a vertical guide. Although each of the rotors had independent rpm control, controlling the twin-cyclocopter in free flight could be extremely challenging.

2. A quad-rotor cyclocopter (weighing 800 grams) capable of tethered flight was built and flight tested (tethered hover). Unlike the twin-cyclocopter, the quad-cyclocopter used a unique two stage transmission where all the rotors rotate at the same rpm.

3. Even though tethered hover could be achieved using the cyclorotor concept, one of the main drawbacks of the present cyclocopter design is the fact that the combined rotor weight (including the pitching mechanism) is almost 50% of the total vehicle weight. Therefore, if this concept have to be efficient, the rotors have to be redesigned for lower weight.

4. A control strategy for the quad-rotor cyclocopter have been developed using the idea of thrust vectoring for pitch, roll and yaw control. This technique have been implemented and validated on the quad-rotor cyclocopter. This shows that it is possible to trim and control a quad-cyclocopter in hover by using just thrust vectoring and without individual rpm control.

Chapter 6

Summary Remarks, Conclusions and Future Work

Micro Air Vehicles is a fast emerging field of research in aerospace engineering and is envisioned to have a wide range of military and civilian applications. Since MAVs are small and compact systems they offer several advantages such as portability, rapid deployment, real-time data acquisition capability, low radar cross section, low noise and low production cost. However, even though the concept of MAV looks attractive, the MAV research is still in its incipient stages. The present status of MAVs is far from being viable for any practical applications. However, it should be noted that only a decade of research has gone into these small vehicles and the key technical barriers are only being identified now. Some of these barriers include small-scale power generation and storage, navigation and communications, propulsion, aerodynamics, and control. One of the most interesting and least understood aspect of small-scale flight is the aerodynamics.

Most of the MAVs today are scaled-down versions of full-scale concepts such as fixed-wings and rotorcrafts. From a vehicle design perspective, the two main problems that inhibit the practical applications of these vehicles are (1) poor aerodynamic efficiency which results in low endurance, and (2) lack of sufficient control authority especially while operating in a gusty outdoor environment.

Unless these vehicles can fly for atleast half an hour, their applications will

be limited. However, the best endurance for a fixed-wing MAV today is 30 mins, while for a rotary wing MAV, it is less than 15 mins. The reasons for low endurance are twofold (1) poor aerodynamic performance of conventional wings at low Reynolds numbers, and (2) lack of efficient propulsion/energy storage systems at these scales. The aerodynamic efficiency of the conventional MAV designs are directly related to the lift-to-drag ratio of the airfoils used. Therefore, by designing better aifoils, the efficiency of these designs can be improved to some extent. However, these improvements may be limited because of the inherent inefficiencies associated with low Reynolds number flow. Efficient propulsion is an enormous challenge at these scales. MAVs have to rely on electric motors because conventional engines become extremely inefficient ($< 5\%$) as they are scaled down. However, electric motors are powered by batteries which are heavy because their energy densities are much lower compared to the hydrocarbon fuels. Because of this reason, for the small-scale flyers, the mass fraction of the propulsion system (batteries/power and motor/transmission) is in excess of 60% of the total vehicle mass.

The next issue with the present MAVs is the lack of control authority, especially in a gusty environment. It is interesting to note that, only the vehicle is scaled down, but the disturbances in the nature (such as gusts) are not. A full-scale aircraft and a 100 gram MAV have to operate in the same disturbances in the environment. As the vehicle is scaled down, the inertia of the vehicle decreases as the cube of size; however, the aerodynamic force only scales down as the square of size and hence they become more suceptible to gusts. Therefore traditional control techniques may become inadequate if the MAV needs to be stable and controllable

in a gusty environment. The present MAV designs cannot tolerate gusts more than a few feets per second.

On one hand, MAVs suffer from all the above limitations. On the other hand, it is interesting to observe both insects and birds fly effortlessly for long durations of time in the same aerodynamic regime, even in gusty conditions. None of the present MAV designs can match the aerodynamic performance of these natural flyers in terms of stability, maneuverability, or efficiency. This may be because of the fact that most of the present MAVs are scaled down versions of full-scale concepts, which are designed for a completely different aerodynamic regime. And most of the research in this area was focussed on making marginal improvements in the performance of these vehicles by designing better wings and rotor blades for the low Reynolds number regime. However, if the efficiency and controllability of small-scale flight need to be dramatically improved, it might be important to switch to radically different solutions for flight. One logical approach would be to understand and implement the aerodynamic mechanisms (such as unsteady aerodynamics, leading edge vortex, etc.) birds and insects use to improve the performance. However, this means moving away from the conventional aircraft designs and investigating out-of-the-box solutions, which may have the potential to utilize some of these unsteady aerodynamic mechanisms and improve both efficiency and controllability of the vehicle. Cycloidal rotor is one such unconventional concept and present research has shown that, if properly designed, this concept can be aerodynamically more efficient than a conventional rotor.

Even though the concept of cycloidal rotors has been around for almost a cen-

tury, there have not been many systematic studies performed on this concept. Most of the studies that have been performed are mostly at relatively larger scales (Re > 100,000). Moreover, none of these studies were comprehensive enough to clearly lay down the design principles for an efficient, flight-capable cyclorotor. Therefore, one of main focusses of the present study was to systematically perform an experimental parametric study by varying the blade design and kinematics to improve the thrust producing capability and power loading of a MAV-scale cyclorotor. Flowfield measurements are crucial in obtaining a fundamental understanding of the cyclorotor aerodynamics and this has not been performed in the past. The current understanding of the flowfield inside a cyclorotor is derrived from the few CFD studies that have been performed. However, many aspects of the flow are still not completely understood. Therefore, systematic flow field measurements were made using the Particle Image Velocimetery (PIV) technique inside the cyclorotor-cage and the rotor-wake to better understand the aerodynamics. It is extremely important to have a comprehensive analysis tool to predict the performance of the cyclorotor. Therefore, the present research also focussed on developing a fully non-linear unsteady aeroelastic model to predict the blade loads and average performance of a MAV-scale cyclorotor. Since, there are no flight-capable cyclocopters, it was important to demonstrate the flightworthiness of this concept. Therefore, a cyclocopter capable of tethered flight has been designed and built. The concluions from different areas of the present study are summarized below.

6.1 Conclusions

6.1.1 Experimental Performance Studies

Experimental parametric studies were conducted on a rotor of span and diameter equal to 6 inches to investigate the effect of the rotational speed, blade airfoil profile, blade flexibility, blade pitching amplitude (symmetric and asymmetric blade pitching), pitching axis location, number of blades with constant chord (varying solidity), and number of blades at same rotor solidity (varying blade chord). These parameters when systematically varied, identified substantial improvements in cyclorotor performance. The following are specific conclusions derived from this study:

1. The force measurements on the cyclorotor showed the presence of a lateral force whose magnitude was comparable to that of the vertical force. The ratio of the lateral force to the vertical force (phase of the resultant force) was found to increase with increasing rotational speed and number of blades. Also, as expected, the thrust coefficient (C_T) remained constant with rotational speed proving that the thrust for a cyclorotor varied as the square of rotational speed. However, the power coefficient (C_P), linearly increased at a very small rate with rotational speed, especially at higher rotational speeds.

2. One of the main drawbacks of the cyclorotor was hypothesized to be the parasitic power associated with the rotor structure (endplates, linkages, etc.,), other than the blades. However, the present study showed that, if the rotor is carefully designed, this parasitic power could be as low as 10–15% of the total

power.

3. The thrust produced by the cyclorotor steadily increased with pitching amplitude up to 45° without showing any signs of blade stall for all the blade airfoil sections that were tested. PIV studies showed that the absence of blade stall at such high pitch angles was because of the high induced velocities causing relatively high inflow angles, which lowered the blade angles of attack. The flow measurements also suggested a form of pitch-rate induced stall delay on the blades at high angles of attack, as well as the formation of a shed leading edge vortex similar to a dynamic stall vortex that is likely responsible for increasing the thrust.

4. Operating the cyclorotor at higher pitching amplitude also resulted in improved power loading, and this trend seemed independent of the number of blades or the blade airfoil sections that were being used. For the majority of the cases tested, the optimum pitching amplitude was observed to be 40°, even though 45° pitching amplitude always produced the maximum thrust. The reason for the higher power loading at higher pitching amplitudes is because the power loading varies inversely with rotational speed, therefore, increasing thrust by increasing the blade section angle of attack seems more efficient than increasing the rotational speed. However, the maximum thrust that can be obtained using this approach would still be limited by the onset of blade stall, and hence will be airfoil dependent.

5. When compared to the flat-plate blades, the NACA 0010 blades produced the

highest values of thrust at all blade pitching amplitudes. The NACA blades also produced higher power loading than the flat plate blades. However, the reverse NACA 0010 blades produced better power loadings at lower pitching amplitudes, even though at higher pitch amplitudes, regular NACA blades performed better. Among the three NACA sections (NACA 0006, NACA 0010 and NACA 0015) tested on the cyclorotor, NACA 0015 had the highest power loading followed by NACA 0010 and then NACA 0006. This may be because at MAV-scale Reynolds numbers, the thicker airfoils are likely to maintain a high lift-to-drag ratio over a wider angle of attack range. However, all the three NACA sections produced similar thrusts at all the pitching amplitudes

6. Using blades that were stiffer in bending and torsion produced higher thrust and power loadings than when using flexible blades because of the reduced aeroelastic effects. With the flexible blades, however, the power loading improved with an increase in blade pitch angle because a larger angle reduces the torsional moment experienced by the blade and also increases the stiffness of the blade in the direction of bending produced by centrifugal effects.

7. Power loading increased with increasing number of blades (i.e., increasing rotor solidity) despite the fact that profile power requirements also increases with solidity. This is because that a larger solidity rotor produces the same thrust at a lower rotational speed and a decrease in the profile power because of the lower operating speed outweighs the increase in profile power due to the larger blade area. This trend remained consistent across a wide range of blade

259

pitching amplitudes.

8. Asymmetric pitching, where the pitch angle at the top is larger than the angle at the bottom, provided a better power loading than symmetric pitching. The reason can be attributed to the virtual camber effect which tends to reduce the effective angle of attack at the top and increase the effective angle of attack at the bottom. For a total peak-to-peak pitching angle of 70°, 45° pitch angle at the top and 25° at the bottom produced the highest power loading. However, increasing the pitch angle at the bottom relative to the top increased the thrust produced at a constant rotational speed.

9. Shifting the pitching axis location away from the leading edge improved the performance, with the optimum pitching axis location being 25–35% chord depending on the blade pitching kinematics. However, the resultant thrust decreased as the pitching axis was moved away from the leading edge. Since the present rotor has a large chord-to-radius ratio, the location of the pitching axis can significantly affect the aerodynamic performance of the cyclorotor because of the virtual camber effect.

10. For a constant solidity, the rotor with fewer number of blades produced higher thrust. 2-bladed cyclorotor had the highest power loading compared to 3- and 4-bladed rotors.

11. The power loading of the optimized cyclorotor was comparable to that of a conventional rotor when operated at the same disk loading. The optimum

configuration based on all the tests was a 4-bladed rotor using 1.3 inch chord NACA 0015 blade section with an asymmetric pitching of 45° at top and 25° at bottom with the pitching axis at 25% chord.

6.1.2 Particle Image Velocimetery (PIV) Studies

Two sets of 2-D PIV measurements, spanwise and chordwise were performed to understand the flowfield of the cycloidal rotor. Following are the specific conclusions derrived from the PIV studies.

1. The cyclorotor was shown to generate relatively high values of thrust even at extremely high blade pitch angles. PIV measurements showed that the blades experienced relatively high inflow velocities, which lowered the angles of attack. The flow measurements also suggested a form of pitch-rate induced stall delay on the blades at high angles of attack, as well as the formation of a leading edge vortex shed similar to a dynamic stall vortex that is likely responsible for increasing the thrust.

2. The spanwise PIV measurements showed the presence of two contra-rotating tip vortices from the two blade tips which convected downwards in a contracting wake pattern.

3. The presence of a sideward force on the cyclorotor was found to be of a magnitude comparable to that of the vertical force. The ratio of the sideward force to the vertical force (phase of the resultant force) was found to vary with rotational speed. A significantly skewed downstream wake structure in the

cross-plane was also found from the PIV measurements, which confirmed the existence of the sideward force.

4. A momentum balance performed using the flow field measurements helped to quantify the vertical and sideward forces produced by the cyclorotor. The estimated momentum values showed good agreement with the force measurements made using load balance. The drag coefficient of the blades was also computed using the momentum deficit approach, and the computed C_d values correlated well with the typical airfoil values for these low Reynolds numbers.

5. The PIV measurements showed that the flowfield inside the cyclorotor-cage was far from uniform and there were significant rotational flows inside the rotor cage, which coupled with the influence of the upper wake on the lower half of the rotor can account for some energy losses inside the cyclorotor.

6.1.3   Aeroelastic Modeling

A refined aeroelastic model that can accurately predict the blade loads and average thrust of a MAV-scale cycloidal rotor was developed. The analysis followed two parallel approaches: (1) second-order non-linear beam finite element analysis with moderately large radial bending, tangential bending and torsional deformation and, (2) multibody based analysis, based on MBDyn applicable for large deformations. Both the analyses used unsteady aerodynamics assuming attached flow. Two different inflow models, single streamtube, and double-multiple streamtube (D-MS) were investigated. The analysis was also used to understand the effect of blade flex-

ibility, unsteady aerodynamics and blade kinematics on the cyclorotor performance. The following are specific conclusions drawn from the aeroelastic analysis:

1. When compared to the experimental measurements, the present analysis was able to predict the magnitude of the resultant thrust vector with sufficient accuracy over a wide range of rotational speeds, pitching amplitudes, number of blades and even for an extremely flexible blade. However, the direction of the resultant thrust vector was not predicted with the same accuracy in all the cases.

2. The multiple streamtube inflow model predicted the instantaneous forces and average thrust more accurately than the single streamtube inflow model. The single streamtube model slightly overpredicted the resultant thrust for most of the cases.

3. Significantly high virtual camber effect was identified for the present rotor which effectively increased the blade lift in the lower half and decreased the lift in the upper half of the blade trajectory. Including the virtual camber effect in the analysis proved to be crucial in an accurate prediction of the blade loads.

4. The key reasons for the lateral force production was identified to be the mechanical lag in the actual blade kinematics (easily modeled within the multibody approach) and the aerodynamic phase lag brought about by the unsteady aerodynamics. Another parameter that had a significant influence on the magnitude of the lateral force (with minimal influence on the vertical force) is the

drag model used for the blades. Without the contribution from the induced drag, the lateral force was always underpredicted when compared with test data.

5. Even though the deformations were dominated primarily by inertial forces, aerodynamic forces also had significant influence on them. This clearly shows the need for a coupled aeroelastic analysis for predicting the blade loads on a cyclorotor with flexible blades.

6. FEM analysis with moderatley large deformation model was unable to predict accurately the deformations and hence blade loads for the 3% thickness-to-chord ratio flexible blades. However, MBDyn was able to predict the thrust accurately for flexible blades at lower rotational speeds ($<$ 1200 rpm) but slightly underpredicted at higher rotational speeds. The underprediction may be attributed to the overprediction of structural deformations. Another reason could be the inaccuracies in the accounting for the effect of deformations in blade aerodynamics forces.

7. The key reason for the lower thrust while using flexible blades was identified to be the reduction in geometric pitch angle due to the large nose down torsional deformation of the blades in the upper half of the circular blade trajectory which is not compensated by the nose-up blade deformation in the bottom half as expected. Also, the study showed that a multibody based analysis is required to predict the deformations accurately for very flexible blades.

6.1.4 Vehicle Development

Flight capability of the cyclocopter concept was demonstrated through tethered hover. A control strategy (using thrust vectoring) was developed and validated for the attitude control of such a vehicle. However, performing controlled, stable untethered hover is beyond the scope of the present work. Given below is the summary and some of the specific conclusions drawn from this study:

1. A twin-rotor cyclocopter (weighing 280 grams) was designed and built. The cyclocopter was capable of tethered hover on a vertical guide. Although each of the rotors had independent rpm control, controlling the twin-cyclocopter in free flight could be extremely challenging.

2. A quad-rotor cyclocopter (weighing 800 grams) capable of tethered flight was built and flight tested (tethered hover). Unlike the twin-cyclocopter, the quad-cyclocopter used a unique two stage transmission where all the rotors rotate at the same rpm.

3. Even though tethered hover could be achieved using the cyclorotor concept, one of the main drawbacks of the present cyclocopter design is the fact that the combined rotor weight (including the pitching mechanism) is almost 50% of the total vehicle weight. Therefore, if this concept have to be efficient, the rotors have to be redesigned for lower weight.

4. A control strategy for the quad-rotor cyclocopter have been developed using the idea of thrust vectoring for pitch, roll and yaw control. This technique

have been implemented and validated on the quad-rotor cyclocopter. This shows that it is possible to trim and control a quad-cyclocopter in hover by using just thrust vectoring and without individual rpm control.

6.2   Contributions to the State of the Art

In the early 20th century, cyclorotor was a VTOL idea competing with the conventional helicopter concept. Also, cyclorotor had the additional advantage of thrust vectoring, which could provide the vehicle both hover and high-speed forward flight capability. However, because of the mechanical complexity of the full-scale cyclorotor designs, none of the early cyclocopters were successful. Meanwhile, conventional rotorcraft technology had made significant progress and many successful helicopters were built. As a result, cyclorotors became less popular and eventually disappeared from the scene for nearly half a century. However, recently, there have been a revival of interest in this technology for small unmanned air vehicles (UAVs and MAVs). The main reason for this is the efficiency and thrust vectoring capability of cyclorotors, which could potentially improve the performance of these small aircrafts. The overall contribution from the present research lies in obtaining a fundamental understanding of the cyclorotor concept at MAV scales.

Even though there have been lot of speculations about the higher efficiency of the cyclorotor concept, there have not been many systematic experiments performed to substantiate this fact. The main contribution of the present research is in generating a sytematic body of experimental data on MAV-scale cyclorotors –

266

both on performance measurements and flowfield studies. These studies have been instrumental in understanding the aerodynamics of cyclorotor at MAV scales.

The present performance measurements are very comprehensive, and the parameters that were varied included rotational speed, blade airfoil profile, blade flexibility, blade pitching amplitude (symmetric and asymmetric blade pitching), pitching axis location, number of blades with constant chord (varying solidity), and number of blades at same rotor solidity (varying blade chord). Identifying the effect of each of these parameters, independently, on the thrust producing capability and efficiency of the cyclorotor system was the most important contribution of this research. The study clearly showed that the cyclorotor can be aerodynamically more efficient (higher power loading at the same disk loading) than a conventional rotor if the blade kinematic parameters, blade airfoil section and blade structure are properly optimized. Another key conclusion was that the cyclorotor can produce much higher thrust values at lower rotational speeds compared to a conventional rotor of the same projected area. This is because of the fact that on a cyclorotor the entire rotor-blade operates at the same velocity.

Some of the previous studies had speculated that unsteady flow mechanisms may enhance the performance of cyclorotors. The current research clearly showed that the unsteady flow mechanisms do improve the lift producing capability of the cyclorotor blades. This was clear from the absence of blade stall up to high pitching amplitudes ($\approx 45°$). This was further verified by PIV measurements, which suggested a form of pitch-rate induced stall delay on the blades at high angles of attack, as well as the formation of a shed leading edge vortex similar to a dynamic

267

stall vortex that is likely responsible for increasing the thrust. PIV studies clearly exposed the flowfield inside the cyclorotor and captured some key flow features such as tip vortices, which improved the understanding of the physics of cyclorotors and will also be instrumental in developing better aerodynamic models in the future. It should be noted that, this was the first experimental flowfield study ever performed on a cyclorotor at any scale.

The other main contribution was in developing a comprehensive aerolastic analysis, which could handle extremely large deformations. Most of the previous analysis on cyclorotors were purely aerodynamic in nature without the effect of deformations. The present model was validated with the experimental results and could be a useful design tool for MAV-scale cyclorotors. The model was also used to explain some of the trends observed in the experimental studies. One of the key contribution of the aeroelastic model was in explaining how the thrust of the cyclorotor drops as the blades are made flexible.

Another key contribution of the present research is in developing two cyclocopters (a twin-rotor and a quad-rotor cyclocopter) capable of tethered hover. Demonstrating the flight-capability of the concept is extremely crucial, especially while investigating out-of-the-box ideas. A control strategy was also demonstrated for the quad-cyclocopter using purely thrust vectoring, with independent pitch, roll, and yaw control.

Overall, the present research has clearly shown that cyclorotor is a viable MAV concept with aerodynamic efficiency comparable or even higher than a conventional rotorcraft, if properly designed. Because of the thrust vectoring capability,

cyclorotor-based MAVs can be extremely attractive where maneuverability is crucial.

6.3 Recommendations for Future Work

There are several areas where more research needs be performed to extend and improve upon the understanding gained from the present research. The performance measurements in the present study was focussed on optimizing the thrust and power loading of the cyclorotor by varying the blade kinematics, blade airfoil section and blade structural design. All these experiments were performed on a rotor with fixed geometry (span and diameter equal to 6 inches). However, it would be instructive to investigate the effect of rotor geometry on the cyclorotor performance. One of the geometrical parameters that can cause a significant impact is the rotor aspect ratio (span/diameter) for a constant diametrical area. Varying the span and diameter of the rotor, independently, could also cause significant improvements in the performance. Another parameter that could be studied is the effect of blade chord, keeping the radius and number of blades constant. Varying blade planform and installing winglets at the blade tips may also improve the performance of the cyclorotor. Since virtual camber has a significant effect on the performance of the rotor, testing a cambered blade to negate the virtual camber effect would be an interesting study. Also, as far as the PIV studies are concerned, in the present work the 2-D PIV measurements were only made at the midspan location. However, it would be useful to obtain the flowfield measurements at different spanwise loca-

tions. A 3-D PIV (stereo PIV) study can also be instrumental in understanding the three-dimensional flowfield of a cyclorotor.

The present study only focussed on hover. However, it is important to understand the forward flight performance of the cyclorotor. The effect of blade kinematics, blade airfoil section and rotor geometry should be investigated at difference advance ratios. It would be significant to note how the optimum blade kinematics would change with advance ratio. Systematic PIV studies should be also performed in forward flight.

Detailed CFD analysis should be developed and validated in order to obtain a deeper understanding of the physics of cyclorotors, both in hover and forward flight. The CFD model could complement the present study by being able to interpret the wealth of experimental data that has been generated. The CFD analysis needs to be coupled with a structural model to develop a comprehensive CFD-CSD analysis of the cyclorotor which can be used as a design and analysis tool for MAV-scale cyclorotors. Also, the lower order model developed in the present research needs to be extended to forward flight. Simultaneous aerodynamic/structural optmization studies should be performed to optimize the aerodynamic performance and the weight of the rotor structure.

Various control strategies should be investigated to perform unconstrained free-flight of the quad-cyclocopter. Feedback control methodologies should be developed for autonomous flight. Another aspect of this research would be investigating various vehicle configurations.

Appendix A

A Brief History of Cyclogyros

The earliest reported work on cyclogyros is in 1909. However, even though some of these early concepts (before Kirsten, 1926) could be classified as cyclogyros, there operational principle was different from the cycloidal rotors as of today.

In 1909, E. P. Sverchkov, a military engineer in St-Peterburg, Russia, developed this aircraft called "Samoljot", also called as "wheel-orthopter" (Fig. A.1(a)) [30]. Even though this concept was very similar to a cyclogiro, it could not be classified precisely. As shown in the figure, it had three flat surfaces and a rudder; rear edge of one of surfaces could be bent, replacing the action of an elevator. Lift and thrust had to be created by paddle wheels consisting of 12 blades, established in pairs under a 120° angle. The pitch angle of set of concave shape blades were changed by the means of eccentrics and springs. The rotor was driven by a 10 HP Bushe engine using a belt transmission. The three-wheel undercarriage was made droppable and was intended for takeoff only. Fabric-covered framework was made of thin-wall steel tubes and bamboo trunks with steel strings inside. Empty weight was about 200 kg. But the vehicle did not pass the tests successfully: It not only has not come off ground, but even has not moved from a place.

Figure A.1(b) shows a cyclogiro that was designed in France some where between 1909 and 1914 [30]. Not much information is available about this project
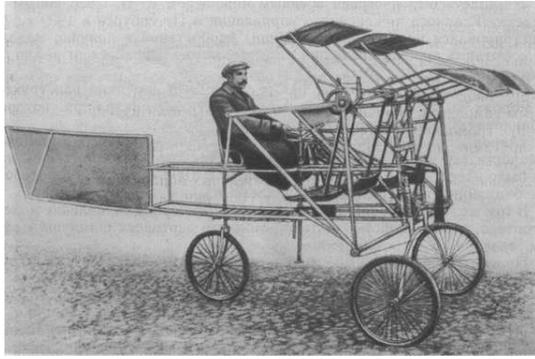
(a) Samoljot (1909) [30].

(b) Unknown french cyclocopter [30].

Figure A.1: **Some early cyclocopters.**
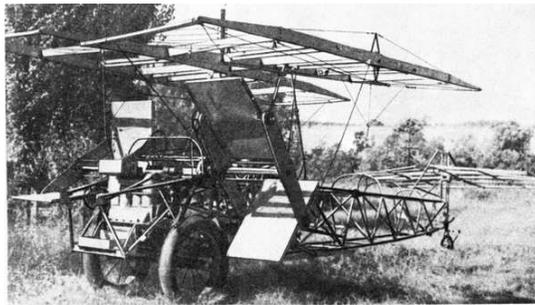
(a) Brooks's cyclogyro (1920s) [30].
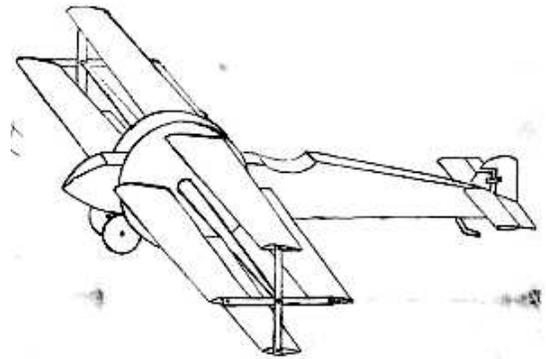
(b) Caldwell's cyclogyro design (1923) [30].

Figure A.2: **Some early cyclocopters.**

except for a video footage which shows two unsuccessful attempts, in one of which the rotor blades fail. The vehicle looked very similar to the present cyclocopter designs and it also had a tail cyclorotor unlike other vehicles build during those times.

In 1920s C. Brooks from Pattonville (Montana) built an aircraft with a "paddle-wheel" actuator (Fig. A.2) [30]. Presence of an assembly frame in front of the "paddle wheel" engine allows to assume that thrust had to be produced by one more

engine with the traditional propeller. There was a short, rotating upper wing, and a side-mounted paddle-wheel arrangement for forward flight. Not much information is available on Brook's aircraft, however, from the photograph of the vehicle, it does not look like that it could have successfully flown.

In 1923 Jonathan Edward Caldwell, an aeronautical engineer from US, filed for a patent on a device he called the "cyclogyro" [30]. The patent was granted in 1927. As shown in Fig. A.2(b), the cyclogyro consisted of an airplane fuselage with two paddle-wheel rotors in place of the wings. The rotors were powered by an engine in the fuselage. Each of the rotors used four high aspect ratio blades, which were cyclically pitched about a horizontal axis. By changing the pitch continually through the entire rotation, the lift of the airfoils could be tuned to produce thrust in any direction. For instance, to lift off vertically the airfoils were pitched to have a positive angle of attack only at the top of their rotation, just generating lift only at that point. In forward flight the angle at the top of the arc would be reduced to make the lift neutral, but they would retain their positive angle even through the forward part of the circle, producing forward thrust. By changing the angle in this fashion, the aircraft could move in any direction, with differential thrust between the two rotors yawing could be acheived.

Around 1937 Caldwell revived his 1923 Cyclogyro VTOL concept and started construction on a modified prototype as shown in Fig. A.3 [30]. It was another far-fetched VTOL plane in the style of the impractical flying machines that graced the covers of magazines like Popular Science through the 1930s. As shown in the figure, the inventor attempted to mount two long three-bladed airfoil-equipped pad-

273

(a) Cyclogyro design.

(b) Details of the design.

Figure A.3: **Caldwell's cyclogyro design (1937) [30].**

dlewheels to the sides of a conventional-looking aircraft fuselage, but this time the axles of the paddlewheels ran fore-and-aft, parallel to the length of the machine's body. The airfoils were geared in such a way that as they were spun by the machine's 125 HP radial engine, they would theoretically produce enough thrust to lift the craft straight up. One of Caldwell's associates later claimed that this craft actually made successful "test-hops" to a height of about six feet.

In 1926, Bruno Nagler of Austria filed a patent for a cyclogiro aircraft with two 4-bladed cycloidal propellers on either side (Fig. A.4) [88]. The blade pitching mechanism was passive with a pitch bearing and a torsional spring. Since the blade c.g. was coincident with the pitching axis, the passive pitch kinematics was completely governed by the aerodynamic force. The idea was that the pilot could control the tension in the springs using a mechanism and thereby obtain the required

Figure A.4: **Nagler's cyclogiro aircraft design (1926) [88].**

(a) Rohrbach cyclogyro (1930s) [30].
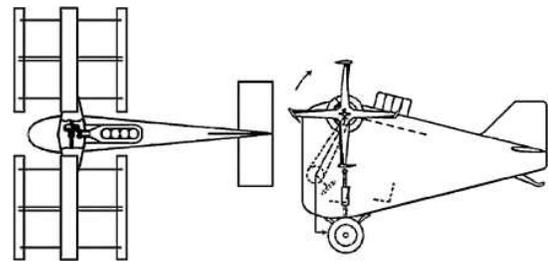
(b) Platt's cyclogyro design (1933) [30].

Figure A.5: **Rohrbach's and Platt's cyclogyros.**

blade kinematics depending on the flight condition. Using this control mechanism the pilot had pitch, roll and yaw control during all times. But there is no information available in literature regarding whether Nagler actually built this vehicle.

During this time, Adolf Rohrbach, a German aero technician designed a cyclogiro, which had two cyclorotors approximately at same position as wings of a high-wing monoplane (Fig. A.5(a)) [30, 89]. In cyclogiros, the blade pitch angle has to be varied differently for different forward speeds. Rohrbach's cyclogiro design was

(a) Schroeder's cyclogyro (1930) [29].

(b) Cyclogyro developed by Rahn Aircraft Corp (1935) [30].

Figure A.6: **Schroeder and Rahn cyclogyros.**

based on extensive calculations. This variation of angles of attack is calculated such that both lift and thrust are developed during a most part of revolution. Rohrbach's cyclogiro, as designed, had a length of 8.6 meters, height of 4.3 meters, and a total span of 10 meters. Blades had an aspect ratio of 14 and length of 4.4 m. Power required was 240 HP, possibly from two motors. Calculated empty weight is 680 kg, useful load (including 3 persons) is 270 kg; gross weight hence is 950 kg. With this weight maximal speed is 200 km/h. Ceiling is 4500 m in forward flight and 500 m in vertical climb. Range of flight is 400 km with passengers and 700 km without passengers.

In 1933, based on Rohrbachs cyclogiro research, Haviland Hull Platt, a US based engineer designed his own independent Cyclogyro (Fig. A.5(b)). His paddle-wheel wing arrangement was awarded a US patent, and underwent extensive wind-tunnel testing at MIT in 1927.

E. A. Schroeder in 1930 developed a Cyclogyro (aka S-1) (Fig. A.6(a)) in San Francisco [30]. This was a single-place, open-cockpit plane with Henderson engine.
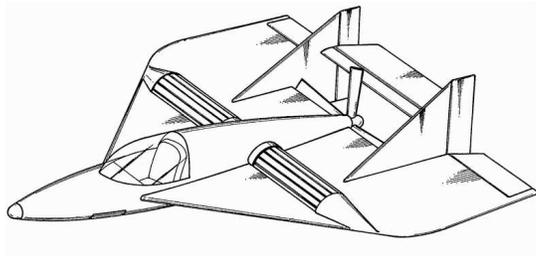
(a) Sharpe's first configuration [30].
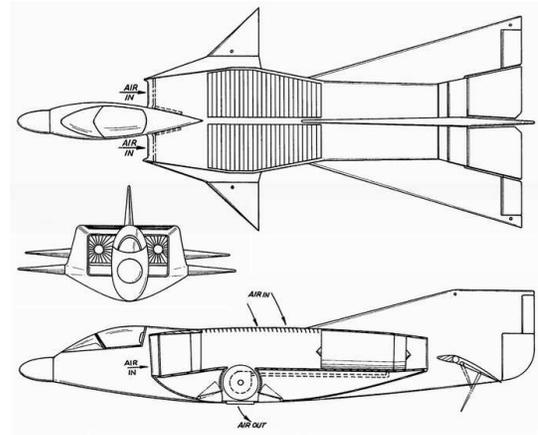
(b) Sharpe's second configuration [30].

Figure A.7: **Cyclogyro lift augmenting device by Sharpe (1977).**

Looked like an ordinary high-wing monoplane, except there were two large cycloidal propellers in front instead of a conventional screw propeller. It was expected that the cycloidal propellers will create both thrust and lift.

In 1935, Rahn Aircraft Corp in Brooklyn, NY, designed and built a one-seater aircraft (Fig. A.6(b)) with two 6 feet rotating wings on each side powered by a 240 HP supercharged Wright Whirlwind [30]. The two rotating wings theoretically would cause the plane to rise or descend vertically, or fly laterally without a conventional propeller up to 100 mph, but it is not recorded whether this 15 feet-long creation ever accomplished any of these feats.

In 1977 Thomas H. Sharpe filed a patent for an aircraft design where cyclogyros were used as lift augmenting device for the aircraft [30]. As shown in Fig. A.7(a), cyclogiro rotors of small radius, covered with casings, are placed in a wing and used as ordinary fans. Angles of incidence are controlled by simplified eccentric mechanism. In horizontal flight, the rotors are disconnected from the engine, and
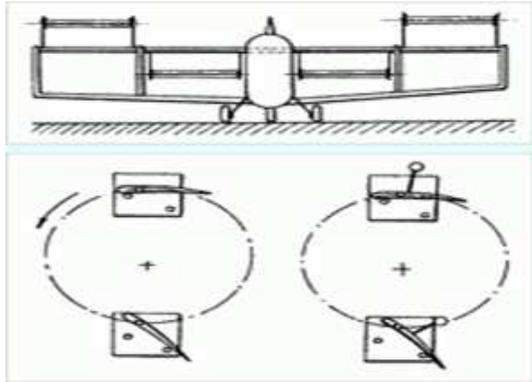
(a) Chabonat's "Propulsive Lifting Rotors" (1976) [30].
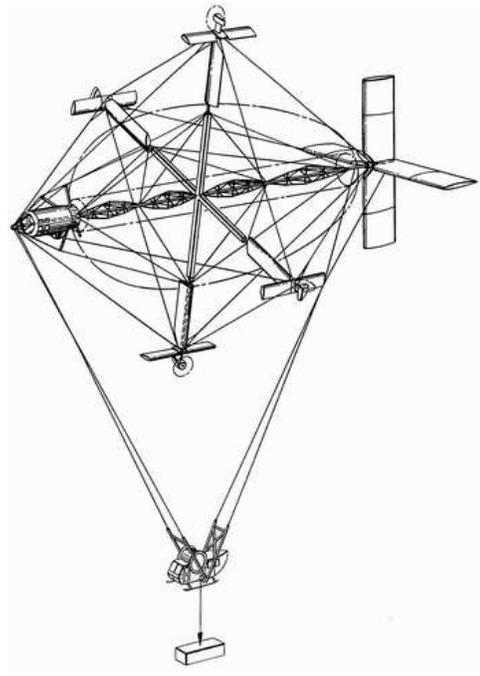
(b) Crimmins's flying crane design (1980) [30].

Figure A.8: **Chabonat's and Crimmins's patents.**

horizontal thrust is created by usual variable-pitch pushing propeller. The longitudinal balancing is provided by an elevator placed in an airflow from propeller. The elevator has an additional shutter for thrust reversing.

The second version of the device (Fig. A.7(b)) is intended for high-speed aircrafts. Turbojet engines and two pairs of air intakes (top and lateral) are used. Transmission from the engines to cyclogiro rotors is hydraulic. In horizontal flight, top air intakes and fan outlets are closed with shutters. The additional control facilites for a hovering flight jet nozzles on the wings and on the vertical stabilizer, supplied with compressed air from turbojet compressors were stipulated.

In 1976 Marcel Chabonat filed a patent for a kind of cyclorotors, which he
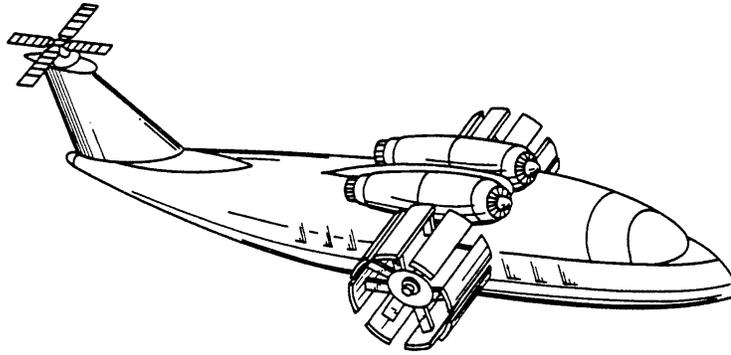
Figure A.9: **Heinz's cyclogiro aircraft design (1992) [30].**

called propulsive lifting rotors (Fig. A.8(a)) [30]. The rotors are two-bladed. In the first version, the variation of an angle of incidence is obtained in a passive fasion using the aerodynamic and/or centrifugal forces. When moving down, the blade produces lift, when moving up it produces thrust. Thus, in the bottom of a cycle, the angle of incidence changes abruptly, with an impact. In the second version, the angle of incidence is changing with the means of profiled cams. It is supposed to have a set of cams for different modes of flight (take-off, climb, cruise flight, descent or landing).

In 1980 Arthur G. Crimmins filed a patent for a "Cyclorotor composite aircraft" (Fig. A.8(b)) [30]. The main purpose of this composite aircraft was to be a flying crane. The body weight of the craft is counterbalanced by aerostatic lift of a balloon, and weight of a cargo by the lift of cyclogiro wings. The wings and thrust means are mounted on turnable pylones, playing also the role of propeller blades. The device can accept a configuration of a "classical" airship, "classical" cyclogiro and all intermediate configurations. Due to this, there are no restrictions on the orientation of the thrust vector and that is what a flying crane needs.

In 1992 Heinz A. Gerhardt filed a patent for a "Paddle wheel rotorcraft" which was essentially a cyclogyro (Fig. A.9) [30]. For this vehicle, the longitudinal balancing was provided either by vertical propeller on a vertical stabilizer, or by second pair of cyclogiro rotors. One main feature of this aircraft was the absence of kinematic management of an angle of incidence of blades. Instead, on each blade the hydrocylinder constantly controlled by the computer provides the required blade kinematics. This way, it is supposed to achieve an optimum performance of each blade at all regimes of flight.

Bibliography

[1] Hundley, R. O., and Gritton, E. C., "Future Technology-Driven Revolutions in Military Operations: Results of a Workshop," RAND National Defense Research Institute DB-110-ARPA, Santa Monica, CA, 1994 Defense Technical Information Center (DTIC) Accession Number ADA285478.

[2] McMichael, J. M., and Francis, USAF (Ret.), C. M. S., "Micro Air Vehicles Toward a New Dimension in Flight," *U.S. Department of Defense Weapons Systems Technology Information Analysis Center (WSTIAC) Newsletter*, Vol. 1, No. 13, JanJul 2000 Originally published online at http://www.darpa.mil/tto/MAV/mav auvsi.html, Aug. 7, 1997.

[3] Mueller, T. and DeLaurier, J., "Aerodynamics of Small Vehicles," *Annual Rev. of Fluid Mech.*, Vol. 35, 2003, pp. 89-111.

[4] Pines, D., and Bohorquez, F., "Challenges Facing Future Micro-Air-Vehicle Development," *Journal of Aircraft*, Vol. 43, (2), March/April 2006, pp. 290–305.

[5] Pereira, J. L., "Hover and Wind-Tunnel Testing of Shrouded Rotors for Improved Micro Air Vehicle Design," Ph.D Thesis, Department of Aerospace Engineering, University of Maryland College Park, September 2008.

[6] Schmitz, F. W., "Aerodynamics of Model Aircraft wing Measurements I", R.T.P. Translation No 2460. Issued by Ministry of Aircraft Production. 1983.

[7] Abbott, I. H., and Von Doenhoff, A. E., *Theory of Airfoil sections*, Dover, New York, 1959.

[8] Riegels, F. W., *Airfoil sections*, Butterworth, London, 1961.

[9] Althaus, D., and Wortmann, F. X., "Stuttgarter profilkatalog I - Experimental results for the laminar wind tunnel of the University of Stuttgart," Friedr. Vieweg and Sohn, Braunschweig, 1972 (English version in 1981).

[10] McMasters, J. and Henderson, M., "Low-Speed Single Element Airfoil Synthesis," Technical Soaring, Vol. 6, 1980, pp. 1-21.

[11] Lissaman, P., "Low-Reynolds-Number Airfoils," *Annual Rev. of Fluid Mech.*, Vol. 15, 1983, pp. 223-239.

[12] Mueller, T. J., and Batill, S. M., "Experimental studies of separation on a two-dimensional airfoil at low Reynolds numbers," *AIAA Journal*, Vol. 20, No.4, 1982, pp. 457–463.

[13] OMeara, M. M., and T. J. Mueller., "Laminar Separation Bubble Characteristics on an Airfoil at Low Reynolds Numbers." *AIAA Journal*, Vol. 25, No. 8, August 1987, pp. 1033–1041.

[14] Bastedo, W. G., Jr., and Mueller, T. J., "The Spanwise Variation of Laminar Separation Bubbles on Finite Wings at Low Reynolds Numbers," *Journal of Aircraft*, Vol. 23, No. 9, pp. 687–694, September 1986.

[15] Pelletier, A., and Mueller, T. J., "Low Reynolds number aerodynamics of low-aspect-ratio, thin/flat/cambered-plate wings," *Journal of Aircraft*, Vol. 37, No.5, 2000, pp. 825-832.

[16] Mueller, T. J., "Aerodynamic Measurements at Low Reynolds Numbers for Fixed Wing Micro-Air Vehicles," Presented at the RTO AVT/VKI Special Course on Development and Operation of UAVs for Military and Civil Applications, VKI, Belgium, September 13–17, 1999.

[17] Laitone, E. V., "Wind Tunnel Tests of Wings at Reynolds Numbers Below 70,000," *Experiments in Fluids*, Vol. 23, 1997, pp. 405–409

[18] Selig M. S., Donovan J. F., and Fraser D. B., *Airfoils at Low Speeds*, Soar Tech Publ., Virginia Beach, VA, 1989.

[19] McArthur, J., *Aerodynamics of wings at low Reynolds numbers: Boundary layer separation and reattachment* PhD thesis, University of Southern California, Department of Aerospace and Mechanical Engineering, 2008.

[20] Carmichael, B., "Low Reynolds Number Airfoil Survey," NASA CR165803, 1981.

[21] Ifju, P. G., Jenkins, D. A., Ettinger, S., Lian, Y., Shyy, W., and Waszak, M. R., "Flexible-Wing-Based Micro Air Vehicles," Paper AIAA-2002-705, AIAA 40th Aerospace Sciences Meeting and Exhibit, Reno, NV, January 14–17, 2002.

[22] Peterson, B., Erath, B., Henry, K., Lyon, M., Walker, B., Powell, N., Fowkes, K., and Bowman, W. J., "Development of a Micro Air Vehicle for Maximum Endurance and Minimum Size," Paper AIAA-2003-416, AIAA 41st Aerospace Sciences Meeting and Exhibit, Reno, NV, January 6–9, 2003.

[23] Brion, V., Aki, M., and Shkarayev, S., "Numerical Simulation of Low Reynolds Number Flows Around Micro Air Vehicles and Comparison Against Wind Tunnel Data," Paper AIAA-2006-3864, AIAA 24th Applied Aerodynamics Conference Proceedings, San Francisco, CA, June 5–8, 2006.

[24] Grasmeyer, J. M., and Keennon, M. T., "Development of the Black Widow Micro Air Vehicle," Paper AIAA-2001-0127, AIAA 39th Aerospace Sciences Meeting and Exhibit, Reno, NV, January 8–11, 2001.

[25] Keenon, M. T., and Grasmeyer, J. M., "Development of the Black Widow and Microbat MAVs and a Vision of the Future of MAV Design," Paper AIAA-2003-2901, AIAA/ICAS International Air and Space Symposium and Exposition, The Next 100 Years Proceedings, Dayton, OH, July 14–17, 2003.

[26] Hein, B., and Chopra, I., "Hover Performance of a Micro Air Vehicle: Rotors at Low Reynolds Number," *Journal of American Helicopter Society*, Vol. 52, (3), July 2007, pp. 254–262.

[27] Chopra, I., "Hovering Micro Air Vehicles: Challenges and Opportunities," Proceedings of American Helicopter Society Specialists' Conference, International Forum on Rotorcraft Multidisciplinary Technology, October 15–17, 2007, Seoul, Korea

[28] Kim, S., Yun, C., Kim, D., Yoon, Y., and Park, I., "Design and Performance Tests of Cycloidal Propulsion Systems," Paper AIAA-2003-1786, 44th AIAA/ASME/ASCE/AHS/ASC Structures, Structural Dynamics, and Materials Conference, Norfolk, Virginia, April 7–10, 2003.

[29] Boirum, C. G., and Post, S. L., "Review of Historic and Modern Cyclogyro Design," Paper AIAA-2009-5023, 45th AIAA/ASME/SAE/ASEE Joint Propulsion Conference and Exhibit, Denver, CO, August 2–5, 2009.

[30] "Cyclogyro History," World-Wide Web document, $http$: $//www.rotoplan.narod.ru/history_e.htm$, May 19, 2007.

[31] Sachse, H., "Kirsten-Boeing Propeller," Technical Memorandum 351, National Advisory Committee for Aeronautics, January 1926.

[32] Kirsten, F. K., "Cycloidal Propulsion Applied to Aircraft," *Transactions of the American Society of Mechanical Engineers*, Vol. 50, (12), 1928, pp 25–47.

[33] "Flying Without Wings or Motors, an interview with F. K. Kirsten (Popular Science 1934)," World-Wide Web document, $http$:

$//blog.modernmechanix.com/2007/09/04/flying - without - wings - or - motors/$, Sept 4, 2007.

[34] "Voith Schneider Propeller," World-Wide Web document, $http : //en.wikipedia.org/wiki/Voith_schneider_Propeller$, Nov 28, 2010.

[35] "Voith Schneider Propeller," World-Wide Web document, $http : //www.renewbl.com/2010/07/16/voith - turbo - supplying - propellers - for - two - jack - up - vessels.html$, July 16, 2010.

[36] Strandgren, C., "The Theory of the Strandgren Cyclogyro," Technical Report 727, National Advisory Committee for Aeronautics, July 1933.

[37] Wheatley, J., "Simplified Aerodynamic Analysis of the Cyclogiro Rotating-Wing System," Technical Report 467, National Advisory Committee for Aeronautics, August 1933.

[38] Wheatley, J. B., and Windler, R., "Wind-Tunnel Tests of a Cyclogiro Rotor," NACA Technical Note No. 528, May 1935.

[39] Taniguchi, K., "An Approximate Solution of the Voith-Schneider Propeller", *Journal of Zosen Kiokai (Trans. Soc. of Naval Arch. of Japan)*, Vol. 74, 1944, pp. 153–161.

[40] Taniguchi, K., "Hydrodynonical Investigations of the Blade Wheel Propeller", *Journal of Zosen Kiokai (Trans. Soc. of Naval Arch. of Japan)*, Vol. 88, 1950, pp. 63–74.

[41] Taniguchi, K., "Studies on a Trochoidal Propeller", Doctor of Engineering Thesis, Tokyo University, 1960.

[42] Haberman, W. L., and Harley, E. E., "Performance of Vertical Axis (Cycloidal) Propellers Calculated by Tanuguchi's Method", Report No 1564. Department of the Navy, David Taylor Model Basin, Hydromechanics Laboratory Research and Development Report. November 1961.

[43] Boschma, J. H., "Modern Aviation Applications for Cycloidal Propulsion," Paper AIAA-2001-5267, AIAA Aircraft, Technology Integration, and Operations Forum Proceedings, Los Angeles, CA, October 16–18, 2001.

[44] Gibbens, R., "Improvements in Airship Control using Vertical Axis Propellers," Paper AIAA-2003-6853, 3rd AIAA Annual Aviation Technology, Integration, and Operations (ATIO) Forum Proceedings, Denver, CO, Nov. 17–19, 2003.

[45] Gibbens, R., Boschma, J., and Sullivan, C., "Construction and Testing of a New Aircraft Cycloidal Propeller," Paper AIAA-1999-3906, AIAA 13th Lighter-Than-Air Systems Technology Conference Proceedings, Norfolk, VA, June 28–July 1, 1999.

[46] McNabb, M., "Development of a Cycloidal Propulsion Computer Model and Comparison with Experiment," M.S. Thesis, Department of Aerospace Engineering, Mississippi State University, December 2001.

[47] Garrick, I. E., "Propulsion of a flapping and Oscillating Airfoil", Technical Report 567, National Advisory Committee for Aeronautics, 1937, pp. 419–427.

[48] Iosilevskii, G., and Levy, Y., "Experimental and Numerical Study of Cyclogiro Aerodynamics," *AIAA Journal*, Vol. 44, (12), 2006, pp 2866–2870.

[49] Iosilevskii, G., and Levy, Y., "Aerodynamics of the Cyclogiro", Paper AIAA-2003-3473, AIAA 33rd Fluid Dynamics Conference and Exhibit, Orlando, FL, June 23–26, 2003.

[50] Levy, Y., "Numerical Simulation of Dynamically Deforming Aircraft Configurations Using Overset Grids," *Journal of Aircraft*, Vol. 38, No. 2, 2001, pp. 349-354.

[51] Benek, J. A., Buning, P. G., and Steger, J. L., "A 3-D Chimera Grid Embedding Technique," Paper AIAA-85-1523, AIAA 7th Computational Fluid Dynamics Conference, Cincinnati, OH, July 15–17, 1985.

[52] Beam, R. M., and Warming, R. F., "An Implicit Factored Scheme for the Compressible NavierStokes Equations," *AIAA Journal*, Vol. 16, No. 4, 1978, pp. 393-402.

[53] Yun, C. Y., Park, I., Lee, H. Y., Jung, J. S., Hwang, I. S., Kim, S. J. and Jung, S. N., A New VTOL UAV Cyclocopter with Cycloidal Blades System, Proceedings of the 60th American Helicopter Society Annual Forum, Baltimore, MD, June, 2004.

[54] Yun, C. Y., Park, I. K., Lee, H. Y., Jung, J. S., Hwang, I. S., and Kim, S. J., "Design of a New Unmanned Aerial Vehicle Cyclocopter," *Journal of American Helicopter Society*, Vol. 52, (1), January 2007, pp. 24–35.

[55] Hwang, I. S., Min, S. Y., Lee, C. H., and Kim, S. J., "Development of a Four-Rotor Cyclocopter," *Journal of Aircraft*, Vol. 45, (6), NovemberDecember 2008, pp. 2151–2157.

[56] Yun, C. Y., Park, I. K., Hwang, I. S., and Kim, S. J., "Thrust Control Mechanism of VTOL UAV Cyclocopter with Cycloidal Blades System," *Journal of Intelligent Material Systems and Structures*, Vol. 16, No. 11-12, December 2005, pp. 937–943.

[57] Hwang, I. S., Hwang, C. P., Min, S. Y., Jeong, I. O., Lee, C. H., Lee., Y. H., and Kim, S. J., "Design and Testing of VTOL UAV Cyclocopter with 4 Rotors," American Helicopter Society 62nd Annual Forum Proceedings, Phoenix, AZ, April 29–May 1, 2006.

[58] Hwang, I. S., Hwang, C. S., and Kim, S. J., "Structural Design of Cyclocopter Blade System," Paper AIAA-2005-2020, 46th AIAA/ASME/ASCE/AHS/ASC Structures, Structural Dynamics and Materials Conference Proceedings, Austin, TX, April 18–21, 2005.

[59] Kim, S. J., Hwang, I. S., Lee, H. Y., and Jung, J. S., "Design and Development of Unmanned VTOL Cyclocopter," Symposium on Aerospace Science and Technology Proceedings, NC, August 12–14, 2004.

[60] "The Development of Cyclogyro," World-Wide Web document, *http* : *//serve.me.nus.edu.sg/cyclocopter/*, Feb 19, 2007.

[61] Yu, H., Bin, L. K., and Beng, T. W., "The Investigtion of Cyclogyro Design and the Performance," Proceedings of the 25th International Congress of the Aeronautical Sciences, Hamburg, Germany, September 3–8, 2006.

[62] Yu, H., Bin, L. K., and Rong, H. W., "The Research on the Performance of Cyclogyro," Paper AIAA-2006-7704, AIAA 6th Aviation Technology, Integration and Operations Conference Proceedings, Wichita, KS, September 25–27, 2006.

[63] Sirohi, J., Parsons, E., and Chopra, I., "Hover Performance of a Cycloidal Rotor for a Micro Air Vehicle," *Journal of American Helicopter Society*, Vol. 52, (3), July 2007, pp. 263–279.

[64] Clark, R., Acuity Technologies Inc., "SBIR A02.07: VTOL to Transonic Aircraft", Final technical report, July 24, 2006.

[65] Siegel, S., Seidel, J., Cohen, K., and McLaughlin, T., "A Cycloidal Propeller Using Dynamic Lift," Paper AIAA-2007-4232, AIAA 37th Fluid Dynamics Conference and Exhibit, Miami, FL, June 25–28, 2007.

[66] Hara, N., Tanaka, K., Ohtake, H., and Wang, H., "Development of a Flying Robot with Pantograph-based Variable Wing Mechanism," Proceedings of the

2007 IEEE International Conference on Robotics and Automation, Roma, Italy, April 10–14 2007, pp. 349–354.

[67] Tanaka, K., Suzuki, R., Emaru, T., Higashi, Y., and Wang HO., "Development of a Cyclogyro-based Flying Robot with Variable Attack Angle Mechanisms," *IEEE/ASME Transaction on Mechatronics*, Vol. 12, No. 5, October 2007.

[68] Nozaki, H., Sekiguchi, Y., Matsuuchi, K., Onda, M., Murakami, Y., Sano, M., Akinaga, W., and Fujita, K., "Research and Development on Cycloidal Propellers for Airships," Paper AIAA-2009-2850, AIAA 18th Lighter-Than-Air Systems Technology Conference, Seattle, Washington, May 4–7, 2009.

[69] Yang, K., Lakshminarayan, V. K., and Baeder, J. D., "Simulation of a Cycloidal Rotor System Using an Overset RANS Solver," To be presented at American Helicopter Society 66th Annual Forum Proceedings, Phoenix, AZ, May 11–13, 2010.

[70] Nakaie, Y., Ohta, Y., and Hishida, K., "Flow Measurements around a Cycloidal Propeller," *Journal of Flow Visualization*, Vol. 16, No. 4, 1978, pp. 393-402.

[71] Leishman, J. G., *Principles of Helicopter Aerodynamics*, Cambridge University Press, Cambridge, UK, 2000.

[72] Migliore, P. G., Wolfe, W. P., and Fanuccif, J. B., "Flow Curvature Effects on Darrieus Turbine Blade Aerodynamics," *Journal of Energy*, Vol. 4, (2), 1980, pp. 49–55.

[73] Mandal, A. C., and Burton, J. D., "The effects of dynamic stall and flow curvature on the aerodynamics of Darrieus turbines applying the Cascade model," *Wind Engineering*, Vol. 18, (6), 1994, pp. 267–282.

[74] Lindenburg, C., "BLADMODE Program for Rotor Blade Mode Analysis," Ecn c02-050, 2003.

[75] Hrishikeshavan, V. and Chopra, I., Design and Testing of a Shrouded Rotor MAV with Anti-Torque Vanes, Proceedings of the 64th Annual National Forum of the American Helicopter Society, Montreal, Canada, April 28–30, 2008.

[76] Scarano, F., "Iterative Image Deformation Methods in PIV," *Measurement Science and Technology*, Vol. 12, 2002, pp. R1–R19.

[77] Ramasamy, M., and Leishman, J. G., "Benchmarking Particle Image Velocimetry with Laser Doppler Velocimetry for Rotor Wake Measurements," *AIAA Journal*, Vol. 45, (11), November 2007, pp. 2622–2633.

[78] Ramasamy, M., Leishman, J. G., Johnson, B., and Huismann, T., "Procedures for Measuring the Turbulence Characteristics of Rotor Tip Vortices," *Journal of the American Helicopter Society*, Vol. 54, (2), April 2009, pp. 022006-1–022006-17

[79] Duraisamy, K., Ramasamy, M., Baeder, J. D., and Leishman, J. G., "High-Resolution Computational and Experimental Study of Rotary Wing Tip Vortex Formation," *AIAA Journal*, Vol. 45, (11), November 2007, pp. 2593–2602.

[80] Ramasamy, M., Johnson, B., and Leishman, J. G., "Tip Vortex Measurements Using Dual Plane Digital Particle Image Velocimetry," American Helicopter Society 64th Annual National Forum Proceedings, Montréal, Canada, April 28–30, 2008.

[81] Ramasamy, M., Johnson, B., and Leishman, J. G., "Understanding the Aerodynamic Efficiency of a Hovering Micro-Rotor," *Journal of American Helicopter Society*, Vol. 53, No. 4, October 2008, pp. 412–428.

[82] Hodges, D. H., and Dowell, E. H., "Nonlinear Equations of Motion for the Elastic Bending and Torsion of Twisted Nonuniform Rotor Blades," NASA TN D-7818.

[83] Datta, A., "Fundamental Understanding, Prediction and Validation of Rotor Vibratory Loads in Steady-Level Flight," Ph.D Thesis, Department of Aerospace Engineering, University of Maryland College Park, September 2004.

[84] Masarati, P., Lanz, M., and Mantegazza, P., "Multistep Integration of Ordinary, Stiff and Differential-Algebraic Problems for Multibody Dynamics Applications," XVI Congresso Nazionale AIDAA, Palermo, September 24–28, 2001, pp. 71.1–10.

[85] Ghiringhelli, G. L., Masarati, P., and Mantegazza, P., "A Multi-Body Implementation of Finite Volume Beams," *AIAA Journal*, Vol. 38, No. 1, January 2000, pp. 131–138, doi:10.2514/2.933.

[86] Strickland, J. H., "The Darrieus Turbine: A Performance Prediction Model Using Multiple Streamtubes," Sandia National Laboratories, Albuquerque, NM, SAND75-0431, October 1975.

[87] Bielawa, R. L., *Rotary Wing Structural Dynamics and Aeroelasticity*, AIAA, Washington, DC, 1992.

[88] Nagler, B., "Improvements in Flying Machines Employing Rotating Wing Systems," United Kingdom Patent No. 280,849, issued November 1926.

[89] Shackleton, W. S., "The Rohrbach Rotating Wing Aeroplane", *Flight*, November 9, 1933, pp. 1122–1124.